TU Delft

Delft University of Technology

A Methodology for the Design of Kite-Power Control Systems

Fechner, Uwe

DOI
10.4233/uuid:85efaf4c-9dce-4111-bc91-7171b9da4b77

Publication date
2016

Document Version
Final published version

Citation (APA)
Fechner, U. (2016). *A Methodology for the Design of Kite-Power Control Systems*. [Dissertation (TU Delft), Delft University of Technology]. https://doi.org/10.4233/uuid:85efaf4c-9dce-4111-bc91-7171b9da4b77

Important note
To cite this publication, please use the final published version (if applicable).
Please check the document version above.

Copyright
Other than for strictly personal use, it is not permitted to download, forward or distribute the text or part of it, without the consent of the author(s) and/or copyright holder(s), unless the work is under an open content license such as Creative Commons.

Takedown policy
Please contact us and provide details if you believe this document breaches copyrights.
We will remove access to the work immediately and investigate your claim.

This work is downloaded from Delft University of Technology.
For technical reasons the number of authors shown on this cover page is limited to a maximum of 10.

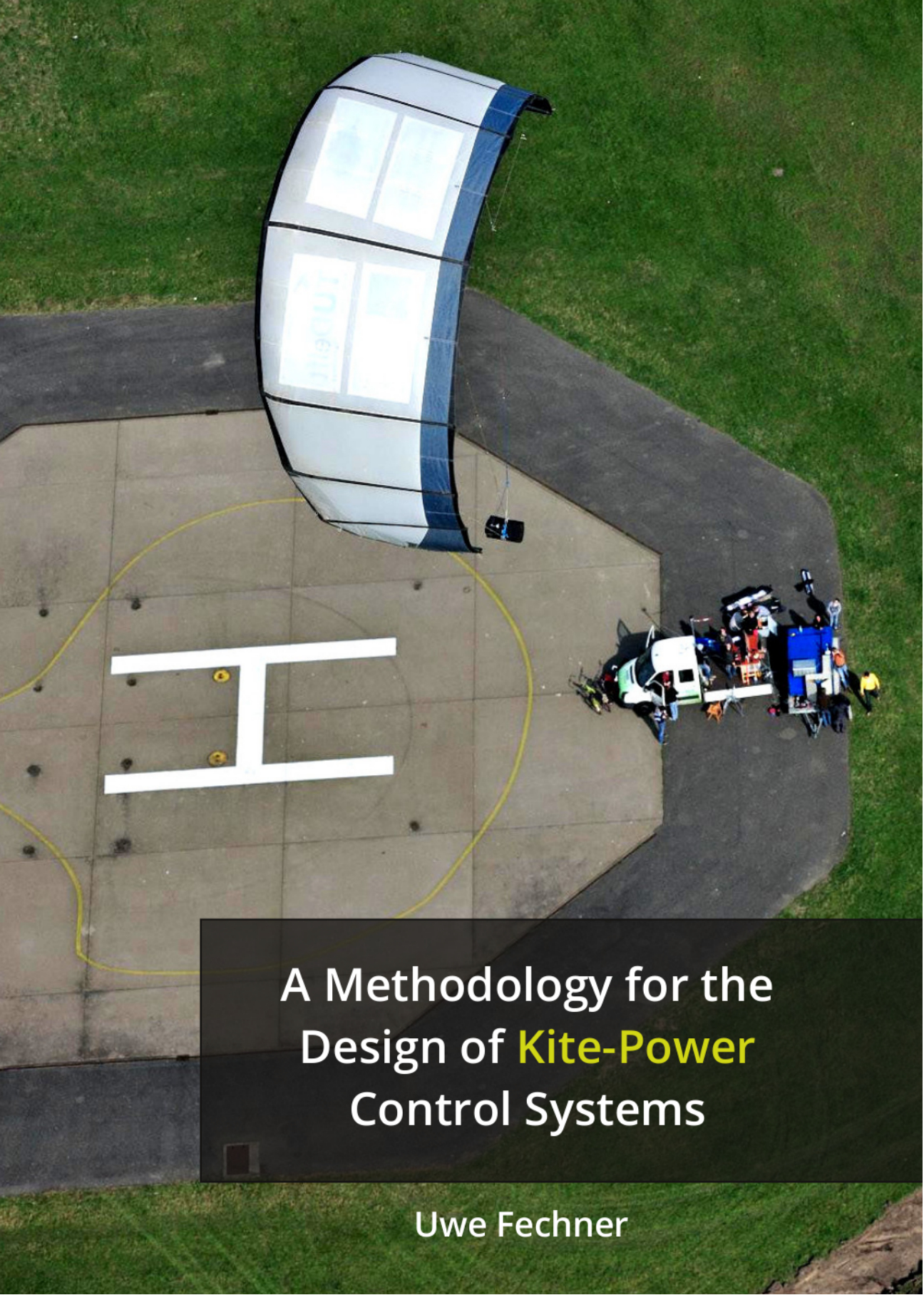

A Methodology for the Design of Kite-Power Control Systems

Uwe Fechner

A Methodology for the Design of Kite-Power Control Systems

Proefschrift

ter verkrijging van de graad van doctor aan de Technische Universiteit Delft, op gezag van de Rector Magnificus prof. ir. K.Ch.A.M. Luyben; voorzitter van het College voor Promoties, in het openbaar te verdedigen op

woensdag 23 november 2016 om 10:00 uur

door

Uwe FECHNER

Master of Science in Elektro- und Informationstechnik
FernUniversität in Hagen, Duitsland

geboren te Berlijn, Duitsland

This dissertation has been approved by the

promotor	Prof. dr. G.J.W. van BUSSEL and
copromotor	Dr.-Ing. R. SCHMEHL

Composition of the doctoral committee:

Rector Magnificus,	chairperson
Prof. dr. G.J.W. van BUSSEL	promotor
Dr.-Ing. R. SCHMEHL	copromotor

Independent members:

Prof. dr. ir. M. MULDER	TU Delft
Prof. dr. R. BABUSKA	TU Delft
Dr. G. LOPES	Robot Care Systems, Den Haag
Dr. M. FONTANA	Scuola Superiore Sant'Anna, Italy
Dr. J. BREUKELS	Allseas Engineering B.V., Delft

ISBN: 978-94-028-0409-6

A Methodology for the Design of Kite-Power Control Systems/
Fechner, U./ 2016

Published by the author
Printed by Ipskamp Printing, Enschede, Netherlands
Copyright ©2016 U. Fechner

Acknowledgements

When I came to Delft in summer 2010 to work for Prof. dr. Wubbo Ockels on kite control I was very enthusiastic: I loved the city of Delft, which is very beautiful, and I enjoyed it a lot to go testing at Valkenburg airfield.

It was exciting to work at the ASSET[1] Institute. This was exactly the kind of environment, in which I always have dreamed to work: Using science and technology in an interdisciplinary, international team to solve real, pressing problems of mankind.

This team consisted of many students and researchers. In particular I want to thank Rolf van der Vlugt, our kite pilot for demonstrating and explaining how to fly a kite and our project leader Aart de Wachter for all the energy he put into the kite power project to make it a success. I want to thank Barend Lubbers, Sergiy Ulyashin, Filip Saad and Jan Harms for their support as researchers and software developers.

Moreover I want to thank my daily supervisor, Dr. Roland Schmehl for proofreading and correcting all of my articles.

I want to thank all of the MSc students of the kite power group for their effort and their input: Jorn Baayen, Claudius Jehle, Antonio Ramos, Moritz Koplin, Marien Ruppert, Jonathan Ramirez, Edwin Schreuder, Johannes Peschel, Pietro Faggiani, Rachel Leutholt, Felix Friedl, Lukas Braun, Mustafa Karadayi and Andres Moreno.

After the ASSET Institute was closed the kite power group became part of the wind energy research group at Delft University of Technology. In this group I got to know many exciting wind energy researchers, who shared their knowledge with me. In particular I want to mention René Bos who helped me with implementing the turbulence model, but also William Anderson, Wei Yu, Zi Wang, Daniel Baldacchino, Ashim Giyanani, Volkan Salma and Gaél Oliveira Andrade, who became good companions.

Furthermore I want to thank Aslı Andaç for joining my life in The Netherlands. Her humour and creativity improved the quality of my life a lot.

Finally I want to thank my promotors Wubbo Ockels († 2014) and Gerard van Bussel for guiding my research and giving useful feedback and all the committee members for investing their time to improve this thesis.

[1] Applied Sustainable Science, Engineering and Technology

Summary

The major goal of this thesis is to provide a methodology to kite power system developers for the design of winch and kite control systems. The focus of this thesis is on soft-wing pumping kite power systems with ground based electricity generation. Secondary questions are: which conversion efficiency can be achieved with a kite power system; how can such efficiency be defined and whether or not it is realistic to assume that kite power has the potential to become cheaper than the cheapest fossil energy resources.

For this research project a combination of practical and theoretical approaches was chosen. In the years 2010-2012 a kite power system prototype with fully automated power cycles was developed, implemented and tested. The development process of the original prototype inspired this work, but does not belong to the core part of this thesis.

At the same time a quasi-static system model was developed and used for system optimization. A year later a dynamic system model was developed and verified against the measurement data. Finally an improved flight path planner and improved controllers were developed, implemented and tested against the verified, dynamic system model. A realistic environmental model that takes the wind shear and wind turbulence into account is added.

The most important performance factors that are identified and defined are: the total efficiency which is the quotient of the average electrical output power and the average mechanical power during reel-out; the cost factor, the quotient of the average electrical output at nominal wind conditions and the nominal generator power. Using the quasi-static system model it is shown, that with a soft wing kite with a maximal lift over drag coefficient of five and a winch with two separate permanent magnet synchronous machines for reel-in and reel-out a total efficiency of more than 50% can be achieved. The results from the thesis indicate that for systems larger than 50 kW and with improved wing designs even higher values are possible.

Furthermore crest factors (quotients of the maximum and average value of a physical quantity) of the tether force and the mechanical power are introduced to be used as

performance indicators. In this thesis such crest factors, well known from electrical engineering are for the first time applied on airborne wind energy systems. It is shown that they are very useful to understand and optimize the process of harvesting wind energy from higher altitudes. With a good control system a crest factor of 1.2 for the force and of 1.5 for the power is achievable as demonstrated in the dynamic simulation presented in this thesis.

For the development and the comparison of control algorithms it is essential to have a fast system model. A real-time model of the kite, the tether and the ground station is presented. It is easy to modify and extend the model, because a high-level programming language (Python) is used. Kite and tether are both modelled as particle system, an approach applicable to both soft and rigid wing kites.

Furthermore a sophisticated environmental model is implemented that includes the wind shear based on an empirically fitted exponential profile law and a turbulent wind field, using the Mann model. This model is useful for studying the influence of turbulence on systems of different size, flying at different heights. In contrast to preliminary expectations of the author it is found that wind turbulence does not have a significant impact on the annual energy production of the investigated system. This limited sensitivity to turbulence might be different for systems smaller than 20 kW or operated at heights lower than 200 m.

The developed modelling approach provides the foundation for highly accurate airborne wind energy simulation tools, which are urgently needed by airborne wind energy developers and researchers.

When this research started there was a hypothesis, that nonlinear model-predictive control (NMPC) was needed for the control of a kite-power system. In the investigated context this hypothesis is found to be wrong: A reliable, robust control system is presented using parameter varying PID controllers and nonlinear-dynamic inversion. This enables the implementation of small and lightweight flying control systems without the need of a very fast system model.

Using the presented methodology it is possible to improve the average mechanical power for a system with a 20 kW generator under nominal wind conditions by nearly a factor of two (from 6 kW to about 12 kW). This progress in research brings kite-power one step closer to commercialization. Further research is needed, but the models, results and conclusions of this thesis can be used as a solid starting point for future kite-power developers and researchers.

This work contributes to the goal to use airborne wind energy to bring clean electricity faster to a lot more people than it would be possible with conventional wind and solar alone. May this thesis be a step forward to a clean, sustainable future.

Keywords: kite control, airborne wind-energy, distributed control, kite-power systems, efficiency, pumping kite-power system

Samenvatting

Het hoofddoel van dit proefschrift is een methodologie te verschaffen voor ontwikkelaars van vlieger-energiesystemen voor het ontwerpen van lier- en vlieger-besturingssystemen. De focus van dit proefschrift is op pompende vlieger-energiesystemen met grondgebonden opwekking van elektriciteit. Secundaire vragen zijn: welke conversie-efficiëntie kan worden bereikt met een vlieger-energiesysteem; hoe kan deze efficiëntie worden gedefinieerd; en of het al dan niet realistisch is om aan te nemen dat vlieger-energie het potentieel heeft om goedkoper te worden dan de goedkoopste fossiele energievoorraden.

Voor dit onderzoeksproject is er gekozen voor een combinatie van praktische en theoretische benaderingen. In de jaren 2010-2012 is er een prototype voor een vlieger-energiesysteem met volledige geautomatiseerde energiecycli ontwikkeld, geïmplementeerd en getest. Het ontwikkelingsproces van het oorspronkelijke prototype inspireerde dit werk, maar behoort niet tot de kern van dit proefschrift.

Tegelijkertijd was een quasi-statisch systeemmodel ontwikkeld en gebruikt voor systeemoptimalisatie. Een jaar later was er een dynamisch systeemmodel ontwikkeld en geverifieerd tegen de meetdata. Tenslotte een verbeterd vliegrouteplanner en verbeterde besturingssystemen waren ontwikkeld, geïmplementeerd en getest tegen het geverifieerd dynamisch systeemmodel. Een realistisch omgevingsmodel dat de windschering en -turbulentie in acht neemt is toegevoegd.

De belangrijkste prestatiefactoren die zijn geïdentificeerd en gedefinieerd zijn: de totale efficiëntie welk de quotiënt van de gemiddelde elektrische vermogensafgifte en het gemiddelde mechanische vermogen gedurende tractiefase; de kostenfactor, het quotiënt van de gemiddelde elektrische afgifte bij nominale windcondities en het nominale generatorvermogen. Met het quasi-statische systeemmodel is het aangetoond dat met een vlieger met een maximale "lift-over-drag" coëfficiënt van vijf en een lier met twee aparte permanente-magneten-synchrone-motor voor tractie and retractie een totale efficiëntie van meer dan 50% kan worden behaald. De resultaten van dit proefschrift geven aan dat voor systemen groter dan 50 kW en met verbeterde vleugelontwerpen zelfs hogere waarden mogelijk zijn.

Daarnaast worden piekfactoren (quotiënten van het maximum en de gemiddelde

waarde van een fysische grootheid) van de kabelkracht en het mechanische vermogen geïntroduceerd om te worden gebruikt als prestatiefactoren. In dit proefschrift worden zulke piekfactoren – welbekend uit de elektrotechniek – voor de eerste keer toegepast op vlieger-energiesystemen. Het is aangetoond dat deze erg bruikbaar zijn om het proces van het oogsten van windenergie op grotere hoogten te begrijpen en te optimaliseren. Met een goed besturingssysteem is een piekfactor haalbaar van 1.2 voor de kracht en 1.5 voor het vermogen, zoals aangetoond in de in dit proefschrift gepresenteerde dynamische simulatie.

Voor de ontwikkeling en de vergelijking van besturingsalgoritmen is het essentieel om een snel systeemmodel te hebben. Een realtime model van de vlieger, de cable, en het grondstation is gepresenteerd. Het is eenvoudig om het model aan te passen en uit te breiden, omdat een hoge programmeertaal (Python) is gebruikt. Vlieger en cable zijn beiden gemodelleerd als een partikelsysteem, een aanpak toepasbaar op zowel vliegers als vaste vleugels.

Bovendien is een geavanceerd omgevingsmodel geïmplementeerd dat de windschering gebaseerd op een empirisch gefitte exponentiële profielfunctie en een turbulent windveld – gebruikmakende van het Mann-model – omvat. Dit model is bruikbaar voor het bestuderen van de invloed van turbulentie op systemen van verscheidene groottes en vliegende op verschillende hoogtes. In tegenstelling tot initiële verwachtingen van de auteur is het aangetoond dat windturbulentie geen significante invloed heeft op de jaarlijkse energieproductie van het systeem in kwestie. Deze gelimiteerde sensitiviteit met turbulentie zou anders kunnen zijn voor systemen kleiner dan 20 kW of in werking op hoogten lager dan 200 meter.

De ontwikkelde modelleeraanpak voorziet in het fundament voor hoog-accurate vlieger-energiesimulatiemiddelen, die dringend nodig zijn voor vlieger-energieontwikkelaars en -onderzoekers.

Toen dit onderzoek startte was er een hypothese dat "Nonlinear Model-Predictive Control" (NMPC) nodig was voor de regeling van een vlieger-energysysteem. Deze hypothese blijkt onjuist te zijn in de onderzochte context: een betrouwbaar, robuust regelsysteem is gepresenteerd gebruikmakende van parametergevarieerde PID-regelaars en niet-lineaire dynamische inversie. Dit stelt de implementatie van kleine en lichtgewicht vliegende regelsystemen zonder de behoefte aan een zeer snel systeemmodel in staat.

Gebruikmakende van de gepresenteerde methodologie is het mogelijk om het gemiddelde mechanische vermogen voor een systeem van een 20-kW-generator onder nom-

inale windcondities met bijna een factor twee te verbeteren (van 6 kW naar ongeveer 12 kW). Deze progressie in onderzoek brengt vlieger-energy een stap dichterbij commercialisatie. Verder onderzoek is nodig, maar de modellen, resultaten en conclusies van dit proefschrift kunnen worden gebruikt als een solide startpunt voor toekomstige vlieger-energyontwikkelaars en -onderzoekers.

Sleutelwoorden: kite control, airborne wind-energy, distributed control, kite-power systems, efficiency, pumping kite-power system

Nomenclature

Latin Symbols

a	acceleration [m/s^2]
A	projected surface area of the kite [m^2]
c	structural damping coefficient of tether segment [Ns/m]
c_0	steering offset the turn rate law (Eq. 4.72)
c_1	steering sensitivity coefficient of the turn rate law (Eq. 4.72)
c_2	gravity sensitivity coefficient of the turn rate law (Eq. 4.72)
$c_{\mathrm{d},0}$	structural unit damping coefficient [Ns]
c_f	crosswind interpolation factor (0..1) (Eq. 6.20)
CF_f	crest factor of the reel-out force [-]
$CF_{\mathrm{f,q}}$	crest factor in the quasi-static simulation [-]
$CF_{\mathrm{f,s}}$	crest factor in the dynamic simulation [-]
c_s	steering coefficient (one point kite model) [-]
D	duty cycle [%]
d_t	tether diameter [m]
F_t	tether force at the winch [N]
$F_{\mathrm{t,k}}$	tether force at the kite [N]
F_h	set value for the maximal (high) tether force at the winch [N]
F_l	set value for the minimal (low) tether force at the winch [N]
I	turbulence intensity [%]
I_w	inertia of the winch as seen from the generator [kg m^2]

i_d	relative depower input of kite control unit (0..1) [-]
i_s	relative steering input of kite control unit (-1..1) [-]
k	spring constant of idealised tether segment [N/m]
k_v	quotient of the optimal reel-out speed and the tether force [m $\mathrm{s}^{-1}\mathrm{N}^{0.5}$]
k_0	unit spring constant [N]
$K_\mathrm{s,D}$	steering-induced drag coefficient of the kite [-]
K_u	anti-windup feedback factor for u_s [-]
K_ψ	anti-windup feedback factor for $\dot{\psi}$ [-]
K_v	anti-windup feedback factor for v_set [-]
$l_\mathrm{s,0}$	initial length of tether segment [m]
$l_\mathrm{t,i}$	tether length at beginning of time step i [m]
l_low	lower limit of the tether length [m]
l_up	upper limit of the tether length [m]
m_KCU	mass of kite control unit [kg]
m_k	mass of kite [kg]
n	number of tether segments [-]
p	exponent of the wind profile power law [-]
r	radius, distance of the kite point relative to the ground station [m]
R	turn radius of the trajectory kite point [m]
u_d	relative depower setting of kite control unit (0..1) (Eq. 4.32)
u_s	relative steering setting of kite control unit (-1..1) (Eq. 4.52)
v_a	apparent wind speed [m/s]
v_o	tether reel-out speed [m/s]

v_{set} set value of the tether reel-out speed [m/s]

$v_{w,ref}$ horizontal wind velocity at the reference height [m/s]

z height of kite or tether segment above ground [m]

Greek Symbols

α angle of attack [rad]

β elevation angle of the kite position [rad]

χ course angle, flight direction [rad]

χ_{set} bearing angle, desired flight direction [rad]

δ_{min} minimal, angular attractor point distance [rad]

η_{cyc} cycle efficiency, product of the pumping efficiency and the duty cycle [%]

η_p pumping efficiency, quotient of net mechanical energy and energy, harvested during reel-out [%]

η_{tot} total efficiency [%]

γ nose mass fraction of the wing [-]

μ dimensionless wind speed gain of the flight path planner [-]

ν ratio of the wind speeds, that can be compensated by the flight path planner [-]

ω norm of the angular velocity of the kite on the unit sphere [rad/s]

ϕ azimuth angle of the kite position [rad]

ψ heading, direction into which the nose of the kite is pointing to [rad]

ρ air density [kgm^{-3}]

σ linear mass density of the tether [kg/m]

ϱ turn radius of the trajectory of the kite point [rad]

Vectors

$\mathbf{a}$	vector of accelerations of tether particles [m/s^2]
$\mathbf{A}, \mathbf{B}$	position of the front and top kite particles [m]
$\mathbf{C}, \mathbf{D}$	position of the right and left kite particles [m]
$\mathbf{d}_\mathrm{i}$	drag force of tether segment i
$\mathbf{e}_\mathrm{x}, \mathbf{e}_\mathrm{y}, \mathbf{e}_\mathrm{z}$	unit vector of the x, y and z-axis of the kite-reference frame
$\mathbf{F}_\mathrm{g}, \mathbf{F}_\mathrm{s}$	gravity and steering forces of kite [N]
$\mathbf{F}_\mathrm{L}, \mathbf{F}_\mathrm{D}$	lift and drag forces of kite [N]
$\mathbf{p}$	vector of positions of tether particles [m]
$\mathbf{p}_\mathrm{k}^\mathrm{SE}$	position of the kite in angular coordinates (β, ϕ) [rad]
$\mathbf{R}$	vector of the residual of the implicit problem/ model
$\mathbf{s}_\mathrm{i}$	special distance of tether particle i to the particle i+1 [m]
$\mathbf{s}_\mathrm{v,i}$	velocity of tether particle $i+1$ relative to particle i [m/s]
$\mathbf{v}_\mathrm{a}$	apparent air velocity [m/s]
$\mathbf{v}_\mathrm{w,k}$	wind velocity at the height of kite [m/s]
$\mathbf{Y}$	state vector of the implicit problem/ model

Abbreviations

AWE Airborne Wind Energy
DTC Direct Torque Control
FPC Flight Path Controller
FPP Flight Path Planner
KCU Kite Control Unit
KPS Kite Power System
LPV Linear Parameter Varying
NDI Nonlinear Dynamic Inversion
NMPC Nonlinear Model Predictive Control
SISO Single Input Single Output
WC Winch Controller

Contents

Summary iii

Samenvatting vii

Nomenclature xi

1 Introduction 1
- 1.1 Background . . . 1
- 1.2 Sustainability . . . 3
- 1.3 Renewable energies . . . 4
  - 1.3.1 Wind energy . . . 5
  - 1.3.2 Solar energy . . . 6
  - 1.3.3 Airborne wind energy . . . 6
- 1.4 Summary and conclusion . . . 9

2 State of Research 11
- 2.1 Previous research . . . 11
- 2.2 Thesis objective . . . 15
- 2.3 Methodology . . . 16
- 2.4 Kite power systems . . . 17
  - 2.4.1 Working principle of a kite power system . . . 17
  - 2.4.2 Types of kite power systems . . . 18
  - 2.4.3 Control of kite power system . . . 18
- 2.5 Thesis structure . . . 19

3 Quasi-Static, Model-Based Performance Analysis 23
- 3.1 Introduction . . . 24
- 3.2 System model . . . 24
  - 3.2.1 Kite kinematics . . . 25
  - 3.2.2 Atmospheric model . . . 25
  - 3.2.3 Aerodynamic performance of tethered kites . . . 25
  - 3.2.4 Simulating the reel-in phase . . . 28

3.2.5 Pumping efficiency, cycle efficiency and duty cycle 29
3.2.6 Optimization 32
3.2.7 Maximal tether force 32
3.2.8 Electrical efficiency and total efficiency 33
3.2.9 Modeling the efficiency of the generator 35
3.2.10 Modelling the efficiency of the motor 36
3.2.11 Specifying the power of a kite power system 37
3.2.12 Python implementation of the system model 37
3.3 Model validation 38
3.3.1 Implemented technology demonstrator 38
3.3.2 Comparison with experimental data 39
3.4 Design of a 31 kW kite power system using a 53.5 kW ground station . 41
3.4.1 Simulation results 42
3.4.2 Performance factors 44
3.5 Summary and conclusion 46

4 Dynamic Modelling **49**
4.1 Introduction 49
4.2 Computational approach 51
4.2.1 Atmospheric model 52
4.2.2 Tether model 54
4.2.3 Point mass kite model 56
4.2.4 Four point kite model 59
4.2.5 Winch model 65
4.2.6 Control system 67
4.2.7 Implementation and accuracy 68
4.3 Model calibration and results 69
4.3.1 Test flight 70
4.3.2 Parking manoeuvres for aerodynamic measurements 71
4.3.3 Identifying the steering sensitivity parameters 72
4.3.4 Model comparison 76
4.3.5 Results: Power production and flight path 76
4.4 Summary and conclusion 78

5 Flight Path Planning in a Realistic Wind Environment **81**
5.1 Introduction . . . 81
5.2 A practical approach to kite control . . . 83
5.2.1 Small earth reference frame . . . 83
5.2.2 Kite Power System (KPS) modelling approaches . . . 85
5.2.3 Environmental conditions . . . 87
5.2.4 Robustness . . . 93
5.3 Flight Path Planner (FPP) . . . 94
5.3.1 Automated power production . . . 95
5.3.2 Lower intermediate state . . . 99
5.3.3 Flying figures of eight . . . 101
5.3.4 Upper intermediate state . . . 108
5.3.5 Performance of the flight-path planner . . . 110
5.4 Summary and conclusion . . . 113

6 Flight Path and Winch Control **117**
6.1 Introduction . . . 117
6.2 Flight Path Control (FPC) . . . 119
6.2.1 Simplified kite system model . . . 120
6.2.2 (Position, heading) flight path controller . . . 124
6.2.3 (Position, heading) FPC with NDI and turn actions . . . 125
6.2.4 (Position, heading, course) FPC with NDI and turn actions . . . 129
6.2.5 Performance of the FPC . . . 129
6.3 Winch control (WC) . . . 133
6.3.1 Simplified winch system model . . . 133
6.3.2 Winch controller design . . . 136
6.3.3 Performance of the WC . . . 139
6.4 Implemented distributed control system . . . 153
6.4.1 Detailed control structure . . . 153
6.4.2 Adapting to changing wind conditions . . . 154
6.4.3 Distributed control . . . 155
6.5 Summary and conclusion . . . 155

7 Simulation Results **159**
7.1 Introduction . . . 159
7.2 System properties and environmental conditions . . . 160

7.3 Adaptations during model and controller integration . . . 161
7.3.1 Adding a model of the Kite Control Unit (KCU) . . . 161
7.3.2 Adapting the flight path planner (FPP) . . . 161
7.3.3 Adapting the controllers . . . 161
7.4 Results . . . 162
7.4.1 Results for average wind speed . . . 162
7.4.2 Results for nominal wind speed . . . 162
7.4.3 Results for high wind speed and high elevation angle . . . 166
7.4.4 Results for high wind speed and high depower settings . . . 169
7.4.5 Optimization results . . . 172
7.4.6 Robustness against high turbulence . . . 174
7.4.7 Comparison with experimental data . . . 179
7.4.8 Power curve and capacity factor . . . 180
7.5 Summary and conclusion . . . 182

8 Conclusions and Outlook 185
8.1 Conclusions . . . 185
8.2 Outlook . . . 186
8.2.1 Simulations . . . 186
8.2.2 Optimization . . . 187
8.2.3 Estimations . . . 187
8.2.4 Testing . . . 187
8.2.5 Control . . . 188
8.2.6 Automated launch and landing . . . 188

A Implementation of the FPC in Python 191

B Results from a flight test on a 400 m to 700 m tether 197

C Summary of the Developed Methodology 199

References 201

Publications 209

Curriculum Vitae 211

CHAPTER 1

Introduction

Contents

1.1 Background **1**

1.2 Sustainability **3**

1.3 Renewable energies **4**

1.3.1 Wind energy 5

1.3.2 Solar energy 6

1.3.3 Airborne wind energy 6

1.4 Summary and conclusion **9**

In this chapter the necessary background information for this thesis will be presented: First, on the motivation of this research and on the role of airborne wind-energy in the context of sustainable development and other renewable energies, second on the different types of airborne wind energy systems in general and of pumping kite power systems in particular.

1.1 Background

The world population is growing, and the demand for energy is rising even faster, especially in the BRIC countries (Brazil, Russia, India and China). According to the International Energy Agency (2012, p. 1) the world energy demand will grow by more than one third until 2035. As Fig. 1.1 shows, wind turbines are often the cheapest choice to provide clean energy, but in many locations the costs for wind energy are still higher

than the costs for electricity from coal-power plants[1], and the average capacity factor[2] of onshore wind turbines is still quite low (in Germany in 2014 about 18.7% according to Ahlgrim, Jim (2015)). A low capacity factor increases the grid integration costs, which are not included in the levelized costs of energy[3] (LCOE) as shown in Fig. 1.1.

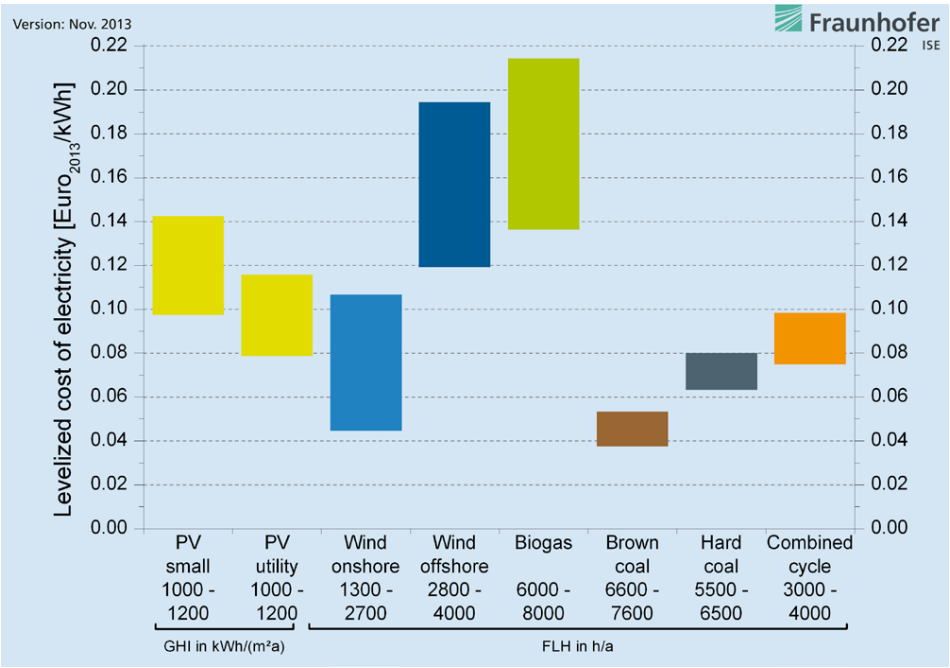

Figure 1.1: *LCOE of renewable energy technologies and conventional power plants at locations in Germany in 2013. The value under the technology refers in the case of PV to the insolation global horizontal irradiation (GHI) in kWh/(m^{2}a), for the other technologies it refers to the number of full load hours (FLH) for the power plant per year. Specific investments are taken into account with a minimum and maximum value for each technology. From: Kost et al. (2013).*

[1] As long as the external costs of coal power on the health of the local population and the effect of coal power plants on global warming are not taken into account.

[2] The capacity factor is defined as the quotient of the average power output over the whole year and the nominal power under optimal wind conditions.

[3] The levelized costs of energy are used to compare the price of different energy sources. They include at least the initial costs, the capital costs, operations and maintenance, performance and fuel costs.

Airborne wind energy (AWE) systems can harvest wind from higher altitudes than conventional wind turbines. At these altitudes the wind is generally stronger and steadier. They use a tethered wing, connected to a winch at the ground. They do not need any tower, therefore the investment costs and the total mass can be significantly reduced. From this fundamental perspective it should thus be possible to produce airborne wind energy at lower costs and more constantly than conventional wind energy.

One of the key challenges on the way to reliable airborne wind energy systems is the control system: A reliable control system is needed to operate the wing even in very turbulent wind conditions. In addition the control system must steer the wing on an optimal path to harvest as much energy as possible. Even though at least one company (Makani Power, now Google) is claiming that it developed an automated kite-power system already in 2008, no working kite-control system design and no performance analysis were published until 2010, when this research was started.

1.2 Sustainability

Becker (2014) wrote: "The world conferences on sustainable development started in 1972, although that term was not used back then". The United Nations Conference on the Human Environment was held in Stockholm in 1972. The main result of the conference was the "Stockholm declaration". "The first principle [of this declaration] focuses on the fundamental right to freedom, equality and adequate living conditions, in an environment that permits a life of dignity and well-being" (Becker 2014).

Twenty years later the "United Nations Conference on Environment and Development" in Rio de Janeiro in 1992 spread the idea of sustainability to many more countries (representatives of 172 countries participated) (Becker 2014) and also raised the awareness of the civil society. The conference report "Our Common Future", also known as "Bruntland Report", states: "Humanity has the ability to make development sustainable to ensure that it meets the needs of the present without compromising the ability of future generations to meet their own needs" (UNWCED, United Nations World Commission on Environment and Development 1987).

Different sustainability models exist, that might help to explain what a sustainable society looks like. One is the model of three spheres of sustainability: It assumes, that environmental, social and economic development goals must be met to be able to reach a sustainable development (see: Fig. 1.2).

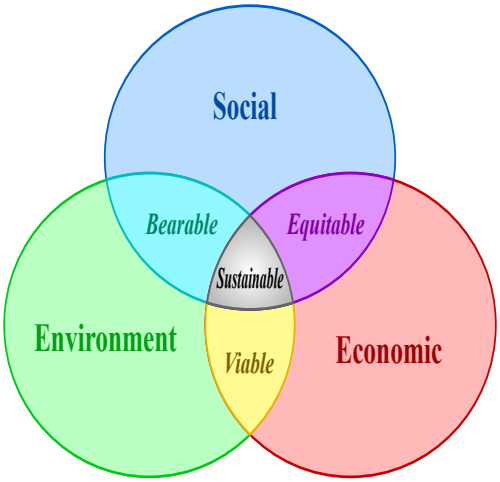

Figure 1.2: *The Three Spheres of Sustainability (Dréko 2006).*

1.3 Renewable energies

To reach the goal of limiting global warming to 2 degree Celsius "... the discharge of greenhouse gases must be reduced by 50-85% by 2050 compared with the year 2000" (Mathiesen et al. 2011).

According to Olivier et al. (2013, p. 33), in 2013 power generation (heat and electricity) was responsible for 38 % of the global greenhouse gas emissions. Using renewable energies, these emissions could be reduced by a factor of 20 to 90[4]. In addition, the residential sector was responsible for 6 % of the emissions and road transport for 16 %. In the residential sector heating and warm water could be provided with renewable energies like solar thermal systems and heat pumps, operated with wind energy. In the road transport sector electrical cars and wind gas (hydrogen or methane, produced with wind power) could be used to replace fossil fuels with renewable energies.

Renewable energies could play a key role in reducing the greenhouse gas emissions. For many countries 100 % renewable energy scenarios have been developed. A very detailed scenario for Denmark can be found in Mathiesen et al. (2011), a meta-study

[4] The median of the levelized CO_2 emissions for coal is 980 g/kWh, for solar photovoltaics 44 g/kWh and for wind 11 g/kWh (NREL, National Renewable Energy Laboratory 2014).

was published in Cochran et al. (2014).

The mitigation of climate change is not the only reason for using renewable energies, there are many more motivations. I just want to mention one additional motivation: Coal power plants have a severe, negative impact on the health and environment, not only in China, but also in Europe. According to Huscher and Smith (2013) in the 27 countries of the European Union (EU) coal power plants cause about 18200 premature deaths per year and cause addition health costs of 15.5 to 42.8 billion EUR per year. Replacing these coal power plants with renewable energy systems would therefore improve the lifetime and health of a lot of people, while reducing the costs for the society at the same time.

Traditionally hydro power is the biggest source of renewable energies. It had 15.7 % world wide share of net energy generation in 2011. The second biggest source was biomass with 3.3 %, followed by wind with 2.8 % (Salvatore 2013). But in many countries the available hydro power resources are already used and cannot be expanded much further. The same is true for biomass. Geothermal energy can only be used efficiently at a few places in the world like Iceland or Turkey. Therefore in the focus of the following sections is only on wind and solar energy, which both have a huge potential and which both can be used at many places of the world.

1.3.1 Wind energy

At the end of 2013 in the EU-28 117.3 GW of wind power systems were installed. In a normal wind year they could provide 8 % of the electricity, consumed . The annual growth in 2013 was about 10 %, which is approximately the same annual growth as the average of the last 10 years (Pineda et al. 2014).

According to Heide et al. (2010) in a 100 % renewable energy scenario for Europe 55 % of the energy should be supplied by wind energy if only wind and solar sources are taken into account. With this mix the needed storage capacity can be minimized: Solar energy is mainly available in summer, and the wind is much stronger in winter (Fig. 1.3).

"For less than 100 % renewable scenarios the fraction of wind power generation increases and that of solar power generation decreases." (Heide et al. 2010).

In Fig. 1.1 the levelized costs of energy (LCOE) of different renewable and other energy sources are compared. You can see that in Germany onshore wind energy is - in most cases - the cheapest source of renewable energy. For these reasons wind energy will be the major source of newly installed renewable energy systems not only now, but

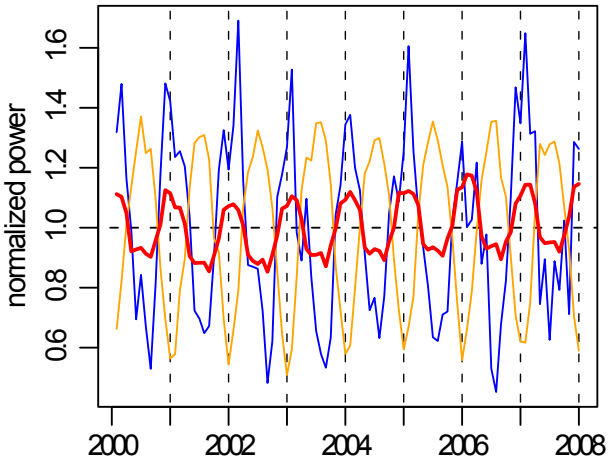

Figure 1.3: *Normalized power of wind energy (blue), solar energy (orange) and the energy consumption (red) in Europe. A lot of wind energy is available in winter, and a lot of solar energy in summer. From: Heide et al. (2010).*

also in the future.

1.3.2 Solar energy

Because the prices for solar energy are dropping fast, solar electricity might become the cheapest resource in the future, but solar energy is available only during day, and for a more constant supply of renewable energy combining solar, wind and other sources is in most cases the most economic solution.

1.3.3 Airborne wind energy

Airborne wind energy systems use a flying device like a wing or a balloon to harvest wind energy. This device is connected to the ground with a tether. An overview about realized systems for electricity generation is shown in Tab. 1.1.

In Fagiano and Milanese (2012) another compact introduction to airborne wind energy is given. While this paper contains a lot of valuable information, the cost estimates are questionable: Solar energy is already much cheaper than the cost projection for 2030 (0.325 $ per kWh) in this paper. The cost estimate for airborne wind (0.02 $ per kWh)

Table 1.1: *Classification of airborne wind energy systems (without vehicle propulsion). Extended version of the classification in Katebi et al. (2013).*

Wing	Generator	Crosswind	Description
soft	ground	yes	pumping kite power system
semi-rigid	ground	yes	pumping tethered wing
rigid	ground	yes	pumping power plane
soft	airborne	yes	continuous generation
rigid	airborne	yes	continuous generation
rotating beam, Magnus effect	ground	no	lighter-than-air system
buoyant high-altitude turbine	airborne	no	lighter-than-air system

is also questionable. When this research was started there was the hypothesis, that a main factor for the underestimation of the costs of airborne wind is, that turbulence was not taken into account when the power curves for airborne wind energy devices were calculated. This hypothesis could not be confirmed in the context of this thesis: Turbulence does not have a significant impact on the energy, harvested by a 20 kW kite power system at a height of 200 m (Sec. 7.4.5).

Diehl (2013) presents a good introduction into the physics of airborne wind energy. This book chapter also includes a classification of airborne wind energy devices. The author introduces the power harvesting factor ζ, which he defined as the quotient of electrically harvested power P and of the wind power P_{area}, that flows through an area of the size of the wing:

$$\zeta = \frac{P}{P_{area}} \tag{1.1}$$

In theory, the author states that a value of $\zeta \approx 30$ could be achieved, and he states that the highest measured value until 2013 was $\zeta = 8$. The higher the value of ζ is, the more power can be extracted with a wing of a given size in a wind field with a given power density.

There are a number of reasons, why airborne wind energy is attractive. These include:

- Tapping the winds of the jet-stream was a major motivation for Wubbo Ockels, Delft University of Technology, who developed the concept of the "Laddermill" (Ockels 2001). He writes, that at a height of 10 km the wind energy density would reach a value of 5000 W/m^2, which is 30 times as high as at 100 m (measurement

data from "De Bilt", The Netherlands).

- Because it is difficult to harvest wind at 10 km height, C. Archer was trying to find "low level jet streams". They occur, when the strong wind is coming down to a hight of less than 3000 m above ground level (Archer et al. 2014). One area are "The Great Planes" in the United States, where low level jets can be found in a height of 200 m to 900 m, depending on the time of the year and the weather conditions. They reach an average wind power density of 4500 W/m^2 in January and 1400 W/m^2 in July.

- When considering the sustainability of wind power devices, the large amount of concrete and steel, needed for the towers is an issue that could be solved with airborne wind energy devices.

- Offshore wind turbines need very large and heavy foundations. Because of the low bending moment of airborne wind energy devices even floating systems could become possible for much lower costs than those of conventional floating turbines.

In thirty years the maximal height of wind turbines increased from 30 m (1980) to 135 m (2010), while the nominal power increased from 30 kW to 7500 kW. For steel towers with a fixed diameter, the costs of the tower increase exponentially with the height (Goudarzi et al. 2014). When optimizing the costs by changing the tower height, this effect causes a severe limit to the economic height. This effect can be mitigated by using different tower design methods, e.g. hybrid towers.

Nevertheless it is unlikely that it would ever be an economic choice, to mount a 500 kW turbine on a 200 m tower. With an airborne wind energy device and a wing, attached to a tether it could become an economic option to operate a 500 kW system at an average height of 200 m or more, because the tether costs increase only linearly with the height. On the other hands, tethers with a long lifetime are needed to keep the costs low in the long run (Bosman et al. 2013).

At an onshore location like Cabauw, The Netherlands the wind at 200 m height is 1.24 times stronger than the wind at 78 m height (a normal height for a 500 kW wind turbine). This means, that the wind energy density is 1.94 times higher.

Therefore, for small to medium wind power generators airborne wind energy devices might become feasible that can operate just above the boundary layer, where the energy of the wind is much higher than nearer to the ground. These kind of devices could

for example be used - in combination with solar power - to supply remote villages with electricity. Using solar power on its own requires huge and expensive batteries, therefore a combination with wind energy is in many cases the better choice.

The transport issues, related to a large tower could be avoided. Maintenance of the generator is easier, as it is located on the ground.

1.4 Summary and conclusion

If mankind wants to survive, the future development must be sustainable. In 2010, the global coal consumption reached 7238 million tons. In 2011 the world resource institute (WRI) wrote: "According to WRI's estimates, 1,199 new coal-fired plants, with a total installed capacity of 1,401,278 megawatts (MW), are being proposed globally" (Yang and Cui 2012).

This would not be a sustainable way to generate electricity, but a threat to mankind. Instead renewable energies should be used, and airborne wind energy could offer new possibilities to harvest the power of the wind at places and in ways, that are not accessible with conventional wind turbines.

One of the challenges of airborne wind energy devices is the development of a reliable and effective control system. This thesis is trying to present a methodology for the development of such control systems.

In the next chapter follows a review of previous research and further more the structure of the thesis is explained.

CHAPTER 2

State of Research

Contents

2.1 Previous research **11**
2.2 Thesis objective **15**
2.3 Methodology **16**
2.4 Kite power systems **17**
2.4.1 Working principle of a kite power system 17
2.4.2 Types of kite power systems 18
2.4.3 Control of kite power system 18
2.5 Thesis structure **19**

2.1 Previous research

Since the first scientific publication about kite control by Diehl (2001, Chap. 8) at least five PhD theses (Ahmed 2014; Fagiano 2009; Furey 2011; Thorpe 2011; Zgraggen 2014) and more than 20 papers have been published on automated kite control, most of them since 2010.

First, I want to discuss the kite, winch and tether models that were used in these publications: Most of them (16 of 26) use a point mass kite model. As shown in (Fechner et al. 2015) these kind of models do not provide sufficiently accurate and stable results for the development and test of real control systems, even though they can be sufficient for a coarse estimation of the average power output. In two publications (Thorpe 2011; Williams et al. 2007) a rigid body model is used. It is currently not known if the turn-rate law, that describes the reaction of a soft kite to steering input (see Sec. 6.2) is valid for rigid wings. In addition, Williams et al. are not using a dynamic winch model and

Thorpe is not using a discretized tether model. Therefore the accuracy of the results, presented by Williams et al. and by Thorpe is limited. Additionally, Williams et al. are also presenting a 4-plate model, but it is not clear if it was used in the overall system model. Williams et al. are also lacking any detailed controller description.

Furey (2011) is using a 10 point particle system as kite model. This is a promising modelling approach, even though a discretized tether is missing. In addition the use of neuronal networks as main control element, as suggested by Furey was not very successful. Two papers (Fagiano et al. 2012) and (Erhard and Strauch 2012) used a quasi-steady model which is a good starting point for the implementation of a controller, but not sufficient for controller validation. One paper (Fechner and Schmehl 2012b) is using an averaged system model, which is only suitable for the derivation of some set values of the controllers and three papers use no kite model at all. In (Fechner and Schmehl 2012b; Jehle and Schmehl 2014) and (Baayen and Ockels 2012) for the development of the controller a real kite power system was used. Even though this is possible, it has severe disadvantages: It is costly, it is very difficult to achieve reproducible results because the wind speed is constantly changing, it is impossible to compare different controllers in exactly the same wind conditions and it is very difficult/ time consuming to test the controller in a broad range of wind speeds.

Now follows a closer look at the control methods, found in the literature: Nonlinear, model predictive control (NMPC) is the control strategy that is used in a large number of publications (9). It can be very useful for theoretical investigations like identifying optimal flight trajectories, but in practise it is hard to implement: NMPC needs a very fast model and an accurate knowledge of the wind field. An accurate model (with a discretized tether and at least a 4-point kite model) with the sufficient simulation speed (at least 10 times faster than real-time) was not implemented until today (2015). Furthermore, to know the 3D wind field in front of the kite, advanced and expensive sensors like LiDAR (Light detection and ranging) would be necessary. LiDAR was already successfully tested with conventional wind turbines (Bottasso et al. 2014), but not yet applied for real-time control of airborne wind energy systems. Therefore, since 2011 many researchers are looking for alternatives. One of the most promising control approaches for the kite trajectory was the three-loop controller, published in (Fagiano et al. 2014): It does not need any information about the kite or the wind field and it works quite well. Even a proof of stability was given. On the other hand it was only verified using a kite on a short tether of constant length. I assume (based on my simulation results) that this

controller would lack precision if used with a long tether of varying length (e.g. 200-500 m) and with a heavy kite. The kite trajectory controller, published in (Jehle and Schmehl 2014) should have a higher precision because it takes the apparent wind velocity and the gravity into account. On the other hand it misses any proof of stability and the authors noticed that it becomes unstable when operating on a short tether (< 200 m) or high feedback-loop delays (> 200 ms). Therefore an improved control algorithm was developed, that is presented in Chap. 6.

Van der Vlugt et al. (2013b) describe a controller, that uses any number of attraction points (n-point controller) and a PI controller for the heading of the kite to follow any predefined trajectory. It was working in practical flight tests, but only the two-point version works reliable. On the other hand the two-point version does not allow to fly downloops (downwards at the sides of the figures-of-eight) and behaves therefore sub-optimal as explained in Sec. 6.2.

Ruiterkamp and Sieberling (2013) describe the system structure and some test results of a pumping airborne wind-energy system using rigid wings. The system is described on a very high level only, the article does not present any details about the control system implementation. Furthermore the presented system model is very much specialised for rigid tethered wings and therefore not applicable for the control and simulation of soft wings, which is the focus of this thesis. Nevertheless this book chapter provides some good information about the effects of scaling: Tether drag is a main factor, that limits the performance of rigid wing kite power systems. The influence of the tether drag can be substantially reduced by up-scaling this kind of AWE systems.

Other control approaches for the flight path were also be presented, e.g. direct inverse control (Novara et al. 2011) or Lyapunov based, nonlinear adaptive control (Baayen and Ockels 2012). From my point of view these model-less approaches are becoming less attractive, because in the years since 2012 the kite-control law (Erhard and Strauch 2012; Fagiano et al. 2014; Jehle and Schmehl 2014) was discovered and published which makes simple and accurate model based control possible.

Wood et al. (2015) present a flight path controller for a kite, that is steered from the ground, using multiple tethers. It uses a Smith predictor to compensate for steering delays. This is problematic because a Smith predictor is very sensitive for deviations of the assumed system delay. The predictive control of the winch as explained in Fechner and Schmehl (2014) is not used any more because it was found to be ineffective in turbulent wind conditions.

With respect to optimization of the flight path and of the set-speed/ set-force of the winch controller the PhD thesis of Fagiano (2009) is presenting many detailed NMPC based approaches and some results. A short version of the work of his group can be found in (Canale et al. 2010; Canale et al. 2009; Fagiano et al. 2010). A weak point of his approach is his choice of optimization parameters: He is optimizing only the average mechanical power output over the whole cycle, not taking generator efficiency and generator power constraints into account. The limitations of his model or his optimization method can be seen in (Fagiano et al. 2010), where he publishes a power curve (Fig. 8) that stays constant at wind speeds between 9 and 25 m/s. According to our simulations the net power must slightly drop above the optimal wind speed of a pumping kite power system, because the reel-in power increases while the reel-out power cannot exceed the maximal generator power. A strength of this paper is, that for the first time calculations not only for one kite power generator, but for kite power farms where made.

A very detailed paper on optimization of the power output and on minimization of variations of the power output is (Fagiano et al. 2012). It looks at the optimization of kite-power systems in the carousel configuration, but also on the optimization of systems that work in pumping mode of operation. From our point of view it has some severe limitations because it makes assumptions that are not valid at least for the kite-power system demonstrator of TU Delft: It assumes a constant reel-in and reel-out speed. Especially the reel-in speed of our demonstrator is not constant at all, but slow in the beginning and than rising a lot when the elevation angle of the kite is increasing. In addition it assumes a neglectable difference between the minimal and maximal tether length which does not hold when trying to optimize the power over the full cycle.

Ahmed et al. (2011) looked at the power optimization problem. A strong point of their paper is the use of a realistic, synchronous generator model. The weak point is the use of only one closed figure-of-eight for reel-in and reel-out. This results in a bad overall performance. One example: The quotient of the peak power and the average power (crest-factor) in their results is bigger than four, whereas my simulations show a quotient of less than two, which reduces the generator costs significantly.

For flight path optimization Costello (2015) is applying "Directional Modifier Adaption". He is presenting not only theoretical, but also practical results which are promising, but limited to the reel-out phase.

Zgraggen et al. (2015) suggested a very different approach: The authors suggest an online optimization algorithm for finding the optimal average elevation and azimuth

angle while reeling out. Zgraggen (2014) and Zgraggen et al. (2014b) describe two methods for the control of the reel-in phase of pumping kite power systems. Missing is a description how to optimize the reel-in speed and force. In Zgraggen et al. (2014a) the kite is reeled in at the side of the wind window at an azimuth angle of 45°. The paper lacks any evidence, that this is the optimal path to reel in the kite. The effects of the intermediate phase (transition between reel-in and reel-out) are not investigated.

Erhard et al. (2015) published a kite power system model and optimization results, based on direct multiple shooting. The results are promising, but a straight line tether model with a kite, that cannot change its angle of attack was used. Therefore the results cannot be applied for lead-edge inflatable kites, that are used in this thesis. Furthermore the results were not validated against a detailed system model, that takes the tether sag and winch dynamics into account.

A literature review of kite- and kite power system (KPS) models is given in Sec. 4.1.

A control system for the full cycle, that was optimized against a realistic kite power system model with a kite, that can actively change the angle of attack was not yet described in the discussed literature. In addition none of the control approaches found is complete: Many describe only the reel-in or reel-out phase, and the only one, that describes the control of the full cycle does not explain the parameter optimization.

In this thesis for the first time a complete, detailed description of an optimized control system for a single line, soft wing kite power system is presented and its operation in a wide range of wind speeds and at different turbulence levels is explained.

2.2 Thesis objective

The objective of this thesis is to develop a systematic approach for the development of optimized controllers for kite power systems.

In the past, a lot of research was focused on the question how to maximize the power output during the reel-out phase of a pumping kite power system. But what about the reel-in phase?[1] A fast dynamic model is needed to find the best trajectories that can optimize the power over the whole cycle.

However, knowing the best trajectories is useless unless you have a controller that can keep the kite on this trajectory. So the next questions are arising: How can a con-

[1] A pumping kite-power system is reeling out the tether from the drum first, and then it is reeling the tether back in again. The time when it is reeling the tether back in is called the reel-in phase.

troller for the trajectory of the kite be implemented? And how can winch controllers be implemented, that can limit the tether force effectively to ensure safe operation while harvesting the maximal possible energy?

The focus of this thesis is the question, how kite-power systems can be build and operated safe and effectively. Out of the scope of this thesis is the question how to implement automated launch and landing.

The performance of kite power system depends a lot on the environmental conditions, the wind speed, profile and turbulence intensity. Therefore the influence of these parameters will be investigated.

2.3 Methodology

The thesis is based on an interdisciplinary approach: A good understanding of meteorology, aerodynamics, material science, embedded systems, electrical and control engineering is needed to identify the challenges of the design of kite-power systems and to find viable solutions.

As far as possible a quantitative, experimental approach is used. Measurements were curried out mainly at Valkenburg Airfield, The Netherlands, using the kite-power system demonstrator of TU Delft. Further research is needed to assess the potential of airborne wind energy at other sites and with wind profile measurements of higher accuracy.

In addition to the experimental approach kite power systems are simulated in different levels of detail, e.g. fast, averaged models, a point mass kite model and multi-point kite models. To the best knowledge of the author for the first time a system model that includes a segmented tether and a detailed generator model is published.

The modelling approach, that is presented should be applicable to a broad range of airborne wind energy systems. Because the modelling software is based on open-source languages and libraries and implemented in a very modular way, it should be easy to reuse and extend it by other research groups and companies.

The focus of this research is not so much the aerodynamic properties of tethered wings, but on the overall system and control performance and design. It is assumed that the aerodynamic properties of the wing, e.g. lift and drag as function of the angle of attack are known.

For the simulation of the wind turbulence the model as described by (Mann 1994) and (Mann 1998) is used, which provides a three dimensional wind field under the as-

sumption of a linear wind shear. The performance of kite-power systems was investigated at wind speeds (converted to 10 m height) in the range of 2.5 to 11 m/s.

For the design of the control system a distributed control approach is used. An important focus is the reduction and compensation of delays in the feed-back loops. For the control of the kite non-linear dynamic inversion (NDI-) and linear parameter varying (LPV-) controllers are used, for the control of the ground-station (winch) three PID controllers. Feed-forward control was investigated and applied, too. The robustness of the control system is analysed using the worst case turbulence data measured at Cabau, The Netherlands in 2011 at 200 m height.

2.4 Kite power systems

The focus of this thesis is the control and optimization of airborne wind energy systems that use the traction power of a tethered inflatable wing in a pumping cycle, as described in van der Vlugt et al. (2013b) and Fechner and Schmehl (2013). The main components of such a single-tether kite power system (KPS) are the wing, the kite control unit (KCU) suspended below the wing by means of a bridle system, the tether and the drum-generator module, which is part of the ground station.

2.4.1 Working principle of a kite power system

The working principle of a pumping kite power system is explained in Fig. 2.1: First, the kite is reeled out while flying cross-wind figures-of-eight. In this phase traction power is harvested and converted by a generator, that is connected to the drum into electrical energy. Then the kite is depowered, steered to zenith and reeled back in again with a low force. For reeling in some of the energy is needed, that was gained during the reel-out phase.

In Fig. 2.2 a 3D view on one power cycle of the kite is shown: The simulation starts at the thick, red dot. The kite is first flying towards an intermediate point at the side of the wind window, then the tether is reeled out while the kite is flying figures of eight. When the maximal tether length is nearly reached if is steered upwards. At a certain height the set force is reduced, the kite depowered and the reel in phase starts. After the reel in phase the next cycle starts.

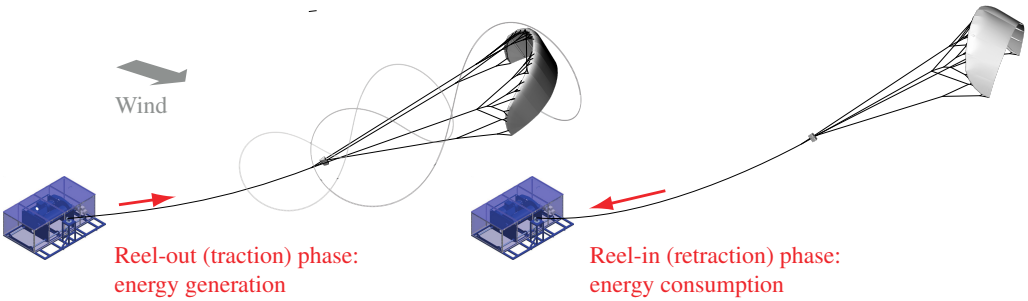

Figure 2.1: *Working principle of the pumping kite power system (van der Vlugt et al. 2013a).*

The model and the controller, that were used for this simulation are explained in Chap. 4 and Chap. 6.

2.4.2 Types of kite power systems

Kite power systems in pumping mode of operation can be built in different ways: First, one, two or three tethers can used. Second, the kite can be a soft, semi-rigid or rigid wing. Soft kites can either leading-edge inflatable (with tubes as structure elements) or ram-air kites.

The advantages of systems with one main tether only are less tether drag and a simpler launch and retrieval system. The advantage of three-line-systems is, that all the control motors and electronics can be at the ground. This increases the system reliability. Two line systems are a compromise: Steering is done from the ground, changing the angle of attack with an actuator in the air.

The demonstrator of Delft University of Technology is a one line system: A kite control unit (KCU), that is placed about 10 m under the kite is used for steering and for changing the angle of attack. In the rest of the Thesis I will mainly focus on this type of system.

2.4.3 Control of kite power system

It is the objective of this work to find a methodology for the development of robust and optimal kite power control systems, which include the automated adoption to changing wind conditions.

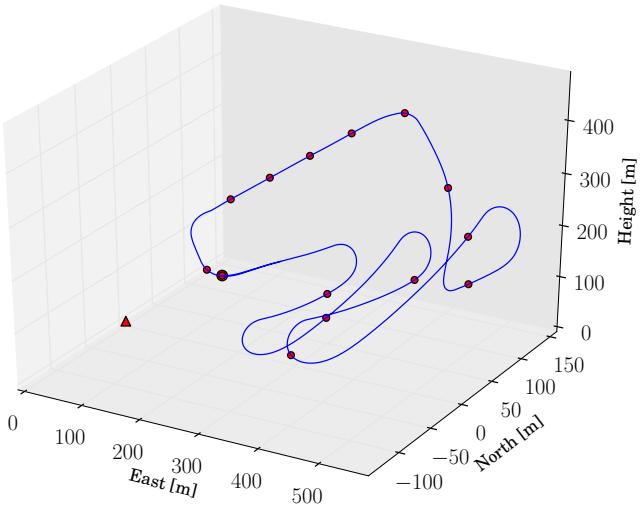

Figure 2.2: *Simulated flight path of a kite, flying at a high wind speed (8.0 m/s at 6 m height). The simulation starts at the thick, red dot. Smaller dots are placed on the flight path in a 10 s interval. The position is shown relative to the ground station, which is marked with a red triangle.*

2.5 Thesis structure

After the introduction in Chap. 1 and the state of the research in this chapter in the third chapter performance criteria for airborne wind energy systems will be identified and a quasi-static, model based performance analysis presented. Conventional performance criteria cannot be applied directly to kite power systems for the following reasons: First, at least kite power systems in pumping mode of operation do not work continuously, therefore the rated generator power will never be the same as the average electrical output at nominal wind speed. Second, airborne wind energy systems can operate in a wide range of altitudes, therefore the definition of the "wind speed at hub height", that is used for conventional wind turbines cannot be applied.

The focus of the fourth chapter is the question, how can a kite-power system be modelled with a sufficient accuracy for trajectory optimization, controller development and for comparing them to wind turbines? A modular, dynamic model was implemented and used partially validated against measurement data.

In chapter five first, the used coordinate system is introduced. The environmental

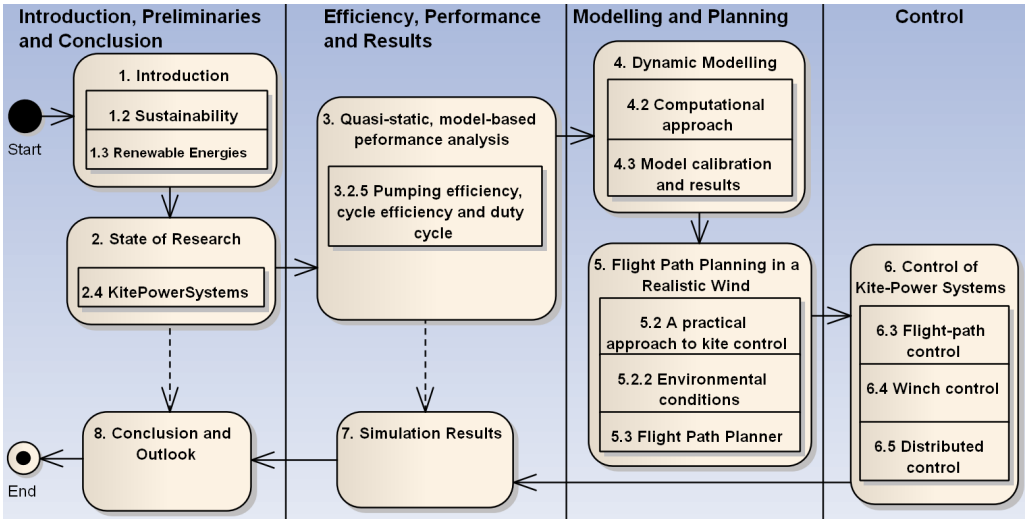

Figure 2.3: *Thesis structure: The chapters and the most important sections are shown. Readers, that are short of time can use the short-cuts, shown as dashed arrows.*

model, using a realistic wind profile and turbulence model is explained. Finally a flight path planner is depicted, that can adapt to changing wind conditions by varying the average elevation angle during reel-out.

Now follows the core part of the thesis, the control system development. Three different flight path controllers are presented and their performance is compared. A winch controller is developed and tested against a simplified 2.5 dimensional model. Further, a distributed control system is developed, because that can be very useful for kite power parks, where the kites fly close to each other. Furthermore algorithms for the automated adaptation to changing wind conditions are presented.

In the chapter seven simulation results for average, nominal and high wind speed are presented. Further more the robustness and stability at high turbulence is analysed. Finally a power curve for a 20 kW kite power system is presented and the capacity factor and energy yield compared with a conventional 20 kW wind turbine.

At the end of the thesis conclusions are drawn and an outlook on future research and development is given.

CHAPTER 3

Quasi-Static, Model-Based Performance Analysis

Contents

3.1 Introduction 24
3.2 System model 24
3.2.1 Kite kinematics 25
3.2.2 Atmospheric model 25
3.2.3 Aerodynamic performance of tethered kites 25
3.2.4 Simulating the reel-in phase 28
3.2.5 Pumping efficiency, cycle efficiency and duty cycle 29
3.2.6 Optimization 32
3.2.7 Maximal tether force 32
3.2.8 Electrical efficiency and total efficiency 33
3.2.9 Modeling the efficiency of the generator 35
3.2.10 Modelling the efficiency of the motor 36
3.2.11 Specifying the power of a kite power system 37
3.2.12 Python implementation of the system model 37
3.3 Model validation 38
3.3.1 Implemented technology demonstrator 38
3.3.2 Comparison with experimental data 39
3.4 Design of a 31 kW kite power system using a 53.5 kW ground station 41
3.4.1 Simulation results 42
3.4.2 Performance factors 44
3.5 Summary and conclusion 46

3.1 Introduction

After giving an introduction to airborne wind-energy systems in general and pumping kite power systems in particular, the focus of this chapter is a closer look at the performance of kite-power systems in pumping mode of operation.

After studying Canale et al. (2010) I assumed, that using generator with 20 kW nominal power, it should be possible to harvest at least 8 kW of power. But during the practical tests in 2012 the kite power team of TU Delft achieved not more than about 6 kW of average mechanical power over the full cycle and only about 3 kW of electrical output.

So the questions arose: Why is the system efficiency so low? How can you define the efficiencies of a pumping kite power system? How can the hardware and the control algorithms be modified to achieve an economical viable total efficiency (see: 3.28)?

In Section 3.2 a simplified system model is presented, that is averaging the power during the reel-out phase and is iterating over the reel-in phase in a two-dimensional projection (see: Fig. 3.1). In later chapters more accurate models will be introduced, but it will be important to remember the efficiency definitions given in section 3.2.5 and also the difference between the nominal electrical generator power and the system power as explained in section 3.2.11.

In Section 3.3 the results from the model are compared to measurement data. First the system properties of the implemented technology demonstrator will be explained, and then the measured mechanical output power is compared with the model results. Measurements of the electrical efficiency are presented. Following, an improved kite power system design for 31 kW is presented in Sect. 3.4.

This chapter is based on Fechner and Schmehl (2013). The introduction and conclusions are rewritten and the nomenclature adapted.

3.2 System model

The system model is averaging over the reel-out phase and iterating over the reel-in phase. It uses quasi-static equations and neglects the dynamics of the kite and of the drum of the ground station. To compensate the non-ideal real-world behaviour a dead time of five seconds without any power generation between reel-in and reel-out is used. Additionally, crest-factors (ratio of maximal and average value) are used to adapt the

model to the real world.

3.2.1 Kite kinematics

To simplify the calculations, it is assumed that the tether is a straight line between the kite and the winch. If the average length $\bar{l}$ of the tether and the elevation angle β are known, the average height $\bar{z}$ of the kite can be calculated as follows

$$\bar{z} = \bar{l} \sin \beta \tag{3.1}$$

3.2.2 Atmospheric model

To determine the wind speed v_{w} at the height of the kite, the least-square power law (Archer 2005) is used. Input parameters are the ground wind speed $v_{\mathrm{w,ref}}$ at 10 m height and the average height during the reel-out phase $\bar{z}$ of the kite. It establishes the relationship between v_w and $v_{\mathrm{w,ref}}$ as

$$v_{\mathrm{w}} = v_{\mathrm{w,ref}} \left(\frac{\bar{z}}{10\ \mathrm{m}} \right)^{p}. \tag{3.2}$$

The standard value of the exponent p is 1/7, whereas for offshore applications a value of $p = 0.11$ is used.

The air density ρ must also be known for the calculation of the tether force. Assuming a constant temperature of 15 °C, according to Stull 2000, p. 6 the air density can be calculated as

$$\rho = \rho_0 \ \exp\left(-\frac{\bar{z}}{H_\rho} \right), \tag{3.3}$$

where $H_\rho = 8.55\ km$, and where the average sea-level density $\rho_0 = 1.225\ kgm^{-3}$.

3.2.3 Aerodynamic performance of tethered kites

The aerodynamic performance of a kite depends on the following parameters:

- projected area[1] of the kite A

[1] The area of the shape of the kite, projected on a plane perpendicular to the tether, while the angle of attack is zero.

- lift to drag ratio L/D
- max. wing loading [N]
- depower capability (quotient of L/D during reel-out and L/D during reel-in)

The lift to drag ratio L/D determines the speed gain, that you get by flying crosswind. Flying crosswind is usually done by flying a figure of eight. This avoids twisting of the tether, which happens, if flying a circle. The pulling force of the kite depends on the apparent wind speed v_a as derived in Schmehl et al. (2013). $v_{t,o}$ is the reel-out speed of the tether, v_w the wind-speed at the height of the kite and β the elevation angle.

$$v_a = (\cos\beta\cos\phi - \frac{v_{t,o}}{v_w})\, v_w \sqrt{1+\left(\frac{L}{D}\right)^2} \tag{3.4}$$

The apparent wind speed v_a is the magnitude of the apparent wind velocity $\mathbf{v}_a$ which is defined as the difference of the wind velocity $\mathbf{v}_w$ and the kite velocity $\mathbf{v}_k$:

$$\mathbf{v}_a = \mathbf{v}_w - \mathbf{v}_k \tag{3.5}$$

Because the maximum force shall be calculated the azimuth angle ϕ can assumed to be to be zero. This results in $\cos\phi = 1$.

To calculate the lift over drag ratio $L/D = C_L^k/C_D$, it is not sufficient to know the lift C_L^k and drag C_D^k coefficients of the kite. The effective tether drag coefficient $C_{D,eff}^t$ has to be taken into account, too (Argatov and Silvennoinen 2010b). If the diameter of the tether is known, the tether drag coefficient can be calculated with the following approximation formula, where A_p is the projected area of the kite, d the tether diameter and C_D^t the drag coefficient of the tether with respect to the perpendicular component of the wind.

$$C_{D,eff}^t \approx 0.31\,\bar{l}\,\frac{d}{A_p}\,C_D^t \tag{3.6}$$

Because only the upper end of the tether is moving with the speed of the kite and the lower end is not moving at all only the average effective tether drag needs to be estimated. The amount of this drag is about 31%[2] of the drag that the tether would have,

[2] Without any wind shear this constant would be 1/3. It can be calculated by integrating the drag force over the length of the tether. Because there is wind shear the lower value of 31% is used.

if the full length of it would move with the speed of the kite through the air. This value was derived by simulating a straight tether where one end was fixed and the other end moved on a circle. The value of $C_{\mathrm{D}}^{\mathrm{t}}$ for a cylinder at Reynolds numbers of about 1e3 is approx. one. Now the total drag C_{D} and thus L/D can be calculated:

$$C_{\mathrm{D}} = C_{\mathrm{D}}^{\mathrm{k}} + C_{\mathrm{D,eff}}^{\mathrm{t}} \tag{3.7}$$

The maximal tether force $F_{\mathrm{t,max}}$ can then be calculated, as derived in (Schmehl et al. 2013), as

$$F_{\mathrm{t,max}} = \frac{1}{2}\,\rho\, v_{\mathrm{a}}^2\, A_{\mathrm{p}}\, C_{\mathrm{D}} \sqrt{1 + \left(\frac{L}{D}\right)^2}. \tag{3.8}$$

This is the force, that the tether and the kite must be able to withstand during normal operation. It must be smaller or equal to the breaking force F_{b} divided by the safety factor S_{t}:

$$F_{\mathrm{t,max}} \leq \frac{F_{\mathrm{t,b}}}{S_{\mathrm{t}}} \tag{3.9}$$

The safety factor S_t must be chosen as high as needed to avoid that the tether breaks before the weak link[3] even if the tether is old and slightly damaged.

The average force is lower, because the kite is not always flying in the centre of the wind window. To take that into account, the crest factor CF_f is introduced, defined as the ratio of the maximal and effective tether force. The effective tether force is the quotient of the average mechanical reel-out power $\overline{P_{\mathrm{m,o}}}$ and the average reel-out velocity $\overline{v}_{\mathrm{t,o}}$. Combining these equations results in:

$$\mathrm{CF}_f = \frac{F_{\mathrm{t,max}}\ \overline{v}_{\mathrm{t,o}}}{\overline{P_{\mathrm{m,o}}}} \tag{3.10}$$

If CF_f is known, then the average mechanical reel-out power can be calculated:

$$\overline{P_{\mathrm{m,o}}} = \frac{1}{\mathrm{CF}_f}\, F_{\mathrm{t,max}}\ \overline{v}_{\mathrm{t,o}} \tag{3.11}$$

[3] At the top of the tether there should be a weak link that disconnects the kite from the tether in case of a high overload. In this situation the kite must become fully depowered and should stay attached to the main tether with a safety line.

The expression $\frac{1}{\mathrm{CF}_f}$ has a similar meaning as the "performance coefficient of the pumping kite generator", that was introduced in Argatov and Silvennoinen (2010a). For "representative solutions", Argatov found a performance coefficient of 0.9, which would result in a crest factor of 1.11. Because Argatov does not take into account the variations of the wind velocity and the impact of gravity (a kite is going downwards faster than upwards, because of it's weight), in reality the crest factor is higher.

Advantages of defining a crest factor: First it can be easily measured in practical tests; second, it can be compared to the theoretical optimum found by Argatov; and third, it can also be used for calculating of the average power output. On the other hand the crest factor depends on the wind fluctuations. Therefore it must be averaged over a longer period and is fully valid only for a specific location.

3.2.4 Simulating the reel-in phase

Simulating the reel-in phase is more difficult than simulating the reel-out phase because the elevation angle during reel-in cannot be actively controlled by steering the kite; only when flying crosswind the elevation angle can be actively controlled. Without flying crosswind the elevation angle rises according to Eq. (3.12). This can only be avoided with a lift over drag ration of zero, which is difficult to achieve. Our approach is to assume a quasi-steady equilibrium and steer the kite towards zenith, while trying to keep the azimuth angle zero. Then the derivative of the elevation angle can be calculated as function of the kite properties $C_{L,i}$ and $C_{D,i}$, the reel-in speed $v_{t,i}$ and the elevation angle β. To calculate the average reel-in speed and reel-in force the following method was used:

1. Initialize the elevation angle of the reel-in phase with the last optimized elevation angle of the reel-out phase.

2. Optimize the actual reel-in speed such that the average power over the whole cycle is maximized, assuming the relation between reel-in speed and reel-in force to be constant over the whole reel-in phase.

3. Increase the simulation time by the time step of the iteration Δt which was chosen to be 100 ms.

4. Increase the elevation angle by $\Delta\beta$ according to Eq. (3.12) . $v_{t,i}$ is the actual reel-in speed.

5. Repeat step 2 to 4 until the minimal reel-in length is reached.

$$\Delta\beta = \frac{v_\mathrm{w}}{l}\left(\frac{L}{D}\left(\cos\beta - \frac{v_\mathrm{t,i}}{v_\mathrm{w}}\right) - \sin\beta\right)\Delta t \tag{3.12}$$

Equation (3.12) is derived from the formula for the tangential velocity in (Schmehl et al. 2013).

In Fig. 3.1 the reel-in trajectory of the kite, using this algorithm, is shown as a solid line. The wind is coming from the left side. First, the tether is reeled out from $x = 200\ m$ to $x = 385\ m$. Then the tether is reeled in while the elevation angle is rising according to Eq. (3.12). Finally a transition phase is needed to decrease the elevation angle and reach the optimal reel-out angle again. In the simulation the path of the transition phase is not calculated, instead an experimentally determined time without power production (5 s) is used.

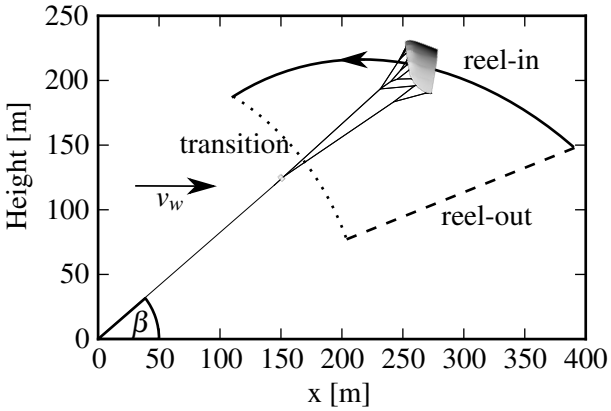

Figure 3.1: *Trajectory of the 29.5 m^2 kite at 7 m/s wind speed that was assumed in the simplified 2d-model of the simulation.*

3.2.5 Pumping efficiency, cycle efficiency and duty cycle

After the average mechanical reel-out power is determined in Eq. (3.11), the average mechanical power over a full cycle shall be calculated. If it would be possible to reel in with zero force, then the duty cycle D would be sufficient to calculate the average mechanical power. The duty cycle is defined as ratio of the reel-out duration Δt_o and the total cycle time:

$$D = \frac{\Delta t_\mathrm{o}}{\Delta t_\mathrm{o} + \Delta t_\mathrm{i}} \tag{3.13}$$

The duty cycle is determined by the winch and the wind speed: if the maximal reel-out and reel-in speed of the winch are the same, then a duty cycle of about 50% gives the highest power output at high wind speeds. At lower wind speeds (and a lower reel-out speed) a better duty cycle can be reached.

To improve the duty cycle at high wind speeds, a winch with a high maximal reel-in speed and a low maximal reel-out speed (at high torque) is needed.

To determine the optimal duty cycle, the average reel-in speed needs to be known. It should be chosen by a power optimization algorithm, taking the following restriction into account:

$$v_\mathrm{t,i} \leq \frac{v_\mathrm{t,i,max}}{\mathrm{CF}_\mathrm{v,i}} \tag{3.14}$$

The minimal crest factor $\mathrm{CF}_{v,i} > 1$ is a system property that depends mainly on the transition time between reel-in and reel-out.

To determine the duty cycle, not only $v_{t,i}$ and $v_{t,o}$ are needed, but also Δt_i and Δt_o. They can be determined, if the reel-in length Δl_t is known. For one cycle, Δl_t is assumed to be the same as the reel-out length. It should be chosen as long as possible, without flying too low (risk of crash and low wind speed) or too high (because of airspace regulations, but also because the weight and the drag of the tether impose a limit). The reel-in duration Δt_i and reel-out duration Δt_o can now be calculated as

$$\Delta t_\mathrm{i} = \frac{\Delta l_t}{v_\mathrm{t,i}}, \qquad \Delta t_\mathrm{o} = \frac{\Delta l_t}{v_\mathrm{t,o}}. \tag{3.15}$$

A certain amount of energy is needed for reeling in. To take this into account, the pumping efficiency η_p of the kite power system is introduced as quotient of the net mechanical energy $E_\mathrm{m,o} - E_\mathrm{m,i}$ and the mechanical energy $E_\mathrm{m,o}$, gained during reel-out:

$$\eta_\mathrm{p} = \frac{E_\mathrm{m,o} - E_\mathrm{m,i}}{E_\mathrm{m,o}} \tag{3.16}$$

This efficiency is mainly determined by the depower capability of the kite, but also by the control system (how fast can the kite switch between power and depower mode).

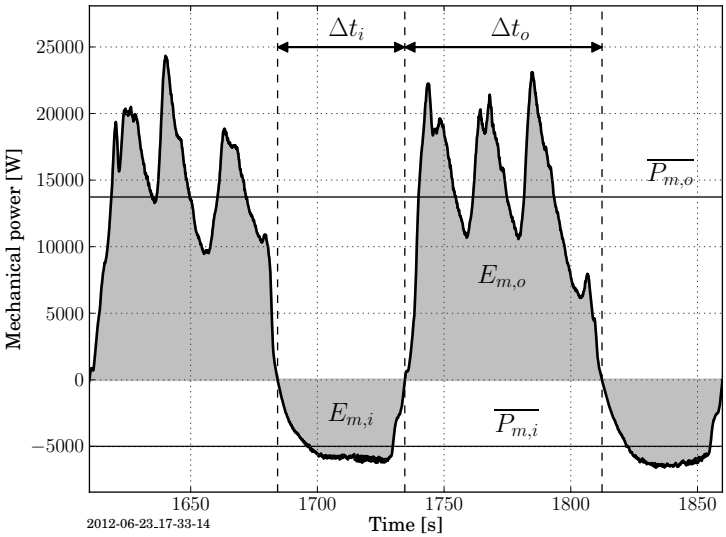

Figure 3.2: *Mechanical power and energy during two cycles. The power curve was measured using a 14* m^2 *kite on June 23, 2013.*

Now the average mechanical power over the full cycle $\overline{P_\mathrm{m}}$ can be calculated:

$$\overline{P_\mathrm{m}} = D\ \eta_\mathrm{p}\ \overline{P_\mathrm{m,o}} \tag{3.17}$$

The last two factors can be combined to the cycle efficiency:

$$\eta_\mathrm{cyc} = D\ \eta_\mathrm{p} = \frac{\overline{P_\mathrm{m}}}{\overline{P_\mathrm{m,o}}} \tag{3.18}$$

This efficiency is a good indication for the performance of a kite power system. It increases at low wind speeds, because in this situation the reel-out time increases, but the reel-in time (limited by the max. reel-in speed of the winch) stays nearly constant. As consequence the duty cycle and thus the cycle efficiency increases. Therefore η_cyc should be given for at least two wind speeds, e.g. the average wind speed and the wind speed that is needed for the nominal power output.

3.2.6 Optimization

Equations (3.17) can be used for a numerical optimization, to determine the optimal height, tether angle and reel-out speed for a given kite-power system, depending on the wind speed.

In addition to Eq. (3.9) the following side condition must be fulfilled during the optimization:

$$v_{\mathrm{t,o}} \leq \frac{v_{\mathrm{t,o}}^{\mathrm{max}}}{S_{\mathrm{v,o}}} \tag{3.19}$$

A safety factor $S_{\mathrm{v,o}} > 1$ is needed to be able to keep the tether force and the reel-out speed below the allowed limits, when there is a wind gust. The force can be reduced by increasing $v_{\mathrm{t,o}}$ very fast (mainly depending on the inertia of the generator and the drum). It can also be reduced by increasing β, but this takes much more time. The safety factor for the reel-out velocity is different from the safety factor for the tether force that was introduced in Eq. (3.9). When the maximum reel-out velocity is exceeded the winch usually stops and the mechanical brakes are activated (to avoid over-voltage and damage to the motor controller). If the wind is strong enough this will result in a force peak that breaks the weak link which should result in a soft landing. The safety factor $S_{\mathrm{v,o}}$ should be chosen such that this becomes sufficiently unlikely without sacrificing more potential power output than necessary.

3.2.7 Maximal tether force

According to the data sheet the ultimate tensile strength of Euroneema®HMPE rope (SK75) from Lankhorst Ropes, The Netherlands is 1073.4 N/mm^2. Therefore the breaking force $F_{t,b}$ can be calculated using the following equation:

$$F_{\mathrm{t,b}} = \frac{\pi}{S_{\mathrm{t}}} \left(\frac{d}{2}\right)^2 1073.4 \, \frac{\mathrm{N}}{\mathrm{mm}^2} \tag{3.20}$$

If a stronger rope is used the diameter of the tether can be reduced, but not only the strength of the tether, but also the lifetime should be taken into account when choosing the tether. It is suggested to choose a safety factor S_{t} of 3.0. A risk analysis should be performed to determine the adequate safety factor for a given application.

3.2.8 Electrical efficiency and total efficiency

For the calculation of the electrical efficiency of the winch first the efficiency of the components have to be determined. This can be done by measurements or by the use of mathematical models, based on the data sheets.

The following efficiencies are taken into account. First of all, the efficiency of the motor and the generator (η_{ei} and η_{eo}). Even if the motor and generator are the same component, these efficiencies won't be the same, because the point of operation will be different. It is very important to take the real point of operation into account, because the efficiencies from the data sheets are usually valid only for the optimal point of operation. Additionally the efficiency of the battery (η_{bat}) is taken into account, but for now the system efficiency is ignored and taken into account later.

If η_p is known, Eq. (3.16) can be solved for $E_\mathrm{m,i}$:

$$E_\mathrm{m,i} = (1 - \eta_\mathrm{p})\, E_\mathrm{m,o} \tag{3.21}$$

To calculate the winch efficiency, the electrical energy, that is produced during one cycle needs to be known. First the electrical reel-out energy is calculated:

$$E_\mathrm{e,o}^\mathrm{gro} = E_\mathrm{m,o}\ \eta_\mathrm{e,o} \tag{3.22}$$

Then the electrical energy that is needed for reeling in is calculated:

$$E_\mathrm{e,i}^\mathrm{gro} = \frac{E_\mathrm{m,i}}{\eta_\mathrm{e,i}} = \frac{(1 - \eta_\mathrm{p})\, E_\mathrm{m,o}}{\eta_\mathrm{e,i}} \tag{3.23}$$

To calculate the net energy, the energy needed for reel-in and divided by the battery efficiency needs to be subtracted from the electrical reel-out energy:

$$E_\mathrm{e}^\mathrm{gro} = E_\mathrm{e,o}^\mathrm{gro} - \frac{E_\mathrm{e,i}^\mathrm{gro}}{\eta_\mathrm{batt}} = \frac{E_\mathrm{m,o}\ (\eta_\mathrm{e,o}\ \eta_\mathrm{e,i}\ \eta_\mathrm{batt} - 1 + \eta_\mathrm{p})}{\eta_\mathrm{e,i}\ \eta_\mathrm{batt}} \tag{3.24}$$

Now the mechanical net energy is calculated:

$$E_\mathrm{m} = E_\mathrm{m,o} - E_\mathrm{m,i} \tag{3.25}$$

The ratio of the electrical gross energy and the mechanical energy is the electrical

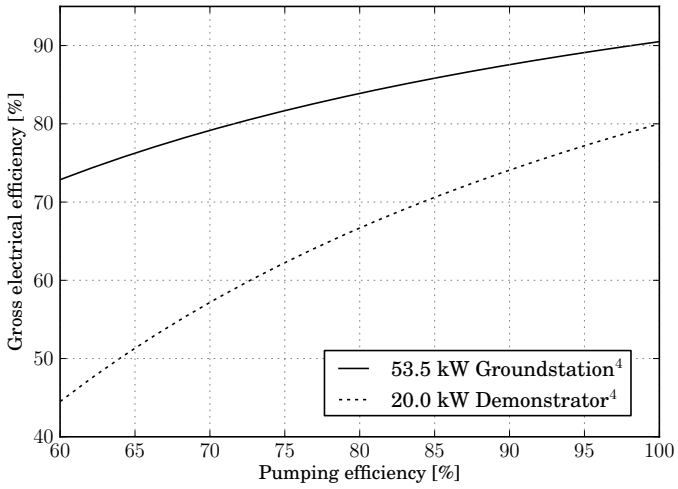

Figure 3.3: *Gross efficiencies of two ground stations. The graph shows that the ground-station efficiency is dependent on the pumping efficiency. The pumping efficiency depends on the aerodynamic performance of the kite.*

gross efficiency:

$$\eta_{\mathrm{e}}^{\mathrm{gro}} = \frac{E_{\mathrm{e}}^{\mathrm{gro}}}{E_{\mathrm{m}}} = \frac{\eta_{\mathrm{e,o}}\ \eta_{\mathrm{e,i}}\ \eta_{\mathrm{bat}} - 1 + \eta_{\mathrm{p}}}{\eta_{\mathrm{e,i}}\ \eta_{\mathrm{bat}}\ \eta_{\mathrm{p}}} \tag{3.26}$$

This result shows that the electrical efficiency of the winch depends on the pumping efficiency and the battery efficiency. Fig. 3.3 shows two examples for this dependency. In both cases a battery with 95% efficiency is used.

For the 20 kW demonstrator a generator efficiency of 80% and a motor efficiency of 79% is assumed. For the 53.5 kW direct drive ground station a motor and generator efficiency of 90% is assumed. A low pumping efficiency has a negative influence on the electrical efficiency. For this kind of kite power system the gross electrical efficiency is always lower than the efficiency of the generator alone!

Now the system efficiency η_{sys} is introduced and defined as

$$\eta_{\mathrm{sys}} = \frac{E_{\mathrm{e}}^{\mathrm{net}}}{E_{\mathrm{e}}^{\mathrm{gro}}} = \frac{E_{\mathrm{e}}^{\mathrm{gro}} - E_{\mathrm{e}}^{\mathrm{brk}} - E_{\mathrm{e}}^{\mathrm{sp}}}{E_{\mathrm{e}}^{\mathrm{gro}}}, \tag{3.27}$$

where $E_{\mathrm{e}}^{\mathrm{brk}}$ is the energy, needed to release the motor brakes, $E_{\mathrm{e}}^{\mathrm{sp}}$ is the energy, needed

for the spindle motor that moves the drum and $E_{\mathrm{e}}^{\mathrm{gro}}$ is the electrical gross energy as defined in Eq. (3.24).

The total efficiency is defined as the product of the cycle efficiency, the electrical efficiency and the system efficiency:

$$\eta_{\mathrm{tot}} = \eta_{\mathrm{cyc}}\ \eta_{\mathrm{e}}^{\mathrm{gro}}\ \eta_{\mathrm{sys}} = D\ \eta_{\mathrm{sys}}\ \frac{\eta_{\mathrm{e,o}}\ \eta_{\mathrm{e,i}}\ \eta_{\mathrm{bat}} - 1 + \eta_{\mathrm{p}}}{\eta_{\mathrm{e,i}}\ \eta_{\mathrm{bat}}} \tag{3.28}$$

The total efficiency expresses the relation between the average electrical net power output over the full cycle and the average mechanical power, that the kite produces during the reel-out phase. As you can see η_{tot} is only positive, if η_{sys} is positive and the following inequality holds:

$$\eta_{\mathrm{e,o}}\ \eta_{\mathrm{e,i}}\ \eta_{\mathrm{bat}} + \eta_{\mathrm{p}}\ >\ 1 \tag{3.29}$$

3.2.9 Modeling the efficiency of the generator

Using a constant efficiency for the motor/generator in the simulation will result in an over-optimistic estimate for the power output of a kite-power system. Better results can be achieved by modelling the efficiencies as two-dimensional scalar fields as a function of the rotational speed and torque. The friction torque of the 20 kW demonstrator was measured experimentally. This was approximated by a combination of a static contribution τ_c and a dynamic, velocity-dependent contribution $c_{\mathrm{v,f}}\ \omega_0$ as defined by the following equation:

$$\tau_{\mathrm{f,o}}\ =\ \tau_{\mathrm{c}}\ +\ c_{\mathrm{vf}}\ \omega_0 \tag{3.30}$$

When the input tether force is known the effective generator torque can now be calculated. Assuming a quasi-steady rotational equilibrium, it is sufficient to take only the tether force, drum radius and friction torque into account:

$$\tau_{\mathrm{g}}\ =\ \frac{F_{\mathrm{t,o}}}{r}\ -\ \tau_{\mathrm{f,o}} \tag{3.31}$$

[4] The 20 kW demonstrator is described in Sect. 3.3.1, the 53.3 kW Groundstation is a hypothetical system with 90% generator and motor efficiency.

Using the generator constant c_g the generator current and the electrical losses can now be calculated:

$$I_{\mathrm{o}} = \tau_{\mathrm{g}}\, c_{\mathrm{g}} \tag{3.32}$$

$$L_{\mathrm{e,o}} = 3\, R_{\mathrm{g}}\, I_{\mathrm{o}}^2\, k \tag{3.33}$$

The DC resistance of each phase, R_g can be taken from the data-sheet. To take the higher resistance at operating frequency due to the skin effect, stray-road-losses and other not explicitly modelled losses into account the factor k is introduced.

The power output and the electrical efficiency can now be calculated:

$$P_{\mathrm{e,o}} = P_{\mathrm{m,o}} - L_{\mathrm{e,o}} - \tau_{\mathrm{f,o}}\, \omega_0 \tag{3.34}$$

$$\eta_{\mathrm{e,o}} = \frac{P_{\mathrm{e,o}}}{P_{\mathrm{m,o}}} \tag{3.35}$$

If at least four values for the motor efficiency are known (for different torques and rotational speeds) the parameters can be fitted to the motor/ generator to obtain a sufficiently accurate efficiency model. An even more accurate (but also more difficult to use) efficiency model can be found in (Tamura 2012).

3.2.10 Modelling the efficiency of the motor

For the reel-in phase, either a separate motor is needed or the generator should be operated as a motor. The efficiency can be calculated in a similar way as the generator efficiency. The differences are the signs in Eq. (3.36 and 3.39) and the commutation of the numerator and denominator in Eq. (3.40) compared to Eq. (3.35).

$$\tau_{\mathrm{m}} = \frac{F_{\mathrm{i}}}{r} + \tau_{\mathrm{f,i}} \tag{3.36}$$

$$I_{\mathrm{i}} = \tau_{\mathrm{m}}\, c_{\mathrm{m}} \tag{3.37}$$

$$L_{\mathrm{e,i}} = 3\, R_{\mathrm{m}}\, I_{\mathrm{i}}^2\, k \tag{3.38}$$

$$P_{\mathrm{e,i}} = P_{\mathrm{m,i}} + L_{\mathrm{e,i}} + \tau_{\mathrm{f,i}}\, \omega_{\mathrm{i}} \tag{3.39}$$

$$\eta_{\mathrm{e,i}} = \frac{P_{\mathrm{m,i}}}{P_{\mathrm{e,i}}} \tag{3.40}$$

3.2.11 Specifying the power of a kite power system

It is suggested to use two figures to specify the power output of a kite power system, the nominal electrical generator power (this is easy to determine and to a certain degree reflects the costs of a ground station) and the system power, which is the average net electrical output at nominal wind speed. The system power is much harder to determine as it depends not only on the ground station but also on the kite, the wind and the performance of the control system.

To describe the cost efficiency of a kite-power system with respect to the generator costs the cost factor CoF is introduced. It is defined as the quotient of the nominal electrical generator power[5] and the system power:

$$CoF = \frac{P_{\text{nom}}}{P_{\text{sys}}} \tag{3.41}$$

This is not the same as $1/\eta_{sys}$ because the system efficiency depends on the average traction power, which can be higher or lower than the nominal generator power (depending on the wind, the kite and the control system).

3.2.12 Python implementation of the system model

The implemented model is based on the theoretical framework defined by Eqs. (3.1) – (3.41). The kite is assumed to be massless and represented by a pair of aerodynamic lift and drag forces (the effect of the mass was simulated, but because it was very small it was neglected). The crosswind motion of the kite is taken into account according to Eq. (3.8). Equation (3.11) is used to calculate the average reel-out power. The global optimizer module interalg (Kroshko n.d.) is used to optimize the power over the full cycle. The parameters available for optimization are the reel-out speed, average height and elevation angle. The difference between the minimal and maximal tether length was assumed to be constant (200 m). The reel-in phase is simulated as described in Sect. 3.2.4. Several iterations are needed for the optimization of reel-in and reel-out phases in order to resolve the interdependencies. For more details the reader is referred to the

[5] The nominal electrical generator power is the power, that the generator or the combination of generator and motor (if both are used in parallel) can provide continuously at nominal reel-out speed, if they have a constant mechanical power input. The nominal reel-out speed is the max. reel-out speed by design divided by the safety factor $S_{v,o}$ (here: 1.2).

Table 3.1: *Groundstation and tether properties*

	Demonstrator	**Groundstation**	**Description**
	20 kW	53.5 kW	
$v_{t,i,max}$	8.0	8.8	maximal reel-in speed by design [m/s]
$v_{t,o,max}$	8.0	4.4	maximal reel-out speed by design [m/s]
$F_{t,max}$	4000	20000	maximal pulling force [N]
P_{nom}	20000	53500	nominal electrical generator power [W]
r	0.1615	0.105	radius of the drum [m]
d	0.004	0.009	diameter of the tether [m]

Table 3.2: *Kite properties*

Property	**Mutiny V2**	**29.5** m^2	**Description**
	kite	kite	
m	20	43.0	total mass of kite, tether and control unit [kg]
A_p	16.5	29.5	projected area of the kite [m^2]
$C_\mathrm{L,o}$	1.0	1.4	lift coefficient of the fully powered kite
$C_\mathrm{D,o}$	0.2	0.2	drag coefficient of the fully powered kite
$C_\mathrm{L,i}$	0.14	0.14	lift coefficient, kite fully depowered
$C_\mathrm{D,i}$	0.07	0.14	drag coefficient, kite fully depowered

method "optimizeFullCycle" of the class "Model" of the simulation program (Fechner et al. 2013). The program suite is available under an open-source license (GPL).

3.3 Model validation

3.3.1 Implemented technology demonstrator

The current technology demonstrator of Delft University of Technology has a generator with a nominal electrical power of 20 kW. It uses a single cable to connect the kite to the ground station and implements the steering of the kite in a control unit suspended below the kite. In Table 3.1 the properties of the demonstrator are presented.

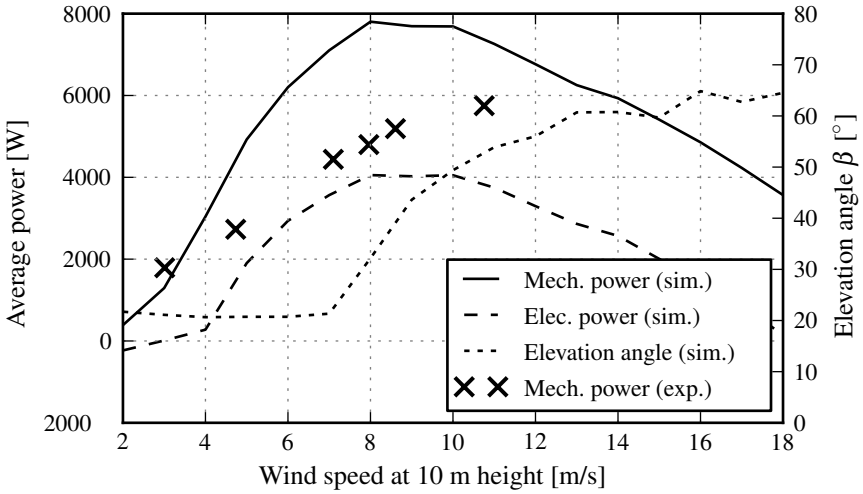

Figure 3.4: *Power output demonstrator*

3.3.2 Comparison with experimental data

Fig. 3.4 shows the simulated power output for the 20 kW Demonstrator of Delft University of Technology. The crosses represent measured values. The main reason for most of the measured values being lower than the simulated values, is that the force control loop of the ground station was not fast enough to reach the C_f factor of 1.1 that was assumed in the simulation. At a wind speed of 3 m/s the force limit is not reached, the force control loop is inactive and simulation matches the measured power output very well.

The fact that the measured power output at 10.8 m/s wind speed does not drop can be explained by the fact that in this situation a smaller kite with a projected area of only 11 m^2 was used. The reader might ask: Why is the maximal average electrical output of a kite-power system with a 20 kW generator only 4 kW? To understand the reasons for this, it is good to look at the efficiency figures in Fig. 3.5:

At 8 to 10 m/s wind speed the pumping efficiency is about 77%. This could be improved by changing the kite such that it doesn't collapse at a lower lift-over-drag ratio than two. The duty cycle is also quite low, about 47 %. The best way to improve this is to build a winch that can reel out slower with a higher force. For a kite of this size a much stronger winch is a better choice so that reeling out at about 1/3 of the wind speed

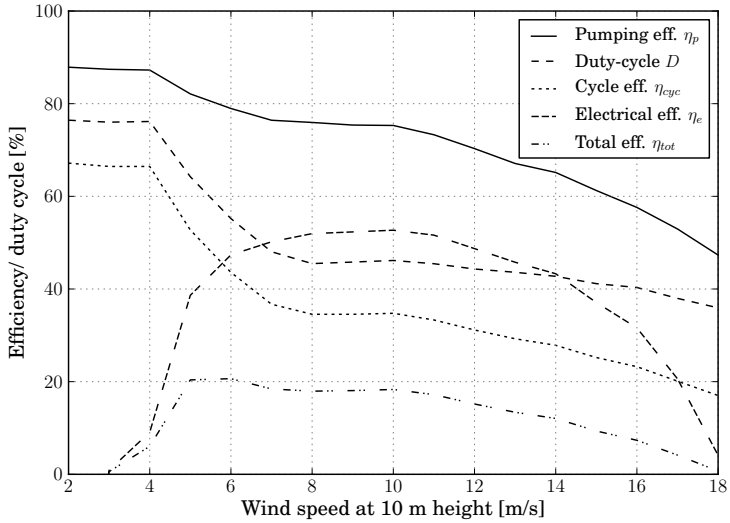

Figure 3.5: *Efficiencies of the demonstrator, simulated. The model parameters for calculating the electrical efficiency were fitted to measured values.*

becomes possible. The electrical efficiency is also very low, only 54 %. Reasons for this: An asynchronous, squirrel cage generator was used together with a very inefficient gearbox and a synchronous belt. One way to get a much better electrical efficiency is to use a synchronous direct drive generator. When all the efficiencies are multiplied the resulting total efficiency is only about 20%. Therefore only 4 kW electrical power can be obtained using a 20 kW generator.

Further model validation is needed, using a controller that optimizes elevation angle, lift-over-drag ratio and reel-in speed in the same way as the model. Additionally more accurate wind profiles are needed for model validation. The real wind speed at the height of the kite can be very different from the estimation, based on the wind profile law Eq. (3.2).

3.4 Design of a 31 kW kite power system using a 53.5 kW ground station

Using the experience with the demonstrator and the described model, a kite power system with a much higher total efficiency was designed. Design goals were a high capacity factor[6] at an average wind-speed of 5.5 m/s in 10 m height and a cut-out speed of at least 18 m/s.

Because not only the generator efficiency, but also the motor efficiency is very important and because the efficiency of a motor drops significantly if it is operated at only 10 % or 20 % of its nominal power the design suggests a separate motor and generator: A generator with high torque and low rotational speed and a motor with about half the nominal power and twice the nominal rotational speed.

The generator is decoupled from the drum during reel-in with a clutch to reduce the friction and to avoid over-voltage. The motor is always connected to the drum and produces about 20 % of the total power during reel-out.

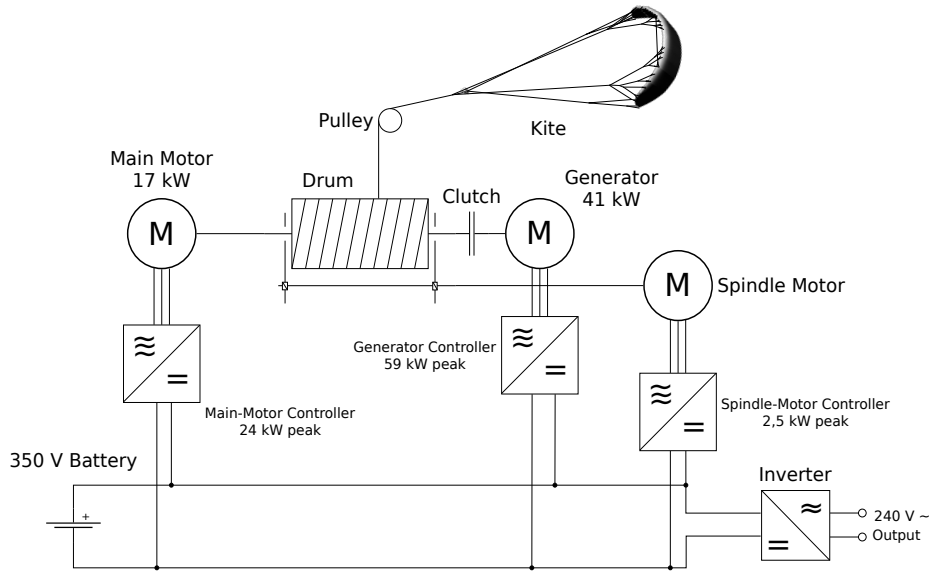

Figure 3.6: *Ground station schematics*

[6] The capacity factor is defined as the quotient of the average power output over the whole year and the system power as defined in Sect. 3.2.11.

For the design, I choose a generator and a motor that were available off-the-shelf. An additional selection criteria was the availability of detailed data sheets. I choose the type "500STK8M" as generator and the type "300STK8M" as motor, both from Alxion, France.

3.4.1 Simulation results

The simulated power curve is shown in Fig. 3.7. The kite-power system now reaches a nominal power output of 31 kW at a wind-speed of 7 m/s. The simulated efficiencies are shown in Fig. 3.8. The total efficiency now reaches a maximum of about 60 % and it reaches 54.6 % at a wind-speed of 7 m/s at nominal power output. At a wind speed of about 5.2 m/s the total efficiency reaches a maximum. In this example the design was done such that the maximum matches approximately the average wind-speed at the deployment site.

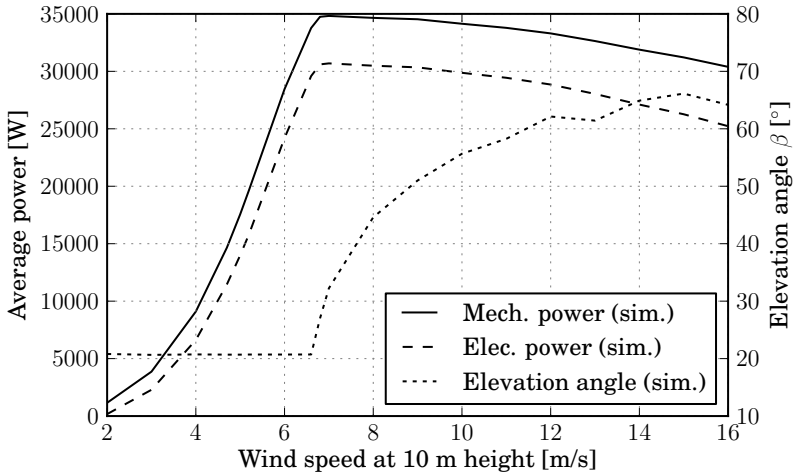

Figure 3.7: *Power output and elevation angle of the simulated direct drive system.*

The simulated reel-in and reel-out velocities and the duty cycle are shown in Fig. 3.9. The diagram is divided into three regions:

1. In region I (for $v_{w,g} < 5.2\ m/s$) the optimal reel-out speed is rising proportionally and the tether force quadratically with the wind speed. Therefore the output power

is rising approximately with the cube of the wind speed. The optimal duty cycle is nearly constant, in this example about 84 %.

2. In region II (for $5.2\ m/s < v_{w,g} < 6.8\ m/s$) the maximal tether force is reached and the reel-out speed is rising twice as fast as in region I. Therefore the output power is rising approximately linearly with the wind speed. The optimal duty cycle drops because the reel-in speed is constant and the reel-out speed rises.

3. In region III (for $v_{w,g} \geq 6.8\ m/s$) the maximal tether force and reel-out speed are reached, the reel-out power is constant and the elevation angle increases with the wind speed. The average output power is slowly falling because the needed reel-in power is rising with the wind speed. The optimal duty cycle is constant but at a lower level than in region I.

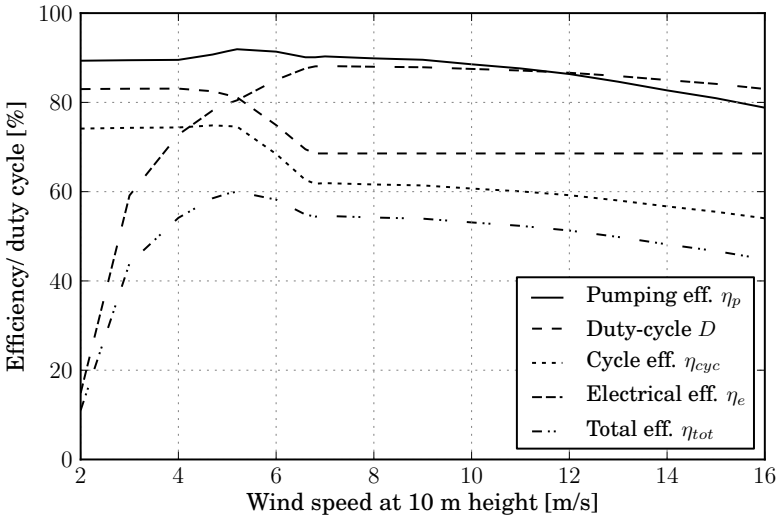

Figure 3.8: *Efficiencies of the simulated direct drive system. At 5.2 m/s the total efficiency reaches its maximum of 60 %.*

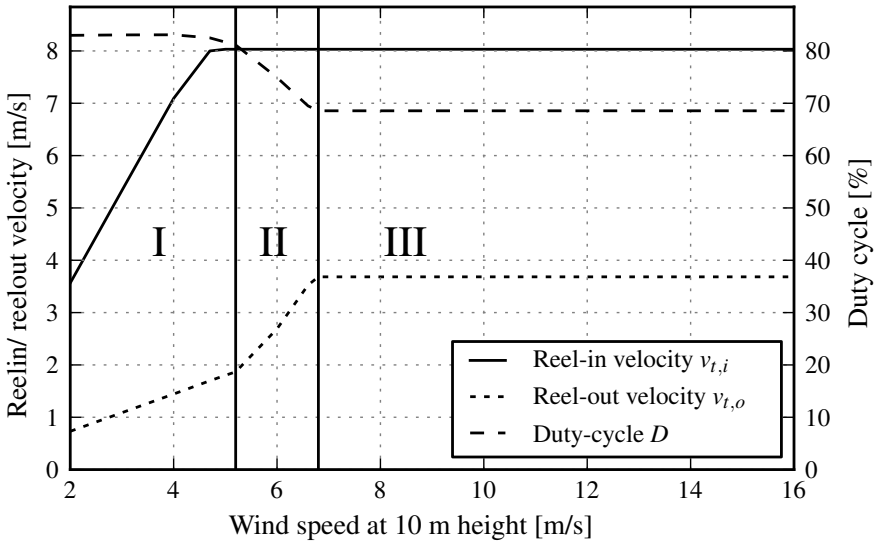

Figure 3.9: *Tether speeds. Region I: $v_{t,o}$ is rising linearly and the optimal tether force quadratically with the wind speed. Region II: the tether force reached its maximum, $v_{t,o}$ is rising twice as fast as in I. Region III: max force and $v_{t,o}$ reached, $P_{m,o}$ approx. constant.*

3.4.2 Performance factors

Table 3.3 gives an overview of the measured and simulated performance factors of the 20 kW[7] demonstrator and of the simulated 31 kW kite-power system, using a 53.5 kW ground station. The measured power output of the 20 kW demonstrator is about 34 % lower than the simulated power output. One of the reasons is that the crest factor for the reel-out force $CF_{f,o}$ is higher than necessary due to the current slow force control loop. Other possible reasons are the uncertainty of the kite properties, especially the lift-over-drag ratio (an error of 10% would result in 20 % less power output) and the uncertainty of the coefficient of the wind profile law p. This coefficient depends heavily on the time of the year and the weather conditions.

[7] Nominal electrical generator power.

Table 3.3: *Performance factors*

	20 kW winch measured	**20 kW winch** simulated	**53.5 kW winch** simulated	**Description**
A_p	16.5	16.5	29.5	projected kite area [m^2]
$F_{t,max}$	4000	4000	20000	max. tether force [N]
η_p	77	77	90	pumping efficiency [%]
D	56	46.8	68.6	duty cycle [%]
η_{cyc}	43	36	61.7	cycle efficiency [%]
η_{tot}	21	18	57	total efficiency [%]
CoF	7.1	4.6	1.7	cost factor
$v_{t,o,max}$	8.0	8.0	4.4	max. reel-out speed by design [m/s]
$\overline{h}$	307	300	272	average height during reel-out [m]
v_w	n.a.	12.0	10.1	wind speed at height of the kite [m/s]
$v_{w,g}$	8.5	8.0	7.0	wind speed at 6 m height [m/s]
$v_{t,o}$	4.24	6.67	3.68	average reel-out speed [m/s]
β	25	25.9	27.9	elevation angle [$^\circ$]
$\overline{P_{m,o}}$	14100	21638	59787	average traction power (reel-out) [W]
P_m	5190	7900	36054	average mech. power (full cycle) [W]
P_{sys}	2595	4000	31000	average electrical system power [W]
$S_{v,i}$	1.1	1.1	1.1	safety factor reel-in speed
$S_{v,o}$	1.2	1.2	1.2	safety factor reel-out speed
$S_{t,f}$	3.37	3.37	3.0	safety factor tether force
$CF_{o,f}$	1.25	1.11	1.11	crest factor reel-out force
$CF_{o,v}$	1.89	1.2	1.2	crest factor reel-out velocity

3.5 Summary and conclusion

In this chapter a simplified model of a pumping kite power system in 2D was developed. Performance factors were identified: The most important performance factor of the airborne and control system is the cycle efficiency η_{cyc} (see Eq. 3.18). It can be increased, if the kite can be reeled in with a lower force (higher depower capability), and if it can be reeled in faster (higher maximal reel-in speed of the ground station). In addition, a fast force control loop is needed for a high cycle efficiency to increase the average reel-out force for given maximal tether force.

The second important performance factor is the electrical gross efficiency $\eta_{\text{e}}^{\text{gro}}$ (see Eq. 3.26). To reach a high value, not only an efficient generator is needed, but the motor/generator must also work efficiently during reel-in. The best design of a drive train, that works efficiently in both modes of operation is still an open question. In this chapter I suggested a separate motor and generator, coupled with a clutch, but other solutions like an electrically excited synchronous generator might also work well. For the design of an efficient kite power system it is necessary to know the efficiency of the electrical machines as function of speed and torque. Because it is very difficult to obtain this data from manufactures, in Sec. 3.2.9 a simplified generator model was developed, that requires only the data at two operation points to calculate the needed coefficients.

Finally an efficient, durable and affordable energy storage is needed to design a cost and energy efficient kite power system. This is very important for off-grid applications, but less important for kite power farms, where one kite can provide the power to reel in another kite.

Selecting the right components and right-sizing them is the key for efficient system design. For doing this, simulations over the full range of the expected wind speeds should be performed. Better simulation tools are needed to support the design process efficiently. The software, presented in Sec. 3.2.12 can be used as starting point for the development of such simulation tools.

Because of the limited accuracy of the averaged simulation model, that was presented in this chapter, but also for controller development, a dynamic, three dimensional system model will be presented in the next chapter.

CHAPTER 4

Dynamic Modelling

Contents

4.1 Introduction 49
4.2 Computational approach 51
4.2.1 Atmospheric model 52
4.2.2 Tether model 54
4.2.3 Point mass kite model 56
4.2.4 Four point kite model 59
4.2.5 Winch model 65
4.2.6 Control system 67
4.2.7 Implementation and accuracy 68
4.3 Model calibration and results 69
4.3.1 Test flight 70
4.3.2 Parking manoeuvres for aerodynamic measurements 71
4.3.3 Identifying the steering sensitivity parameters 72
4.3.4 Model comparison 76
4.3.5 Results: Power production and flight path 76
4.4 Summary and conclusion 78

4.1 Introduction

The averaged kite-power system model that was presented in the last chapter already allows some insight in the performance of kite-power systems, but it is not sufficient for the development of kite control systems or kite-state estimators. To get deeper insight in

the performance of kite-power systems, but also for trajectory optimization, controller and estimator development three dimensional, dynamic system models are needed.

A dynamic model of a two-line kite is derived in (Diehl 2001). Variations of the angle of attack are not taken into account and the simplicity of the model allows for an analytical derivation of a state space representation based on four dynamic states. Further expanding on this model, Ahmed et al. (2011) proposed a kite power system model with three degrees of freedom (DOF), in which the kite is represented as a point mass at the end of the straight tether of variable length. Assuming a rigid wing with constant aerodynamic properties, the steering forces are derived as functions of the roll angle.

A discretisation of the tether as a multibody system has been proposed by Williams et al. (2007), using a Lagrangian approach to derive the equations of motion in generalised coordinates. The advantage of this approach is the direct incorporation of constrains which results in a compact problem formulation. This model used rigid tether segments, connected by spherical joints, which is not sufficient for modelling the tether force and implementing the force control loop, because the flexibility of the tether is reducing force peaks already a lot. In addition it is adding and removing point masses during the simulation to simulate reel-out and reel-in of the tether. According to our experience this causes artificial discontinuities in the model which makes it difficult to implement the force control loop. For the kite it also used a point mass model.

A model that uses a discretised tether with point masses connected by springs was published in Gohl and Luchsinger (2013). The aerodynamics of the kite were modelled using the vortex lattice method, which means that it is using an advanced kite model. On the other hand it was not mentioned if the dynamics of the winch were modelled at all and no details were published on the question how reeling in and out was modelled. Other authors presented detailed generator and winch models (Ahmed et al. 2011; Coleman et al. 2013), but no or only a very simple model for the kite and the tether.

Coupling fluid and structural dynamic solvers for wind turbine applications has been studied by Viré (2012) and Viré et al. (2012), while fluid-structure interactions methods have been applied to kite aeroelastic behaviour by Bosch et al. (2014). These kind of models might be useful for the design of improved kites, but they are very computational intensive and currently at least one order of magnitude slower than real-time (Bosch et al. 2014).

This chapter presents a model where the dynamics of all major system components

– the tether, the kite and the generator – are taken into account, with a focus on a novel discretised tether model which allows smooth reel-in and reel-out. It is soft real-time capable and thus suitable for the training of kite pilots and winch operators, but can also be used for software in the loop testing of KPS control systems, the development of estimation algorithms and for the optimization of flight trajectories.

An improved one-point kite model is presented, that allows to change the angle of attack during simulation time and uses look-up tables to calculate the lift and drag as function of the angle of attack. It also takes the increased drag when flying around corners into account. In addition it uses a correction term to match the influence of gravity. This model can already be sufficient for optimizing flight trajectories.

For controller development a four-point kite model is devised, the most simple point mass model that has rotational inertial in all axis. This avoids discontinuities in the kite orientation which make the one-point kite model uncontrollable in certain flight manoeuvres. In addition it is very close to a fully physical model: Many model parameters like the height and width of the kite and the height of the bridle can just be measured and do not need to be identified. Only the steering sensitivity parameters need to be identified because they depend on the flexibility of the kite which is not explicitly modelled.

This chapter will first explain the atmospheric model, then the tether model and the two kite models and finally the winch model. Furthermore, the control system is briefly explained. Subsequently a systematic approach for the model calibration is presented, with the goal to match the conditions of a real flight as good as possible.

In the results section major parameters like force, speed, power and flight trajectory as obtained from the point mass model and the four point model are compared with data, measured using the Hydra kite of Delft University of Technology. Finally conclusions are drawn about the performance and accuracy of the described models and which improvements are still needed.

This chapter is based on (Fechner et al. 2015). The introduction and conclusions are rewritten and the grammar and nomenclature adapted.

4.2 Computational approach

One of the requirements when building the model was, that it has to be (soft-) real-time capable. On the other hand, the programming effort should be limited and it should be easy to adapt the model to different kite power systems. It was found that high-level

modelling tools like Simulink or Modellica were not capable to simulate a discretised tether that is reeling in or out in real-time. Therefore general purpose programming languages are used that make low-level optimizations of the modelling code possible.

The kite and the tether are modelled as a particle system, using discrete point masses which are connected by spring-damper elements. This has the advantage of a coherent model structure for which efficient mathematical methods for solving the stiff equation system exist (Eberhardt et al. 2000). For describing the positions of the particles a ground fixed reference frame is used, where the x-axis is pointing east, the y-axis north and the z-axis upwards. The origin is placed at the ground station.

The state vector of the system was constructed using the states of the tether particles, the states of the kite particles (only needed for the the four point kite model, because otherwise the last tether particle also represents the kite) and the scalar states of the winch (generator). Because no accurate, real-time measurements of the wind speed at the height of the kite were available, an atmospheric model, describing the wind profile, was also needed.

4.2.1 Atmospheric model

To determine the wind speed v_w at the height of the kite and at the height of each tether segment, the power law (Stull 2000) and the log law (Burton et al. 2001, p. 19) are used. Input parameters are the ground wind speed $v_{w,ref}$ and the current height z of the kite or tether segment. The ground wind speed used in this chapter was measured at $z_{ref} = 6.0$ m. The power law establishes the relationship between v_w and $v_{w,ref}$ as

$$v_{w,exp} = v_{w,ref} \left(\frac{z}{z_{ref}} \right)^p \tag{4.1}$$

with the exponent p as fitting parameter. The logarithmic law, which according to (Burton et al. 2001, p. 20) is more accurate than the least-square power law, can be written in the following form

$$v_{w,log} = v_{w,ref} \frac{\log(z/z_0)}{\log(z_{ref}/z_0)}, \tag{4.2}$$

where z_{ref} is the reference height and z_0 is the roughness length. For this paper not only the ground wind speed $v_{w,ref}$ is measured, but once per flight additionally the wind speed at two more heights, z_1 and z_2. Then, a wind profile is fitted to these three wind speeds.

To make a fit with three (speed, height) pairs possible, Eqs. (4.2) and (4.1) are combined in the following way

$$v_{\mathrm{w}} = v_{\mathrm{w,log}} + K\,(v_{\mathrm{w,log}} - v_{\mathrm{w,exp}}). \tag{4.3}$$

The fit is done by varying the surface roughness z_0 and K until v_w according to Eq. (4.3) matches the measured wind speed at all three heights. The exponent p is chosen according to

$$p = \frac{\log(\,v_{\mathrm{w,exp}}(z_1)\,/\,v_{\mathrm{w,ref}}\,)}{\log(z) - \log(z_{\mathrm{ref}})}, \tag{4.4}$$

which results in $v_{\mathrm{w,exp}}(z_1) = v_{\mathrm{w,log}}(z_1)$.

Assuming a constant temperature of 15 °C and an average sea-level density of $\rho_0 = 1.225\ kgm^{-3}$, according to Stull (2000, p. 6) the air density can be calculated as

$$\rho = \rho_0\ \exp\left(-\frac{z}{H_\rho}\right), \tag{4.5}$$

where z is the height and $H_\rho = 8.55$ km. An example for a fitted wind profile is shown in Fig. 4.1, using the parameters from Table 4.3.

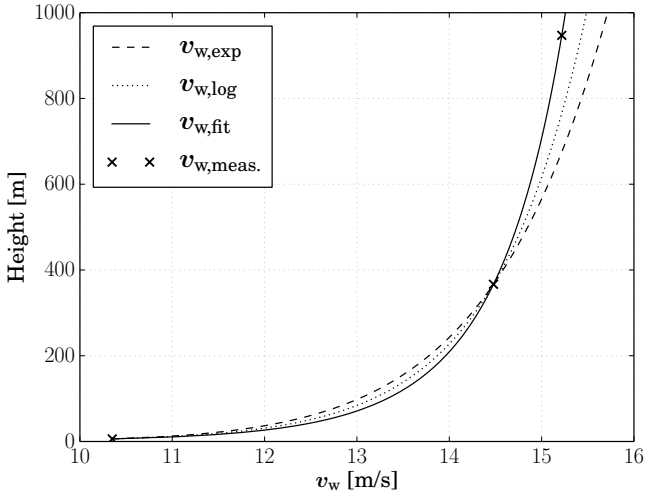

Figure 4.1: *Wind profile according the logarithmic law (dotted), the power law (dashed) and the fitted wind profile (solid), a linear combination of the others. Cross symbols represent measured values.*

4.2.2 Tether model

The tether is modelled as a fixed number of lumped masses, connected with n spring damper elements as shown in Fig. 4.5. To simulate reel-in and reel-out the initial length of the tether segments l_s is varied according to

$$l_s = \frac{l_{t,i}}{n} + \frac{v_{t,o}\,(t - t_i)}{n}, \tag{4.6}$$

where $l_{t,i}$ is the tether length at the beginning of the i-th time step, $v_{t,o}$ the reel-out velocity, t the simulation time and t_i the simulation time at the beginning of the i-th time step.

This length is then used to calculate the spring and damping constants

$$k = k_0\,\frac{l_0}{l_s}, \tag{4.7}$$

$$c = c_{d,0}\,\frac{l_0}{l_s}, \tag{4.8}$$

where l_0 is the initial length of the tether segments at the beginning of the simulation. The differential equations of the particle system are formulated as an implicit problem

$$F(t, \mathbf{Y}, \dot{\mathbf{Y}}) = 0, \tag{4.9}$$

$$\mathbf{Y}(t_0) = \mathbf{Y}_0, \tag{4.10}$$

$$\dot{\mathbf{Y}}(t_0) = \dot{\mathbf{Y}}_0. \tag{4.11}$$

The state vector $\mathbf{Y}$ of the particle system is defined as

$$\mathbf{Y} = (\mathbf{p}, \mathbf{v}), \tag{4.12}$$

where $\mathbf{p}$ and $\mathbf{v}$ comprise the positions and velocities of the particles, respectively. For solving the problem only the residual $\mathbf{R} = F(t, \mathbf{Y}, \dot{\mathbf{Y}})$ needs to be programmed. The vector $\mathbf{R}$ consists of two partitions, the residual of the position vectors and its derivatives, and the residual of the velocity vectors and its derivatives,

$$\mathbf{R} = (\mathbf{R}_p,\ \mathbf{R}_v). \tag{4.13}$$

The first partition can be calculated from Newton's law, $\mathbf{a} = \dot{\mathbf{v}}$. To calculate the second partition the particle forces must be known. On each particle are acting the forces of the spring damper element above and below the particle. In addition, half of the aerodynamic drag forces of the tether segments above and below of each particle have to be taken into account.

With $\mathbf{f}_{s,i}$ denoting the tensile force of segment i and $\mathbf{d}_i$ denoting the aerodynamic drag force of this segment as calculated in Eq. (4.21), the forces acting on the i-th particle can be calculated according to

$$\mathbf{f}_i = \mathbf{f}_{s,i-1} + \mathbf{f}_{s,i} + \frac{1}{2}\left(\mathbf{d}_i + \mathbf{d}_{i-1}\right). \tag{4.14}$$

The first and the last particle have to be treated differently: For $i = 0$ the lower spring force has to be replaced with the tether force as experienced by the ground station, and for the last tether particle the aerodynamic force of the kite has to be taken into account.

The spring forces are calculated according to Hooke's law

$$\mathbf{f}_s = \left(k\left(\| \mathbf{s}_i \| - l_s\right) + c\left(\frac{\mathbf{s}_i}{\| \mathbf{s}_i \|} \cdot \mathbf{s}_{v,i}\right)\right)\frac{\mathbf{s}_i}{\| \mathbf{s}_i \|} \quad , \tag{4.15}$$

with l_s, k and c calculated according to Eqs. (4.6) – (4.8) and with

$$\mathbf{s}_i = \mathbf{p}_{i+1} - \mathbf{p}_i \, , \tag{4.16}$$

$$\mathbf{s}_{v,i} = \mathbf{v}_{i+1} - \mathbf{v}_i \, . \tag{4.17}$$

Linear springs with a different stiffness for the extension and compression regimes are used. The stiffness for compression is much lower to model the behaviour of flexible bridle and tether lines, yet provide some structural stability.

The aerodynamic drag of any tether segment is calculated in the following way: First the wind speed at the height of the i-th tether segment $\mathbf{v}_{w,s,i}$ is calculated using Eq. (4.3). Then, the average segment velocity is calculated as

$$\mathbf{v}_{s,i} = \frac{1}{2}\left(\mathbf{v}_{i+1} + \mathbf{v}_i\right), \tag{4.18}$$

which leads to the apparent air velocity

$$\mathbf{v}_{\mathrm{a,s,i}} = \mathbf{v}_{\mathrm{w,s,i}} - \mathbf{v}_{\mathrm{s,i}}. \tag{4.19}$$

Under the assumption that the cable is not starting to vibrate due to vortex induced vibrations, the drag of a cylinder is mainly caused by the component of $\mathbf{v}_{\mathrm{a,s,i}}$ that is perpendicular to the tether segment $\mathbf{s}_{\mathrm{i}}$ calculated as

$$\mathbf{v}_{\mathrm{a,s},i,\perp} = \mathbf{v}_{\mathrm{a,s,i}} - \left(\mathbf{v}_{\mathrm{a,s,i}} \cdot \frac{\mathbf{s}_{\mathrm{i}}}{\| \mathbf{s}_{\mathrm{i}} \|} \right) \frac{\mathbf{s}_{\mathrm{i}}}{\| \mathbf{s}_{\mathrm{i}} \|} . \tag{4.20}$$

Using this velocity component, acting on the tether segment is resulting in

$$\mathbf{d}_{\mathrm{i}} = \frac{1}{2} c_{\mathrm{d,t}} \rho \ \| \mathbf{v}_{\mathrm{a,s},i,\perp} \| \| \mathbf{s}_{\mathrm{i}} \| \ d_{\mathrm{t}} \ \mathbf{v}_{\mathrm{a,s},i,\perp}, \tag{4.21}$$

where $c_{\mathrm{d,t}}$ is the tether drag coefficient and d_{t} the tether diameter.

4.2.3 Point mass kite model

The point mass model proposed by Diehl (2001, pp. 139–144) represents the kite as a discrete mass moving under the action of an aerodynamic force vector. It is also denoted as “one point” or “1p” model. Steering is incorporated by an aerodynamic side force which depends linearly on the steering input. This model does not account for rotational inertia, assuming that the wing is always aligned with the local relative flow experienced during flight. Expanding on the original work, the model presented in the following allows for tether deformation and a variable angle of attack.

Reference frame

The kite reference frame (x, y, z) is defined on the basis of the local tether geometry and relative flow conditions. As illustrated in Fig. 4.2 the z-axis is aligned with the last tether segment. The x- and y-axes are constructed such that the apparent air velocity vector $\mathbf{v}_{\mathrm{a}} = \mathbf{v}_{\mathrm{w}} - \mathbf{v}_{\mathrm{k}}$ is in the xz-plane. This is based on the assumption that the wing is always aligned with the apparent wind velocity and that the sideslip velocity vanishes

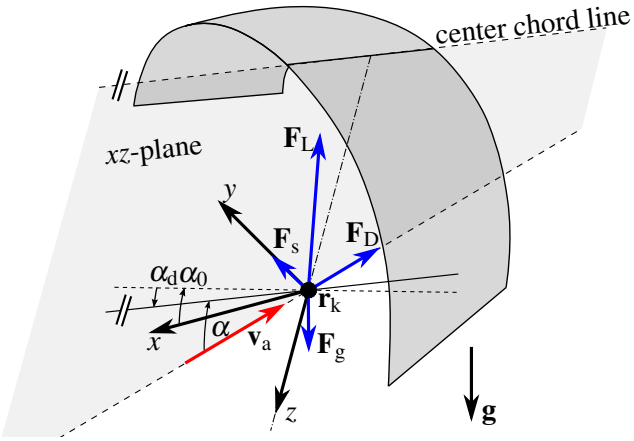

Figure 4.2: *Kite reference frame (x,y,z) of the point mass kite model. The physical wing is included here for the purpose of illustrating the concept of angle of attack and the assumed alignment with the relative flow.*

correspondingly. The vector base is calculated as

$$\mathbf{e}_z = -\frac{\mathbf{s}_{n-1}}{\| \mathbf{s}_{n-1} \|}, \tag{4.22}$$

$$\mathbf{e}_y = \frac{\mathbf{v}_a \times \mathbf{e}_z}{\| \mathbf{v}_a \times \mathbf{e}_z \|}, \tag{4.23}$$

$$\mathbf{e}_x = \mathbf{e}_y \times \mathbf{e}_z. \tag{4.24}$$

The unit vector $\mathbf{e}_x$ is also called *heading*, because it describes the orientation of the wing.

External forces

The external force $\mathbf{F}_k$ acting on the point mass representation of the kite comprises contributions of aerodynamic lift $\mathbf{F}_L$ and drag $\mathbf{F}_D$, the aerodynamic side force $\mathbf{F}_s$ and the

gravitational force $\mathbf{F}_\mathrm{g}$

$$\mathbf{F}_\mathrm{L} = \frac{1}{2}\,\rho\, v_\mathrm{a}^2 A\, C_\mathrm{L}(\alpha)\, \frac{\mathbf{v}_\mathrm{a}\times\mathbf{e}_\mathrm{y}}{\parallel \mathbf{v}_\mathrm{a}\times\mathbf{e}_\mathrm{y} \parallel}, \tag{4.25}$$

$$\mathbf{F}_\mathrm{D} = \frac{1}{2}\,\rho\, v_\mathrm{a}^2 A\, C_\mathrm{D}(\alpha)\, (1+K_\mathrm{s,D}\,|u_\mathrm{s}|)\, \frac{\mathbf{v}_\mathrm{a}}{\parallel \mathbf{v}_\mathrm{a} \parallel}, \tag{4.26}$$

$$\mathbf{F}_\mathrm{s} = \frac{1}{2}\,\rho\, v_\mathrm{a}^2 A\, \frac{A_\mathrm{side}}{A}\, c_\mathrm{s}\, (u_\mathrm{s}+u_\mathrm{s,c})\, \mathbf{e}_\mathrm{y}, \tag{4.27}$$

$$\mathbf{F}_\mathrm{g} = (m_\mathrm{k}+m_\mathrm{KCU})\, \mathbf{g}, \tag{4.28}$$

$$\mathbf{F}_\mathrm{k} = \mathbf{F}_\mathrm{L}+\mathbf{F}_\mathrm{D}+\mathbf{F}_\mathrm{s}+\mathbf{F}_\mathrm{g}. \tag{4.29}$$

It should be emphasised that the drag force increases as the kite is steered due to kite deformation. Also, the steering force is based on the side area of the kite rather than the top area of the kite. The factored term A_side/A represents a parametrized description of a kite's geometry. The constant c_s describes the steering sensitivity of the kite and has to be determined experimentally. The influence of the steering on the drag is described by $K_\mathrm{s,D}$. The empirical value of $K_\mathrm{s,D} = 0.6$ is used. The variable $u_\mathrm{s,c}$ is a correction term for the influence of gravity on the turn rate of the kite. It is calculated as follows

$$u_\mathrm{s,c} = \frac{c_\mathrm{2,c}}{v_\mathrm{a}}\, \sin\psi\, \cos\,\beta. \tag{4.30}$$

Equation (4.30) is derived from the turn rate law as presented in Eq. (4.72). The correction factor $c_\mathrm{2,c}$ must be chosen such that the identified parameter c_2 of the one-point model matches the measurements. Without this correction the influence of gravity in this model was more than a factor of two higher.

Calculation of lift and drag as function of the angle of attack

Under the following assumptions:

- The kite-tether angle depends linearly on the depower settings u_d;
- the kite-depower angle has the value α_0 for $u_\mathrm{d} = u_\mathrm{d,0}$;
- the maximal depower value of $u_\mathrm{d} = u_\mathrm{d,max}$ corresponds to a kite-tether angle of $\alpha_0 - \alpha_\mathrm{d,max}$.

Then, the angle of attack can be calculated with the following formula

$$\alpha = \arccos\left(\frac{\mathbf{v}_a \cdot \mathbf{e}_x}{v_a}\right) - \alpha_d + \alpha_0, \tag{4.31}$$

where α_0 is the angle between the kite and the cable when the kite is fully powered as shown in Fig. 4.3 and α_d is the additional angle resulting from reeling out the depower line

$$\alpha_d = \frac{u_d - u_{d,0}}{u_{d,max} - u_{d,0}}\, \alpha_{d,max}, \tag{4.32}$$

where $u_{d,0}$ is the value of the depower control input that is needed for the fully powered kite (maximal L/D) and $u_{d,max}$ and $\alpha_{d,max}$ the values for u_d and α_d respectively that are needed for the fully depowered kite.

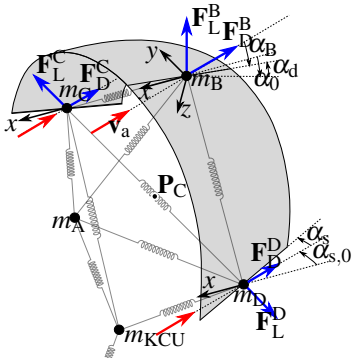

Figure 4.3: *Angle of attack α, apparent air velocity v_a, depower angle α_d and α_0 of the four point kite model. Steering is accomplished by changing α_s. Sideslip is possible.*

Figure 4.4 shows the lift coefficient C_L and the drag coefficient C_D as functions of the angle of attack α. The curves are established using the models of lift and drag coefficients of stalled and unstalled airfoils from Spera (2008), yet experience based modifications were made to better fit the coefficients of the non-ordinary wing section of a leading edge inflatable tube kite.

4.2.4 Four point kite model

The point mass kite model can be sufficient to simulate and optimize the flight path of a power kite, because it is controllable during the power cycle and the simulated

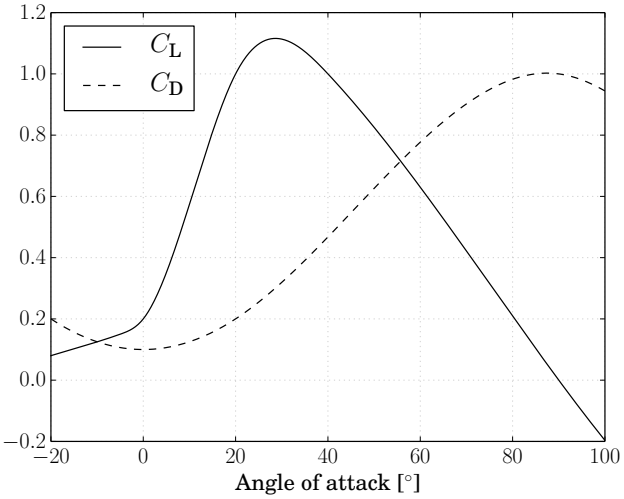

Figure 4.4: *The lift and the drag coefficients as function of the angle of attack.*

tether forces are close to the measured values. In addition the point mass model can be used to calculate the initial orientation of more complex models. However, it is not a good choice for the development and optimization of flight-path control algorithms, because the reaction of the kite to steering inputs is problematic: A point mass kite has no rotational inertia, therefore its yaw angle is *jumping* when the sign of v_a is changing. This is non-physical behaviour. In these situations controllability is lost. Therefore, we will now investigate a four-point kite model (4p model) in order to obtain a more realistic and robust model.

Geometry and mass distribution

The most simple particle-system based kite model that has rotational inertia in all axis is a four point kite model, which we will use from now on. The points of the this model are defined in Fig. 4.5.

The kite mass m_k is distributed to points **A** to **D** according to Eqs. (4.33) – (4.37) while the mass of the kite control unit m_KCU plus half of the mass of the last tether segment are

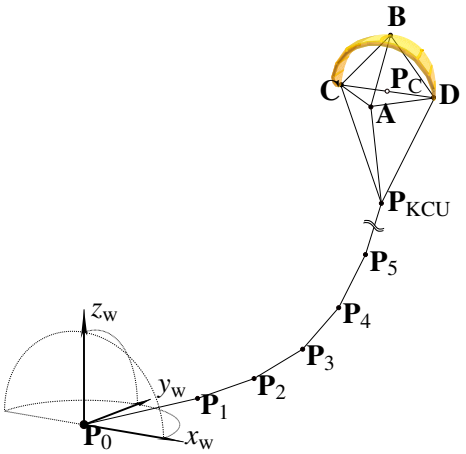

Figure 4.5: *Four point model of the kite defined by points* **A**, **B**, **C** *and* **D**. *Points* $\mathbf{P}_0$ *to* $\mathbf{P}_{\mathrm{KCU}}$ *discretize the tether.*

used as the mass of $\mathbf{P}_{\mathrm{KCU}}$

$$m_{\mathrm{PKCU}} = m_{\mathrm{KCU}} + \frac{l_{\mathrm{t}}\,\sigma}{2\,n}, \tag{4.33}$$

$$m_{\mathrm{A}} = \gamma\, m_{\mathrm{k}}, \tag{4.34}$$

$$m_{\mathrm{B}} = 0.4\,(1-\gamma)\, m_{\mathrm{k}}, \tag{4.35}$$

$$m_{\mathrm{C}} = 0.3\,(1-\gamma)\, m_{\mathrm{k}}, \tag{4.36}$$

$$m_{\mathrm{D}} = 0.3\,(1-\gamma)\, m_{\mathrm{k}}, \tag{4.37}$$

where γ is the nose mass fraction of the wing, n the number of tether segments, l_{t} the current tether length and σ the linear mass density of the tether. The simulation of typical flight manoeuvres at low apparent air velocities has shown that a value of $\gamma = 0.47$ reproduces well the dive-down behaviour of the Leading Edge Inflatable (LEI) tube kites employed in the current study.

The virtual centre position of the kite, $\mathbf{P}_{\mathrm{C}}$ is defined as

$$\mathbf{P}_{\mathrm{C}} = \frac{1}{2}\,(\mathbf{C}+\mathbf{D}). \tag{4.38}$$

The origin of the kite reference frame is at **B**. The unit vectors $\mathbf{e}_{\mathrm{x}}, \mathbf{e}_{\mathrm{y}}$ and $\mathbf{e}_{\mathrm{z}}$ are defined

as

$$\mathbf{e}_z = \frac{\mathbf{P}_C - \mathbf{B}}{\| \mathbf{P}_C - \mathbf{B} \|}, \tag{4.39}$$

$$\mathbf{e}_y = \frac{\mathbf{C} - \mathbf{D}}{\| \mathbf{C} - \mathbf{D} \|}, \tag{4.40}$$

$$\mathbf{e}_x = \mathbf{e}_y \times \mathbf{e}_z. \tag{4.41}$$

To parametrize the shape of the kite only three values need to be defined: The height of the kite h_k (distance between $\mathbf{P}_C$ and $\mathbf{B}$), the height of the bridle h_b (distance between $\mathbf{P}_C$ and $\mathbf{P}_{KCU}$) and the width of the kite w_k (the distance between $\mathbf{C}$ and $\mathbf{D}$).

Initial conditions

To calculate the initial positions of the kite particles, the point mass kite model from Sec. 4.2.3 is used. The initial unit vectors of the kite reference frame ($\mathbf{e}_{x,0}, \mathbf{e}_{y,0}$ and $\mathbf{e}_{z,0}$) are calculated using the kite position, the orientation of the last tether segment and the apparent air velocity (Eqs. (4.22), (4.23) and (4.24)).

When these vectors are known, the positions of the kite particles at zero force can be defined by the following equations

$$\mathbf{P}_C = \mathbf{P}_{KCU} - h_b\, \mathbf{e}_{z,0}, \tag{4.42}$$

$$\mathbf{A} = \mathbf{P}_C + d_{n,r}\, w_k\, w_{rel}\, \mathbf{e}_{x,0}, \tag{4.43}$$

$$\mathbf{B} = \mathbf{P}_C - h_k\, \mathbf{e}_{z,0}, \tag{4.44}$$

$$\mathbf{C} = \mathbf{P}_C + 0.5\, w_k\, w_{rel}\, \mathbf{e}_{y,0}, \tag{4.45}$$

$$\mathbf{D} = \mathbf{P}_C - 0.5\, w_k\, w_{rel}\, \mathbf{e}_{y,0}, \tag{4.46}$$

where $d_{n,r}$ is the relative nose distance, a kite dependant factor in the order of 0.2. In combination with the nose mass fraction γ the factor $d_{n,r}$ can be used to tune the rotational inertia and the centre of gravity. The distance from $\mathbf{C}$ to $\mathbf{D}$ is calculated using the tip-to-tip distance of the kite w_k multiplied with the relative kite width w_{rel} which is a factor in the order of 0.9 and reflects the fact that the aerodynamic steering forces do not act on the tips of the kite, but a little bit further inwards.

During the simulation, the aerodynamic forces are applied to surfaces that are attached to the kite particles. This causes them to change their positions, and from the

current positions the unit vectors of the kite reference frame can then be calculated using Eqs. (4.39) – (4.41).

Projected air velocities and angles of attack

The aerodynamic model assumes surfaces attached to the top particle **B** and to the side particles **C** and **D**. The sole purpose of particle **A** is to achieve rotational inertia and to realistically place the centre of gravity, therefore no aerodynamic force is attached to this particle.

The lift forces are determined based on the part of the apparent velocity that is perpendicular to the leading edge as suggested in (Obert 2009). For the surface attached to the top particle, this is the apparent velocity in the xz-plane $\mathbf{v}_{\mathrm{a,xz}}$. For the surfaces attached to the side particles, the apparent velocity in the xy-plane $\mathbf{v}_{\mathrm{a,xy}}$ is needed. These can be calculated as follows

$$\mathbf{v}_{\mathrm{a,xz}} = \mathbf{v}_{\mathrm{a}} - (\mathbf{v}_{\mathrm{a}} \cdot \mathbf{e}_{\mathrm{y}})\, \mathbf{e}_{\mathrm{y}}, \tag{4.47}$$

$$\mathbf{v}_{\mathrm{a,xy}} = \mathbf{v}_{\mathrm{a}} - (\mathbf{v}_{\mathrm{a}} \cdot \mathbf{e}_{\mathrm{z}})\, \mathbf{e}_{\mathrm{z}}. \tag{4.48}$$

For the top surface of the kite the angle of attack can be calculated as follows

$$\alpha_{\mathrm{B}} = \pi - \arccos\left(\frac{\mathbf{v}_{\mathrm{a,B},xz} \cdot \mathbf{e}_{\mathrm{x}}}{\| \mathbf{v}_{\mathrm{a,B},xz} \|}\right) - \alpha_{\mathrm{d}} + \alpha_0. \tag{4.49}$$

The angle α_{d} is the change of the angle between the kite and the last tether segment due to the change of the depower settings. The value of α_{d} is between zero when fully powered and – for the leading edge inflatable tube kites used at Delft University of Technology – about 30° when fully depowered. If the reel-out length of the depower tape, the height of the bridle, the height of the kite and the power-to-steering-line distance are known, α_{d} can be calculated geometrically; In many cases the linear approximation given by Eq. (4.32) is sufficient.

For the side surfaces of the kite the angles of attack can be calculated as follows

$$\alpha_{\mathrm{C}} = \pi - \arccos\left(\frac{\mathbf{v}_{\mathrm{a,C},xy} \cdot \mathbf{e}_{\mathrm{x}}}{\| \mathbf{v}_{\mathrm{a,C},xy} \|}\right) - \alpha_{\mathrm{s}} + \alpha_{\mathrm{s},0}, \tag{4.50}$$

$$\alpha_{\mathrm{D}} = \pi - \arccos\left(\frac{\mathbf{v}_{\mathrm{a,D},xy} \cdot \mathbf{e}_{\mathrm{x}}}{\| \mathbf{v}_{\mathrm{a,D},xy} \|}\right) + \alpha_{\mathrm{s}} + \alpha_{\mathrm{s},0}, \tag{4.51}$$

where α_s is the change of the angle of attack caused by the steering line difference. For $\alpha_{s,0}$ a value of 10° is assumed. With the steering offset $u_{s,0}$ – which is in practice unavoidable and caused by asymmetries in the steering system – α_s can be calculated as follows

$$\alpha_s = \frac{u_s - u_{s,0}}{1 + K_{d,s}(\alpha_d/\alpha_{d,max})}\ \alpha_{s,max}. \tag{4.52}$$

The value of $\alpha_{s,max}$ (in the order of 20°) must be chosen such that the steering sensitivity of the kite model matches the steering sensitivity of the kite to be simulated. The factor $K_{d,s}$ describes the influence of the depower angle α_d on the steering sensitivity: depending on the geometry of the bridle it has a value in the range of $1 < K_{d,s} < 2$. A value of 1.5 means that the fully depowered kite needs 2.5 times the steering input as a fully powered kite to achieve the same turn rate (under the condition that the apparent wind speed is the same).

Aerodynamic forces

Steering is accomplished by changing the angle of attack for the side surfaces differentially. The aerodynamic forces that act on **B**, **C** and **D** can be calculated according to Eqs. (4.53) – (4.58), where A_{side}/A is the relative side area of the kite and ρ the air density.

$$\mathbf{F}_L^B = \frac{1}{2}\,\rho\, v_{a,B,xz}^2\, A\, C_L(\alpha_B)\, \frac{\mathbf{v}_{a,B} \times \mathbf{e}_y}{\| \mathbf{v}_{a,B} \times \mathbf{e}_y \|}, \tag{4.53}$$

$$\mathbf{F}_L^C = \frac{1}{2}\,\rho\, v_{a,C,xy}^2\, A \frac{A_{side}}{A}\, C_L(\alpha_C)\, \frac{\mathbf{v}_{a,C} \times \mathbf{e}_z}{\| \mathbf{v}_{a,C} \times \mathbf{e}_z \|}, \tag{4.54}$$

$$\mathbf{F}_L^D = \frac{1}{2}\,\rho\, v_{a,D,xy}^2\, A \frac{A_{side}}{A}\, C_L(\alpha_D)\, \frac{\mathbf{e}_z \times \mathbf{v}_{a,D}}{\| \mathbf{e}_z \times \mathbf{v}_{a,D} \|}, \tag{4.55}$$

$$\mathbf{F}_D^B = \frac{1}{2}\,\rho\, K_D\, v_{a,B}^2\, A\, C_D(\alpha_B)\, \frac{\mathbf{v}_{a,B}}{\| \mathbf{v}_{a,B} \|}, \tag{4.56}$$

$$\mathbf{F}_D^C = \frac{1}{2}\,\rho\, K_D\, v_{a,C}^2\, A \frac{A_{side}}{A}\, C_D(\alpha_C)\, \frac{\mathbf{v}_{a,C}}{\| \mathbf{v}_{a,C} \|}, \tag{4.57}$$

$$\mathbf{F}_D^D = \frac{1}{2}\,\rho\, K_D\, v_{a,D}^2\, A \frac{A_{side}}{A}\, C_D(\alpha_D)\, \frac{\mathbf{v}_{a,D}}{\| \mathbf{v}_{a,D} \|}. \tag{4.58}$$

The coefficient K_D is required to achieve the same lift-to-drag ratio for the straight flying four point kite as for the one point kite. It can be calculated from

$$K_D = \left(1 - \frac{A_{side}}{A}\right) \kappa \tag{4.59}$$

where $\kappa = 0.93$ was needed to compensate the higher drag coefficients of the side areas, compared to the top area, caused by $\alpha_{s,0}$.

4.2.5 Winch model

The winch is seen as the assembly of an asynchronous generator, a gearbox and a drum around which the tether is wound. The generator is used as motor during the reel-in phase and the sign of the generator's torque determines the direction of the energy flow. The winch model combines the differential equations for the inertial system and an expression for the torque-speed characteristics of the generator.

Inertial dynamics of the winch

The differential equations for the winch are again defined as an implicit problem

$$F(t, \mathbf{Y}_e, \dot{\mathbf{Y}}_e) = 0, \tag{4.60}$$
$$\mathbf{Y}_e(t_0) = \mathbf{Y}_{e,0}, \tag{4.61}$$
$$\dot{\mathbf{Y}}_e(t_0) = \dot{\mathbf{Y}}_{e,0}. \tag{4.62}$$

The vector $\mathbf{Y}_e$ is the extended state vector of the implicit problem and consists of tether length $l_{t,i}$ and the tether velocity $v_{t,o}$

$$\mathbf{Y}_e = (l_{t,i}, v_{t,o}). \tag{4.63}$$

In order to solve this problem the residual $\mathbf{R}_e = F(t, \mathbf{Y}_e, \dot{\mathbf{Y}}_e)$ is to be calculated, with $\mathbf{R}_e$ defined as

$$\mathbf{R}_e = \begin{bmatrix} v_{t,o} - \dot{l}_{t,i} \\ a_{t,o} - \dot{v}_{t,o} \end{bmatrix}. \tag{4.64}$$

Here, $a_{t,o}$ is the acceleration of the tether at the ground station. Under the assumption of an inelastic interconnection of the generator and drum through the gearbox, the acceleration can be calculated as

$$a_{\mathrm{t,o}} = \frac{1}{I_{\mathrm{w}}} \frac{r}{n} \left(\tau_{\mathrm{g}} + \tau_{\mathrm{d}} - \tau_{\mathrm{f}}\right), \tag{4.65}$$

where I_{w} is winch inertia as seen from the generator, r the drum radius, n the gearbox ratio, τ_{g} the generator torque, τ_{d} torque exerted by the drum on the generator and τ_{f} the friction torque.

The torque exerted by the drum depends on the tether force that is exerted on the drum, which equals the norm of the force on the first tether particle

$$\tau_{\mathrm{d}} = \frac{r}{n} \parallel f_{s,0} \parallel. \tag{4.66}$$

The friction is modelled as the combination of a viscous friction component with the friction coefficient c_{f} and the static friction τ_{s}

$$\tau_{\mathrm{f}} = c_{\mathrm{f}}\, v_{\mathrm{t,o}} + \tau_{\mathrm{s}}\, \mathrm{sign}(v_{\mathrm{t,o}}). \tag{4.67}$$

4.2.5.1 Torque profile of the asynchronous generator

To determine the torque-speed profile of the asynchronous generator, the equivalent circuit representation suggested by Wildi (2002, p. 326) is used. Under the assumption of negligible stator resistance, τ_{m} can be expressed as a function of $v_{\mathrm{t,o}}$ and the synchronous generator speed v_{s} as

$$\tau_{\mathrm{g}} = \alpha \frac{v_{\mathrm{s}} - v_{\mathrm{t,o}}}{1 + \beta\, (v_{\mathrm{s}} - v_{\mathrm{t,o}})^2}. \tag{4.68}$$

It is assumed that the generator voltage E is increasing linearly with the set speed, up to the nominal voltage E_{n} at the nominal synchronous speed $v_{\mathrm{s,n}}$ of the generator

$$E = \begin{cases} E_{\mathrm{n}} \dfrac{v_{\mathrm{s}}}{v_{\mathrm{s,n}}} & \text{if } \mid v_{\mathrm{s}} \mid \leq v_{\mathrm{s,n}} \\ E_{\mathrm{n}} & \text{if } \mid v_{\mathrm{s}} \mid > v_{\mathrm{s,n}} \end{cases}. \tag{4.69}$$

Table 4.1: *Properties of the ground station of Delft University of Technology*

Ground station	
Gearbox ratio n [-]	6.2
Drum radius r [m]	0.1615
Inertia I_w [kg m^2]	0.328
Viscous friction coeff. c_f [Ns]	0.799
Static friction τ_s [Nm]	3.18
Rotor resistance R_r [mΩ]	72.7
Self inductance L [mH]	2.97
Nominal synchronous speed $v_{s,n}$ [m/s]	4.09
Nominal voltage E_n [V]	231

As derived in (Schreuder 2013b), the parameters α and β can be expressed as

$$\alpha = \begin{cases} \dfrac{E_\mathrm{n}^2\, r}{v_\mathrm{s,n}^2\, R_\mathrm{r}\, n} & \text{if } \mid v_\mathrm{s} \mid \leq v_\mathrm{s,n} \\ \dfrac{E_\mathrm{n}^2\, r}{v_\mathrm{s}^2\, R_\mathrm{r}\, n} & \text{if } \mid v_\mathrm{s} \mid > v_\mathrm{s,n} \end{cases} \tag{4.70}$$

$$\beta = \frac{L^2}{R_\mathrm{r}^2}\,\frac{n^2}{r^2}, \tag{4.71}$$

where R_r is the rotor resistance and L is the generator's self inductance. These generator parameters could either be measured or estimated based on known torque data. The properties of the implemented system are shown in Tab. 4.1.

4.2.6 Control system

In this section a brief description of the control system is given. Further details can be found in (Vlugt et al. 2013b) and (Fechner and Schmehl 2012b). The control system, used for the simulations of this chapter is simpler than the approach, presented in Chap. 5.

Flight path planning and control

For the automated power production a simple flight path planner is used: The kite is always steered towards one of three points: During reel-in and parking it is steered towards zenith (directly above the ground station). During reel-out it is steered to a point on either the right or left side of the wind window (Vlugt et al. 2013b).

The orientation of the kite (the heading angle) is controlled. Great circle navigation is used to determine the heading needed to steer towards the target point. The difference between the required heading and the actual heading is the error signal that is going into a PI controller that is controlling the steering signal i_s of the kite control unit. In addition the KCU has an input i_d for the depower signal. The set value i_d is low during reel-out and high during reel-in (predefined, fixed values).

The steering signal differentially changes the length of the left and right steering lines, the depower signal changes the length of the steering lines relative to the length of the depower lines. The actuators are modelled such that they have a maximum speed (derivative of the output control signals u_s and u_d). They use a P-controller to control the output signal. In addition a delay of 150 ms was implemented in the model. The delay is mainly caused by the motor controllers.

Winch control

During reel-out the winch is using a set value for the reel-out speed in addition to a maximal value of the tether force. The speed is used as long as the maximum tether force is not exceeding the set value, otherwise the synchronous speed is increased to limit the force. A parameter varying PID controller is used to track the set values.

During reel-in, different values for the set force and set speed are used. Soft transitions are implemented for the set values when switching between reel-in and reel-out.

4.2.7 Implementation and accuracy

The Radau5DAE solver (Hairer and Wanner 1996) from version 2.4 of the Assimulo suite (Anderson et al. 2013) is used for solving the differential algebraic system, as it offered the best performance.

Real-time simulation based on the numerical model

Because for software-in-the-loop testing of kite control components a batch simulation is not sufficient, a soft real time simulator was implemented. The real-time simulation is executed in the following way: After the start of the simulation a new system state is calculated in fixed time intervals of currently 50 ms. The new state is then published and used by the KPS controller to calculate new values for steering and depower settings of the kite and for the set-value of the reel-out speed of the winch. These values are assumed to be constant during the next time interval. Within one simulation time interval, the implicit equation system solver uses as many time-steps as necessary to calculate a solution with the specified precision.

Model and measurement accuracy

The solver that was used allows it to specify a maximum error. This error was set to 1.8 cm for the position states and to 0.03 cm/s for the velocity states. The tether was discretised with seven particles.

The wind sensor at the ground has an accuracy of 5% plus 0.5 knots. The tether force was measured with an accuracy of $1\% \pm 10$ N, the reel-out speed with $2\% \pm 0.05$ m/s.

4.3 Model calibration and results

For the calibration of the model the following steps are needed:

1. determine the physical system properties (Table 4.2) and enter them as parameters into the model;
2. determine the wind profile;
3. determine the lift-over-drag ratio of the kite as function of the depower settings;
4. determine the steering coefficients of the kite;
5. validate the average and maximum force during reel-out;
6. validate power output over the full cycle.

The one-point model, the four-point model and the HYDRA kite of Delft University of Technology are compared. The models were tuned to match the kite properties as much as possible.

4.3.1 Test flight

For parameter fitting and validation the measurements of a test flight were chosen, that took place at the Maasvlakte II, The Netherlands on 23 June 2012. The wind was very strong and the wind profile was expected to be similar to offshore conditions. This flight was chosen because it contains different flight manoeuvres, e.g. parking the kite at zenith at different heights and with different depower settings. This allows for a partial validation of the lift-over-drag properties of the kite as function of the depower settings.

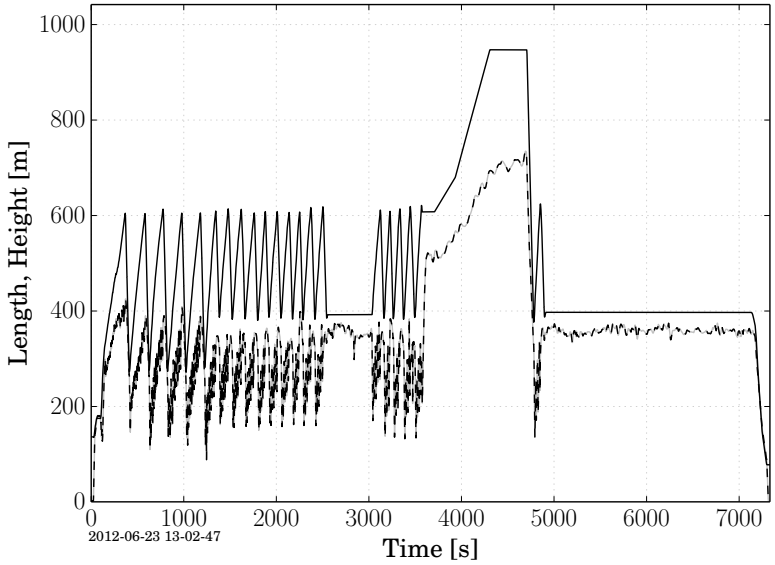

Figure 4.6: *Measured reel-out tether length l_t (solid) and height z_k (dashed) of the kite during a test flight on 23 June 2012 at the Maasvlakte II, The Netherlands.*

Table 4.2: *Properties of the HYDRA kite, bridle, KCU and tether of Delft University of Technology*

Kite	
Projected wing surface area A [m^2]	10.18
Mass including sensors m_k [kg]	6.21
Width w_k [m]	5.77
Height h_k [m]	2.23
Relative side area A_side/A [%]	30.6
Bridle	
Height h_b [m]	4.9
Bridle line diameter [mm]	2.5
Kite Control Unit	
Mass m_KCU [kg]	8.4
Main Tether	
Diameter d_t [mm]	4.0
Mass per m [kg/m]	0.013
Unit damping coefficient c_0 [Ns]	473
Unit spring constant k_0 [N]	614600

4.3.2 Parking manoeuvres for aerodynamic measurements

The lift-over-drag ratio and the wind profile were determined by keeping the kite pointing towards the small-earth zenith without reeling in or out. Subsequently, it was waited until a force equilibrium was reached. In this situation the elevation angle of the tether is depending mainly on the lift-to-drag ratio, and the tether force is mainly depending on the wind speed at the height of the kite.

The measurements of Table 4.4 were used to calibrate the L/D of the kite and the sensitivity to changes of u_d by changing $u_{\mathrm{d},0}$ and $\alpha_{\mathrm{d,max}}$ (see Eq. (4.32)).

In addition, this data was used to tune the wind profile coefficients z_0 and K according to Eq. (4.3). The parameters $z_0, u_{\mathrm{d},0}, \alpha_{\mathrm{d,max}}, K$ and $c_{d,t}$ were fitted until the force and the elevation angle for all three measurements matched with an error of less than one $\pm\sigma$. The results are shown in Table 4.3 and the resulting wind profile in Fig. 4.1. The

Table 4.3: *Identified system parameters*

Fitted parameters		
$u_{d,0}$ [%]	21.3	depower offset
z_0 [m]	2.0e-4	surface roughness
K [-]	1.0	wind profile correction
$\alpha_{d,max}$ [^{o}]	31.00	max. depower angle
$c_{d,t}$	0.96	tether drag coefficient
Measured parameters		
u_{max} [%]	42.47	max. depower setting

Table 4.4: *Forces and elevations β while parking*

Test case	$v_{w,ref}$ $[ms^{-1}]$	l_t $[m]$	u_d	Force [N]	σ_f	β [°]	σ_β
Parking 392a	10.35	392.0	25.1%	850.5	309.8	65.9	2.0
Parking 392b	9.59	392.0	27.9%	551.3	125.1	60.6	0.9
Parking 947	10.02	947.2	28.0%	552.8	57.2	49.3	0.9

value of $\alpha_{d,max}$ is very close to the geometrically derived value of about 30°. The tether drag coefficient is very close to the value of about 1.0, that was suggested by Fechner and Schmehl (2013, p. 253).

4.3.3 Identifying the steering sensitivity parameters

According to Erhard and Strauch (2013, p. 149) the turn rate of the kite around the straight line between the kite and the tether should depend on the steering input α_s, the apparent air velocity v_a, the elevation angle β and the orientation of the kite ψ in following way

$$\dot{\psi} = c_1 \, v_a \, (u_s - c_0) + \frac{c_2}{v_a} \sin\psi \cos\beta. \tag{4.72}$$

The steering offset c_0 was added here, because it had a relevant effect in the flight tests.

To fit the parameter c_2 the relative kite width w_{rel} was varied and to fit c_1 the maximal steering angle $\alpha_{s,max}$ until the measured values c_1 and c_2 matched the simulated values within 1%.

The results of a parameter fit of the first cycle of the above mentioned test flight

are shown in Table 4.5, where ρ is the Pearson product-moment correlation coefficient between the measured yaw rate and the turn rate estimated by using Eq. (4.72) and σ is the standard deviation of the estimated turn rate. All data was filtered by calculating a moving average over two seconds before plotting and performing the parameter fitting. The diagrams in Fig. 4.7 illustrate the measured yaw rate, the turn rate estimated by

Table 4.5: *Fitted turn rate law parameters of the Hydra kite. Values based on the measurements and on the one point and four point kite model.*

Fitted steering parameters			
$\alpha_{s,max}$ [^{o}]	15.9	maximal steering	
w_{rel} [%]	91.0	relative kite width	4p model
c_s	2.59	steering coefficient	1p model
$c_{2,c}$	0.93	correction factor	1p model
	Measured	**1-point**	**4-point**
u_d [%]	26.0	26.0	26.0
c_0 [–]	-0.003	-0.004	-0.003
c_1 [rad /m]	0.261	0.264	0.262
c_2 [rad m/s^2]	6.28	6.20	6.27
ρ (PCC)	0.9933	0.9999	0.9995
σ [rad/s]	0.002	0.0002	0.0006

using Eq. (4.72) and the relationship between the estimated and measured/ simulated yaw/ turn rates. The term *heading rate* is used for the derivative of the heading angle while the term *yaw rate* is used for the value that was measured by the gyroscope of the inertia measurement unit of the kite that was aligned with its z-axis. The numerical derivative of the heading angle of the IMU was too noisy to be used.

For the parameter $K_{d,s}$, the influence of the depower settings on the steering sensitivity a value of 1.5 was used. This value was estimated based on the geometry of the kite and the bridle. To verify this value, it is suggested to fly figures of eight with a fully depowered kite. This was not done yet in practice. The data measured during the reel-in phase of the kite was not sufficient to validate this parameter because - without flying crosswind - the turn rate of the kite is highly influenced by the turbulence of the wind. The data was too noisy to be useful.

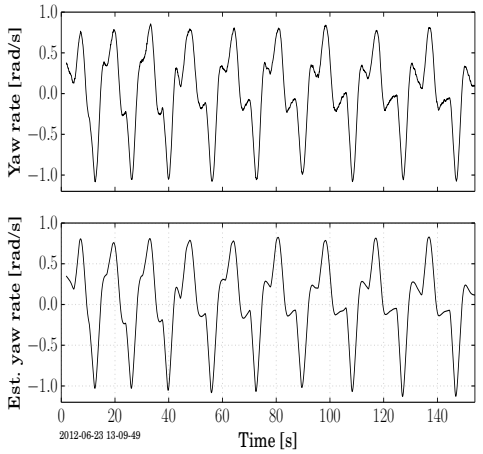

(a) *Measured and estimated yaw rate. The reason for the negative peaks, compared to the simulation are probably measurement errors.*

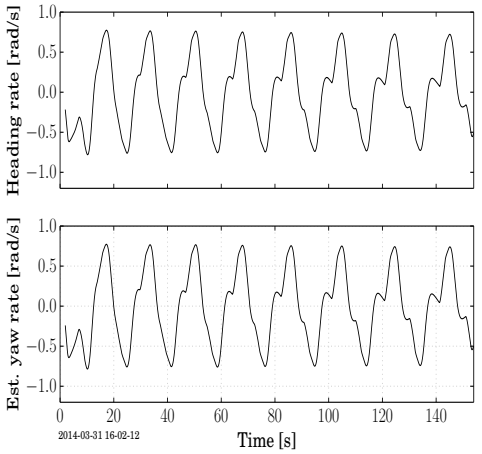

(b) *Simulated and estimated heading rate. The estimation is based on the turn rate law (Eq. 4.72), using the fitted parameters c_0, c_1 and c_2.*

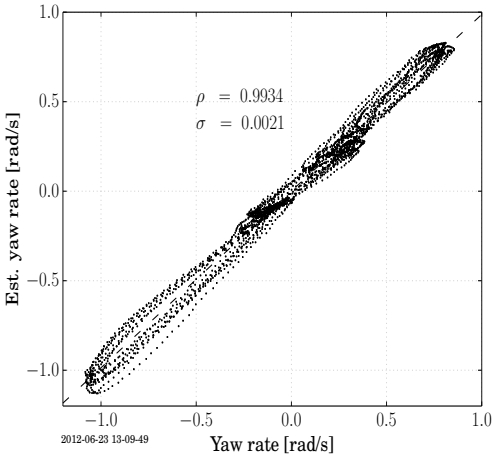

(c) *Estimated vs. measured yaw rate. The diagram shows a good match of the estimation with the measurement.*

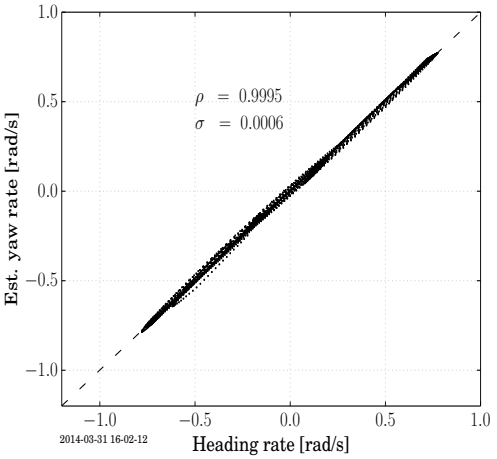

(d) *Estimated vs. simulated heading rate. The diagram shows a very good match of the turn rate law and the dynamic simulation.*

Figure 4.7: *Accuracy of the turn rate law applied to the measured and simulated reel-out phase of the kite. Only the simulation results of the four point model are shown, because the results for the point mass model look very much the same. ρ is the Pearson product-moment correlation coefficient.*

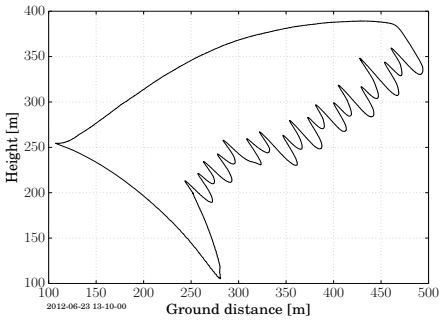

(a) *Measured flight path.*

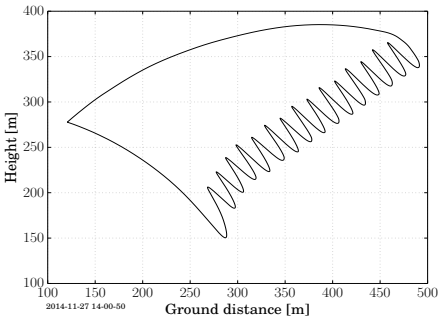

(b) *Simulated flight path, four point model. Efficiency error: 1.8%.*

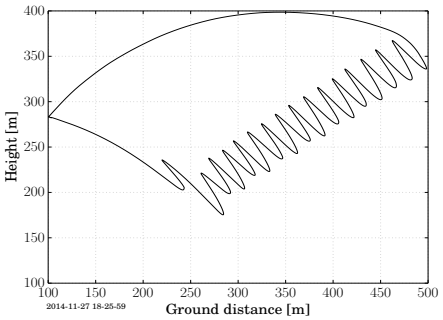

(c) *Simulated flight path, point mass model. Efficiency error: 3.1%. Reel in unstable.*

Figure 4.8: *Measured and simulated flight paths of one cycle as seen from the side. It can be seen that the minimal and the maximal height are simulated more accurately with the four point model.*

With the point mass model it was difficult to achieve stable parking, using the control parameters of the flight experiment: It was always oscillating around the desired position and therefore flying crosswind even it should not. Therefore the calibration parameters from the four point model had to be used instead.

4.3.4 Model comparison

A first comparison of four model variations (one point kite and four point kite model combined with either a straight or a segmented tether) can be done by parking the kite (steering it towards zenith) in a quasi-steady wind field. The results are shown in Tab. 4.6. A ground wind speed of 8 m/s and a turbulence intensity of 1% and an exponential

Table 4.6: *Comparison of the tether force and the elevation angle of a kite, parking at a line length of 392 m. The simulated results of the one point and the four point model, combined with a straight and a segmented tether are compared.*

Model	Force [N]	σ_f	β [°]	σ_β
1p, straight tether	749.7	16.4	74.7	0.05
1p, segmented tether	727.5	9.2	70.7	0.02
4p, straight tether	685.7	5.0	69.0	0.02
4p, segmented tether	670.2	3.2	68.5	0.02

wind profile with $p = 1/7$ were used for these simulations. The difference of the force and of the elevation angle between the most simple and most complex model are about 10%. Much bigger is the difference in the dynamic behaviour: The variance of the tether force of the four-point model with a segmented tether is more than five times smaller than the variance, using the one point model with a straight tether. The reason for this is the damping, that is induced by the segmented tether and four point kite.

A realistic model of the non-linear damping of the system is essential for the design of the force controller of the ground station.

4.3.5 Results: Power production and flight path

When simulating figures of eight flight manoeuvres with the parameters identified in Sect. 4.3.2 the result as shown in column *Sim. I* in Table 4.7 was disappointing: The computed average power was about 50% lower than the measured value. To achieve

a better match between simulation and measurements it was necessary to increase $u_{d,0}$ from 21.3% to 23.4% and to decrease the depower setting during reel-in by 2.1% as shown in column *Sim II*. This can be justified first with inaccuracies during the parameter identification and second with a shift of $u_{d,0}$ by different apparent wind velocities and/or a creeping of the depower/ steering lines.

The point mass model (Table 4.7 column *Sim. III*) was tuned slightly differently to match the measured power output and to achieve a similar flight trajectory. Nevertheless, the errors between the point mass kite model and the measurements were higher, for example an error of 3.1% instead of 1.8% for the cycle efficiency η_{cyc}. (The value p_{av} is

Table 4.7: *Parameters of measured and simulated pumping cycles. The best results were achieved with the four point kite simulation Sim. II. The cycle efficiency η_{cyc} is the product of the pumping efficiency η_p and the duty cycle (Fechner and Schmehl 2013).*

	Measured	**Sim. I**	**Sim. II**	**Sim. III**
$v_{w,ref}$ [m/s]	9.51	9.51	9.51	9.51
$u_{d,ri}$[%]	42.2	42.2	40.1	44.1
$u_{d,0}$ [%]	-	21.30	23.40	20.80
L/D, reel-out	-	4.13	4.64	4.53
$F_{t,o}$ [N]	2942.	2213.	2876.	2956.
$F_{t,i}$ [N]	653.	379.	600.	570.
$v_{t,o}$ [m/s]	1.99	1.20	1.89	1.88
$v_{t,i}$ [m/s]	-7.28	-7.22	-7.69	-7.66
p_{av} [W]	3726.40	1953.10	3681.50	3735.80
η_p [%]	79.10	83.00	79.70	81.70
D [%]	78.70	85.30	80.30	80.40
η_{cyc} [%]	62.20	70.80	64.00	65.70

the average mechanical power over the whole cycle, and η_{cyc} is the cycle efficiency, the quotient of the mean mechanical power and the average mechanical reel-out power).

A two dimensional projection of flight trajectory, height of the kite vs. the ground distance, is a suitable means for visualisation and comparison of different flights. In Fig. 4.8 the measured and the simulated flight path of one cycle is shown. The maximum height differs by less than 5%. The minimum height differs by about 45 m. One reason

for this are the inaccuracies of the Global Navigation Satellite System (GNSS) based height measurement.

4.4 Summary and conclusion

The computed dynamic response of the kite to steering inputs compares well to the response measured during test flights. In all situations the estimated turn rate of the wing was within $\pm 14\%$ of the full range of the experimentally measured values while the standard deviation was only $\pm 0.1\%$ of the full range. Similar results, but limited to the steering of a kite on a tether of a fixed length were presented by Erhard and Strauch (2013) and Fagiano et al. (2014).

By modifying the parameters c_s and $c_{2,c}$ the proposed, empirical point mass model can be adapted to match all parameters of the turn rate law. Compared to the proposed four point model it runs faster but is less accurate and can become dynamically unstable at low tether forces.

In Jehle and Schmehl (2014) it was assumed that the turn-rate law derived by Erhard and Strauch (2013) and Fagiano et al. (2014) would only be valid for ram-air kites. We found, that it is valid for lead edge inflatable kites, too.

The parameters of the mechanistic four point model can be derived from the physical properties of any soft kite and any asynchronous generator. Only small changes are required for other kites and generators. It is well suited for controller development and can be used not only for the pumping cycle operation of the kite, but also for the simulation of launching, landing and airborne parking.

For a full model validation of a specific system, two enhancements of the test design are needed: First, accurate wind measurements at the height of the kite. Second, an accurate measurement of the maximum and minimum L/D of the kite and of the depower offset $u_{d,0}$.

The presented models have shown to be easily adaptable and well suited for flight path optimization and the development of KPS estimators and KPS controllers. While the corrected one-point model with an adapted flight path controller can be sufficient for flight-path optimization, the four point model is better suited for controller validation in a broader range of flight conditions.

Even though the accuracy of the predicted power output is not yet sufficiently validated, the one point model, using the correction according to Eq. (4.30) is predicting the

influence of gravity on the turn rate much better than the uncorrected point mass models and the four point model has a much more realistic dynamic response to the steering input than simpler models while still being reel time capable. The source code is published under the GNU LGPL License in the context of the FreeKiteSim (Fechner et al. 2014) project.

CHAPTER 5

Flight Path Planning in a Realistic Wind Environment

Contents

5.1 Introduction 81
5.2 A practical approach to kite control 83
5.2.1 Small earth reference frame 83
5.2.2 Kite Power System (KPS) modelling approaches 85
5.2.3 Environmental conditions 87
5.2.4 Robustness 93
5.3 Flight Path Planner (FPP) 94
5.3.1 Automated power production 95
5.3.2 Lower intermediate state 99
5.3.3 Flying figures of eight 101
5.3.4 Upper intermediate state 108
5.3.5 Performance of the flight-path planner 110
5.4 Summary and conclusion 113

5.1 Introduction

In the previous chapter a dynamic system model was presented. In this chapter the model will be extended by a more realistic, turbulent wind environment. A flight path planning algorithm will be presented, that allows to adapt for changing wind conditions.

A key advantage of a kite power system is the possibility to adjust and modify the flight trajectory of the wing over a broad range. This operational envelope is constrained by hardware limits of the wing and the control system, safety limits and limits due to flight physics. The purpose of the flight path planner is to design the operation for optimal performance while complying with the imposed constraints.

Highly sophisticated methods for the optimization of a closed flight path, that combines reel-in and reel-out in a single figure-of-eight exist (Zanon and Diehl 2013), and with some restrictions can also be applied for flight paths with multiply circles during reel-out (Horn and Diehl 2013). These methods have two limitations: First, only very simple kite power system models can be used during the optimization process. This makes it impossible to take limitations like the maximal tether force in a turbulent wind field realistically into account because this force heavily depends on the tether sag which is neglected by fast, analytic kite power system models. Second, at least in (Zanon and Diehl 2013) and (Horn and Diehl 2013) not even a crest factor of the power is mentioned. This leads to the assumption, that the power was optimized, without taking system limits (max. power, max. force) into account. Therefore the theoretically optimal trajectories, that were found are meaningless in practice.

The focus of Ruiterkamp and Sieberling (2013) is the control and flight performance of a tethered, rigid wing system, but it also provides some details of the flight path planner. For flying figure-of-eight manoeuvres the authors are using a large number of attractor points on a lemniscate instead of two attractor points and two turns, as suggested in this chapter. This has the disadvantage, that control loop delays are more problematic, because much more control commands have to be executed in the same time. Furthermore they are using a direct line for reeling in (not possible with a flexible wing) and a constant elevation angle for reel-out. Partially their design decisions might be related to the fact, that they are using a rigid wing and not a leading edge inflatable kite, which is used as reference system in this chapter.

In this chapter a flight-path planner is presented, that constructs the flight path from a set of simple sections, composed of straight lines and circle segments when projected on a spherical surface. The flight path can be optimized using a small set of parameters. The peak power can be limited by changing both the elevation angle and the depower settings (i. e. the angle of attack) during reel-out. The development of this algorithm is inspired by looking at the way a human pilot steers a kite and is robust against sensor errors and control loop delays.

Even though the planner was developed for the lead-edge inflatable soft wings, that are used by the KPS demonstrator of Delft University of Technology, it can – in principle – be used for any wing. The main limitation of the this chapter is, that flying circles instead of figures-of-eight was not investigated. There are at least two advantages of flying figures-of-eight: Firstly, it is easy to estimate the wind direction at the height of the kite by comparing the power of the left and the right half of the figure (Zgraggen et al. 2015). This is more challenging when flying circles, because circles are asymmetrical. Furthermore, flying down-loops (directly downwards) cannot be avoided when flying circles, but it can easily be avoided when flying figures-of-eight. In some situations down-loops should be avoided due to security concerns. When concrete numbers are given for certain parameters, this are empirically derived values for the 20 kW prototype of Delft University of Technology. Nevertheless the paths, presented in this chapter have a generic character, they should be applicable for kitepower systems with any wing and any size (at least in the range of 1 kW to 1 MW), only some parameters, e.g. $\delta\chi, \delta\chi_{\text{int}}, w_{\text{fig}}$ and h_{fig} might have to be adapted. The most relevant content of this chapter is also published as book chapter in Fechner and Schmehl (2016c).

5.2 A practical approach to kite control

5.2.1 Small earth reference frame

To understand how the control system is working it is necessary to introduce the small earth reference frame. This name is chosen as an analogy to the geographic coordinate system, describing a position on planet earth: It makes clear to the reader that navigation methods, used on earth (like great circle navigation to find the shortest way between two points on the sphere) can also be used to navigate kites[1]. The position of the kite[2] and the ground station are measured in the "Earth Centered Earth Fixed" reference frame. The position of the kite relative to the ground station has to be converted into the "Wind Reference Frame" $(x_{\text{w}}, y_{\text{w}}, z_{\text{w}})$ as shown in Fig. 5.1. The origin of the wind reference frame is placed at the anchor point of the tether and its x_w axis is always pointing in the direction of the averaged wind velocity. To obtain the coordinates of the kite in the

[1] The equivalent of the latitude is the elevation angle, and the equivalent of the longitude is the azimuth angle. The equivalent of the north pole is called zenith.

[2] If not defined otherwise, the centre of gravity of the combination of kite and KCU defines the position of the kite.

small earth reference frame its position is projected on the unit sphere around the origin of the wind reference frame. Now, the position of the kite can be described with two angles, the azimuth angle ϕ and the elevation angle β. The movement of the kite in the direction of the tether is determined by the winch controller and can be ignored by the kite controller. The objective of the flight path controller as described in this thesis is to fly the kite on a prescribed trajectory that is adapted to the wind conditions.

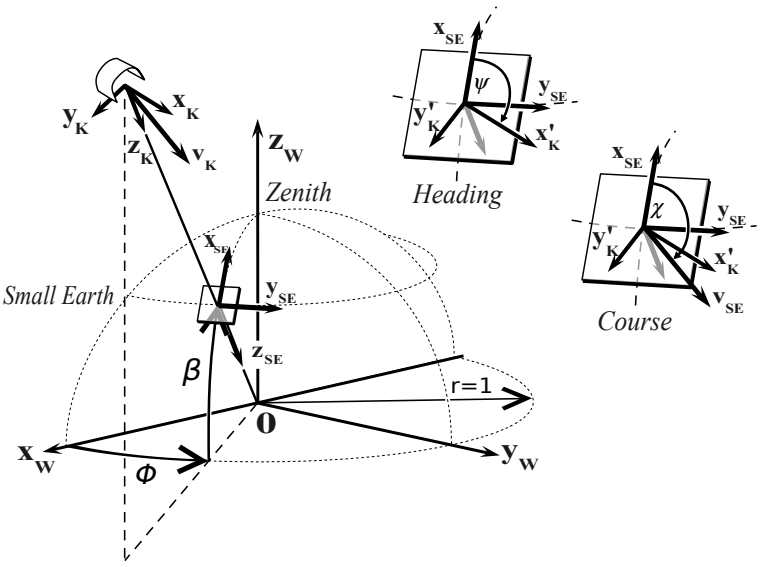

Figure 5.1: *Small earth reference frame. The position of the kite is projected on a half sphere with the radius of one. The elevation angle β and the azimuth angle ϕ describe the position of the kite, the angle ψ its orientation. The course angle χ is the angle between the direction towards zenith and the velocity vector of the centre of mass of the kite as projected on the tangential plane touching the position of the kite on the half sphere.*

In Fig. 5.1 the vectors $\mathbf{x}_k, \mathbf{y}_k, \mathbf{z}_k$ define the body-fixed kite reference frame. In this chapter, the combination of the wing and the kite control unit (KCU) is seen as kite. The $\mathbf{y}_k$ axis is defined by the vector from the left to the right wing tip, the $\mathbf{z}_k$ axis is pointing downwards from the position of the kite parallel to the upper part of the tether, and the $\mathbf{x}_k$ axis is orthogonal to $\mathbf{y}_k$ and $\mathbf{z}_k$. The heading angle ψ is the angle between the direction towards zenith and the vector $\mathbf{x}_k$ as projected on the tangential plane touching the position of the kite on the half sphere. If tether is not straight, $\mathbf{z}_k$ and $\mathbf{z}_{SE}$ are not aligned.

For flight path planning and for the design of the flight path controller a straight tether is assumed, but the validation of the controller is done against the dynamic system model as explained in Chap. 4 where tether sag and roll movements of the kite are taken into account.

The heading angle and thus the course of the kite can be controlled to steer the kite from its current position to any attractor point, but also to fly turns with a well defined radius. The control objective of the kite control subsystem is to control the heading angle and thus indirectly the course of the kite. This can be achieved by controlling the steering signal that is sent to the control pod of the kite. By introducing the small earth reference frame and using the course angle (or heading angle) as the controlled variable the kite control problem has been reduced to a SISO problem (Baayen and Ockels 2012).

In addition the magnitude of the angular velocity of the kite point will be used, defined as

$$\omega = \sqrt{\dot{\beta}^2 + \dot{\phi}^2 \cos^2 \beta} \,. \tag{5.1}$$

This equation follows from an "addition theorem" for angular velocities. This angular velocity of the kite point on the unit sphere ω should not be confused with the angular velocity of the kite body around the tether axis.

5.2.2 Kite Power System (KPS) modelling approaches

While a very detailed, 3D KPS model taking the tether sag and the orientation of the kite in all three directions into account was presented in the last chapter, for the design of the flight path planner (FPP) and flight path controller (FPC) simpler models are proposed: These models assume a straight tether and a kite, that is attached to it with a bridle such that the roll and the pitch of the kite are constrained. Only the heading angle remains as free variable to control the course of the kite. The relationship between the course angle (a kinematic property) and the heading angle is discussed in the next paragraph.

In principle, the flight path planner, presented in this chapter is planning the course angle of the kite point as function of the time. The course angle χ is the angle between the velocity vector of the kite point, projected on the unit sphere, and the vector that is pointing towards zenith. The course angle χ follows the heading angle ψ with an offset due to gravity. The steering actuator of the kite control unit allows direct control of the heading angle, but only indirect control of the course angle. In Fig. 5.2 the heading and the course angle during reel-out are shown. During the reel-in phase the angular speed ω

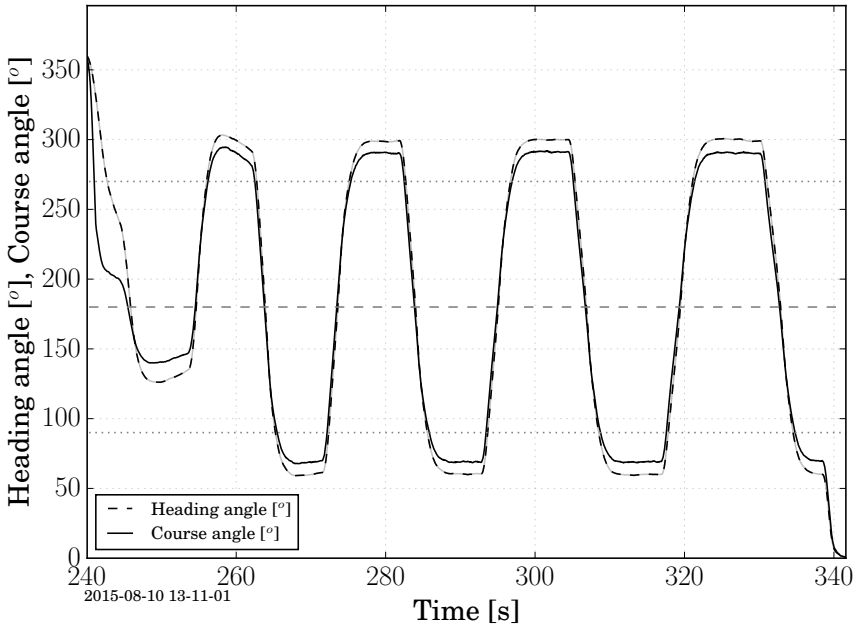

Figure 5.2: *Heading and course angle while flying figure of eight manoeuvres in nominal wind conditions (Tab. 5.1). The deviation from the horizontal direction (dotted lines at* 90° *and* 270°) *is about* 8° *larger for the heading than for the course because of gravity. Both angles are nearly constant when the kite is flying on a great circle towards an attractor point, and they are changing fast during the turning manoeuvres. The dashed line at* 180° *represents the vertical flight direction towards ground. The diagram is based on a simulation using the four point kite model as described in Chap. 4.*

can become very small. This means, that the course direction is not defined any more. In such a situation the heading of the kite is planned to keep the nose of the kite pointing to zenith and thus the kite airborne.

While a simple, kinematic kite model is sufficient for the FPP and FPC during normal operation, it is insufficient for the system verification. Furthermore it is not sufficient for the control of a kite, that is flying on a lose tether. This situation (which might happen for example during launch and landing) is not investigated in the context of this thesis.

5.2.3 Environmental conditions

For this thesis three sites are used to obtain wind data, all of them located in The Netherlands: First, Maasvlakte II, an artificial peninsula in the North Sea near Rotterdam. The kite power group of TU Delft did a test campaign at this location in 2012. Second, the former naval airbase Valkenburg near Leiden. At this location a lot of flight tests took place in the years 2010 to 2015, usually monthly. Third, wind data from the 213 m high KNMI-mast in Cabauw are used. This was the only location from which it was possible to obtain measurement data with 10 minutes resolution at large heights for at least a full year.

In the investigated scenario a maximal, allowed height of 600 m is assumed and a minimal tether length of 300 m. Further it is assumed that the maximal tether length and the maximal, allowed height are identical. In practice a safety margin needs to be added.

Wind speed distribution

For the location Cabauw an average wind speed of 4.26 m/s at 10 m height was measured. A wind speed of 7.28 m/s at 98.7 m height and of 8.56 m/s at 131.6 m height was estimated. These heights are the average reel-out heights in the first and the second scenario, when an average elevation angle $\beta_{\text{set}} = 26^\circ$ is assumed. This elevation angle gives the optimal wind speed gain μ as will be shown in Sec. 5.3.5.

The estimated cumulative probability distribution function (CDF) of the ground wind speed is shown in Fig. 5.3. Ground wind speed is defined as the wind speed at 10 m height.

The KPS used in the simulations is designed such that it reaches its nominal power at a wind speed, that is exceeded about 20% of the time. According to the CDF this is 6.0 m/s at 10 m height.

Vertical wind profiles

For the location Maasvlakte II, which has nearly offshore wind conditions no long-term wind profile averages are used, but only the estimated wind profile from one flight as described in Sec. 4.2.1. During the test campaign at this location it was permitted to fly at up to 1000 m height.

For the near-shore location Valkenburg the exponential wind profile law with a coefficient $p = 1/7$ is assumed. The maximum flight height at this location is usually 300 m.

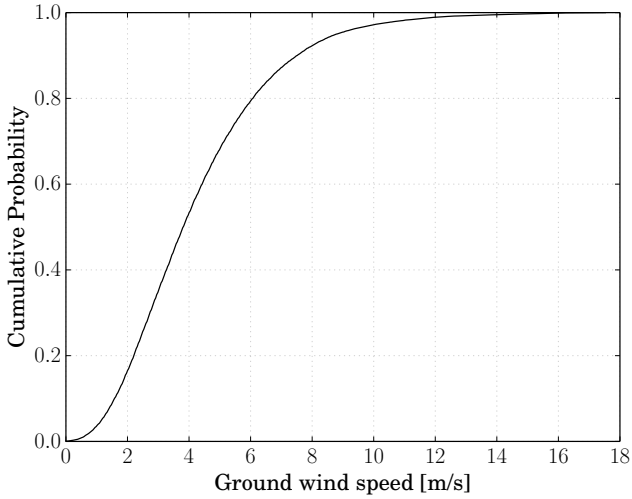

Figure 5.3: *Cumulative probability distribution function (CDF) of the ground wind speed, measured at Cabauw, The Netherlands in 2011.*

Sometimes (depending on the wind direction) it is permitted by the air traffic control to operate a kite at up to 500 m.

Wind data from Royal Netherlands Meteorological Institute (KNMI 2011) at the inland location Cabauw, The Netherlands was used and the wind profile fitted, using the power law according to Eq. 3.2. A coefficient $p = 0.234$ was obtained, which is significantly larger than for the location Valkenburg. This is to be expected because Cabauw is a lot further away from the shore than Valkenburg. The wind profile is shown in Fig. 5.4.

Turbulence

The relative turbulence intensity I, the ratio of the standard deviation of the wind speed within 10 minute intervals and the 10 minute wind speed average is calculated, based on the Cabauw data set from Royal Netherlands Meteorological Institute (KNMI 2011). Three scenarios are chosen for the simulation: The average ground wind speed of 4.26 m/s, the wind speed for nominal power of 6.0 m/s and the maximal wind speed for operation without the need to depower the kite during reel-out, which will be derived

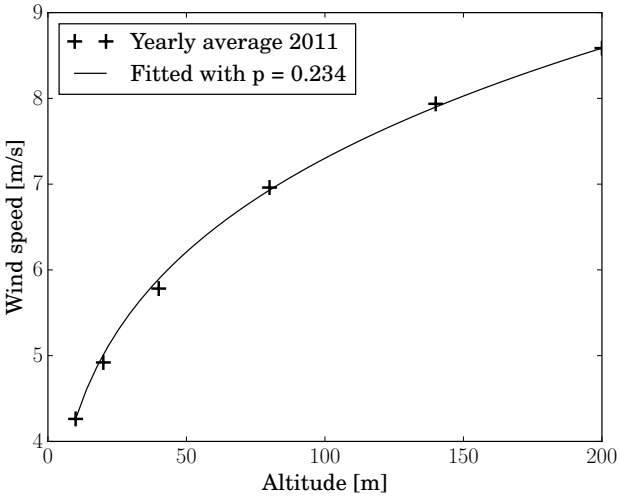

Figure 5.4: *Wind profile at Cabauw based on measured data from KNMI, The Royal Netherlands Meteorological Institute (2011). It was fitted using the power law (solid). Cross symbols represent measured values.*

in Sec. 5.3.5. The parameters of the three environmental scenarios are shown in Tab. 5.1.

Table 5.1: *Simulation scenarios, based on the wind data from Cabauw 2011. Three average ground wind speeds are used. The average turbulence intensities at 98.7 m and 197.4 m height are shown.*

$v_{w,g}$	I_{99}	I_{197}	Description
4.26 m/s	8.5 %	6.3 %	Average wind speed
6.00 m/s	9.7 %	7.2 %	Nominal wind speed
9.20 m/s	9.8 %	7.9 %	High wind speed

The turbulence is modelled in three dimensions, using the Mann model as described by Mann (1994) and Mann (1998). The resulting homogeneous velocity field is obtained by a 3D FFT[3] of the spectral tensor. Randomization is done by a white noise vector to give the wave numbers a random phase and amplitude.

A wind field of 4050 x 100 x 500 points with 2 m resolution is pre-calculated. To

[3] Fast Fourier Transformation

obtain the 3D wind speed vector at any given position a 3rd order spline interpolation is used. To take the time dependency of the wind into account, the product of the simulation time and the average wind speed at the height of the kite is added to the x-coordinate before the wind vector lookup. The turbulent component of the wind field is periodic in all directions, because it is generated using reverse FFT. The size of the wind field is chosen such that the wind speed sequence repeats every 13.5 minutes at a wind speed of 10 m/s.

Table 5.2: *Parameters of the Mann model, used to generate the 3D wind field, taken from IEC(2005)*

Param	Value	Description
γ	3.9	anisotropy parameter (zero for isotropic turbulence)
σ_{iso}	0.55 σ_1	standard deviation of the wind speed in case of isotropic turbulence
σ_1	see Tab. 5.1	standard deviation of the wind component at the average height during reel-out in the mean wind direction
l	33.6 m	turbulence length scale for an average height of more than 60 m

Fig. 5.5 shows the wind speed as a function of the time as calculated using the Mann model.

Parking[4]

When developing an autopilot, the first milestone is to keep the kite stable in the air: This is the simplest goal of control development, but already requires a complete control system, an orientation sensor, a PID controller and an actuator for steering the kite.

Parking can be achieved by steering the nose of the kite towards zenith, towards a point directly above the ground station. If the reel-in speed is zero, then the kite will never reach the zenith position. Instead, it will approach a position with about zero degree azimuth and an elevation angle that depends on the lift-over-drag ratio of the kite, it's mass and the wind speed. In Fig. 5.6 a 3D view of a simulated, parking kite is shown.

[4] Parking a kite means to keep the kite airborne with as little movement as possible. This can be done by steering the kite towards zenith $(\beta, \phi) = (90^o, 0^o)$). The resulting elevation angle will mainly depend on the L/D ratio of the kite. From a control perspective this is a problem similar to the inverted pendulum.

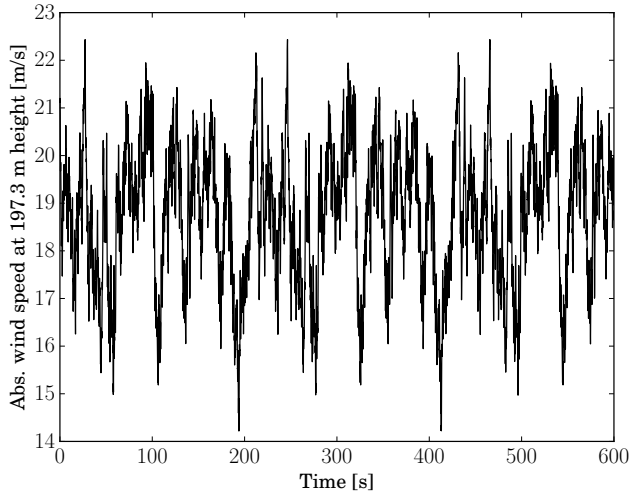

Figure 5.5: *Simulated wind speed as function of the time in the high speed scenario ($v_{\mathrm{w,g}} = 9.2\ m/s$, $I_{197} = 7.9\%$). The wind speed varies between 14.2 and 22.5 m/s. The changes can be as fast as 4 m/s^2.*

When the kite is parked in the centre of the wind window ($\phi = 0$) the elevation angle can be calculated as follows

$$\beta \;=\; \arctan\left(\frac{L - m\,g}{D}\right) \tag{5.2}$$

where L is the lift force of the kite, D the effective drag force of kite and tether and $m\,g$ the gravity force.

A test for the performance (speed, accuracy and stability) of the flight-path controller can be implemented in the following way:

1. Reel out the tether until 300 m tether length are reached.
2. Wait until an equilibrium is reached, e.g. for 120 s.
3. Turn off the autopilot. After some time the kite will fall to the side. Wait until abs $\phi \;\geq\; 30\,^{\mathrm{o}}$.
4. Turn on the autopilot.

5. Measure the overshoot of the azimuth angle: $\Delta\phi = \max(\text{abs}(\phi)) - 30\,^{\text{o}}$.

6. Measure the recovering time t_r from turning on the autopilot until $\text{abs}(\phi) \leq 3^{\text{o}}$.

With this test two parameters ($\Delta\phi$ and t_r) can be determined that quantify the performance of the flight path controller for given wind conditions.

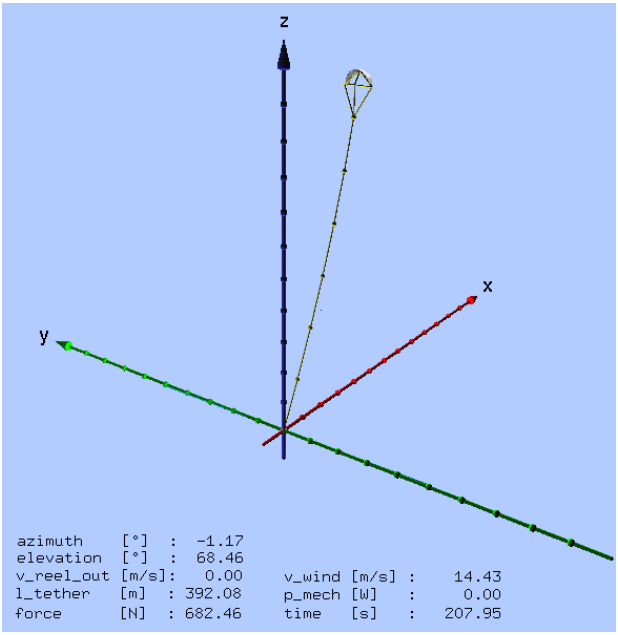

Figure 5.6: *Parking kite in the 3D view. The scale is 40 m per axis tick. The kite is enlarged by a factor of five for better visibility.*

Flying figure of eight manoeuvres

The second milestone is to fly figure of eight manoeuvres on a constant tether length. In ideal crosswind operation ($\phi = 0,\ \beta = 0$) the tether force can be increased by a factor of $\frac{1}{2}(C_\text{L}/C_\text{D})^2$ (Loyd 1980). Depending on the lift to drag ratio of the wing this can be a factor of one or two orders of magnitudes and hence significantly contribute to power extraction. Therefore it is very important to implement a flight path planner, that can design crosswind flight manoeuvres and convert them into a series of steering com-

mands. The minimal radius of the turning manoeuvres should also be well controlled, because components like GNSS sensors stop to work, if the turn radius is too small[5].

5.2.4 Robustness

Both, the flight-path planner and the flight-path controller need to achieve a very high level of robustness. The design, that is explained in the following sections is based on the following robustness requirements. The numbers are derived from the accuracy and time delay, that can be achieved using reasonably priced, commercially available sensors and actuators and need to be adapted accordingly.

- Estimation error for the heading $\psi_{err} \leq 5^{\circ}$, simulated using white noise. The reason for this is, that such a estimation error is hard to avoid because of the flexible structure of the wing. If the measurement error is higher, then statistical methods must be used to achieve a sufficiently accurate estimate.

- Estimation error for the course $\chi_{err} \leq 5^{\circ}$, simulated using white noise.

- Measurement error for the kite position $|\mathbf{p}^{\mathrm{SE}}_{\mathrm{k,err}}| \leq 4^{\circ}$. An error, smaller than this can be achieved even with ground based angular sensors. They are useful as backup solution, when the airborne sensors fail. Ground based angular sensors always have an unavoidable error due to tether sag.

- A total control loop delay during normal operation of $50\ ms \leq \tau \leq 200\ ms$ and during parking of $50\ ms \leq \tau \leq 500\ ms$. A maximum delay of 200 *ms* is achievable with off-the-shelf positioning sensors and wireless links. In case of a sensor or link failure it is important, that the system remains airborne even with a slower backup- solution.

- Ground wind speed $2\ m/s \leq v_{\mathrm{g}} \leq 15\ m/s$. At lower wind speeds the kite can be kept airborne using reverse pumping, but this is beyond the scope of this thesis. At higher wind speeds the kite can be parked at zenith. During parking the kite can stay airborne even at ground wind speeds, that are 2-3 times as high as 15 m/s.

[5] The reasons for this phenomena are not yet well understood: One possible reason is the magnitude of the angular accelerations, another possible reason is the speed of change of the set of satellites, that are in view of the GNSS antenna.

- Relative wind turbulence at a height of 200 m $I_{200} \leq 26.5$ % for the nominal wind speed, because this was the highest turbulence intensity recorded at the reference site (Cabau, The Netherlands) in 2011.

5.3 Flight Path Planner (FPP)

Flight path planning can be based on an ordered list of positions that describe the desired flight path. A variation of this approach is to use a list of positions, that the kite shall be steered towards, without the goal that it shall actually pass these positions. Based on the experiences with the KPS demonstrator of TU Delft the following approach is suggested: Fly either to zenith, or to an intermediate point, or to the right or the left hand side of the wind window. In Fig 5.7 these positions are depicted.

Reeling in while steering towards zenith has the advantages that first, the wind speed in the direction of the tether and thus the reel-in force is low (directly at zenith in quasi-static equilibrium it would be zero). Second, the kite is rising at the end of the reel-out phase and thus storing potential energy in the kite, that later helps for the reel-in phase. This is more efficient than to use an electrical storage only. If the reel-out energy is converted to electricity, stored in a battery and then a portion of it is used to drive a motor to reel in the kite, this has an efficiency of about $90\% * 80\% * 95\% \approx 68\%$, where the three numbers on the left are the estimated generator, motor and battery efficiency. Increasing the height of the kite during the reel-out phase converts wind energy into potential energy. This can be used without any losses to reduce the tether forces during reel-in. Within certain limits a heavier kite thus increases the overall efficiency. On the other hand a higher mass of the kite makes launching and landing more difficult and increases the minimal required wind speed.

Flying towards an intermediate point after the reel-in phase helps to mitigate the force peak, that can happen otherwise when the kite is coming down too fast. Using two attractor points on the right and left hand side of the wind window is the easiest way to fly figures of eight during reel-out. Flying figures of eight avoids twisting of the tether, which happens if one flies circles only.

In addition it was found useful to define "turn" actions. An example: turn the kite to the right, when it reaches the azimuth angle $\phi = \phi_{\mathrm{sw}}$ on the right of the wind window, until the course angle $\chi > 270^{\mathrm{o}}$. If the duration of the turn action is additionally limited by a time limit, then it is very robust against sensor or communication failures.

With a combination of flying towards an attractor point and turn actions any flight path can be planned.

Design goals of the flight path planner

Design goals of a good FPP are:

1. a high effective wind speed (Eq. 5.28) at the height of the kite;
2. a low crest factor of the reel-out force and reel-out power;
3. a high turn radius to limit the steering effort and the additional drag, caused by steering;
4. a low steering effort also when flying straight;
5. a reel-in phase with low effective wind speeds;
6. short transition phases;
7. low force overshoot at the transition from reel-in to reel-out;
8. the FPP must take the system requirement of a high robustness for sensor errors and delays into account;
9. good controllability of the maximal and minimal height;
10. good controllability of the effective wind speed and thus reel-out power. This is especially important at high wind speeds, but also at medium wind speeds with high turbulence.

The design goals (2) and (3) are competing requirements, as are the goals (6) and (7). Therefore a good compromise needs to be found.

5.3.1 Automated power production

The high-level control suggested for automated power production is shown in Fig. 5.8. It does not include parking and automated launch and landing.

Flight path planning happens in the 2D plane, spanned by the azimuth and elevation axis. This is a projection of a half sphere on the flat plane which causes a distortion of lines and circles: The shortest line from one point on the sphere to another point is a great circle, which is only a straight line in the 2D plane for $\beta = 0$. Furthermore turn

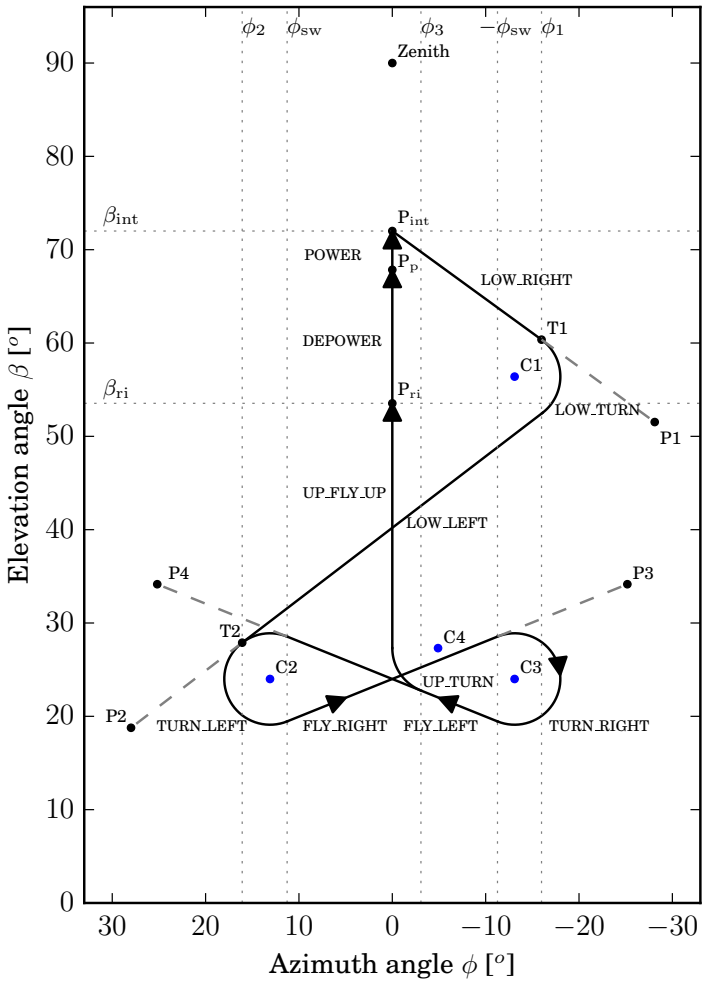

Figure 5.7: *Schematic drawing of the planned flight-path at* 24° *average elevation during reel-out. Five attractor points (P*1 *to P*4 *and Zenith) and four turns (around C1 to C4) are needed for automated power production. The minimal attractor point distance is* $\delta_{min} = 15°$. *At an elevation angle of* $\beta = \beta_{ri}$ *the kite is depowered. As a consequence the force drops and the reel-in phase begins. When the minimal tether length is reached at* P_P *the kite is powered again. When it is powered to a well defined level the intermediate state begins. It is now steered towards P*1. *The position of* P_p *is not planned by the FPP, but measured and used as input for the planned flight path. In the first cycle this position is identical to the parking position. The UP_TURN can be performed on the right or the left hand side of the wind window as defined in Tab. 5.5.*

manoeuvres with a constant turn radius are not circles in this flat plane projection, but they get more and more distorted the higher the elevation angle β is. For achieving easy understanding by the reader, this distortion is neglected in Fig. 5.8 and Fig. 5.10, the shortest line between two points is shown as straight line and turn manoeuvres with a constant radius are shown as circle segments.

The initial condition for automated power production is a kite, parked at a high elevation angle on a short tether ($l_t = l_{low}$). When activated, the high-level controller enters the state POWER. In this state, the angle of attack is changed to the set value for reel-out. When this goal is reached to at least δu_d percent the controller is switching into the lower intermediate state INT_LOW. In this state the kite is first flying to the right, then makes a turn and is finally flying to point $P2$ on the left of the wind window. When an azimuth angle on the figure-of-eight trajectory is reached ($\phi < \phi_2$), then it enters the state FIG_8.

In this state the kite is forced to fly figures-of-eight, the tether is reeled out and power is harvested. When either the height or the tether length reach an upper limit and the kite is near the centre of the wind window, then the controller switches into the upper transition state INT_UP.

The upper transition state begins with a turn towards zenith. Then the kite flying straight upwards, slowing down while still harvesting energy. When the wind speed dependent elevation angle $\beta = \beta_{ri}$ is reached the controller switches into the state DEPOWER. In this state the kite is depowered and the set value of the tether force is reduced. After a short transition time the winch begins to reel in.

In the state DEPOWER the elevation angle will increase (assuming the lift force of the kite to be positive). When the lower tether length is reached ($l_t = l_{low}$) the controller switches to the lower intermediate state INT_LOW and the next cycle begins.

The state transition table for the high-level control is shown in Tab. 5.3. The settings of the winch depend on the state of the high-level flight path controller. The value Δu_d is calculated by the winch controller. It is an additional depowering of the kite for the purpose of limiting the power output at high wind speeds. δu_d is a constant in the order of 70% and determines, to which degree the powering has to be finished before flying to the side. This improves the reliability of the system, because the kite cannot be controlled well while it is depowered. Therefore it is useful to have it powered to a certain level before flying turn maneuvers.

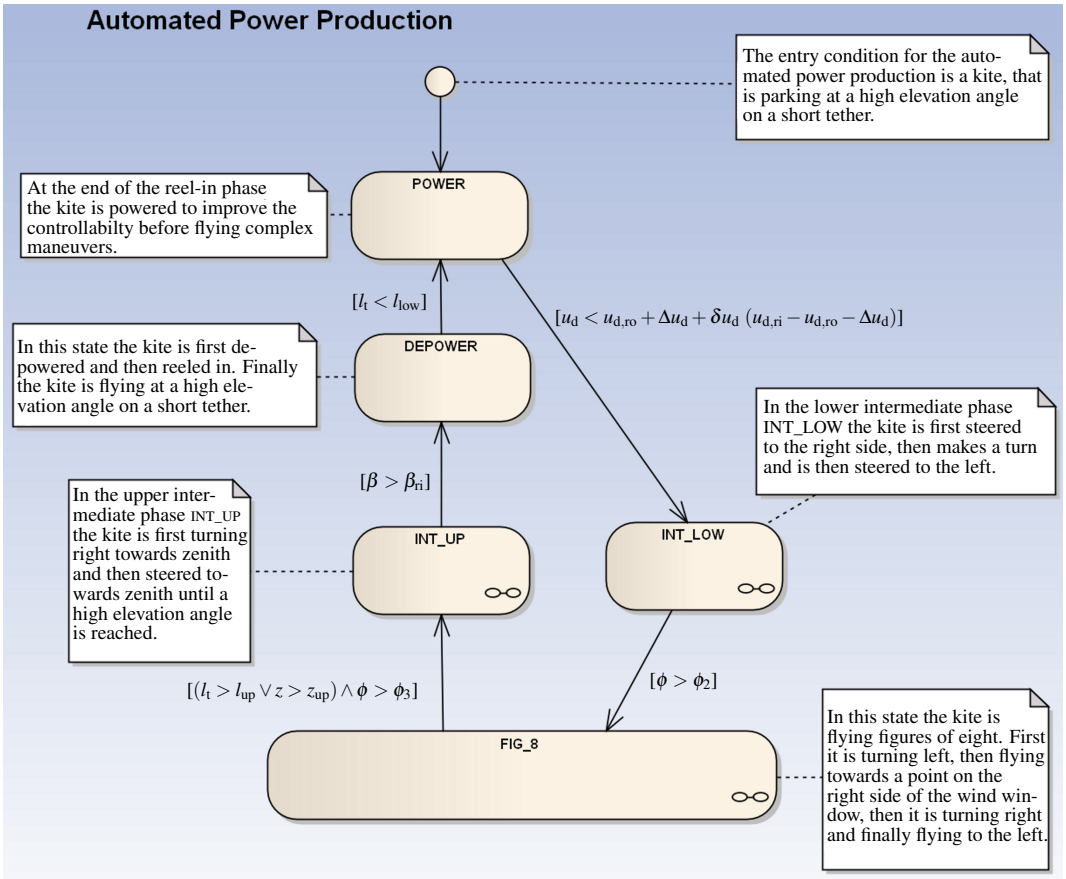

Figure 5.8: *Finite state diagram, explaining the states of the high-level controller that are needed for automated power production.*

Table 5.3: *Finite states and state transitions of the high-level flight path controller during automated power production. It activates one of the sub-controllers for the planning of the flight-sections. In addition it changes the angle of attack of the kite by changing the depower setting* u_{d}.

State	Next state	$u_{\mathrm{d,set}}$	Condition
PARKING	POWER	$u_{\mathrm{d,ro}} + \Delta u_{\mathrm{d}}$	Event START_POWER_PRODUCTION
POWER	INT_LOW	$u_{\mathrm{d,ro}} + \Delta u_{\mathrm{d}}$	$u_{\mathrm{d}} < u_{\mathrm{d,ro}} + \Delta u_{\mathrm{d}} + \delta u_{\mathrm{d}} \left(u_{\mathrm{d,ri}} - u_{\mathrm{d,ro}} - \Delta u_{\mathrm{d}}\right)$
INT_LOW	FIG_8	$u_{\mathrm{d,ro}} + \Delta u_{\mathrm{d}}$	Event EXIT(INT_LOW)
FIG_8	INT_UP	$u_{\mathrm{d,ro}} + \Delta u_{\mathrm{d}}$	Event EXIT(FIG_8)
INT_UP	DEPOWER	$u_{\mathrm{d,ro}} + \Delta u_{\mathrm{d}}$	Event EXIT(INT_UP)
DEPOWER	POWER	$u_{\mathrm{d,ri}}$	$l_{\mathrm{t}} < l_{\mathrm{low}}$

5.3.2 Lower intermediate state

The design goals of the lower intermediate state are:

- A low force overshoot. This overshoot is caused by the acceleration of the kite which happens when it is coming down too fast due to gravity.
- A low loss of total efficiency. If the kite is flying too far to the side of the wind window to limit the force overshoot, then more time and energy is lost then necessary.
- A low undershoot of the minimal elevation angle. This low undershoot prevents the kite from going too far down, which can cause a safety risk and also reduces the power output because of the lower wind velocities at lower heights.

The suggested design (Fig. 5.7, section LOW_RIGHT, LOW_TURN and LOW_LEFT) keeps the gradient of the flight path identical to the gradient of the straight parts of the figure of eight. The state diagram of the controller is shown in Fig. 5.9. The state transition table is shown in Tab. 5.4.

For the KPS of TU Delft an offset of $\delta\chi_{\mathrm{int}} \approx 32^{\circ}$ is needed to compensate for the time delay $\delta t \approx 2s$ between the command to stop turning and the kite actually stopping to turn. This value mainly depends on the rotational inertia of the kite, but also on the speed of the steering actuators and has to be determined emperically.

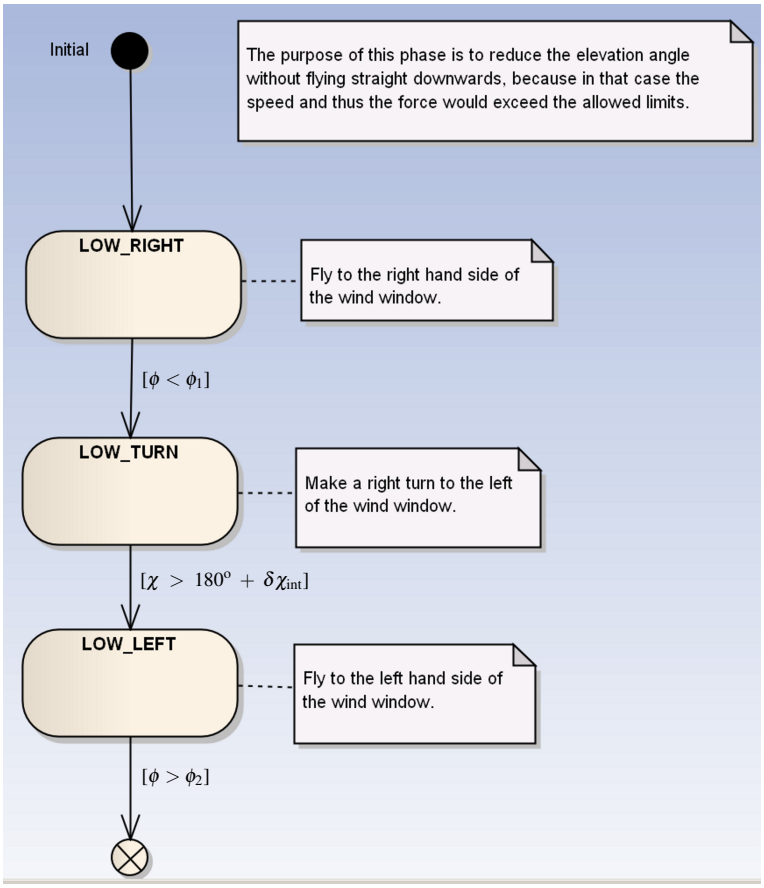

Figure 5.9: *Finite state diagram, explaining the states of the lower intermediate state INT_LOW. In this state the elevation angle of the kite is decreased with a well defined gradient as fast as possible while avoiding an unacceptable force overshoot.*

Table 5.4: *Finite sub-states of the lower intermediate phase INT_LOW.*

State	Next state	$\mathbf{p}_{\mathrm{k,set}}^{\mathrm{SE}}$	$\dot{\chi}_{\mathrm{set}}$	Condition
Initial	LOW_RIGHT	P_1	from PID	always
LOW_RIGHT	LOW_TURN	–	$\dot{\chi}_{turn}$	$\phi < \phi_1$
LOW_TURN	LOW_LEFT	P_2	from PID	$\chi < 180 + \delta\chi_{\mathrm{int}}$
LOW_LEFT	Final	–	$-\dot{\chi}_{turn}$	$\phi > \phi_2$

Table 5.5: *Finite sub-states of the figure-eight flight path planner. Flying figures of eight is finished not before the upper height z_{up} or the upper tether length l_{up} is reached. The final up-turn is always started such that it ends at $\phi = 0$.*

State	Next state	$\mathbf{p}_{\mathrm{k,set}}^{\mathrm{SE}}$	$\dot{\chi}_{\mathrm{set}}$	Condition
Initial	TURN_LEFT	–	$\dot{\chi}_{turn}$	always
FLY_LEFT	TURN_LEFT	–	$\dot{\chi}_{turn}$	$\phi > \phi_{\mathrm{sw}}$
TURN_LEFT	FLY_RIGHT	P_3	from PID	$\chi > 270^{\mathrm{o}} - \delta\chi$
FLY_RIGHT	TURN_RIGHT	–	$-\dot{\chi}_{turn}$	$\phi < -\phi_{\mathrm{sw}}$
TURN_RIGHT	FLY_LEFT	P_4	from PID	$\chi < 90^{\mathrm{o}} + \delta\chi$
FLY_LEFT	LAST_LEFT	–	from PID	$(l_{\mathrm{t}} > l_{\mathrm{up}} \vee z > z_{\mathrm{up}}) \wedge \phi <= \phi_3$
LAST_LEFT	Final	–	$-\dot{\chi}_{turn}$	$\phi > \phi_3$
FLY_RIGHT	LAST_RIGHT	–	from PID	$(l_{\mathrm{t}} > l_{\mathrm{up}} \vee z > z_{\mathrm{up}}) \wedge \phi >= -\phi_3$
LAST_RIGHT	Final	–	$\dot{\chi}_{turn}$	$\phi < -\phi_3$

5.3.3 Flying figures of eight

When a flight path controller is implemented, that supports to fly towards a given point and to make turns, then flying figures of eight can be implemented as shown in Fig. 5.10.

The sub-state diagram 5.11 shows the four sub-states of the controller for flying figures-of-eight. In Tab. 5.5 the outputs and the switch conditions of the four different sub-states are explained in detail. An offset of $\delta\chi \approx 112^{\circ}$ is needed to compensate for the time delay $\delta t \approx 2s$ between the command to stop turning and the kite actually stopping to turn. This value mainly depends on the rotational inertia of the kite, but also on the speed of the steering actuators.

The figure-eight flight path planner has the following inputs and outputs:

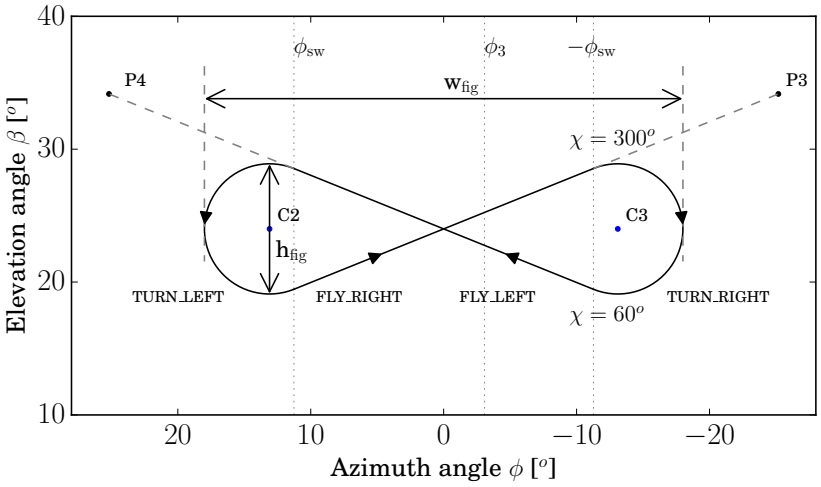

Figure 5.10: *Four-step flight path planner for flying figures-of-eight: First, turn left, then steer towards P_3, then turn right and finally steer towards P_4 . Repeat with step one. The length of the dashed lines towards P3 and P4 is the minimal attractor point distance δ_{min}. Schematic drawing, see remark at the beginning of Sec. 5.3.1.*

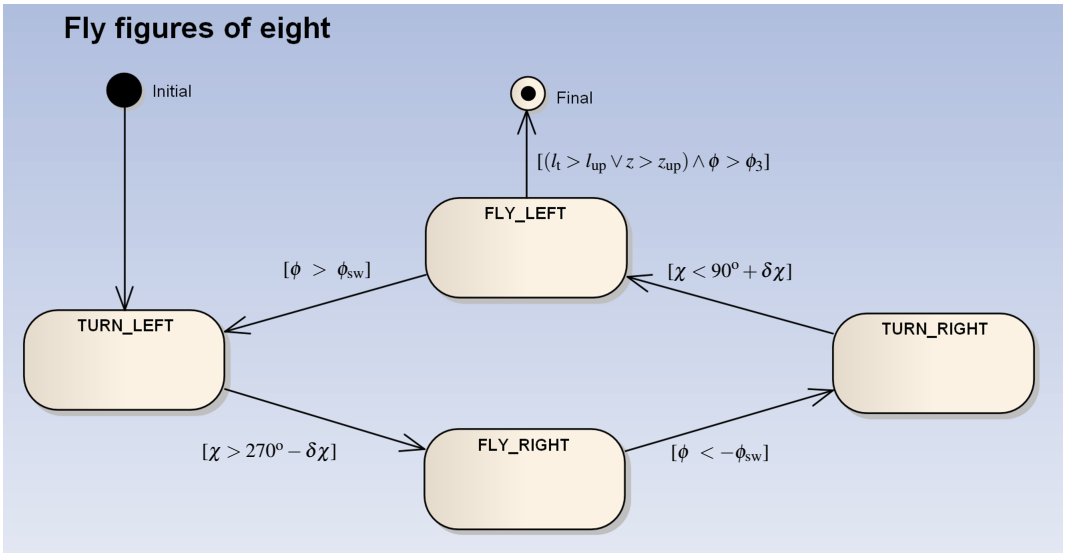

Figure 5.11: *Finite sub-state diagram, showing the sub-states and the transition conditions of the figure-of-eight controller. This sub-state machine is active in the state FIG_8 of the high-level controller. The states LAST_LEFT and LAST_RIGHT are omitted for simplicity.*

- IN: Set value for the average elevation angle $\overline{\beta_{\text{set}}}$.
- IN: Kite course angle χ and orientation angle ψ.
- IN: Azimuth angle of the kite position ϕ.
- OUT: Boolean value PID_{active}.
- OUT: Set value of the position $\mathbf{p}_{\text{k,set}}^{\text{SE}}$ when the PID is active.
- OUT: Set value for the turn rate $\dot{\psi}_{\text{set}}$ when the PID is not active.

The flight path planner can be parametrized using the angular width w_{fig}, the angular height h_{fig} of the figure-of-eight and the minimal attractor point distance δ_{min}, which is defined as the angular distance on the unit sphere between the kite position and the current attractor point at which it stops flying towards this attractor point and starts to make a turn. When these values are given, then $P_3, P_4, \dot{\psi}_{turn}$ and ϕ_{sw} can be calculated. First, the radius ϱ of the turns is calculated as

$$\varrho = \frac{h_{\text{fig}}}{2} \,. \tag{5.3}$$

Looking at Fig. 5.12 it can be seen that the rate of change $\dot{\chi}$ of the course angle can be equated to the ratio of the tangential kite velocity $\mathbf{v}_{\text{k},\tau}$ and the radius of curvature R.

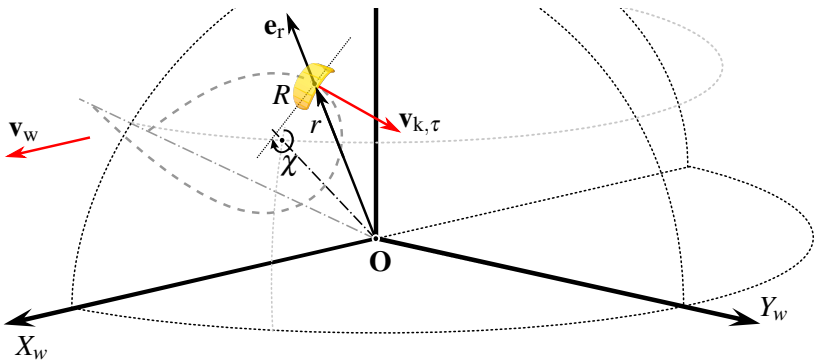

Figure 5.12: *For the turns of the kite, a turn radius of R can be defined. It can be converted into the angular turn radius ϱ using the definition $\varrho = R/r$.*

Using Eq. 5.4 where r is the radial coordinate of the kite point and ω is the angular velocity of the kite point

$$\mathbf{v}_{\mathrm{k},\tau} = r\,\omega \tag{5.4}$$

the following formula for the rate of change of the course angle is derived:

$$\dot{\chi}_{\mathrm{turn}} = \frac{\mathbf{v}_{\mathrm{k},\tau}}{R} = \frac{r}{R}\,\omega = \frac{\omega}{\varrho}. \tag{5.5}$$

The turn rate, that is needed to fly a turn with this radius can be calculated using the measured angular velocity of the kite ω according to Eq. 5.5.

The azimuth angle of the centre point of the left turning circle is defined by the given geometry as

$$\phi_{\mathrm{C2}} = \frac{w_{\mathrm{fig}}}{2} - \varrho\,. \tag{5.6}$$

Combining the equation of the right turning circle and the tangent is resulting in two expressions for the azimuth and elevation of the switch point:

$$\phi_{\mathrm{sw}} = \phi_{\mathrm{C2}} - \frac{\varrho^2}{\phi_{\mathrm{C2}}}, \quad \beta_{\mathrm{sw}} = \sqrt{\varrho^2 - (\phi_{\mathrm{sw}} - \phi_{\mathrm{C2}})^2} + \beta_{\mathrm{set}}\,. \tag{5.7}$$

The slope k of the line towards P_4 can now be calculated as

$$k = \sqrt{\frac{\phi_{\mathrm{C2}} - \phi_{\mathrm{sw}}}{\phi_{\mathrm{sw}}}} \tag{5.8}$$

Using the expressions (5.7) and (5.8) and the definition of δ_{min} the spherical coordinates of the attractor points P3 and P4 are given by:

$$P_3 = \left(-\phi_{\mathrm{sw}} - \delta_{\mathrm{min}}\sqrt{\frac{1}{1+k^2}},\ \beta_{\mathrm{sw}} + \delta_{\mathrm{min}}\,k\sqrt{\frac{1}{1+k^2}}\right), \tag{5.9}$$

$$P_4 = \left(\phi_{\mathrm{sw}} + \delta_{\mathrm{min}}\sqrt{\frac{1}{1+k^2}},\ \beta_{\mathrm{sw}} + \delta_{\mathrm{min}}\,k\sqrt{\frac{1}{1+k^2}}\right). \tag{5.10}$$

Calculation of the angular turning radius ϱ

To avoid high variations of the effective wind speed $v_{\mathrm{w,e}}$ when flying at a high elevation angle it is useful to decrease the turning radius when the elevation angle increases. How the crest factor increases with the elevation angle is shown in Fig. 5.15: For an elevation angle of $\approx 26^\circ$ the wind speed gain is nearly constant, but for high elevation angles it is dropping faster and faster. Adapting the turn radius can be done according to the following, linear formula:

$$\varrho = \varrho_{max} - (\varrho_{max} - \varrho_{min}) \frac{\beta_{\mathrm{set}} - \beta_{\mathrm{min}}}{\beta_{\mathrm{max}} - \beta_{\mathrm{min}}} \tag{5.11}$$

Based on the experience with the KPS demonstrator of TU Delft, the following values are suggested:

$$\beta_{\mathrm{min}} = 20^\circ \tag{5.12}$$
$$\beta_{\mathrm{max}} = 60^\circ \tag{5.13}$$
$$\varrho_{min} = 3^\circ \tag{5.14}$$
$$\varrho_{max} = 5^\circ \tag{5.15}$$

Calculation of $C1$, ϕ_1 and ϕ_2

The azimuth angle of C1 was chosen to be equal to the azimuth of C3:

$$\phi_{\mathrm{C1}} = \phi_{\mathrm{C3}} = -\phi_{\mathrm{C2}} \tag{5.16}$$

The elevation angle was chosen according to the following formula:

$$\beta_{\mathrm{C1}} = \beta_{\mathrm{int}} - k1 + k2\, \beta_{\mathrm{set}} \tag{5.17}$$

The coefficients k1 and k2 are chosen such that first, the centre points C1 and C3 become identical for $\beta_{\mathrm{set}} = \beta_{\mathrm{max}}$. The reason for this choice is, that at such high elevation angles of the figure of eight a force overshoot during the first cycle does not happen. The second condition for choosing k1 and k2 is, that the worst case force overshoot for $\beta_{\mathrm{set}} = \beta_{\mathrm{min}}$ is negligible while the time for the lower transition state is still as short as possible. The following values satisfy these conditions for the kite power system demonstrator of Delft

University of Technology:

$$k1 \;=\; 18.6^\circ \tag{5.18}$$

$$k2 \;=\; 0.11 \tag{5.19}$$

When β_{C1} is known, ϕ_1 can be calculated as follows:

$$\begin{aligned}\phi_1 \;=\; & \frac{1}{\phi_{c1}\left(\beta_{c1}^2 - 2\beta_{c1}\beta_{\text{int}} + \beta_{\text{int}}^2 + \phi_{c1}^2\right)}\Big(\beta_{c1}^2\phi_{c1}^2 - 2\beta_{c1}\beta_{\text{int}}\phi_{c1}^2 \\ & - \beta_{c1}\sqrt{\phi_{c1}^2 r^2\left(\beta_{c1}^2 - 2\beta_{c1}\beta_{\text{int}} + \beta_{\text{int}}^2 + \phi_{c1}^2 - \varrho^2\right)} + \beta_{\text{int}}^2\phi_{c1}^2 \\ & + \beta_{\text{int}}\sqrt{\phi_{c1}^2\;\varrho^2\left(\beta_{c1}^2 - 2\beta_{c1}\beta_{\text{int}} + \beta_{\text{int}}^2 + \phi_{c1}^2 - r^2\right)} + \phi_{c1}^4 - \phi_{c1}^2\;\varrho^2\Big)\end{aligned} \tag{5.20}$$

The elevation angle at the beginning of the lower intermediate state, β_{int} should be measured for each cycle. In Fig. 5.7 it is assumed to be

$$\beta_{\text{int}} \;=\; 72^\circ\,. \tag{5.21}$$

For the calculation of ϕ_3 geometric knowledge is used: the flight path during the state LOW_LEFT must cross the line $\phi = 0$ at the average elevation of the centre points C1 and C2:

$$\beta_{\text{M}} \;=\; \frac{1}{2}\;(\beta_{\text{C1}} + \beta_{\text{C2}}) \tag{5.22}$$

With these parameters the azimuth angle ϕ_2 can be calculated as:

$$\begin{aligned}\phi_2 \;=\; & \frac{1}{\beta_M^2 - 2\beta_M\beta_{c1} + \beta_{c1}^2 + \phi_{c1}^2}\Big(-\beta_M^2\beta_{c1} + 2\beta_M\beta_{c1}^2 - \beta_M\;\varrho^2 - \beta_{c1}^3 \\ & - \beta_{c1}\phi_{c1}^2 + \beta_{c1}\;\varrho^2 + \sqrt{\phi_{c1}^2\;\varrho^2\left(\beta_M^2 - 2\beta_M\beta_{c1} + \beta_{c1}^2 + \phi_{c1}^2 - \varrho^2\right)}\Big)\end{aligned} \tag{5.23}$$

Calculation of ϕ_3

Using the basic rules of geometry the azimuth angle, needed in the exit condition of Tab. 5.5 is derived as

$$\phi_3 \;= \varrho \;- \sqrt{\frac{k^2\;\;\varrho^2}{k^2+1}}\,. \tag{5.24}$$

5.3.4 Upper intermediate state

The design goals of the upper intermediate state are:

1. To bring the kite out of the power zone, while still harvesting energy.
2. To realize a fast and smooth transition.

The state diagram of the upper intermediate state is shown in Fig. 5.13. The angle β_{ri} at which this state is left needs to be optimized depending on the wind conditions. A first approximation the β_{ri} is determined as:

$$\beta_{\text{ri}} = k_5 + k_6\, \beta_{\text{set}} \tag{5.25}$$

with

$$k_5 = 37.5^\circ \tag{5.26}$$

and

$$k_6 = \frac{1}{2} \tag{5.27}$$

Both constants k_5 and k_6 should be optimized using a dynamic system model. Instead of using a pre-calculated value of β_{ri} it is also possible to use a switch condition, that depends on the reel-out power. For example, the condition could be to end the reel-out phase when the reel-out power drops to 40 % of the average mechanical power in the state FIG_8. Such a dynamic switch condition is less dependent on the average wind speed or on the L/D of the kite.

The state transition table of the upper intermediate phase is shown in Tab. 5.6. At the end of the upper intermediate state the kite is depowered and the set force of the winch changed, which is not shown in Tab. 5.6.

Table 5.6: *Finite sub-states of the upper intermediate phase INT_UP. An offset of $\delta\psi \approx 60^\circ$ is needed to compensate for the time delay δt_{up} between the command to stop turning and the kite actually stopping to turn.*

State	Next state	$\mathbf{p}^{\text{SE}}_{\text{k,set}}$	$\dot{\chi}_{\text{set}}$	Condition
Initial	UP_TURN	–	$\dot{\chi}_{turn}$	always
UP_TURN	UP_FLY_UP	*Zenith*	from PID	$\psi > 360^\circ - \delta\psi \ \vee \ \psi < \delta\psi$
UP_FLY_UP	Final	*Zenith*	from PID	$\beta > \beta_{\text{ri}}$

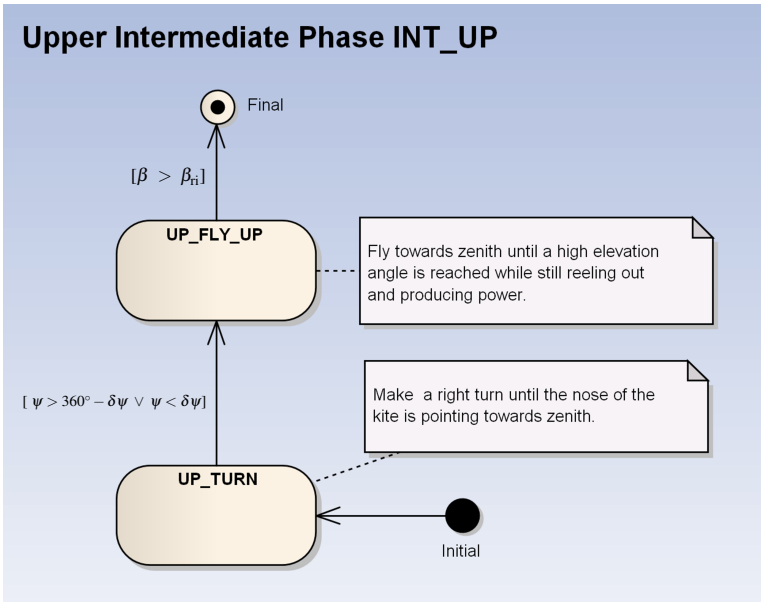

Figure 5.13: *Finite state diagram, explaining the states of the upper intermediate state INT_UP. In this state the kite first turns towards zenith and is then flying upwards while still producing power. This significantly increases the duty cycle D and helps to reduce the forces at the beginning of the reel-in phase, because the reel-in phase begins at a higher elevation angle.*

5.3.5 Performance of the flight-path planner

In Fig. 5.14 the planned flight paths for a set value of 20, 40 and 60 degrees are shown. Worth noticing is, that the the centre points $C1$ and $C3$ coincide for $\beta_{\text{set}} = 60°$.

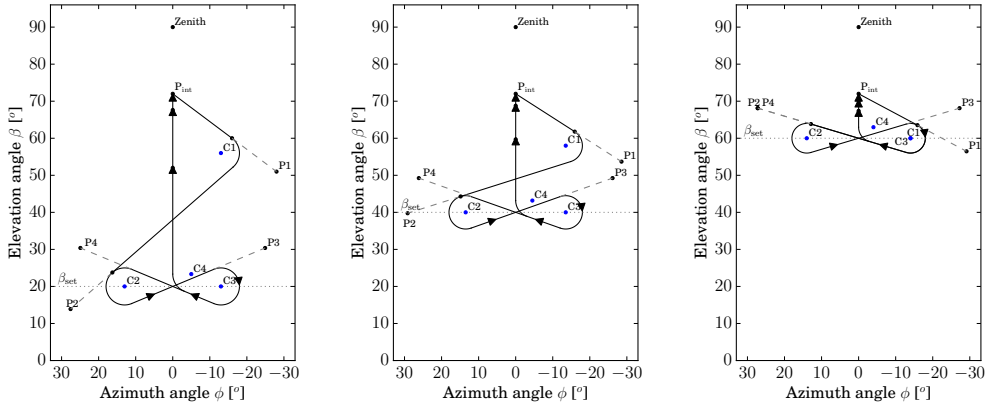

(a) $\beta_{\text{set}} = 20°$ (b) $\beta_{\text{set}} = 40°$ (c) $\beta_{\text{set}} = 60°$

Figure 5.14: *Planned flight path for low, medium and high set values of the average elevation angle. For $\beta_{\text{set}} = 60°$ the coordinates of the centre points $C1$ and $C3$ and of the attractors $P2$ and $P4$ become identical. This means, that there is a direct transition from the power state to flying figures of eight manoeuvres. Schematic drawings, see remark at the beginning of Sec. 5.3.1.*

Some of the design goals, mentioned in Sec. 5.3 can be verified with a quasi-static analysis. The effective wind speed at the position of the kite $v_{\text{w,e}}$ can be calculated as

$$v_{\text{w,e}} = v_{\text{w}} \cos\beta \cos\phi \tag{5.28}$$

Combining Eq. 5.28 with the exponential wind profile law Eq. 3.2 results in

$$\frac{v_{\text{w,e}}}{v_{\text{w,g}}} = \left(\frac{z}{z_{\text{ref}}}\right)^{p} \cos\beta \cos\phi. \tag{5.29}$$

With $\mu = v_{\text{w,e}}/v_{\text{w,g}}$ and $z = l_{\text{t}} \sin\beta$ where l_{t} is the tether length and β the elevation angle

the nondimensional wind speed gain is obtained:

$$\mu = \left(\frac{l_\mathrm{t} \sin\beta}{z_\mathrm{ref}} \right)^p \cos\beta \cos\phi. \tag{5.30}$$

The quasi-static crest factor of the force $CF_\mathrm{f,q}$ (quotient of the maximal and average tether force) while flying figures of eight at a given tether length and average elevation angle can now be calculated as:

$$CF_\mathrm{f,q} = \left(\frac{\mu_\mathrm{max}}{\mu_\mathrm{av}} \right)^2 \tag{5.31}$$

The dependency of μ and $CF_\mathrm{f,q}$ as a function of the average elevation angle β_set is shown in Fig. 5.15. As one can see, μ can be varied by a factor of 1.53 while the CF_f range does not exceed the value of 1.2. Keeping the crest factor below this limit is a design choice: Up to this value electrical machines still work without loosing much efficiency.

Furthermore Fig. 5.15 shows, that at an elevation angle $\beta_\mathrm{set} \sim 26^\circ$ the crest factor reaches it's minimum of $CF_\mathrm{f} \simeq 1.00$. This happens, because at lower part of the figure-of-eight the effective wind is higher due to the term $\cos\beta$ and at the upper parts the effective wind is higher due to the wind profile. This would make an elevation angle of $\beta_\mathrm{set} = 26^\circ$ the optimal choice for operating at nominal wind speed, were the nominal power output is just reached, assuming the tether drag can be neglected. Fig. 5.16 shows the optimal elevation angle as function of the wind shear coefficient p.

Another research question was: How big is the wind speed ratio ν, that can be compensated by changing the average elevation angle? Definition:

$$\nu = \frac{\mu_\mathrm{av,max}}{\mu_\mathrm{av,min}} \tag{5.32}$$

where $\mu_\mathrm{av,max}$ is the average wind speed gain at $\beta = \beta_\mathrm{opt}$ and $\mu_\mathrm{av,min}$ is the average wind speed gain at $\beta = \beta_\mathrm{max}$. The value ν depends on the coefficient p of the wind profile law as shown in Fig. 5.17.

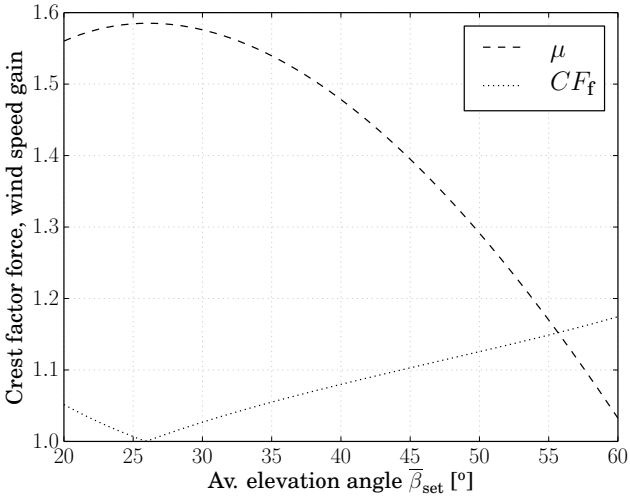

Figure 5.15: *The dimension less wind speed gain* μ *and the crest factor of the tether force* CF_{f} *as function of the average elevation angle* $\overline{\beta_{\text{set}}}$*. The tether length is* $l_{\text{t}} = 300$ *m and* $p = 0.234$ *as approximated for Cabauw.*

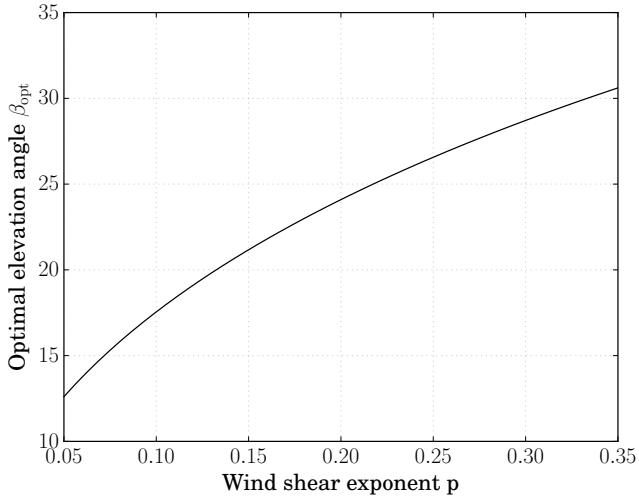

Figure 5.16: *The optimal elevation angle* β_{opt} *for a maximized wind speed gain* μ *as function of the the wind shear exponent p.*

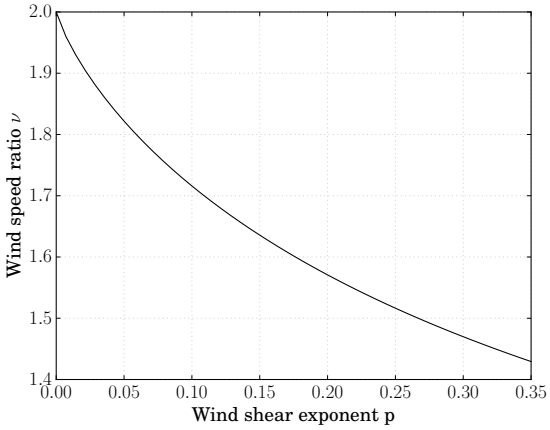

Figure 5.17: *Ratio* ν *of the effective wind speed between the optimal and the maximum elevation angle as function of the wind shear. Without wind shear a value of* $\nu = 1.98$ *can be achieved by changing the average elevation angle, with a wind shear exponent of* $p = 0.234$ *a value of* $\nu = 1.53$ *is achievable.*

For the scenario Cabauw this means, that the system can be operated up to a ground wind speed of $v_{\mathrm{w,max}} = 1.53\, v_{\mathrm{w,nom}} = 9.2\, m/s$ without increasing the depower settings during reel-out, assuming a negligible turbulence. According to the measured wind distribution (Fig. 5.3) this means, that 96% of the time it is not necessary to change the angle of attack to limit the maximal power (again assuming a neglectable turbulence).

5.4 Summary and conclusion

At the beginning of this chapter the small-earth reference frame was introduced. This reference frame provides a coordinate system which makes it possible to split the control problem into two SISO problems: The control of the flight path and the control of the reel-out speed of the winch. Then the wind profile and turbulence intensity of a Dutch onshore site were presented and the modelling of three typical wind field scenarios were explained.

After determining the basic robustness requirements a flight path planning algorithm was presented, that allows to plan a flight path on the two dimensional small earth using only a small set of optimization parameters: The width and height of the figure of eight

w_{fig} and h_{fig}, the average elevation angle during reel out β_{set}, the elevation angle for starting the depower state β_{ri} and the minimal attractor point distance δ_{min}. The height of the figure of eight h_{fig} is varied automatically, depending on β_{set}.

For compensating the steering delay of the kite and the kite control unit it is proposed to use the three empiric parameters $\delta\chi$, $\delta\chi_{\text{int}}$ and $\delta\psi$. They need to be manually tuned such that the error between the planned and the actual flight path is minimized.

Finally the quasi-static performance of the suggested FPP was analysed and it was shown, that it can extend the maximal wind velocity, at which the system can be operated without lowering the lift coefficient of the wing for the given site by a factor of $\nu = 1.53$. This significantly reduces the loss of efficiency above the nominal wind speed, that is inherent for pumping kite power systems.

The next chapter will focus on the flight path and winch controllers, that are needed to follow the desired flight path.

CHAPTER 6

Flight Path and Winch Control

Contents

6.1 Introduction . . . 117
6.2 Flight Path Control (FPC) . . . 119
6.2.1 Simplified kite system model . . . 120
6.2.2 (Position, heading) flight path controller . . . 124
6.2.3 (Position, heading) FPC with NDI and turn actions . . . 125
6.2.4 (Position, heading, course) FPC with NDI and turn actions . . . 129
6.2.5 Performance of the FPC . . . 129
6.3 Winch control (WC) . . . 133
6.3.1 Simplified winch system model . . . 133
6.3.2 Winch controller design . . . 136
6.3.3 Performance of the WC . . . 139
6.4 Implemented distributed control system . . . 153
6.4.1 Detailed control structure . . . 153
6.4.2 Adapting to changing wind conditions . . . 154
6.4.3 Distributed control . . . 155
6.5 Summary and conclusion . . . 155

6.1 Introduction

In the previous chapter a flight path planner was presented, that allows the system to adapt to changing wind conditions. In this chapter the planner will now be extended

with advanced controllers, so that the system is able to work robustly in turbulent and changing wind conditions.

While in 2010 no publications were available describing a successfully implemented kite-power control system, over the last years many papers on this topic were published (see Sec. 2.1). In contrast, apart from the conference paper of Fechner and Schmehl (2012a) no literature is available that describes a complete kite-power control system for a kite and a winch working in pumping mode of operation and using a kite-control unit.

In Fig. 6.1 the overall structure of the control system is illustrated. The User Interface (UI) provides top and front view displays for the current position of the kite, numerical displays for the current altitude, tether reel-out speed and force, generated power etc. Connected to the UI is the finite state machine (FSM) controlling the operational

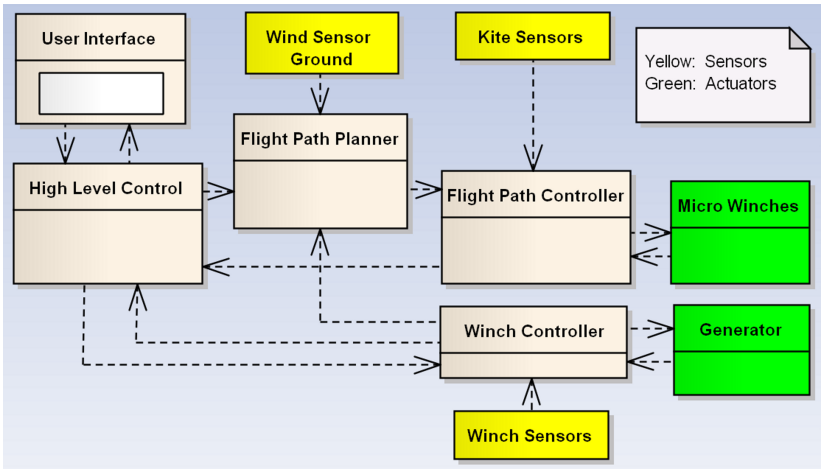

Figure 6.1: *Control system structure. The High Level Control block is implemented, using a finite state machine (FSM).*

state of the system: starting, landing, reel-out and reel-in. It gives control commands to the flight path planner and the winch controller. The flight path planner calculates the optimal flight trajectory depending on the current wind velocity, the system state and the current tether force and generator power.

The winch controller manages the drum/generator module. Mounted on a sled which is driven by a spindle motor, this linear-displacement module ensures that the tether is evenly fed onto the drum. At low wind speeds the winch controller optimizes the combination of reel-out speed and force to achieve maximum traction power. At high

wind speeds this controller keeps the average force as high as possible without exceeding the maximal force. In the reel-in phase the winch controller ensures that the tether tension never drops below the required minimal value for robust flight control of the kite, while minimizing the reel-in time and reel-in energy.

The objective of the flight path controller is to minimize the error between the actual and the planned flight path. It uses an LPV controller, which controls the heading and the course of the kite, and a navigator, which provides the set values for the LPV controller. The flight path controller needs a good estimation of the kite state. The kite state is composed of the kite position, velocity and orientation and is estimated based on the information from the following sensors:

- a high-end GNSS sensor, attached to the main strut of the kite;
- an inertia measurement unit, attached at the same place;
- the reel-out length and force as measured by the winch;
- wind speed sensor at the ground, attached to a mast of 6 m height.

The use of angular sensors, that measure elevation and azimuth angle of the tether was investigated by Peschel (2013) and can improve the accuracy of the estimated kite position in case of GNSS errors or failures.

The main focus of this chapter is the implementation of the "Flight Path Controller" and the "Winch Controller" as shown in Fig. 6.1. The control problem is split into four sub-tasks: First, the trajectory of the kite as projected on the unit sphere is treated as a 2D control problem (Sec. 6.2). This is separated from the control of the reeling speed of the winch (Sec. 6.3), which determines the tether length and force. The trajectory control is split into a flight-path planning (Sec. 5.3) and a flight-path control (Sec. 6.2) problem. The sub-system controllers need to be supervised and their parameters adapted to the wind conditions by a high-level control system. This is presented in Sec. 6.4. Finally, in Sec. 6.5 the results are summarized and the developed methodology is explained. A short version of the content of Sec. 6.2 can be found in Fechner and Schmehl (2016a).

6.2 Flight Path Control (FPC)

In this section first, a simplified model is presented of a kite, attached to a fixed length tether. Then three different flight path controllers are explained: first, a simple PID

heading controller, then a more advanced controller using NDI and turn actions, and finally a controller that uses also its course in addition to the heading of the kite. In Sec. 6.2.5 the performance of the controller using NDI and turn actions under different wind conditions and also in the presence of large sensor errors is depicted.

6.2.1 Simplified kite system model

The simplified, 2D kite system model is composed of a model of the kite, attached to a fixed length tether, a model of the kite control unit and a formula to estimate the angular kite speed ω as defined in Eq. 5.1.

This model is valid for any airborne wind energy system with the following limitations: The effect, that the kite accelerates due to gravity when flying downwards is not taken into account, and the rotational inertia, that delays the reaction on steering inputs is not taken into account as well. On the other hand, the influence of gravity on the turn rate of the kite is correctly modelled. The numeric examples, given below are obtained from the properties of the Hydra kite of Delft University of Technology. They are only used as test case and do not limit the generality of the model.

The complete system model - including the flight path controller block - is shown in Fig 6.2. The test case is to fly the kite to the centre of the wind window, pointing the nose to zenith. The initial condition is an elevation and azimuth angle of 45 degrees with the nose pointing downwards. Goal is to reach a small final azimuth error as fast as possible while avoiding any oscillations. In practice this manoeuvre can be useful to avoid an obstacle or to prepare for landing. In equilibrium the elevation angle only depends on the lift-over-drag ratio of kite and tether and cannot be controlled by the flight path controller.

The triangular wind speed test signal is shown in Fig. 6.3. It allows to test any given wind speed range fast while challenging the stability of any feedback controller due to its infinite spectrum.

The model of the kite is shown in Fig. 6.4. Inputs are the relative steering u_s, the apparent wind speed v_a, the initial elevation angle β_0, the angular speed ω and the initial values for the heading ψ_0 and the azimuth angle ϕ_0. Outputs are the heading angle, its derivative and the position of the kite as defined by the elevation and azimuth angles.

The heading angle of the kite is calculated by using the turn rate law (Eq. 6.9) to obtain the turn rate and then integrating it to obtain the heading angle. The position of the kite is calculated by decomposing the angular speed ω into the derivatives of the

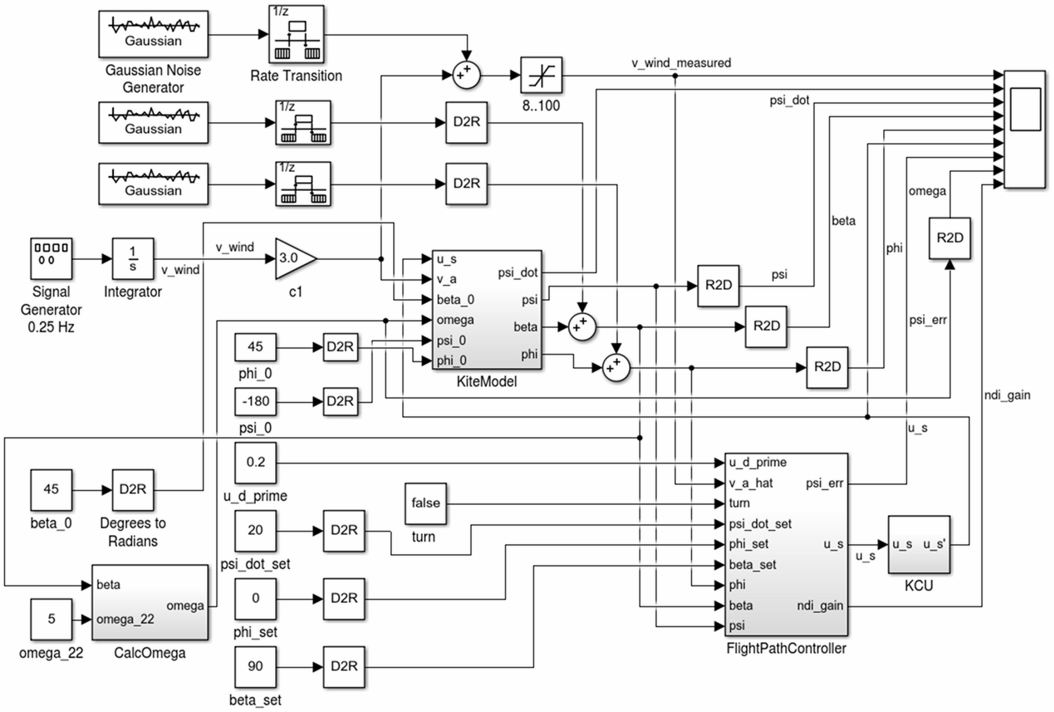

Figure 6.2: *Block diagram, showing the simplified system model, used as basic test for the development of the flight path controller. Gaussian noise can be added to the sensor data (elevation, azimuth and apparent wind speed). The apparent wind speed is modelled as triangular signal, varying between 12 and 24 m/s (Fig. 6.3). The model is composed of the block CalcOmega, that calculates the angular speed, the kite model and the KCU model. The D2R blocks convert degrees to radian, the R2D blocks do the opposite.*

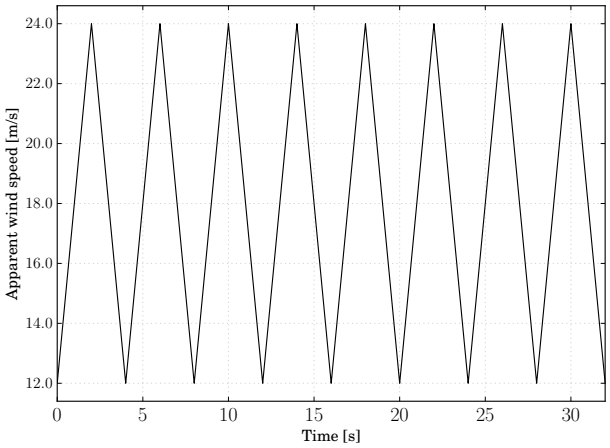

Figure 6.3: *Triangular wind speed signal, varying between 12 and 24 m/s as used for the parking tests. This range was chosen, because for flying figures of eight at an average ground wind velocity the apparent wind speed at the kite is between 19 and 24 m/s. While parking, it can be a little bit lower, therefore the lower limit was extended to 12 m/s.*

azimuth and elevation angles under the assumption, that the course is identical to the heading and then integrating the these derivatives.

It is assumed, that the angular speed of the kite ω is depending only on the elevation angle and calculated according to Eq. 6.1. This equation assumes, that the angular speed reaches the constant value ω_{22} at an elevation angle of 22° [1] and an angular speed of zero at $\beta = \beta_{\max}$, in this test case 73°. This angle is the elevation angle of the Hydra kite while parking at 300 m tether length at a ground wind speed of 6 m/s. The kite reaches the highest possible quasi-static elevation angle when parked. It can fly crosswind only at a lower elevation angle and reaches the maximal crosswind speed (and thus maximal value of ω) at $\beta = \beta_{\text{opt}}$.

$$\omega = \frac{\beta_{\max} - \beta}{\beta_{\max} - \beta_{\min}} \omega_{22} \tag{6.1}$$

The model of the steering part of the KCU is shown in Fig. 6.5. It captures the system delays, models the P-controller, used for the position control of the servo drive

[1] According to Fig. 5.16 this is approx. the optimal elevation angle for a wind profile exponent of $\alpha = 1/7$

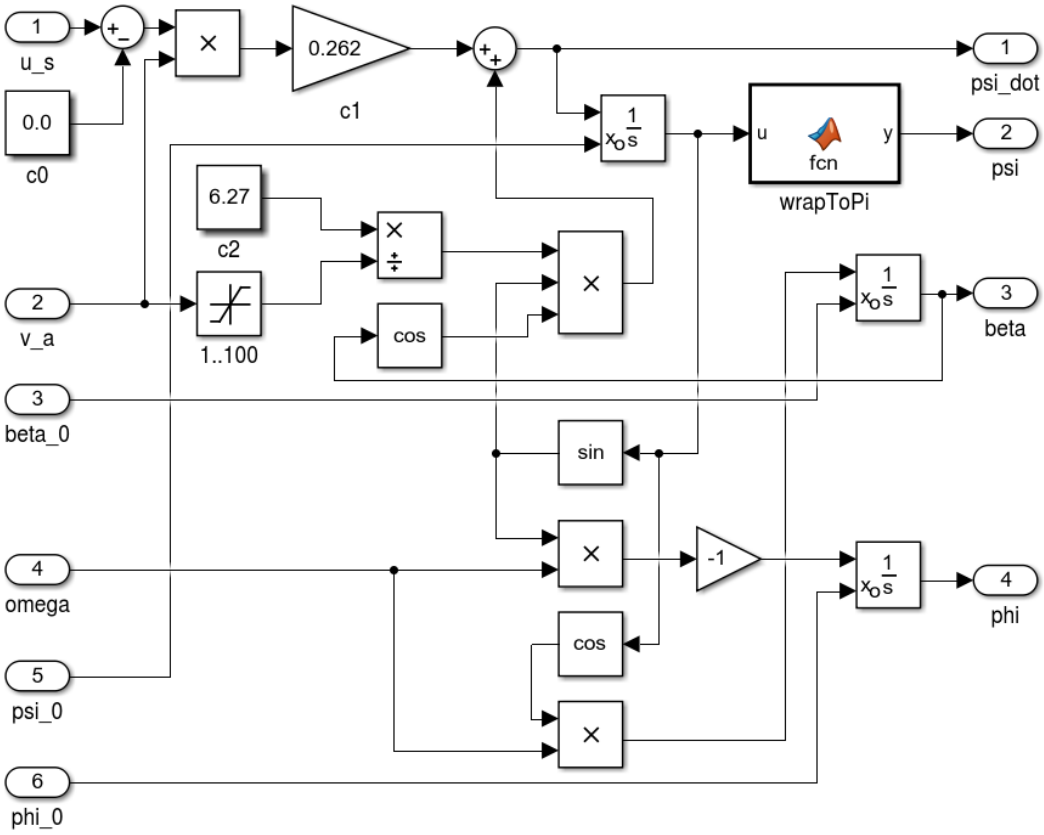

Figure 6.4: *Block diagram, showing the simplified kite model, used for the development of the flight path controller. Inputs are the relative steering u_s, the apparent wind speed v_a, the initial elevation angle β_0, the angular speed ω and the initial values for the heading ψ_0 and the azimuth angle ϕ_0. Outputs are the heading angle, its derivative and the position of the kite as defined by the elevation and azimuth angles. For a detailed explanation see Sec. 6.2.1*

.

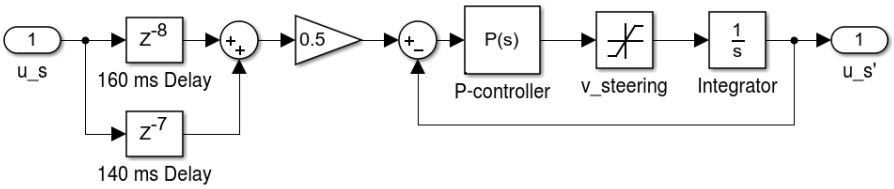

Figure 6.5: *Block diagram, showing the steering part of the KCU model. The delay of 150 ms includes the delay of the sensors, the wireless link, the controller and the actuator. The amplification of the P-controller is 3.0, the steering speed is limited to* $\pm 0.2\ s^{-1}$*. The model of the depower drive-train is identical except for the speed limit, that is lower,* $\pm 0.1\ s^{-1}$ *instead of* $\pm 0.2\ s^{-1}$*.*

and also takes the limited speed of the steering motor into account. The model of the depower actuator is the same except for the speed limit, that is lower, $\pm 0.1\ s^{-1}$ instead of $\pm 0.2\ s^{-1}$.

6.2.2 (Position, heading) flight path controller

This flight path controller has the desired kite position $\mathbf{p}_{\mathrm{k,set}}^{\mathrm{SE}} = (\beta_{\mathrm{set}},\ \phi_{\mathrm{set}})$ and the normalized depower setting u_{d}' as inputs and the steering output u_{s} as output. A block diagram is shown in Fig. 6.6. The "Navigator" block calculates the desired flight direction χ_{set} using great circle navigation as explained by Baayen and Ockels (2012) and Veness (1999) according to the following formulas:

$$y = \sin(\phi_{\mathrm{set}} - \phi)\ \cos(\beta_{\mathrm{set}}) \tag{6.2}$$

$$x = \cos\beta\ \sin\beta_{\mathrm{set}} - \sin\beta\ \cos\beta_{\mathrm{set}}\ \cos(\phi_{\mathrm{set}} - \phi) \tag{6.3}$$

$$\chi_{\mathrm{set}} = \mathrm{atan2}(-\mathrm{y},\ \mathrm{x}) \tag{6.4}$$

This angle is then compared with the heading of the kite. The difference is fed into a PID controller, that uses the steering signal u_{s} to steer the nose of the kite into the calculated flight direction.

This controller works only sufficiently well, if the P, I and D settings are varied, depending on the depower settings u_{d}. To achieve this, first u_{d} is normalized by introducing

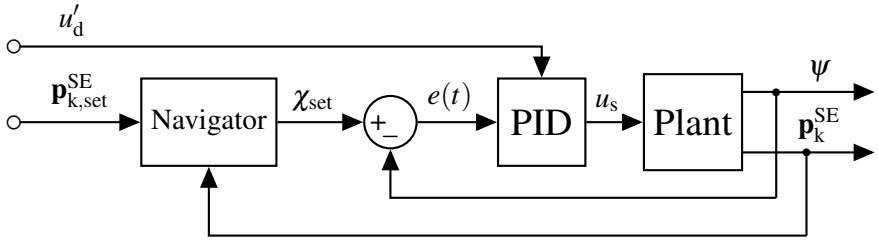

Figure 6.6: *Block diagram of the ($\mathbf{p}^{SE}_k$, ψ) flight path controller. The inputs are the target position of the kite $\mathbf{p}^{SE}_{k,set}$ and the normalized depower setting u'_d which is used to vary the P, I and D parameters. The outputs are the actual kite position $\mathbf{p}^{SE}_k$ and the heading angle ψ.*

a new variable u'_d which is in the range $0 < u'_d < 1$ for $u_{d,0} < u_d < u_{d,max}$ as

$$u'_d = \frac{u_d - u_{d,0}}{u_{d,max} - u_{d,0}} \tag{6.5}$$

Then the P, I and D parameters are calculated as

$$P = P_d\, u'_d + P_p\, (1 - u'_d) \tag{6.6}$$

$$I = I_d\, u'_d + I_p\, (1 - u'_d) \tag{6.7}$$

$$D = D_d\, u'_d + D_p\, (1 - u'_d) \tag{6.8}$$

where P_d is the proportional gain, needed for the fully depowered kite during reel-in and P_p is the proportional gain, needed for the fully power kite during reel-out. This controller is used for all practical test results, presented in this thesis. It needs six parameters, that need to be optimized, which is difficult to achieve. In addition this controller is not explicitly compensating the gravity forces. That means, that the average elevation angle and the form of the trajectory are strongly dependent on the wind speed and the tether length, which makes it difficult to optimize the trajectory.

6.2.3 (Position, heading) FPC with NDI and turn actions

Because the response of the plant (the kite) depends on the apparent wind speed v_a, the kite mass and the position of the kite in a non-linear way, accuracy and robustness can be improved by linearising the plant model. This is done using the nonlinear, dynamic

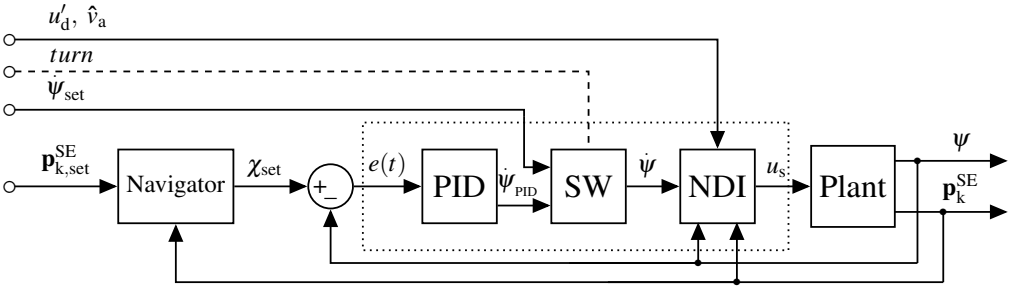

Figure 6.7: *Block diagram of the ($\mathbf{p}^{SE}_k$, ψ) flight path controller with nonlinear dynamic inversion (NDI) and turn actions. The inputs for the normalized depower setting u'_d and the limited apparent wind velocity $\hat{v}_a$ are always used. During the turns additionally the set value of the turn rate $\dot{\psi}_{set}$ is used, otherwise the target position of the kite $\mathbf{p}^{SE}_{k,set}$. The outputs are the actual kite position $\mathbf{p}^{SE}_k$ and the heading angle ψ.*

inversion (NDI) block as shown in Fig. 6.7. In addition the FPC is using a switch (the block "SW"), that connects the input of the NDI block during the turn actions to the set value $\dot{\psi}_{set}$ from the FPP, and otherwise to the value, calculated by the PID controller and navigator, based on the position of the attraction point $\mathbf{p}^{SE}_{k,set}$, the current position $\mathbf{p}^{SE}_k$ and the current heading angle ψ.

To derive the equations for the NDI block the turn-rate law as introduced in 4.72 is used

$$\dot{\psi} \;=\; c_1\, v_a\, (u_s - c_0) \;+\; \frac{c_2}{v_a}\, \sin\psi\, \cos\beta \tag{6.9}$$

and extended to include the influence of the depower settings u_d. The normalized depower settings u'_d are used as calculated in Eq. 6.5. Now the variable u'_s is introduced which is equivalent to the expression $u_s - c_0$ in Eq. 6.9, but includes the influence of u'_d as

$$u'_s \;=\; \frac{u_s - u_{s,0}}{1 + K_{d,s} u'_d} \tag{6.10}$$

in the same way as it was done in Eq. 4.52. The factor $K_{d,s}$ describes the influence of the normalized depower setting u'_d on the steering sensitivity. According to the experience of the kite pilot and researcher Rolf van der Vlugt, depending on the geometry of the bridle $K_{d,s}$ has a value in the range of $1 < K_{d,s} < 2$. By combining Eq. 6.10 with 6.9 we

obtain:

$$\dot{\psi} = c_1 \, v_a \, \frac{u_s - u_{s,0}}{1 + K_{d,s} u'_d} + \frac{c_2}{v_a} \, \sin\psi \, \cos\beta \tag{6.11}$$

and solve it for u_s. This results in:

$$u_s = \frac{1 + K_{d,s} u'_d}{c_1 \, v_a} \left(\dot{\psi} - \frac{c_2}{v_a} \, \sin\psi \, \cos\beta \right) + u_{s,0} \, . \tag{6.12}$$

The apparent wind speed of at the kite v_a must be measured or estimated. NDI does not work for very low apparent wind speeds because the steering command u_s would go to infinity. Therefore the limited, apparent wind speed $\hat{v}_a$ is introduced and used for the NDI block defined as

$$\hat{v}_a = \begin{cases} v_{a,min} & \text{if } v_a \leq v_{a,min} \\ v_a & \text{else} \end{cases} \tag{6.13}$$

where $v_{a,min}$ is the minimal apparent wind speed, that is required for steerability.

Special care is needed for the implementation of anti-windup control: Using an anti-windup PID controller is not sufficient, because limiting the turn rate $\dot{\psi}$ does not effectively limit u_s. The anti-windup PID controller structure with integrated NDI as shown in Fig. 6.8 addresses this issue. This controller is based on the theory as presented by Visioli (2006).

This controller limits the turn rate $\dot{\psi}$ and the actuation u_s separately such that the following conditions are full filled:

$$|\dot{\psi}| \leq \dot{\psi}_{max} \tag{6.14}$$

and

$$|u_s| \leq u_{s,max} \, . \tag{6.15}$$

The turn rate limit should be chosen such that the centrifugal forces do not exceed the limits, given by the structural strength of the kite and the KCU. In addition the allowed rotational acceleration, that the IMU sensors can handle must not be exceeded. Furthermore a high turn rate can reduce the accuracy of any GNSS sensor significantly.

The actuation limit $u_{s,max}$ must be chosen such that the side areas of the kite are not getting into stall. It can be useful to reduce $u_{s,max}$ even further for the following reasons: First, to reduce the wear of the steering system and second, to reduce the time that is needed to steer into the opposite direction.

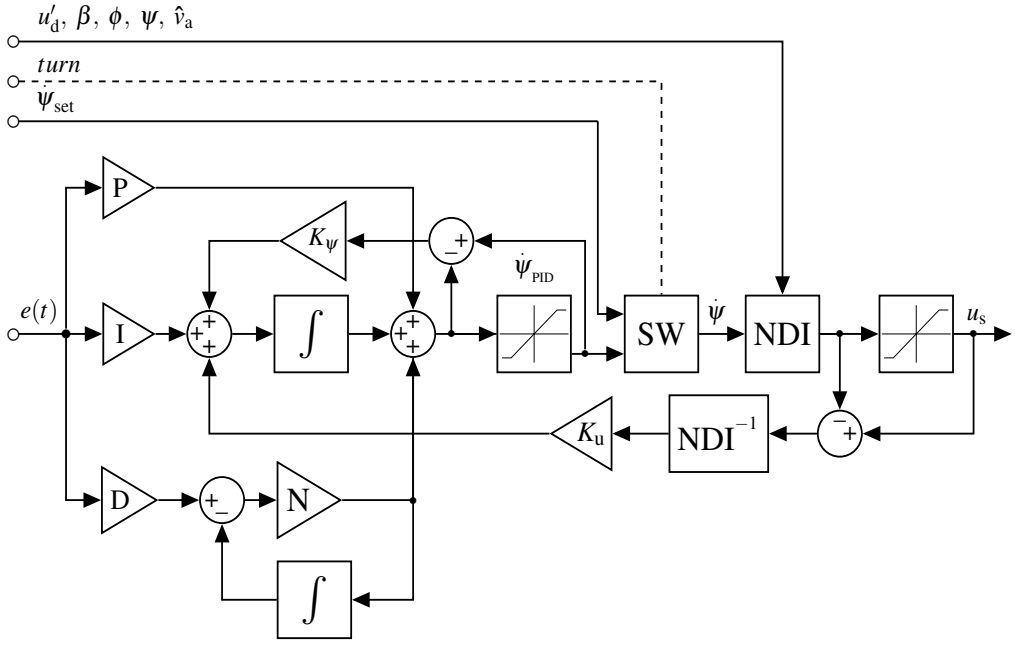

Figure 6.8: *Block diagram of the the PID controller with integrated NDI block, turn actions and anti-windup, using back calculation. K_ϕ and K_u control the anti-windup behaviour with respect to the turn-rate and steering actuator limits. The limiter in the centre limits the turn rate, the limiter on the right the steering signal itself. The connection of u'_d, β, ϕ, ψ, $\hat{v}_a$ with the inverse NDI block is not shown. The factor N is the low pass filter constant of the D part of the controller.*

6.2.4 (Position, heading, course) FPC with NDI and turn actions

The accuracy of the controller can be improved further, if not only the heading angle is controlled in a feedback loop, but also the course angle: A difference between the course and the heading angles is induced (i) by the gravity forces and (ii) by wind turbulences.

On the other hand the course of the kite can only be controlled when it is moving. For controlling a kite, that is moving only very slowly in the small earth projection the heading angle the must be used. Therefore a linear parameter varying (LPV) controller is used, that uses mainly the course angle at high angular velocities ($\omega > 2.275\ \omega_{\text{up}}$) and only the heading angle, for $\omega < \omega_{\text{up}}$. Both angles are fused according to the following algorithm:

$$k_\chi = \begin{cases} min\left(\frac{\omega - 0.8}{1.2},\ 0.85\right) & \text{if } \omega > \omega_{\text{up}} \\ 0.0 & \text{else} \end{cases} \tag{6.16}$$

$$\begin{aligned} x &= \sin\psi\ (1 - k_\chi) + \sin\chi\ k_\chi \\ y &= \cos\psi\ (1 - k_\chi) + \cos\chi\ k_\chi \\ \psi' &= \text{atan2}(x, y) \end{aligned} \tag{6.17}$$

The value of k_χ is limited to 0.85. This avoids the kite to get too slow when flying figures of eight at a very high elevation angle. The block diagram of this controller is shown in Fig. 6.9.

6.2.5 Performance of the FPC

In Fig. 6.11 the flight path (elevation angle vs. azimuth angle) of a kite in calm wind conditions, $v_a = 25\ m/s$ (no turbulence) is shown. The error compared to the desired flight path is very low, less than 1° both for elevation and azimuth. There is a small asymmetry in the turns: The increase of the turn rate is fast at the beginning and slower at the end of the turn. The reason is that the controller, active during the turns is faster than the PID controller, that is active while flying towards an attractor point.

The most important performance criteria are, how much is the desired maximum elevation exceeded and how much the minimum elevation falls below the desired value, since these deviations have a negative impact on the crest factors of force and power and thus on the average power output. In addition an undercut of the desired minimal elevation can also have a negative impact on the safety of the system. For this test case, the error margin is $|\Delta\beta| \leq 0.6\ ^o$.

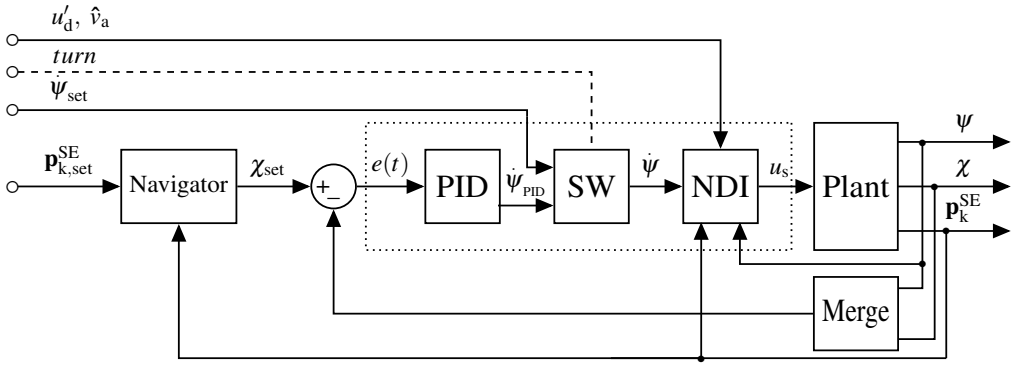

Figure 6.9: *Block diagram of the flight path controller with nonlinear dynamic inversion (NDI) and turn actions, using a linear combination of the heading and course angles as feedback parameter of the inner control loop. This linear combination is calculated by the "Merge" block as defined in Eq. 6.17. The inputs for the normalized depower setting u'_d and the limited apparent wind velocity $\hat{v}_a$ are always used. During the turns additionally the set value of the turn rate $\dot{\psi}_{set}$ is used, otherwise the target position of the kite $\mathbf{p}^{SE}_{k,set}$. The outputs are the actual kite position $\mathbf{p}^{SE}_k$ and the heading ψ and course χ.*

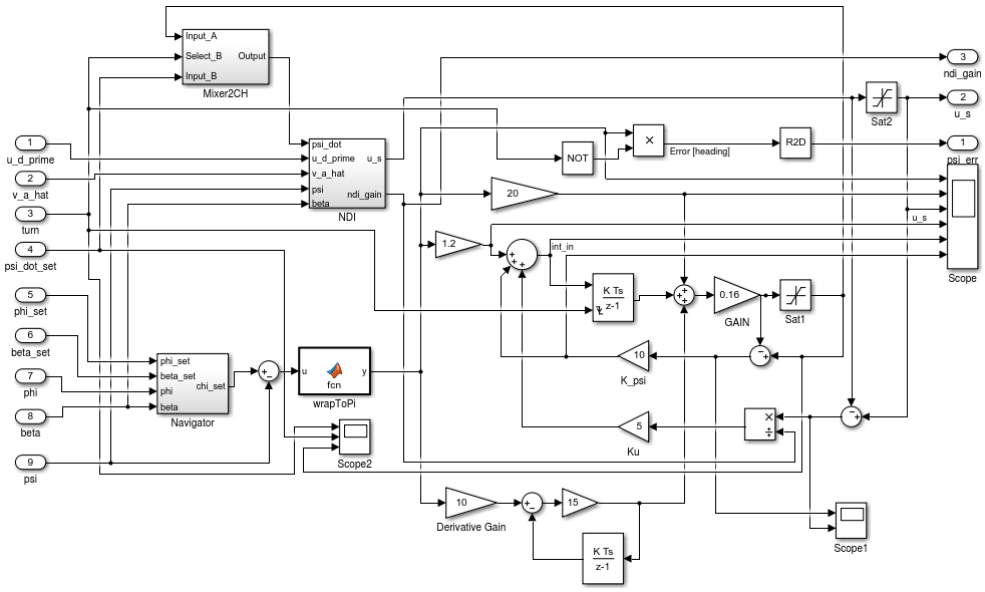

Figure 6.10: *Simulink block diagram of the flight path controller, using discrete time integrators.*

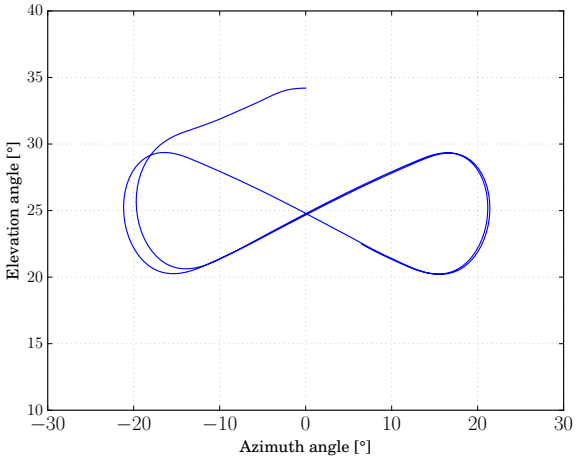

Figure 6.11: *Flight path at calm wind conditions, $v_a = 25m/s$, no turbulence, no sensor errors. The elevation error is $|\Delta\beta| \leq 0.6\,^o$.*

In Fig. 6.12 the flight path is shown, when the apparent wind speed was varied between $v_a = 23\ m/s$ and $v_a = 35\ m/s$ with a period time of 4 s. According to Fig. 7.19 these values correspond to a turbulence intensity of 26.5 % while flying figures-of-eight at an average wind speed of 6 m/s at 10 m height. This was the largest turbulence intensity, recorded at 200 m height at the location Cabauw, The Netherlands in 2011. Therefore these values are used as extreme test case for the robustness of the controller.

In Fig. 6.13 the flight path is shown, when in addition to the varying wind speed sensor errors were introduced. To simulate sensor errors Gaussian noise generators were used with a sample time of $1s$ and the following values for the variance: 4° for the azimuth and elevation angle, 5° for the heading and 4 m/s for the apparent wind speed.

The results show a very good accuracy under calm wind condition and a sufficient accuracy even under very difficult conditions.

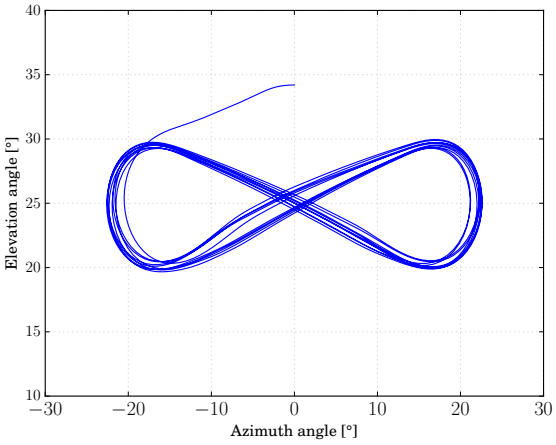

Figure 6.12: *Flight path with strong variations of the apparent wind speed, $v_a = 23..35m/s$, no sensor errors. The elevation error is $|\Delta\beta| \leq 1.3\ ^o$.*

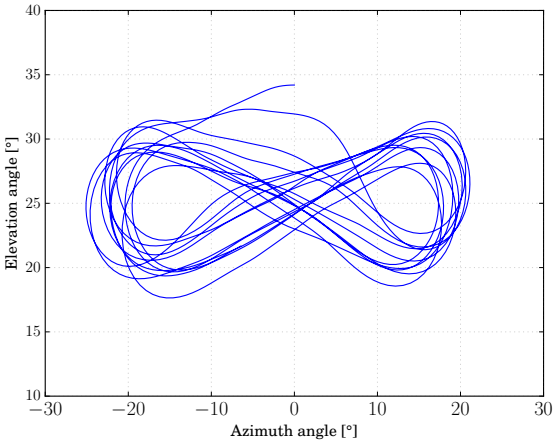

Figure 6.13: *Flight path with strong variations of the apparent wind speed, $v_a = 23..35m/s$ and large sensor errors. The variance was 4° for the azimuth and elevation sensors, 5° for the heading and $4\ m/s$ for the v_a sensor. The maximum elevation error stays within $|\Delta\beta| \leq 2.6\ ^o$.*

6.3 Winch control (WC)

For a kite power system, the reel-out speed of the winch must be controlled such that the maximal tether force is never exceeded, while the reel out speed should be optimized for maximal power over the full cycle at wind speeds below rated wind speed. To keep the kite controllable, also a minimal tether force limit has to be kept[2]. In addition, special settings can be needed for launching and parking. The simplified system model, that was used for designing the winch controller, is explained in the next section while the winch controller design is explained thereafter.

6.3.1 Simplified winch system model

For the development of the winch controller the dynamic model as described in Chap. 4 is more complex than needed. Therefore a 2.5 dimensional system model is developed that captures the main characteristics of a kite power system as seen from the winch. The model is shown in Fig. 6.14.

For this model a subset of the states of the FPP is used. A comparison of the states of the flight path planner and those, used by the simplified winch system model is shown in Tab. 6.1. The term "state" is in this chapter used for the discrete states of the Finite-State-Machines (FSMs) of the control system and should not be confused with the state variables of the (mostly continuous) state vector, that can be used to describe any point in time of the physical state of the dynamic kite-power system. Furthermore the term "phase" is used for the reel-in phase and the reel-out phase. They are defined by the dynamic state of the KPS: If $v_t > 0$ the system is in the reel-out phase, if $v_t < 0$ it is in the reel-in phase. There is a small time delay between a change of the state of the control system and a change of the phase of the KPS.

The simplified system model averages over the figure of eights. It uses the quasi-static equations for the cross wind speed as calculated in Eq. 6.18 during the reel-out phase and the apparent wind speed during reel-in (without flying cross-wind) as calculated in Eq. 6.19. Both equations are derived in Schmehl et al. (2013). The crosswind interpolation factor $0 \leq c_f \leq 1$ is used to control the linear interpolation between reel-in and reel-out as shown in Eq. 6.20.

[2] In theory, a kite with a kite control unit can also be controlled in free flight with zero tether force. In this thesis this is not investigated. The flight path controller as explained in the last section is designed for controlling the kite only as long as the tether force is the dominating force, compared to gravity.

Table 6.1: *States of the Flight Path Planner (FPP) and equivalent states of the simplified winch controller (WC). Refer to Fig. 5.7 to better understand the FPP states.*

FPP State	Simplified WC State	Description
LOW_RIGHT	ssIntermediate	fly towards the intermediate point P1
LOW_TURN		turn to the left
LOW_LEFT	ssLowLeft	fly to the left towards P2
TURN_LEFT	ssKiteReelOut	reel-out the tether
FLY_RIGHT		while flying crosswind
TURN_RIGHT		figures of eight
FLY_LEFT		
UP_TURN	ssWaitUntil	wait until high elevation
UP_FLY_UP		fly upwards until $\beta = \beta_{\text{ri}}$
DEPOWER	ssDepower	depower the kite and reel-in
POWER	ssPower	power the kite

$$v_{\text{a,ro}} = \left(\cos\beta\cos\phi - \frac{v_{\text{t,o}}}{v_{\text{w}}}\right) v_{\text{w}} \sqrt{1+\left(\frac{L}{D}\right)^2} \tag{6.18}$$

$$v_{\text{a,ri}} = v_{\text{w}} \sqrt{1 - 2\,\frac{v_{\text{t,o}}}{v_{\text{w}}}\,\cos\beta\cos\phi + \left(\frac{v_{\text{t,o}}}{v_{\text{w}}}\right)^2} \tag{6.19}$$

$$v_{\text{a}} = c_{\text{f}}\, v_{\text{a,ro}} + (1-c_{\text{f}})\, v_{\text{a,ri}} \tag{6.20}$$

The crosswind interpolation factor has the value $c_{\text{f}} = 1$ in the state FIG_8 and $c_{\text{f}} = 0$ otherwise, with a smooth transition between the states. The lift is varied according to the depower setting u'_{d}. This parameter varies between zero and one (in contrast to the parameter u_{d}, which is varied in the smaller range $u_{\text{d,min}} \leq u_{\text{d}} \leq u_{\text{d,max}}$).

The model assumes the azimuth angle ϕ to be zero most of the time. This means, most of the time it is in the centre of the wind window. Only in the lower intermediate phase INT_LOW it is smoothly increased from zero to 30° and then decreased back to

zero to mitigate the force peak at the beginning of the reel-out phase. The model further assumes the elevation angle to be low during the reel-out phase and high during the reel-in phase with a smooth transition in between.

The core of the system model is the finite state machine "CentralControl". Firstly, it generates the boolean values depower, azimuth, elevation and crosswind. When these values are low, all the continuous parameters $u_\mathrm{d}, \phi, \beta$ and the crosswind interpolation factor c_f have their minimum value. When the generated boolean values are high, these continuous parameters have their maximum value. When the generated boolean values switch from low to high, the blocks "CalcParameters" and "CalcBeta" produce a smooth transition. The resulting timing diagrams are shown in Fig. 6.15.

The parameters, calculated by the blocks "CalcParameters" and "CalcBeta" are fed into the block "WindAndKite". It uses the ground wind speed as calculated by the block "Wind" as additional input. The first test case is using an average wind speed of 8 m/s, modulated with a triangular signal of 0.25 Hz between 5.6 and 10.4 m/s. For testing the robustness of the controller some noise[3] can be added.

In addition to Eq. 6.20 the Eqs. 6.21 to 6.24 define the WindAndKite model:

$$F = \frac{1}{2}\,\rho\, v_\mathrm{a}^2\, A\, \sqrt{C_\mathrm{L}^2 + C_\mathrm{D}^2} \tag{6.21}$$

$$C_\mathrm{L} = C_\mathrm{L,min} + (C_\mathrm{L,max} - C_\mathrm{L,min})\,(1 - u_\mathrm{d}) \tag{6.22}$$

$$C_\mathrm{D,k} = C_\mathrm{D,min} + (C_\mathrm{D,max} - C_\mathrm{D,min})\,(1 - u_\mathrm{d}) \tag{6.23}$$

$$C_\mathrm{D} = C_\mathrm{D,k} + 0.31\,\frac{l_\mathrm{t}\, d}{1000\, A} \tag{6.24}$$

where d is the tether diameter in mm, A the projected area of the kite, l_t the tether length. The aerodynamic parameters of the kite are described with the minimum and maximum lift coefficients of the kite $C_\mathrm{L,min} = 0.2$, $C_\mathrm{L,max} = 1.0$ and the minimum and maximum drag coefficients $C_\mathrm{D,min} = 0.1$, $C_\mathrm{D,max} = 0.2$. An approximation of the effective tether drag is taken into account with Eq. 6.24. Furthermore, Eq. 3.1 is used to calculate the height of the kite and Eq. 3.2 and 3.3 to calculate the wind speed and the air density ρ at the height of the kite.

The "WindAndKite" model calculates the tether force at the winch. This signal is going into the "WinchController" and the "DriveTrain". The block "DriveTrain" imple-

[3] Band limited, integrated white noise with a sampling time of 0.1 s and a noise power of 0.1 W.

ments the equations, derived in Sec. 4.2.5. It uses the set speed and the force, imposed from the tether as input and has as outputs the acceleration and actual speed of the tether. The speed output of the block "DriveTrain" is fed back into the block "WinchController". In addition, the speed signal is integrated to calculate l_t, the reel-out length of the tether. A lower and a higher limit of the tether length l_{low} and l_{high} are used to create events for the state machine "CentralControl".

Finally, the block "CalcResults" uses the speed and force signals to calculate the average and maximal cycle power and the maximal tether force. It is using the cycle, starting with the first positive edge of the signal "powered" up to the second positive edge of this signal.

6.3.2 Winch controller design

The winch controller as shown in the block digram 6.16 has seven inputs: First, the high and low tether force F_h and F_l (the set values of the tether forces, determining when the force control shall be activated[4]), and the set speed v_{set}. The second set of inputs are the actual (measured) tether force F_t and the reel-out speed v_{ro}. Finally a boolean input INT_LOW, that is active in the lower intermediate phase of the power cycle, and an input for the constant k_v. If v_{set} is NaN, then v_{set}'''' is calculated according to Eq. 6.25.

$$v_{set}'''' = k_v \sqrt{F_t} \tag{6.25}$$

The only output needed to control the winch is the set speed of the motor controller v_{set}'''. The basic operation is explained in Fig. 6.17. The velocities $v_{t,h}$ and $v_{t,l}$ that are needed for terminating the states lower force control (F_LOW_CTRL) and upper force control (F_HIGH_CTRL) are calculated according to Eqs. 6.26 and 6.27:

$$v_{t,l} = 1.1\ k_v \sqrt{F_l} \tag{6.26}$$

$$v_{t,h} = 0.9\ k_v \sqrt{F_h} \tag{6.27}$$

The constant factors 0.9 and 1.1 are added to achieve a hysteresis of 10% for activating and deactivating the force controllers to avoid oscillations due to noise. For 10 % wind turbulence intensity a hysteresis of 10 % is a good choice. Increasing the hysteresis decreases the average power output, but luckily this effect is weak. On the other hand

[4] This is not the same as the maximal and minimal tether force due to the overshoot of the force controller.

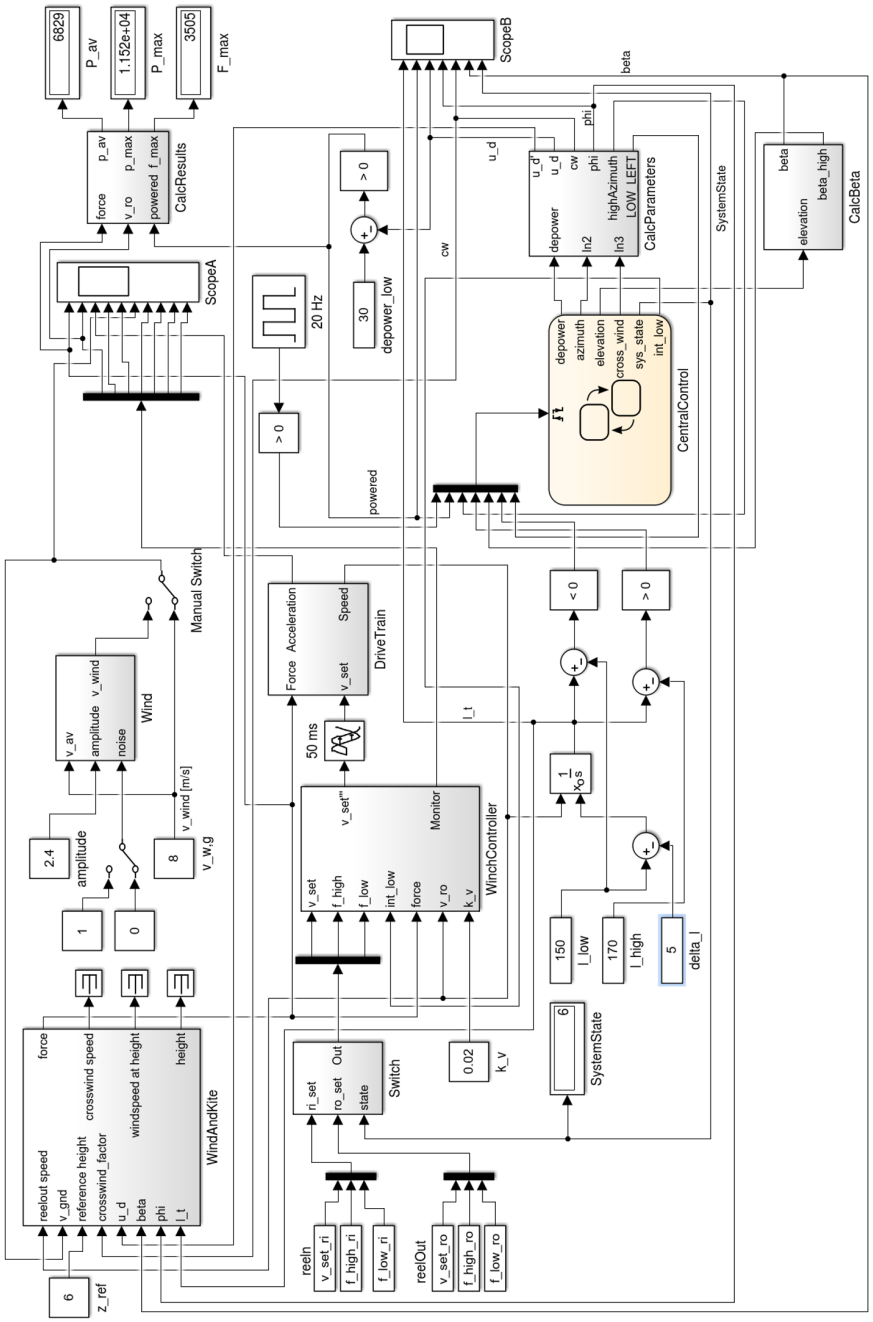

Figure 6.14: *Block diagram, showing the simplified system model, used for the development of the winch controller.*

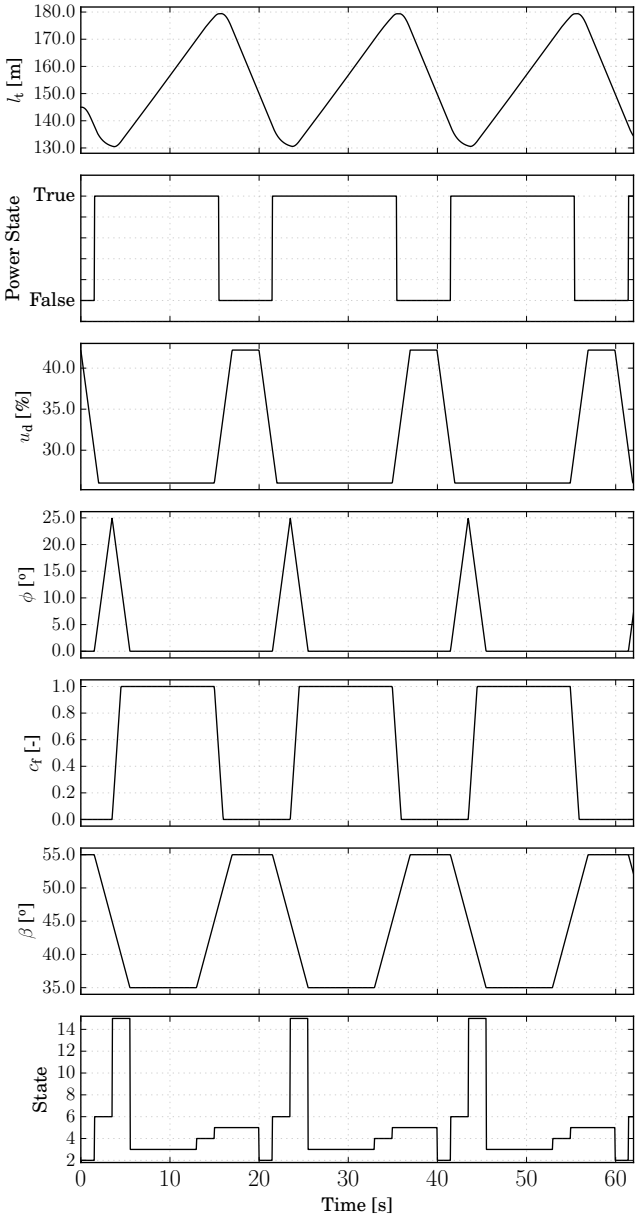

Figure 6.15: *Tether length and simulation control parameters of the simplified simulation at 8 m/s wind speed at 6 m height. The states are: ssPower (2), ssIntermediate (6), ssLowLeft (15), ssKiteReelOut (3), ssWaitUntil (4) and ssDepower (5) as defined in Tab. 6.1. The small difference between the maximum and minimum tether length is only choosen to show the intermediate phases in more detail.*

increasing the hysteresis improves the stability and testability of the controller, because switching between different modes of operation happens less often.

The controller has the following features, not present in previous designs (Schreuder 2013a):

1. Different controllers are used for the control of the upper and lower tether force;
2. if the force limits are inactive, then the set value of the reel-out speed is calculated to be proportional to the square root of the force as suggested by Fechner and Schmehl 2012b;
3. a PI speed controller is added to ensure stable speed control even in the presence of high control loop delays;
4. during reel-in and reel-out different values for F_{low} are used: A low value during reel-out, to avoid that the kite is reeled in during the reel-out phase at low wind speeds; and a high value during reel-in to ensure that the maximum reel-in speed is reached fast. This improves the duty cycle "D" and thus the total efficiency η_{tot};
5. for the transition between reel-in and reel-out, an optimized set force transient according to Eqs. 6.28 and 6.29 is used to avoid the force overshoot that is happening otherwise. The time t_t is the time of the transition from F_LOW_CTRL to F_HIGH_CTRL in the lower intermediate phase (see: Fig. 6.17).

$$F_{\text{set,INT_LOW}} = \begin{cases} F_{\text{low,ri}} & \text{if } s_{\text{w}} = \text{F_LOW_CTRL} \\ F_{\text{low,ri}} + (F_{\text{high,ro}} - F_{\text{low,ri}})(g(t - t_{\text{t}})) & \text{if } s_{\text{w}} = \text{F_HIGH_CTRL} \end{cases} \tag{6.28}$$

$$g(t - t_{\text{t}}) \;=\; 1 - \left(\min\left(\frac{t - t_{\text{t}}}{2}, 1 \right) \right)^2 \tag{6.29}$$

6.3.3 Performance of the WC

In Fig. 6.18 the changes to the set force F_{set} over the full power cycle are shown. The set force during reel-in is about 37.5 % of F_{max} to allow a fast transition from reel-out to reel-in. At the end of the reel-in phase the set force is reduced to 7.5 % of F_{max} to

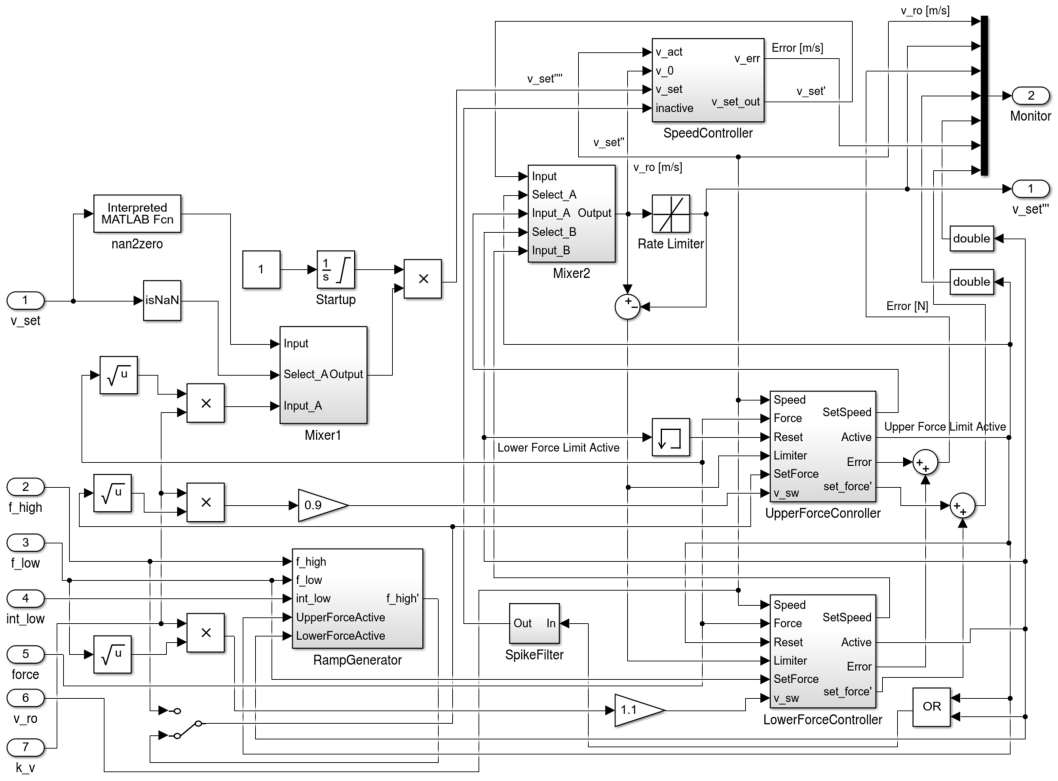

Figure 6.16: *Block diagram, showing the implementation of the winch controller. Three PID controllers, the speed controller, the upper and the lower force controller are used. One of them is active at one point in time. If no force limit is active, then the set speed is calculated proportional to the square root of the force. The mixer block no. two merges the set speed values from the three sources normal operation, upper force controller and lower force controller. Mixer one is used to switch between automatic and manual operation.*

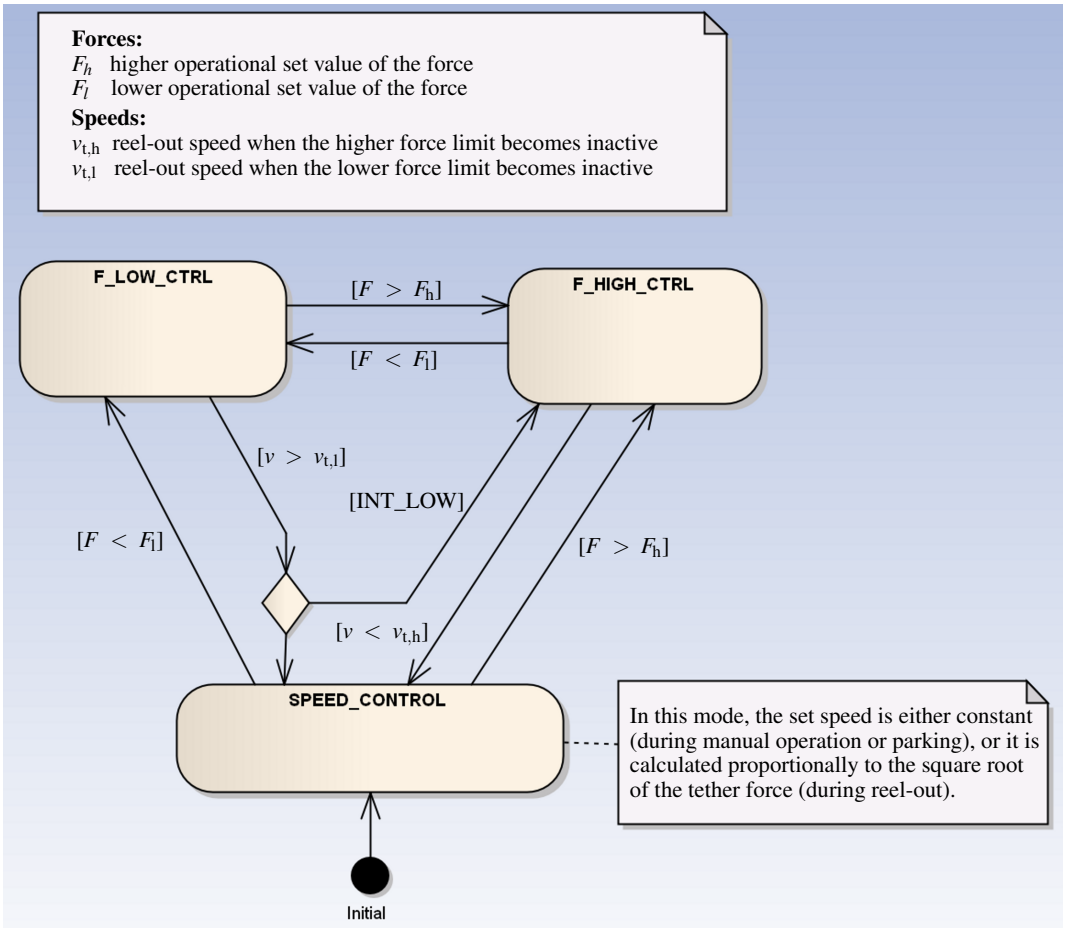

Figure 6.17: *Finite state diagram, explaining the states of the low-level winch controller. It is operating in the state SPEED_CONTROL or in one of two force control states, one for controlling the higher force limit F_h and one for keeping the lower force limit F_l. When the SPEED_CONTROL is active, either a fixed speed value, or a value, that is proportional to the square-root of the tether force is used as set value for the reel-out speed.*

slow down the reel-in speed to about zero. Then the set force is increased gradually from $F_{\text{low,ri}}$ to $F_{\text{high,ro}}$ to avoid any force overshoot. During the transition from reel-out to reel-in the set force is zero for a short period of time. In this situation the speed controller is active.

In Fig. 6.19 it is shown what happens if there is no smooth slope of the set force during the transition from reel-in to reel-out: This results in a force overshoot of about 36%. The transition, using the quadratic function Eq. 6.29 gives the best results with respect to the force overshoot and the settling time if compared to linear or exponential transition functions.

Three diagrams, Fig. 6.20, 6.21 and 6.22 show kind of "normal" operation scenarios at low (3 m/s), medium (5 m/s) and high (8 m/s) ground wind speed and a medium level of wind speed fluctuations.

Fig. 6.23 shows an extreme scenario and is used to verify the performance and stability of the winch controller: The wind speed is varied between 0 and 9 m/s at 6 m height with a period time of 8 s.

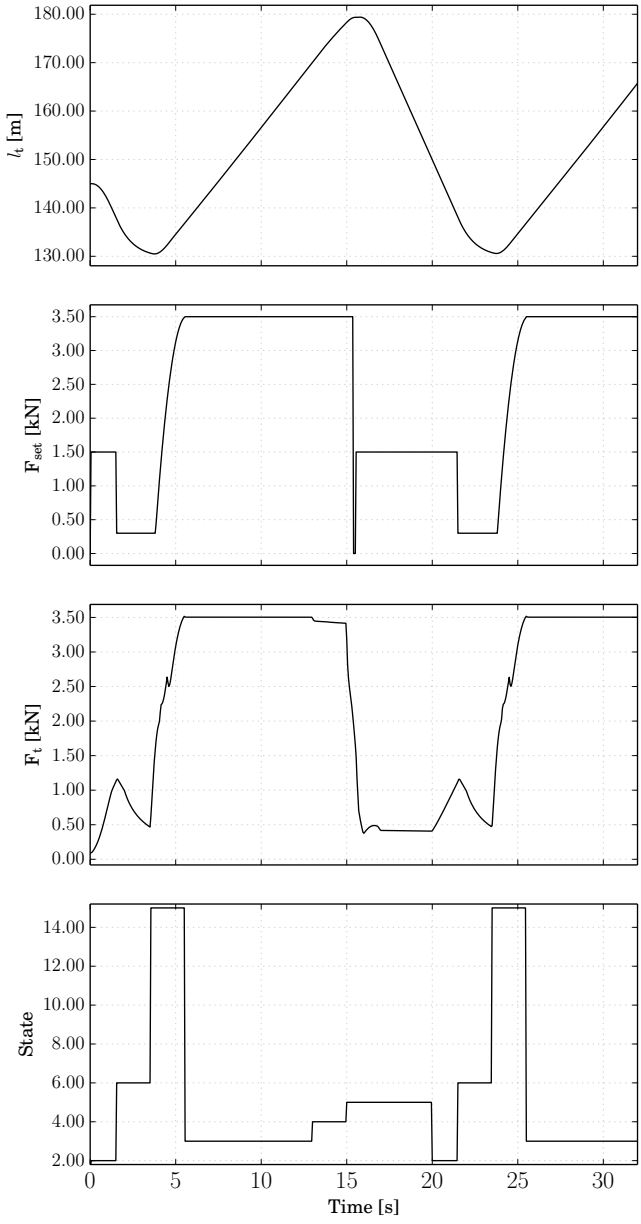

Figure 6.18: *Tether length, set force, actual force and the control state of the simplified simulation model at 8 m/s wind speed in 6 m height. The states are: ssPower (2), ssIntermediate (6), ssLowLeft (15), ssKiteReelOut (3), ssWaitUntil (4) and ssDepower (5) as defined in Tab. 6.1. The small difference between the maximal and minimal tether length is only choosen to show the intermediate phases in more detail.*

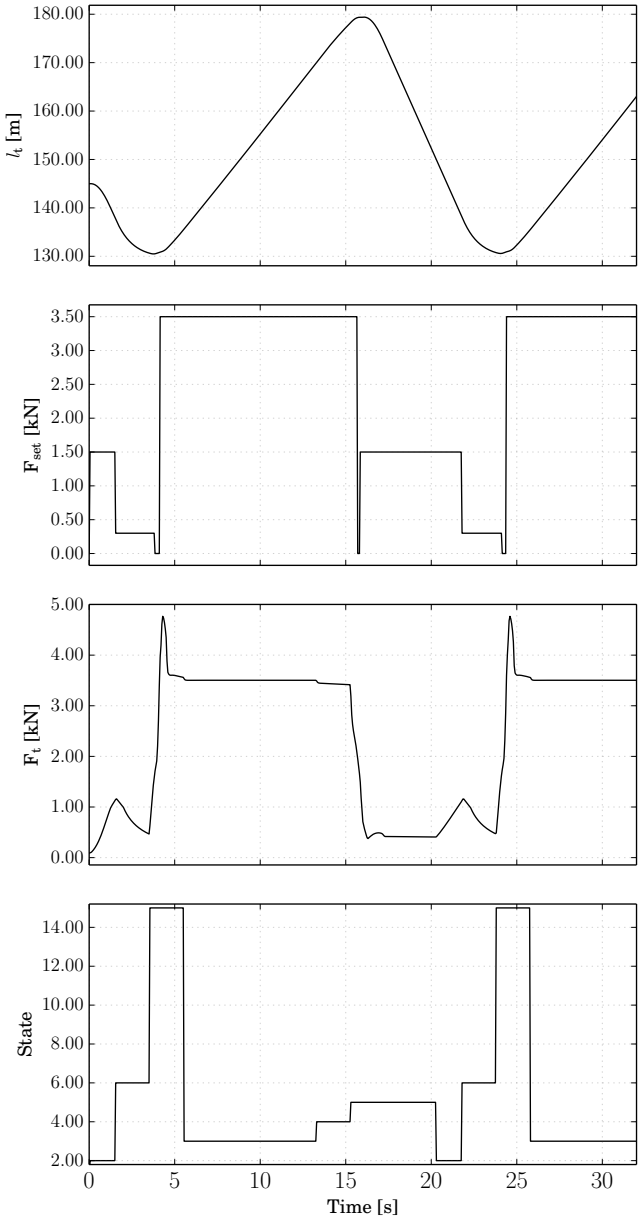

Figure 6.19: *Tether length, set force, actual force and the control state of the simplified simulation without a smooth set value generation at 8 m/s wind speed in 6 m height. Without a smooth slope of the set force during at the beginning of the reel-out phase there is a high force overshoot of about 36%.*

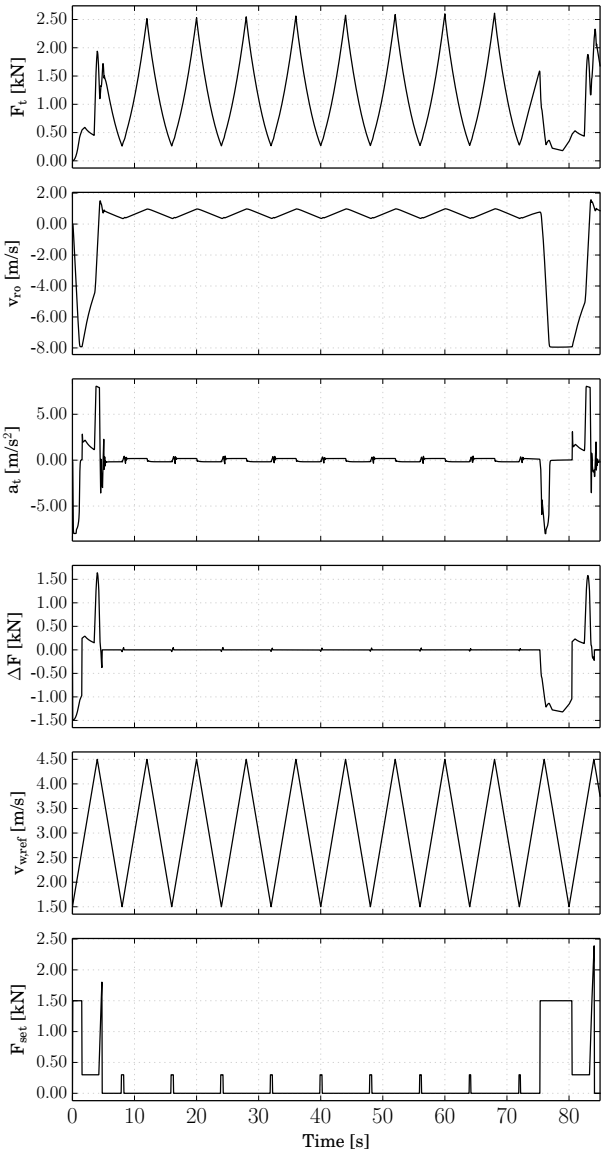

Figure 6.20: *Actual force F_t, reel-out speed v_{ro}, acceleration a, force error ΔF, wind speed $v_{w,ref}$ and set force F_{set} according the simplified simulation for $v_{w,ref} = 3 \pm 1.5$ m/s at 6 m height. A value of $F_{set} = 0$ means: speed control is active. The reel-out speed is proportional to the wind speed, the force proportional to the square of the wind speed.*

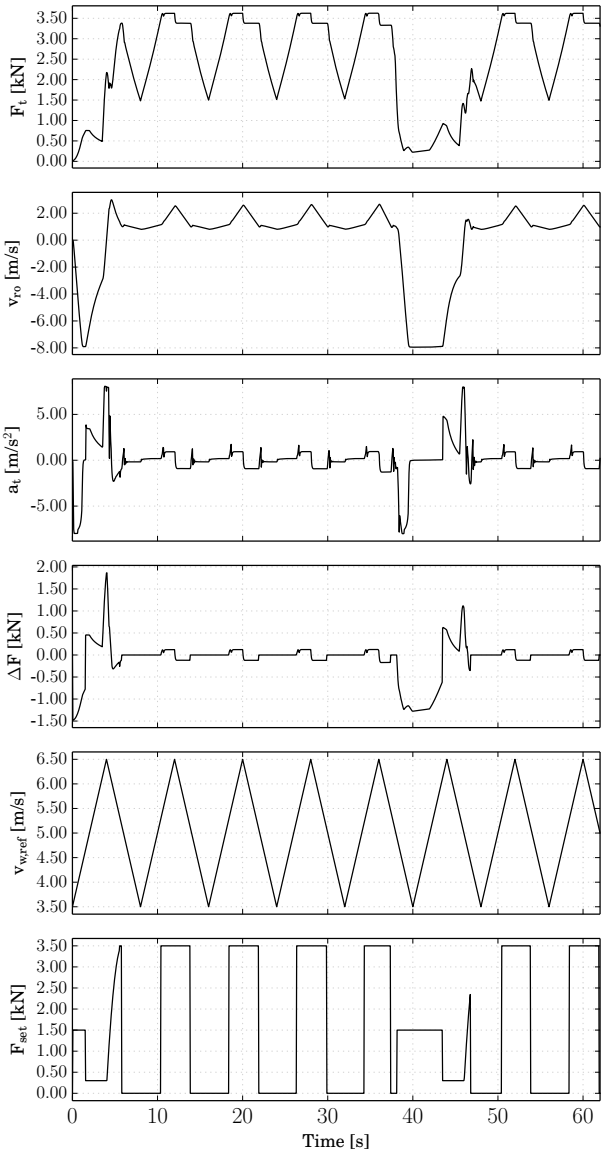

Figure 6.21: *Actual force F_t, reel-out speed v_{ro}, acceleration a, force error ΔF, wind speed $v_{w,ref}$ and set force F_{set} according the simplified simulation for $v_{w,ref} = 5 \pm 2.4$ m/s at 6 m height. A value of $F_{set} = 0$ means, that speed control is active. The upper force limit becomes active at wind speeds of about 5.25 m/s. The force error during the reel-out phase is less than ± 170 N.*

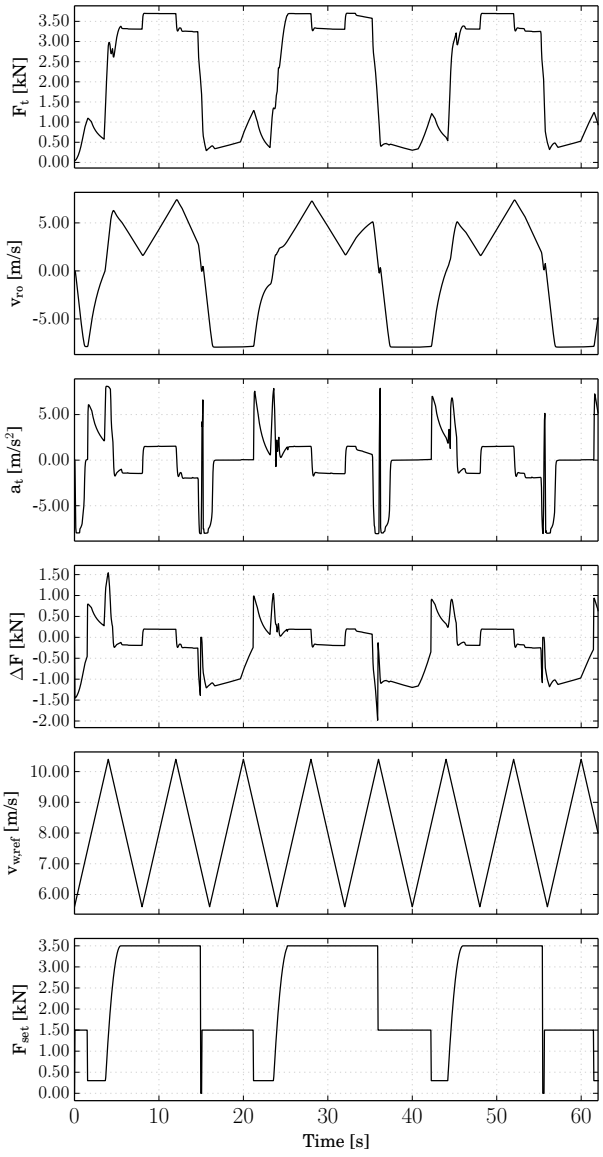

Figure 6.22: *Actual force F_t, reel-out speed v_{ro}, acceleration a, force error ΔF, wind speed $v_{w,ref}$ and set force F_{set} for $v_{w,ref} = 5 \pm 2.4$ m/s at 6 m height. A value of $F_{set} = 0$ means, that speed control is active. The upper force limit is constantly active during reel-out. The force error during the reel-out phase is less then ± 230 N. The quadratic slope of the set force is perfectly avoiding a force overshoot in the second cycle, while slightly overcompensating the force overshoot during the first and last cycle.*

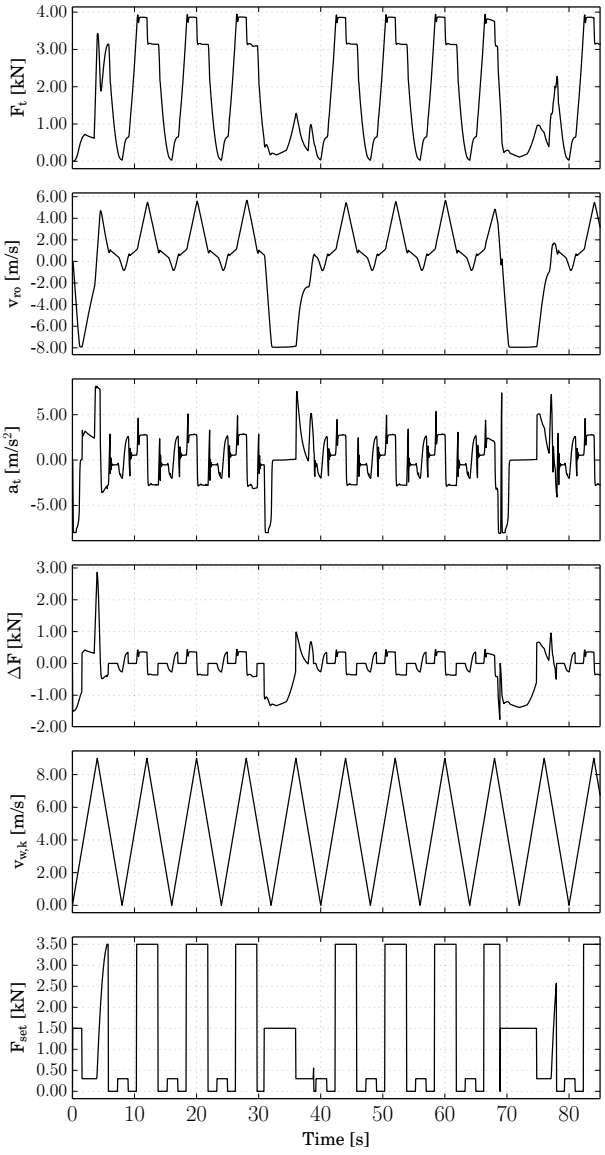

Figure 6.23: *Actual, simulated force F_t, reel-out speed v_{ro}, acceleration a, force error ΔF, wind speed $v_{w,ref}$ and set force F_{set} for $v_{w,ref} = 4.5 \pm 4.5$ m/s at 6 m height. A value of $F_{set} = 0$ means, that speed control is active. Upper force control, lower force control and speed control are all used during reel-out. This is an extreme scenario to verify the stability and performance of the winch controller. The force overshoot above $F_h = 3500$ N is less than 440 N, the force undershoot below $F_l = 300$ N is less than 270 N.*

Influence of the force control loop delay

Simulation results for a force control loop delay of 50 ms are shown in Fig. 6.23. Simulation results for a force control loop delay of 20 ms and 150 ms are shown in Fig. 6.24 and Fig. 6.25. In all scenarios the PID controllers were optimized to minimize any force overshoot.

The parameters of the three scenarios are shown in Tab. 6.2. It can be seen, that with 20 ms delay a good robustness and performance can be achieved. With 50 ms delay the performance is less good, the average reel-out force has to be reduced by less than 12.5% compared to an ideal controller. A delay of 150 ms, as it is currently present in the ground station of the kite-power demonstrator of TU Delft causes a large performance decrease. It is necessary to reduce the average reel-out force to about 3200 N to avoid that the design limit of 4000 N is exceeded. This is a reduction of 20 %, compared to a system with an ideal controller.

These results are specific for the the 20 kW winch of the TU Delft KPS demonstrator. The kite properties are not relevant, because the simulation model does not take them into account. Further research is needed to generalize these results for winches with different properties (maximum acceleration, inertia).

Reasons for force control loop delays

The question arises: What are the reasons for the control loop delays? Can they be avoided?

There are three main reasons for these delays: First, the force sensor amplifier. Second, the digital control system and third, the controller of the motor/ generator.

The delay of the filter of the currently used load cell amplifier is about 60 ms. The author assumes that this delay could be reduced to 20 ms without increasing the noise level in an unacceptable way, because three times of the current noise level (0.25 %) would be acceptable and should allow the use of a much faster filter. The delay of the digital control system (currently about 80 ms) could be reduced to 1 to 5 ms by replacing the current PLC and C#/ Windows based control system by a fast, real-time capable implementation, for example by using C++ and the OROCOS control framework.

The problem, that remains is the motor controller itself: PWM based motor controllers can have a dynamic torque response time as high as 150 ms (Harvest Ltd. 2016). With modern drives, using closed loop vector control it is possible to achieve response

Table 6.2: *Parameters of the low level winch controller for different force control loop delays. K_v is the anti-windup feedback factor for the set speed, used by the force controllers. The lower force controller has the integrator constant I_l.*

Loop delay	P	I	I_l	D	K_v	ΔF [N]	F_l [N]	F_h [N]
20 ms	1.99e-4	1.5e-2	1.5e-2	1.0e-6	3214	< 200	300	3800
50 ms	1.44e-4	7.5e-3	7.5e-3	3.0e-6	2309	< 500	300	3500
150 ms	1.56e-4	3.8e-3	1.14e-2	7.5e-6	3078	< 800	400	3200

times as low as 10 ms (EcoDriveCN 2016). As long as an asynchronous motor/ generator is used, Direct Torque Control (DTC) can be an even better solution: Motor controllers with a torque control delay of less than 5 ms are commercially available (ABB 2011). In theory, DTC can also be used with synchronous machines (which are the preferred choice for this application because of the higher efficiency). In practice, to the best of the authors knowledge currently no motor controllers are commercially available, that implement DTC for electrically excited synchronous machines.

In the past, electrical machines and their controllers were only optimized either for fast control, or for high efficiency. For this application a combination of motor/generator and motor controller (bidirectional DC/AC converter) is needed, that is fast and efficient at the same time. Further research is needed to achieve this goal.

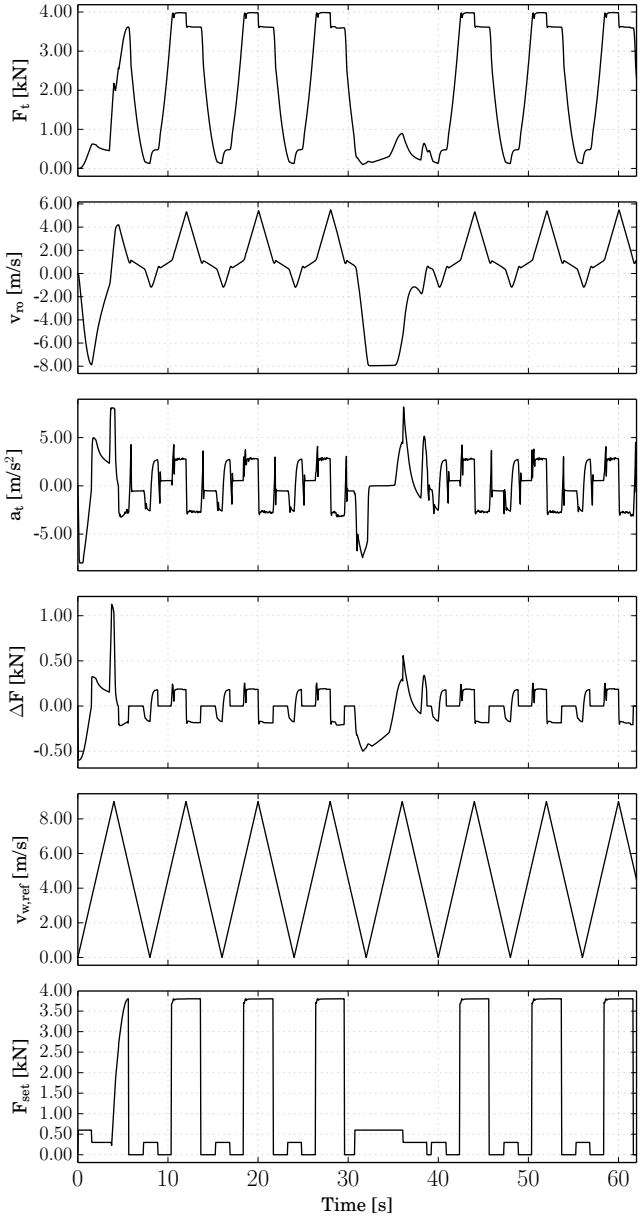

Figure 6.24: *Plots, showing the performance of the winch controller, if a force control loop with a delay of 20 ms is used. The error of the force controller ΔF during the reel-out phase as shown in the 4th diagram stays below ± 200 N, which is ± 5 % of the maximum force.*

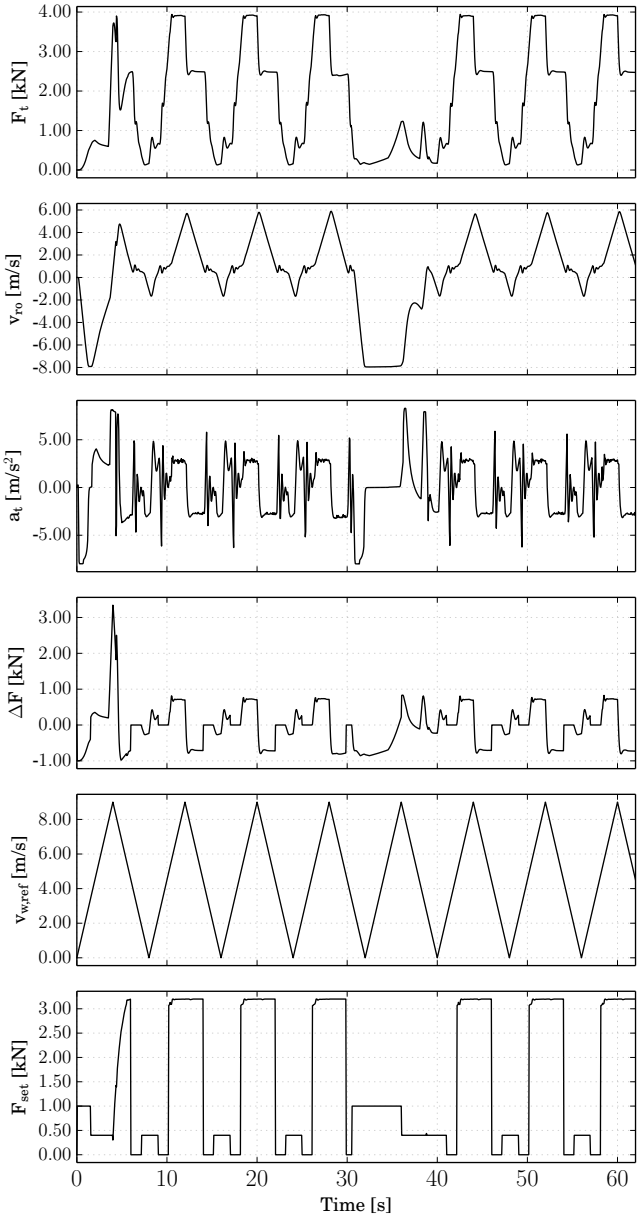

Figure 6.25: *Plots, showing the performance of the winch controller, if a force control loop with a delay of 150 ms is used. The error of the force controller ΔF during reel-out as shown in the 4th diagram is below ± 800 N, which is ± 20 % of the maximum force.*

6.4 Implemented distributed control system

A version, using the simple FPC as explained in 6.2.2 was implemented for the kite power demonstrator of Delft University and tested in Massvlakte 2, The Netherlands as described in (Fechner and Schmehl 2012a).

The more advanced controllers as described in this chapter were also implemented and tested, but only against the detailed system model as described in Chap. 4.

6.4.1 Detailed control structure

In Fig. 6.26 the resulting, detailed control structure is shown. On the right hand side the software components that provide the sensor data from the kite and the ground are shown. In principle only the position, velocity and orientation of the kite; the position of the lower end of the tether (the groundstation) and wind speed and direction are needed. From this data the block SystemStateEstimator calculates the coordinates of the kite in the small earth reference frame (elevation and azimuth) and the heading of the kite.

The HighLevelControl block at the top left controls the main state of the system as shown in Fig. 5.8. It switches between the states POWER, INT_LOW (lower intermediate phase), FIG_8, INT_UP (upper intermediate phase) and DEPOWER. Depending on the main state, the block FlightPathPlanner generates the attractor points (targetElevation and targetAzimuth) and the set value of the turn rate for the turn actions. Both are needed by the FlightPathController.

The FlightPathController (FPC) calculates the course and/or the heading, needed to fly towards the given attractor point using the great circle navigation procedure, as explained by Baayen and Ockels (2012) and Veness (1999). In the simplest case a parameter varying PI controller is used with the bearing (desired heading) as set point and the measured heading as actual value. The output of this LPV controller is then used as steering input for the kite. The simplest FPC is using only the depower setting u_d to vary the PID parameters.

More advanced FPCs as explained in Sec. 6.2.3 also uses the current position of the kite in the wind window and the apparent wind velocity to linearise the plant with nonlinear, dynamic inversion. The most advanced controller (Sec. 6.2.4) is not only controlling the heading of the kite, but also the course.

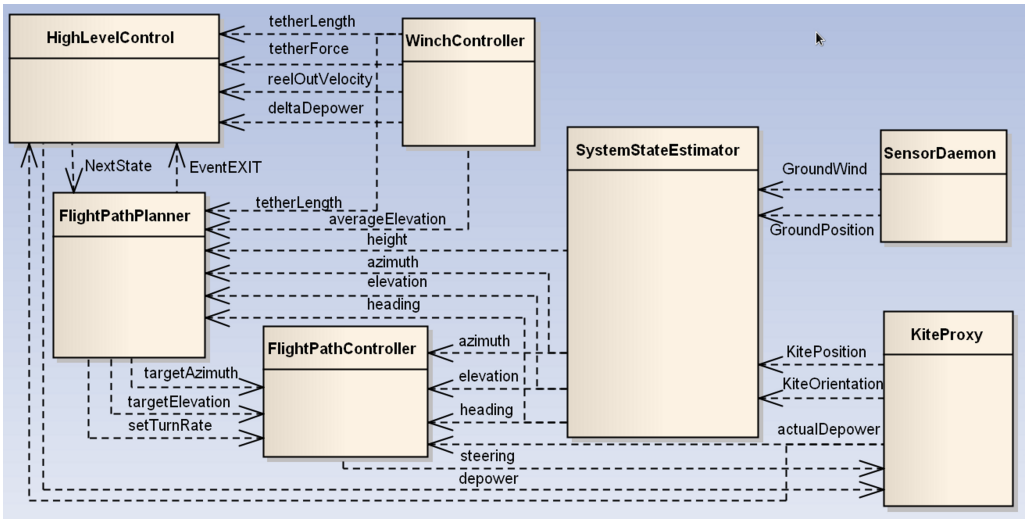

Figure 6.26: *Detailed control structure*

6.4.2 Adapting to changing wind conditions

Adapting to changing wind conditions is mainly achieved by the winch controller (WC): First, the reel-out speed is controlled to be proportional to the square root of the tether force. In this way the reel-out power is optimized for low to medium wind speeds. For high wind speeds the tether force and the generator power must be limited.

The main mechanism to limit the tether force is the upper force controller of the WC. This is the fastest way to limit the tether force, if a soft kite with a KCU is used: For the kite power demonstrator of Delft University of Technology the time, to increase the reel-out speed from 30% to 100% of the maximum value is about 0.7 s. The time, to depower the kite from 0% to 70% is about 2 s, so about three times slower.

Two approaches are used to limit the maximal reel-out power: First, by changing the average elevation angle, second, by sending a value of $\Delta u_\mathrm{d} > 0$ to the high level controller. Pre-optimized values for the average elevation angle and the depower settings are used, based on the estimated wind speed, the estimated wind profile coefficient and the estimated turbulence intensity. These values are obtained by running the simulation against the detailed system model as described in Chap. 4, extended with the turbulence model as described in Sec. 5.2.3.

In addition, the actual (measured or estimated) mechanical power P_m is compared

with a desired upper value P_{up}. If $P_m > P_{up}$, then the depower settings of the kite are increased until the desired limit is reached again.

For the reel-in phase the winch controller is operated in force control mode. The set force uses pre-optimized values, depending on the estimated wind speed at the average height of the kite.

6.4.3 Distributed control

Distributed control systems use sensors and actuators at different places, that are part of at least one critical control loop and usually connected via a wireless link. When designing the control algorithm the properties of this link (latency, packet losses) have to be taken into account. Using distributed control is necessary for the implementation of a reliable kite power control system mainly because using a GNSS turned out not to be sufficient to determine the position of the kite reliably (Fechner and Schmehl 2012a; Peschel 2013; Ranneberg 2013). GNSS sensors can fail for a lot of different reasons (Lu et al. 2015). Therefore for commercial kite power systems at least an additional position sensor is needed, for example angular sensors that measure the elevation and azimuth angles directly at the place where the tether is leaving the winch. There are additional reasons why a distributed control system with the controller at the ground has big advantages: Test and development of new controllers on a desktop computer is much easier and faster than doing the same thing on an embedded computer attached to the kite. And for implementing and testing of computational intensive control algorithms like "non-linear model predictive control" it is a big advantage if a powerful but heavy control computer at the ground can be used.

6.5 Summary and conclusion

In this chapter a the control methodology for the design of kite power control systems is presented:

First, simplified 2D models are developed, one for the winch and one for the kite that capture the main, physical characteristics of the sub-systems. Then the control algorithms are implemented in Simulink and tested against the simplified models.

It is shown, that both the flight-path controller (FPC) and the winch controller (WC) are stable even in the presence of large changes of the wind speed, sensor errors and sys-

tem delays. The FPC works sufficiently well with system delays of up to 200 ms. The WC has the best performance with force control loop delays of not more than 20 ms. Stable operation is shown for delays up to 150 ms to the cost of significant overall performance degradation.

Finally the controllers are integrated with the dynamic 3D model as described in Chap. 4. In this step the controller parameters have to be adapted and the switch conditions of the flight path planner have to be extended and modified to achieve the desired accuracy and performance.

For a seamless integration it is necessary to convert the simplified models and the controllers to Python, using the same structure and the same building blocks as in Simulink. As an example, the code of the FPC is shown in Appendix A. This is needed for (soft) real-time control, but also useful because the algorithms and the solvers that are used can be controlled in more detail. A much better understanding of the different ways to handle algebraic loops and to migrate from continues to discrete control is gained in this step.

The question might arise, if the findings of this chapter are applicable not only to the analysed 20 kW system, but also to larger or different type of kite power systems. The design methodology as described in Appendix B is generally applicable, while the numerical values are not. The numerical values depend on a lot of factors: The type of the electrical machine (asynchronous, synchronous PM, synchronous electrically excited), the presence and properties of a gearbox, the drum diameter and inertia, the properties of the actuator, that is changing the angle of attack of the wing and finally the size and the aerodynamic properties of the wing. There might be systems, where the force control speed of the winch is of secondary importance, because the force can already be limited effectively just by changing the angle of attack of the wing.

In the next chapter the designed controllers will be tuned and validated against the dynamic model in a realistic wind environment.

CHAPTER 7

Simulation Results

Contents

7.1 Introduction 159
7.2 System properties and environmental conditions 160
7.3 Adaptations during model and controller integration 161
7.3.1 Adding a model of the Kite Control Unit (KCU) 161
7.3.2 Adapting the flight path planner (FPP) 161
7.3.3 Adapting the controllers 161
7.4 Results 162
7.4.1 Results for average wind speed 162
7.4.2 Results for nominal wind speed 162
7.4.3 Results for high wind speed and high elevation angle 166
7.4.4 Results for high wind speed and high depower settings 169
7.4.5 Optimization results 172
7.4.6 Robustness against high turbulence 174
7.4.7 Comparison with experimental data 179
7.4.8 Power curve and capacity factor 180
7.5 Summary and conclusion 182

7.1 Introduction

In the last chapters the flight path planner and the controllers were developed and presented. The focus of this chapter is to demonstrate the results of complete system, integrating all components in the dynamic 3D simulator within a turbulent wind field. The main results of this chapter are presented in Fechner and Schmehl (2016b).

Table 7.1: *Properties of the HYDRA-20 kite, KCU, Winch and tether.*

Kite	
Projected wing surface area A [m^2]	20.36
Mass including sensors m_k [kg]	10.58
Width w_k [m]	8.16
Height h_k [m]	3.15
Relative side area A_side/A [%]	30.6
Kite Control Unit	
Mass m_KCU [kg]	11.0
Winch	
Max. force F_max [N]	8000.0
Main Tether	
Diameter d_t [mm]	6.0
Mass per m [kg/m]	0.013
Unit damping coefficient c_0 [Ns]	473
Unit spring constant k_0 [N]	614600

7.2 System properties and environmental conditions

The system as described in Chap. 4 was used as starting point, but it was up-scaled to achieve a capacity factor of about 40 % at the onshore location Cabau. The nominal generator power of 20 kW was not changed, but the size of the kite and the maximal tether force are increased by a factor of two. Details are given in Tab. 7.1.

The flight of the kite is simulated in a turbulent, 3D wind field. The conditions of the onshore location Cabauw, The Netherlands are used as reference. Three different wind conditions are investigated: 4.26 m/s, 6.0 m/s and 9.2 m/s at 10 m height. The turbulence intensities at the average reel out height of 197 m are 6.3 %, 7.2 % and 7.9 % respectively. For further details see Sec. 5.2.3.

7.3 Adaptations during model and controller integration

The flight path and winch controller as explained so far were developed using simplified 2D models. After translating the Simulink controllers into Python and integrating them with the 3D system model it became obvious that some changes were needed, because the 3D model behaves significantly different. These changes are explained in this section.

7.3.1 Adding a model of the Kite Control Unit (KCU)

First of all, a KCU model was implemented, that is working in the same way as shown in Fig. 6.5. The KCU translates the set values for depower and steering into the length of the depower line and the line length difference of the steering lines. Both drive trains use a P controller as feed-back loop.

7.3.2 Adapting the flight path planner (FPP)

The elevation angle of P_2, but - only for the first figure of eight - also for P_3 and P_4 had to be adjusted to minimize the errors. For the attractor point P_2 an elevation offset of $-2.4°$ is needed, and during the first figure-of-eight for the attractor points P_3 an offset of $-2.4°$ and for P_4 an offset of $-2.0°$ (see: Fig. 5.7).

How to derive the optimal parameters of the flight path planner is subject for future research. If the current system model is used, the smallest value of w_{fig} gives the highest average power output. It is not clear though, if this matches reality, because the increase of drag while steering was not yet measured directly. As a good compromise between maximal power output and high robustness for sensor errors the value $w_{\text{fig}} = 36°$ was chosen, which is about four times the average turn radius. This ensures, that the time, that the kite is flying towards an attractor point on a straight line is about the same as the time for the turns, which means that half of the time feed back control is active. This ensures the capability of the controller to correct even large flight path errors and thus robustness.

7.3.3 Adapting the controllers

The winch controller is adapted in the following way:

- During the power phase and the lower transition phase (the states LOW_RIGHT, LOW_TURN and LOW_LEFT) force control is not used;
- instead, speed control is used in the power phase with a set value for the speed of zero.

The kite controller was adapted in the following way:

- When the kite is not flying crosswind, in particular when it is steering towards zenith, only the heading of the kite is controlled ($k_\chi = 0$).
- A common factor for the P, I and D blocks is introduced which is called gain μ. A value of $\mu = 0.04$ instead of $\mu = 0.16$ was determined to achieve stability and a good tracking performance. This change is needed, because in the simplified model the rotational inertia of the kite is not taken into account. To determine this value, first the gain was reduced until the control was stable. Then μ was modified until the maximal tracking error over the full cycle was less than one degree.

7.4 Results

7.4.1 Results for average wind speed

The 3D flight path of the kite, flying at average wind speed is shown in Fig. 7.1. In addition, at 2D diagram - height vs. ground distance - is shown. The influence of the turbulence is hardly visible.

In Fig. 7.2 the tether force at the ground station and the reel-out speed are shown, and in Fig. 7.3 the mechanical power vs. the reel-out speed. Force and power peaks appear at the beginning of the reel-out phase, but also at the end of each turn while flying figures of eight, because gravity is accelerating the kite. These peaks are not causing any problems because they are still far below from the system limits.

7.4.2 Results for nominal wind speed

The 3D flight path of the kite and its 2D projection is shown in Fig. 7.4 for the nominal wind speed. It is very similar to the flight path at average wind speed. The main difference is, that the kite is flying faster and the cycle time decreases from 201 s to 148 s. In

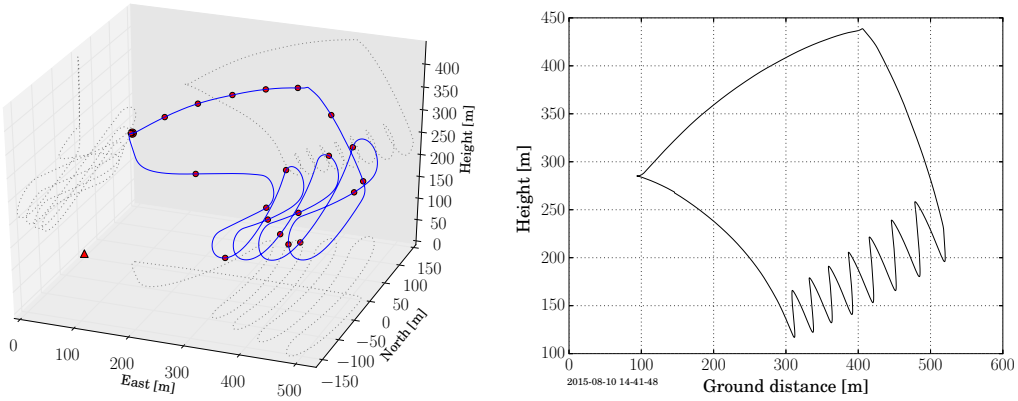

Figure 7.1: *Simulated flight path of the kite, flying at the average speed of 4.26 m/s at 10 m height. The simulation starts at the thick, red dot. Smaller dots are placed on the flight path in a 10 s interval. The position is shown relative to the ground station, which is marked with a red triangle.*

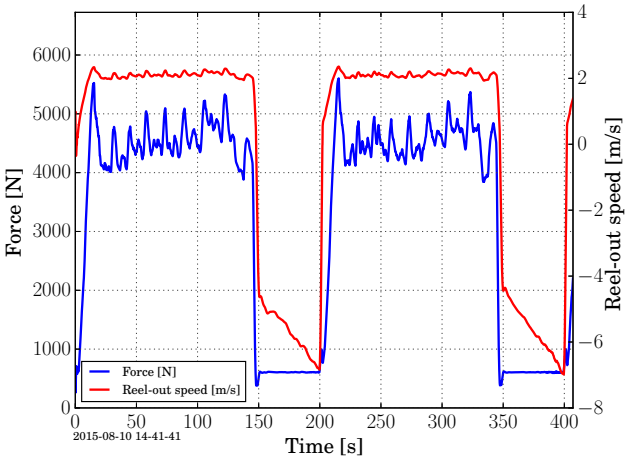

Figure 7.2: *Tether force at the ground and reel-out speed for two power cycles at the average wind speed of 4.26 m/s at 10 m height. The force is fluctuating due to flying figures of eight and due to the wind turbulence. The reel-out speed is fluctuating, too, but a lot less because the speed controller keeps the speed proportional to the square root of the force. During reel-in the speed is continuously increasing, because the elevation angle increases and it because more and more easy to reel in the kite.*

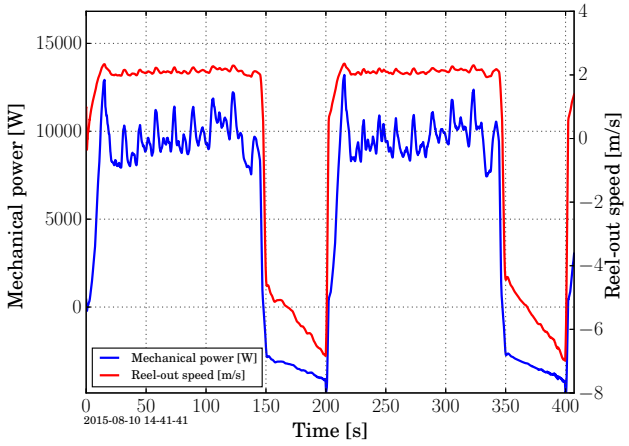

Figure 7.3: *Mechanical power and reel-out speed for two power cycles at the average wind speed of 4.26 m/s at 10 m height. The average reel-out power is about 9432 W, the average reel-in power -3405 W.*

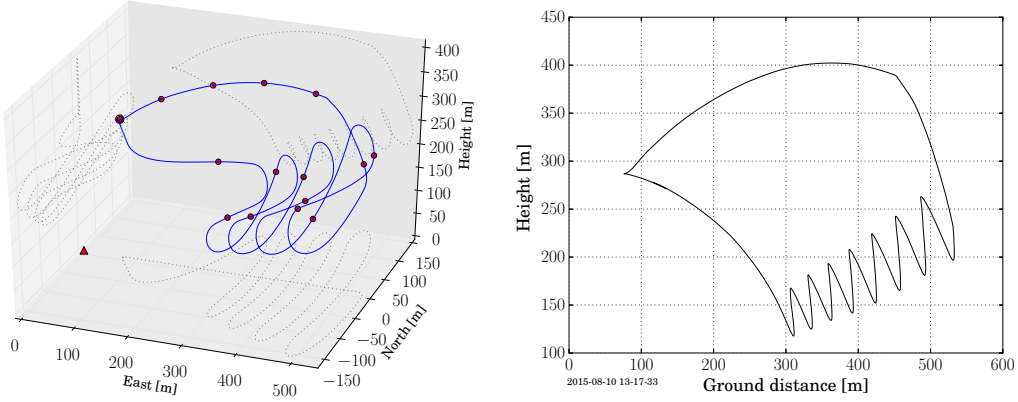

Figure 7.4: *Simulated flight path of the kite, flying at the nominal speed of 6.0 m/s at 10 m height. The simulation starts at the thick, red dot. Smaller dots are placed on the flight path in a 10 s interval. The position is shown relative to the ground station, which is marked with a red triangle.*

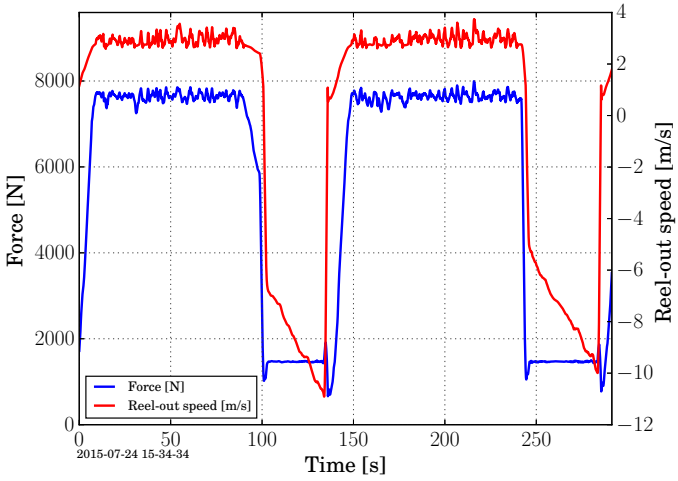

Figure 7.5: *Tether force at the ground and reel-out speed for two power cycles at the nominal wind speed of 6 m/s at 10 m height. The tether force is close to the maximal value of 8000 N. The reel-out speed is quite constant. Only when the force exceeds the value of 7600 N the upper force controller becomes active and the reel-out speed increases to limit the tether force.*

Fig. 7.5 the tether force at the ground station and the reel-out speed are shown, and in Fig. 7.6 the mechanical power vs. the reel-out speed. Any force peaks are mitigated by the winch controller, the power peaks limited to below 30 kW by controlling the depower settings.

In Fig. 7.7 the actual value of the relative steering of the kite and the height are shown. The largest steering signal is needed during the initial turn because at this point in time the apparent wind speed is still quite low. During reel-out the needed steering input is decreasing with the height because the turn radius is increasing. During the turns the steering input is quite high with an average value of about 20 % and peaks of about 40 %. When the kite is flying on a greater circle towards an attractor point, the steering is quite constant at a low level of about ± 2 % just compensating gravity.

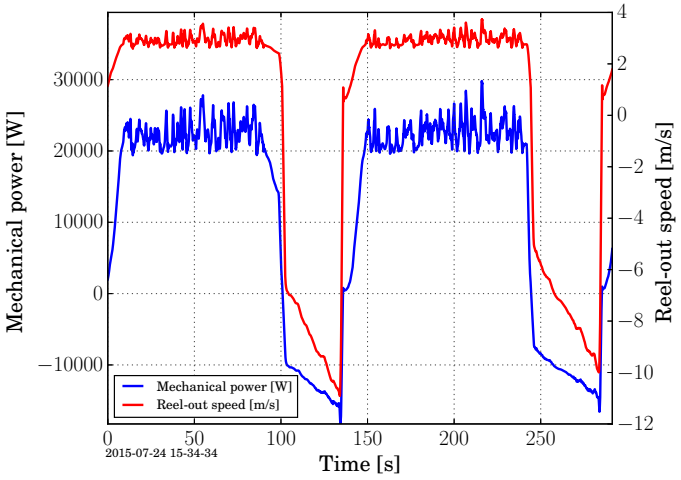

Figure 7.6: *Mechanical power and reel-out speed for two power cycles at the nominal wind speed of 6 m/s at 10 m height. The average reel-out power is about 21284 W, the average. The power needed for reeling in increases approx. linearly from 10000 W in the beginning to 15500 W at the end of the reel in phase.*

7.4.3 Results for high wind speed and high elevation angle

The 3D flight path of the kite at 9.2 m/s ground wind speed and its 2D projection are shown in Fig. 7.8. The average reel-out elevation angle has been increased to limit the maximal power. Reel-in and reel-out happen at nearly the same elevation angle. This is an advantage, because the lower intermediate state can be skipped.

In Fig. 7.9 the tether force at the ground station and the reel-out speed are shown, and in Fig. 7.10 the mechanical power vs. the reel-out speed. The average mechanical power over the full cycle is with 10.5 kW about 12 % lower than for the nominal wind speed. The main reason is the lower average reel-out force. The set value for the upper force has to be decreased, because the force variations are larger due to the increased crest factor at higher elevation angles (Fig. 5.15).

To achieve these results, a sophisticated control of the angle-of-attack is needed, as shown in Fig. 7.11. When the elevation angle was lower than the average elevation angle and thus the effective wind speed higher, then the depower settings where increased by $\Delta u_{\mathrm{d,h}}$. Furthermore, the depower settings were decreased when the power dropped below

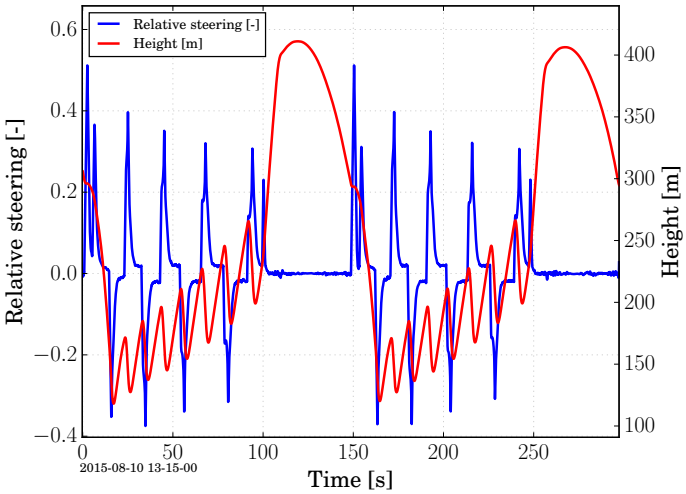

Figure 7.7: *Actual value of the relative steering and height for two power cycles at the nominal wind speed of 6 m/s at 10 m height. The largest steering signal is needed during the initial turn because at this point in time the apparent wind speed is still quite low. During reel-out the needed steering input is decreasing with the height because the turn radius is increasing.*

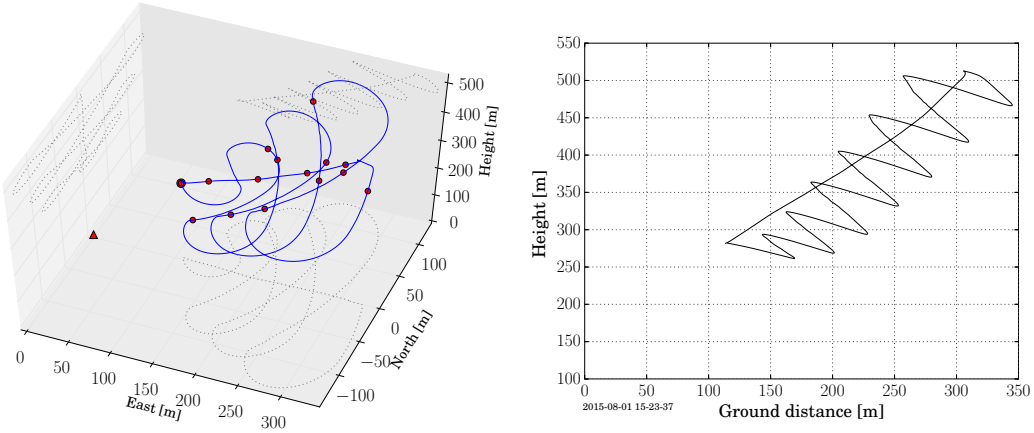

Figure 7.8: *Simulated flight path of the kite, flying at the high speed of 9.2 m/s at 10 m height. The kite is reeled out at about 58 ^{o} elevation angle to limit the maximal power to 30 kW. Reel-in and reel-out happen at about the same elevation angle, therefore the lower intermediate state can be skipped.*

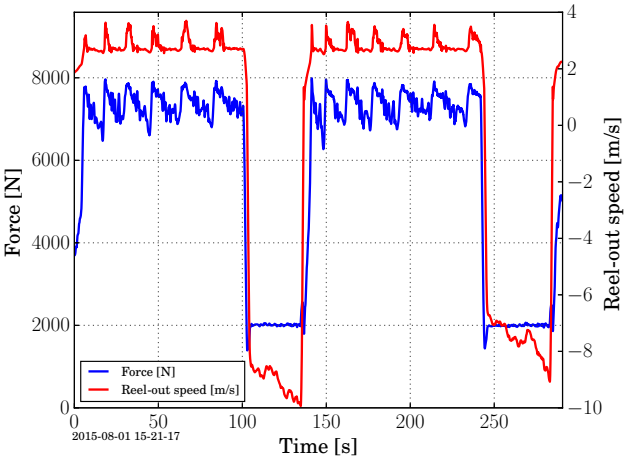

Figure 7.9: *Tether force at the ground and reel-out speed for two power cycles at the nominal wind speed of 9.2 m/s at 10 m height. The variations of the force and the reel-out speed are much higher than at lower wind speeds. The reason for this is, that the kite is flying at a high elevation angle and the effective wind speed is changing a lot during the figures of eight. Nevertheless the force and the power stay within the allowed limits.*

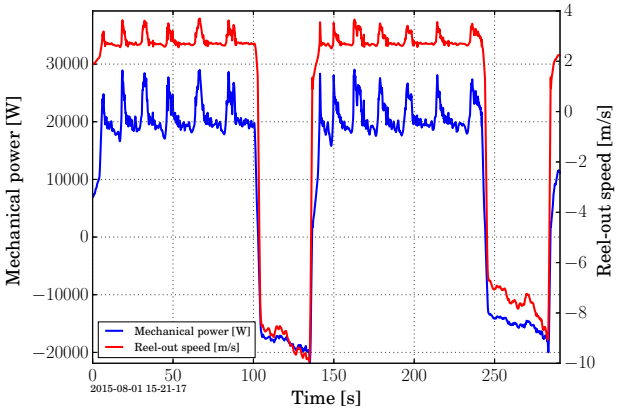

Figure 7.10: *Mechanical power and reel-out speed for two power cycles at the high wind speed of 9.2 m/s at 10 m height. The average reel-out power is about 20498 W, the average reel-in power 14381 W.*

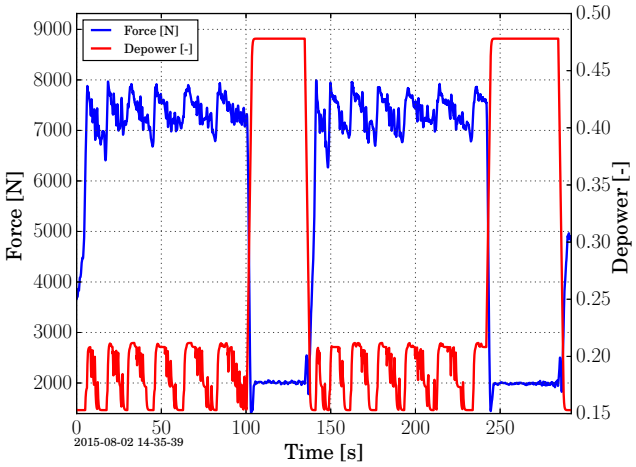

Figure 7.11: *Force and depower settings of the kite for two power cycles at the high wind speed of 9.2 m/s at 10 m height. The kite is reeled out at a heigh elevation angle which requires large changes of the depower settings to compensate the changes in the effective wind speed.*

20 kW. In this way the crest factor of the power could be decreased and the average power output increased. Disadvantage: The lifetime of the depower actuators decreases.

7.4.4 Results for high wind speed and high depower settings

The 3D flight path of the kite at 9.2 m/s ground wind speed and its 2D projection are shown in Fig. 7.12. The average reel-out elevation angle has been increased to limit the maximal power. Reel-in and reel-out occur at a very different elevation angle, therefore power production time is lost for the intermediate state. The cycle time increased to 170 *s* due to the slower reel-in phase.

In Fig. 7.13 the tether force at the ground station and the reel-out speed are shown, and Fig. 7.14 gives the mechanical power vs. the reel-out speed. The average mechanical power over the full cycle is 9.83 kW which is about 6.6 % lower than the results shown when reeling out at a high elevation angle, see Sec. 7.4.3

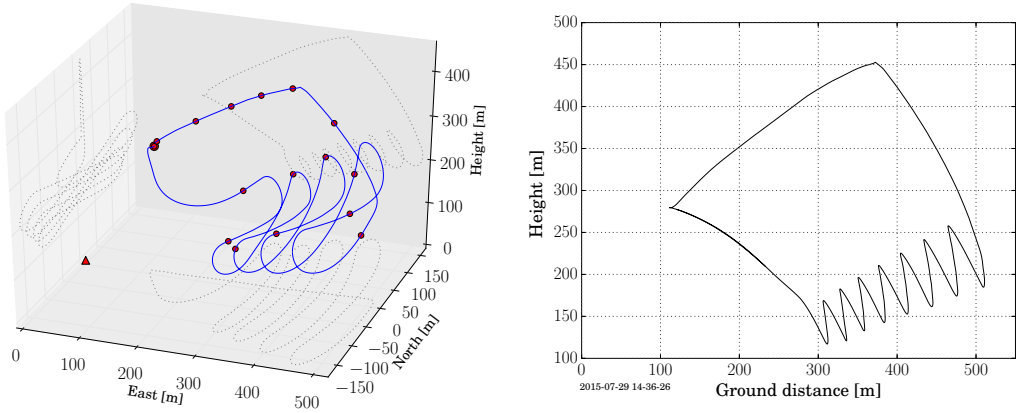

Figure 7.12: *Simulated flight path of the kite, flying at the high speed of 9.2 m/s at 10 m height. The kite is depowered to limit the power to 30 kW.*

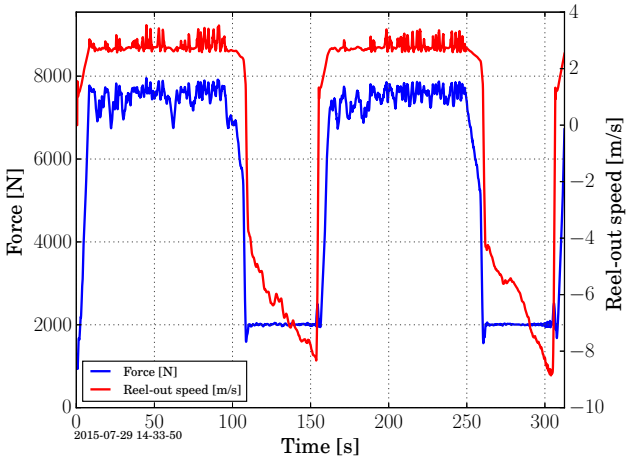

Figure 7.13: *Tether force at the ground and reel-out speed for two power cycles at the nominal wind speed of 9.2 m/s at 10 m height, using a high depower setting to limit the maximal power. The variations of the force and the reel-out speed are mainly due to the wind turbulence and not so much due to flying figures-of-eight.*

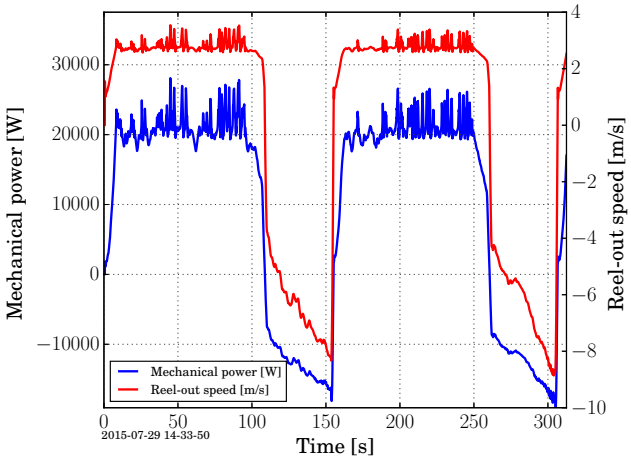

Figure 7.14: *Mechanical power and reel-out speed for two power cycles at the high wind speed of 9.2 m/s at 10 m height. The average reel-out power is about 19981 W, the average reel-in power 12937 W.*

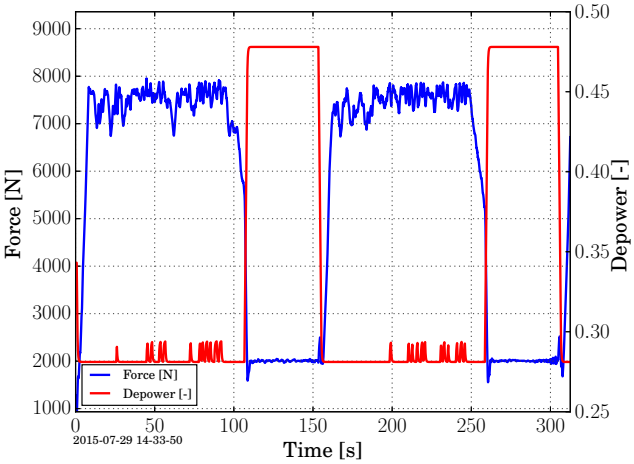

Figure 7.15: *Force and depower settings of the kite for two power cycles at the high wind speed of 9.2 m/s at 10 m height. The depower settings are increased, if the power exceeds 24500 W. The depower actuator is significantly less active than in Fig. 7.11.*

7.4.5 Optimization results

To obtain the results shown above, the following, manual optimization procedure is applied:

- For low wind speeds, the average elevation angle during reel-out, the parameter k_v of the reel-out speed controller and the reel-in force are varied until the local optima of the average mechanical power does not vary more than 2%.
- For medium wind speeds, in addition to the parameters mentioned above, the upper force F_{up} and the gain of the upper force controller are varied such the the maximal force is never exceeded, but also such that the maximal power stays below 150 % of the nominal generator power. By increasing this gain the crest factor of the force decreases, but the crest factor of the power increases. Therefore it is necessary to find a good compromise.
- For high wind speeds, in addition to changing the average elevation angle the depower settings are varied to reduce the crest factor of the power. This is shown in Fig. 7.11. The amount of the addition depower $\Delta u_{d,h}$ also has to be optimized.

For low and medium wind speed the parameters k_5 and k_6 of Eq. 5.25, for calculating the switch condition from reel-out to reel-in, are also optimized. The optimized values for the controlled parameters are shown in Tab. 7.2, furthermore the values for the optimized results.

Table 7.2: *Optimized parameters*

$v_{w,g}$	**4.26 m/s**	**6 m/s**	**9.2 m/s**
F_{ri} [N]	641.6	1478.8	2015.0
F_{up} [N]	7650.0	7650.0	7650.0
k_5 [°]	37.5	37.5	37.5
k_6 [-]	0.5	0.5	0.5
β_{set} [-]	24.0	24.0	54.7
$u_{d,h}$ [%]	0.0	0.0	2.0

Optimization results are shown in Tab. 7.3. The optimal set values for the maximal reel-in force $F_{ri,max}$ for a broader range of ground wind speeds are shown in Fig. 7.16.

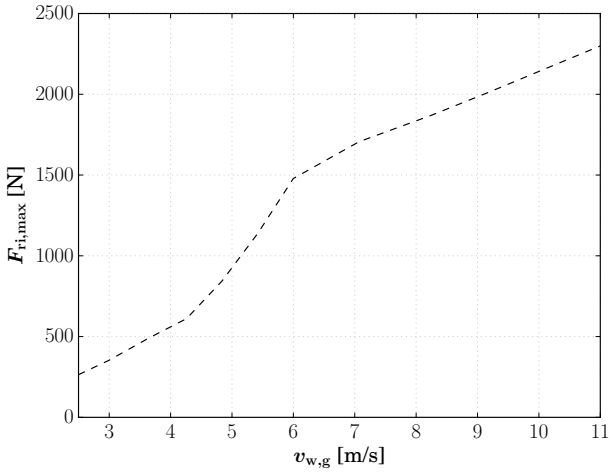

Figure 7.16: *Optimal set value of the maximal reel-in force as function of the ground wind speed at 10 m height. If the set value is too high, then the pumping efficiency is getting too low, if it is too low, then the duty cycle becomes too low. In between there is an optimum.*

The crest factor is the quotient of the maximal and the average value of a physical quantity. The crest factor for the force should be near one, because the costs increase more than proportional with the peak force. This is less critical for the power. A normal electric motor/ generator can handle 150% of it's nominal power for a short amount of time without problem.

The results show, that the performance of the system is very good for average wind speed (62.7% cycle efficiency), good for the nominal wind speed (58.3% cycle efficiency) and still reasonable well for high wind speeds (54.5% cycle efficiency and a crest factor for the reel-out power of 1.43).

Compared to the results of the averaged simulation without explicit turbulence in Tab. 3.3 the new results are about the same: 62.7% cycle efficiency instead of 61.7% and a crest factor of the reel-out force of 1.10 instead of 1.11. The reason is, that the effects of turbulence can be compensated by adapting the angle of attack via the depower settings.

It can already be concluded, that a turbulence intensity of 7.2% does not have a detrimental effect on the average power output, given a proper controller and an adequate control strategy.

Table 7.3: *Power, forces, crest factors and efficiencies*

$v_{w,g}$	**4.26 m/s**	**6 m/s**	**9.2 m/s**	**Description**
$P_{m,av}$ [W]	5677.0	11970.0	10523.0	average mechanical power
D [%]	72.7	72.7	73.0	duty cycle (Eq. 3.13)
η_p [%]	86.3	80.2	74.6	pumping efficiency (Eq. 3.16)
η_{cyc} [%]	62.7	58.3	54.5	cycle efficiency (Eq. 3.18)
$CF_{P,ro}$ [-]	1.40	1.49	1.43	crest factor reel-out power
$P_{max,ro}$ [-]	13206.0	29797.7	28685.1	maximal reel-out power
$CF_{F,ro}$ [-]	1.26	1.10	1.11	crest factor reel-out force
$F_{max,ro}$ [-]	5604.0	7995.8	7914.3	maximal reel-out force

7.4.6 Robustness against high turbulence

High levels of turbulence can cause different problems:

1. The force limit might be exceeded;
2. the power limit might be exceeded;
3. the angle of attack might drop below zero which can result in a collapse of the kite;
4. the angle of attack might become too high which can result in stall;
5. the force can became too low; in such situation the controllability of the kite is lost.

In the first test case that was analysed, the highest turbulence intensity was used that was recorded at projected ground wind speeds in the range of 5.5 to 6.5 m/s (average wind speed). The highest turbulence intensity for a 10 minute interval recorded in 2011 was 26.5%. Without any changes to the default controller settings this resulted in maximal force of about 8200 N (not a big problem) and a maximal power of about 44 kW. This would cause problems, because the currents on the DC link would exceed the design limits.

It is necessary to adapt the control parameters to stay within the defined limits of safe operation. The adapted parameters are shown in Tab. 7.4.

Table 7.4: *Controller parameters for normal and high turbulence at 6 m/s ground wind speed.*

I_{197}	**7.2%**	**26.5%**	**Description**
P_{up} [W]	24500	21100	upper power
δu_{d} [%]	0.0	5.3	additional depower
τ_{d} [ms]	150	50	depower delay

This resulted in a reduced power output as shown in Tab. 7.5. In practice this is not a problem, because such a high turbulence levels are very rare. If the system has to be operated at a lower hight or in other environments with higher turbulence, then a mechanical brake could be used to reduce the power peaks. This would improve the robustness and would make it unnecessary to reduce the average reel-out power in wind conditions with a high turbulence intensity.

Table 7.5: *Performance for normal and high turbulence at 6 m/s ground wind speed. At lower wind speed high turbulence intensities do not reduce the average mechanical power, but increase it. Therefore the overall influence of turbulence on the energy yield is low.*

I_{197}	**7.2%**	**26.5%**	**Description**
$P_{\text{m,av}}$ [W]	11970.0	9246.0	average mechanical power
D [%]	72.7	76.1	duty cycle (Eq. 3.13)
η_{p} [%]	80.2	76.9	pumping efficiency (Eq. 3.16)
η_{cyc} [%]	58.3	58.6	cycle efficiency (Eq. 3.18)
$CF_{\text{P,ro}}$ [-]	1.49	1.74	crest factor reel-out power
$P_{\text{max,ro}}$ [-]	29797.7	28515.4	maximal reel-out power
$CF_{\text{F,ro}}$ [-]	1.10	1.26	crest factor reel-out force
$F_{\text{max,ro}}$ [-]	7995.8	7984.7	maximal reel-out force

The 2D projection of the flight path is shown is shown in Fig. 7.17. One can see the influence of the turbulence, but the deviations from the planned flight path are still small and without any negative impact on stability or performance.

The wind speed at the kite is shown in Fig. 7.18. It varies between 7.9 and 17.6 m/s, which is a very large range. It also varies fast, up to -24.9 m/s^2.

The apparent wind speed at the kite is shown in Fig. 7.19. The variations of the apparent wind speed during reel-out is smaller than the variation of the wind speed at

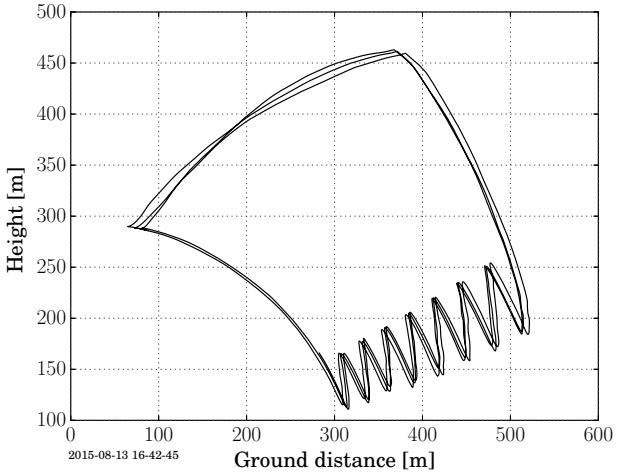

Figure 7.17: *Simulated flight path of the kite, flying at the nominal speed of 6.0 m/s at 10 m height and a turbulence intensity of 26.5%, which was the highest value that was recorded at Cabauw, The Netherlands in 2011. The turbulence is well visible, but not causing any problems.*

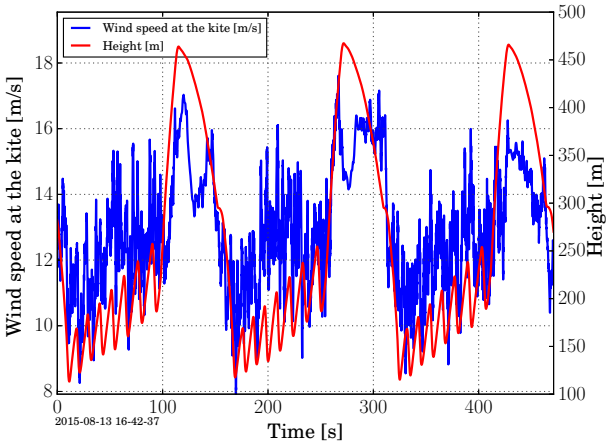

Figure 7.18: *Wind speed at the height of the kite, flying at the nominal speed of 6.0 m/s at 10 m height and a turbulence intensity at 200 m height of 26.5%. The minimum wind speed is 7.9 m/s, the maximum 17.6 m/s and the fastest change of the wind speed is -24.9 m/s^2.*

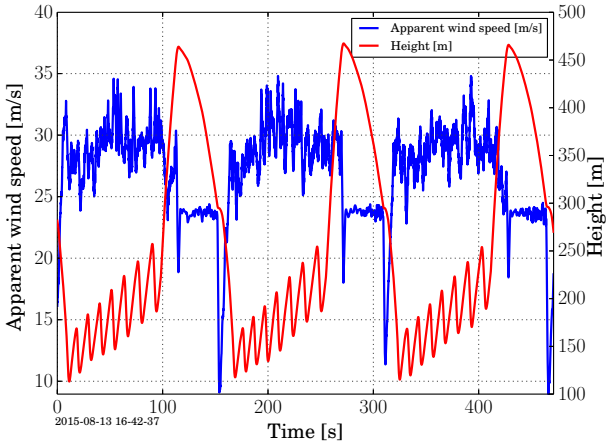

Figure 7.19: *The apparent wind speed at the kite, flying at the nominal speed of 6.0 m/s at 10 m height and a turbulence intensity at 200 m height of 26.5%. The minimal apparent wind speed is 9.0 m/s, the maximum 34.8 m/s and the highest apparent wind acceleration* $\dot{v}_a = 43.7\ m/s^2$.

the height of the kite. Reasons for this are the inertia of the kite and the active angle attack control. During the lower intermediate state there is a large dip in the apparent wind speed.

In Fig. 7.20 the tether force at the ground station and the reel-out speed are shown. The force varies a lot, but never exceeds the limit of 8000 N. Fig. 7.21 shows the mechanical power vs. the reel-out speed. The average power had to be reduced to keep the power peaks below 30 kW.

In Fig. 7.22 the angle of attack is shown. It always stays within zero and 20° which means, that it neither buckles nor stalls. The dips during the reel-out phase are due to the active depower control, that is used to limit the power.

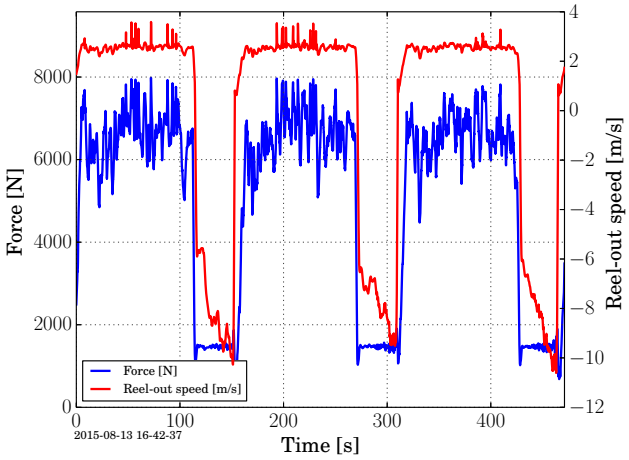

Figure 7.20: *Tether force at the ground and reel-out speed for three power cycles at the nominal wind speed of 6.0 m/s at 10 m height and a turbulence intensity at 200 m height of 26.5%.*

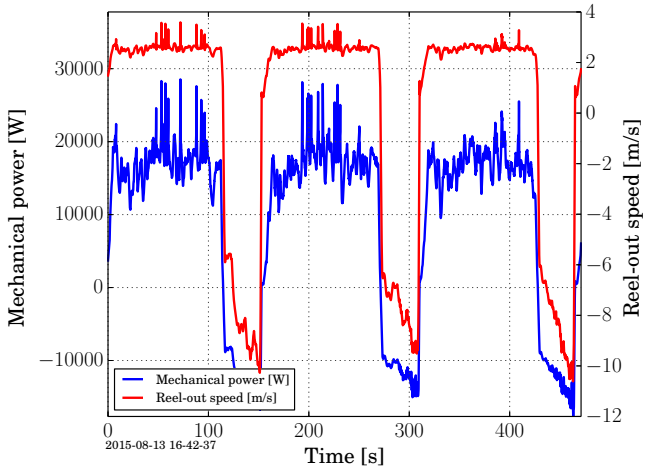

Figure 7.21: *Mechanical power and reel-out speed for three power cycles at the nominal wind speed of 6 m/s at 10 m height and a turbulence intensity at 200 m height of 26.5%. The high power peaks are problematic. The average reel-out power had to be limited to 16659 W, which is about 22% less than the average reel-out power at 7.2% turbulence intensity.*

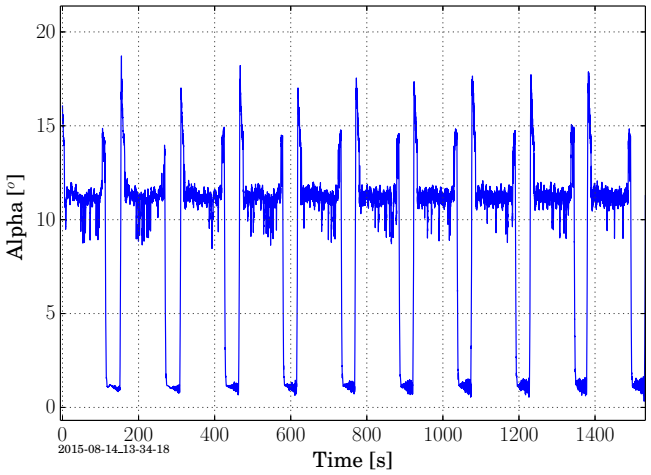

Figure 7.22: *Angle of attack α for 10 power cycles at the nominal wind speed of 6 m/s at 10 m height and a turbulence intensity at 200 m height of 26.5%. The angle of attack is always positive and always lower than 20°. This means, the kite neither buckles nor stalls.*

7.4.7 Comparison with experimental data

A comparison of the performance factors for nominal operation of the simulated kite power system and experimental data from 2012 is shown in Tab. 7.6. For a visual understanding of the differences, please compare Fig. 7.6 and Fig. B.2.

The main improvements of the simulated system are: First, the nominal force is increased by a factor of two. This allows a lower reel-out speed and thus a better duty cycle D. Second, the maximum reel-in speed is slightly increased (from 9 m/s to 11 m/s) which also improves the duty cycle. Third, the improved control system, which results in a lower crest factor $CF_{\mathrm{P,ro}}$ and thus a higher average power. Furthermore adjusting the elevation angle and the depower settings dynamically also allows to operate the system closer to the absolute power limit of 30 kW. In total the average mechanical power is increased in the simulation by 86 % compared to the best, measured cycle and by 97 % compared to the average of the best eight cycles.

[1] In 2011 the data of six test flights was recorded, in 2012 the data of 25 test flights in different wind conditions. Only during one flight the kite was flying power cycles with a maximal tether length of 700 m, which gave the best results. All other flights operated on a shorter tether due to airspace restrictions.

Table 7.6: *Performance factors for nominal operation of the optimized, simulated system, the best cycle measured 2012 and the average of the eight best cycles[1] 2012. Both systems have a generator with 20 kW nominal power and use the same lift and drag coefficients of the wing.*

	Simulation 2015	Best Cycle 2012	Av. 2012	Description
$P_{m,av}$ [W]	11970	6436	6081	average mechanical power
D [%]	72.7	62.0	55.1	duty cycle (Eq. 3.13)
η_p [%]	80.2	77.0	76.4	pumping efficiency (Eq. 3.16)
η_{cyc} [%]	58.3	47.8	42.1	cycle efficiency (Eq. 3.18)
$CF_{P,ro}$ [-]	1.49	1.87	1.98	crest factor reel-out power
$P_{max,ro}$ [-]	29798	25132	28901	maximal reel-out power

7.4.8 Power curve and capacity factor

In Fig. 7.23 the power curve of the 8000 N kite power system is shown. The probability distribution function (PDF) of the wind speed is shown in Fig. 7.24. It is based on the wind data, measured at Cabau, The Netherlands at 200 m height, but then transformed to the reference height of 10 m by dividing the wind speed by 2.265 according to the average, exponential wind profile.

By multiplying both functions and integrating over all wind speeds the average power can be calculated. The results are presented in Tab. 7.7.

Table 7.7: *Power output and capacity factor of a kite power system with a nominal electrical power rating of 10055 W. A down time due to maintenance of 18 days per year is assumed to calculate the net power and the net capacity factor. Limiting the power output by changing the reel-out elevation β instead of adapting the angle of attack only is slightly more efficient. Compared to a wind turbine with 12 m diameter on a 20 m tower with a generator of the same power rating the average power is about the same, but the capacity factor two times higher.*

	Adapting β	Constant β	20kW wind turbine
Gross average electrical power [W]	4042.1	4037.5	3991.3
Net average electrical power [W]	3840.0	3835.6	3791.8
Gross capacity factor [%]	40.2	40.2	20.0
Net capacity factor [%]	38.2	38.1	19.0

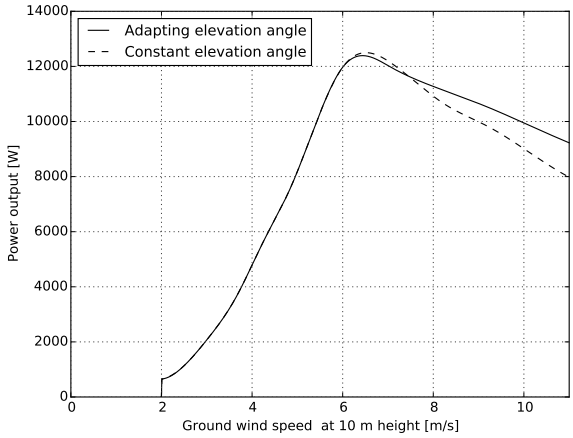

Figure 7.23: *Average mechanical power of a kite power system, using a 20 kW generator with a maximal tether force of 8000 N. Increasing the average elevation angle at high wind speeds increases the power output due to the shorter transition phase, but also increases the wear of the depower actuator.*

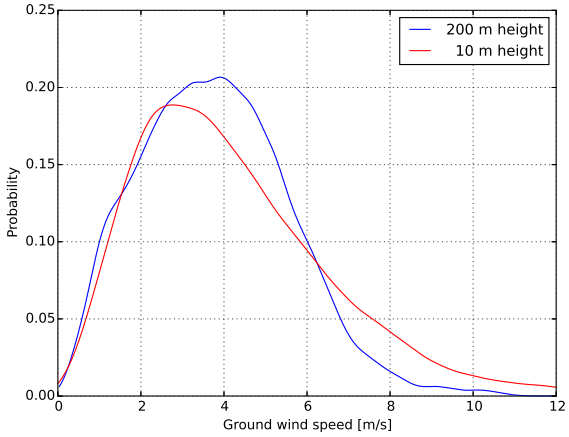

Figure 7.24: *Probability distribution functions (PDFs) of the wind speed at Cabau, The Netherlands in 2011. The distribution at 200 m height is used and converted to the reference height of 10 m by multiplying the wind speed with* $1/2.265$ *according to the exponential wind profile law. Compared to the distribution, measured at 10 m height the distribution at 200 m is more compact. Wind speeds above 11 m/s did not occur.*

7.5 Summary and conclusion

In this chapter the simulation results of operating a 20 kW kite power system in a turbulent wind environment were presented:

First, the adaptions that were needed when integrating the controllers, that were developed against simple 2D and 2.5D models with the 3D dynamic system model as presented in Chap. 4 were explained. Then the simulation results for four different wind conditions were presented. It was shown, that stable and consistent results are obtained in any of the investigated wind conditions.

Different ways of limiting the power at high wind speeds were investigated. It is slightly more effective to increase the elevation angle at high wind speeds than to change the depower settings only, but only if the angle of attack is constantly adapted during reel-out. This corresponds well to the results, obtained with the optimization routines in Sec. 3.4.1, that were based on a simplified 2D model.

The robustness of the control system has been shown for a turbulence intensity of 26.5 % at 200 m height and nominal wind speed. To improve the robustness against even stronger wind gusts it is suggested to add a mechanical brake to the generator that can limit the power input of the electrical machine.

Compared to the experimental results as shown in Appendix B the average power output in nominal wind conditions can be improved by a large extend. Improvements of 86 % to 97 % have been calculated. Of these improvements 17 % are due to an improved ground station with lower, nominal reel-out speed and a higher maximal reel-in speed, but the major part of the improvement (69 %) is due to the new control system design.

Finally power curves for 600 m maximal tether length were presented showing that a capacity factor of about 38% can be reached with a maximal tether force of 8000 N. This can be translated in a value of about 667 N per kW nominal, electrical power for the given site.

This shows, that reliable kite power systems can be designed and controlled, that have a much higher capacity factor than wind turbines with the same generator power. This can be an important advantage mainly for off-grid applications, because a smaller battery storage is needed, when the capacity factor increases, and the battery costs are a major part of the total system costs.

Another advantage of kite power systems is, that they don't need a tower. This can reduce the total system mass by a factor of three, or even by a factor of six, if also the mass of the foundation is taken into account. Therefore the use of airborne wind energy

systems could be a good choice for locations with bad transport infrastructure, where the transport of a wind turbine, tower and crane it is not possible or too expensive. The challenge of discontinues power production due to the pumping mode of operation can be overcome by either cheap, short term storage like supercapacitors, or by phase-shifted operation in wind parks.

Further research is needed on flight path optimization, kite state estimation, automatic launch and landing and on comparing different system concepts.

CHAPTER 8

Conclusions and Outlook

Contents

8.1 Conclusions 185
8.2 Outlook 186
8.2.1 Simulations 186
8.2.2 Optimization 187
8.2.3 Estimations 187
8.2.4 Testing 187
8.2.5 Control 188
8.2.6 Automated launch and landing 188

8.1 Conclusions

In this thesis the first, complete methodology for the development of a control system for airborne wind energy devices was presented. It uses only well established control approaches, the resulting control system is robust for system delays and wind turbulence and the methodology can be applied by any electrical or control engineer. A system, using a 20 kW generator, a single-line tether and a leading-edge inflated tube kite was used as example, but the methodology can in principle be applied to all airborne wind energy systems in pumping mode of operations, because all of these systems can be modelled as particle system and all of them need flight-path and winch control. Some modelling and control approaches, in particular the dynamic system model and the flight path planner and -controller can also be applied to systems, that use onboard power generation. A particle system for modelling the tether and the wing can be used for any airborne wind energy system.

For pumping mode of operation the performance factors duty cycle, pumping efficiency, cycle efficiency and total efficiency as defined in Chap. 3 are very important: For understanding and comparing different systems, try to get these numbers from the manufacturer. From the point of view of the author a total efficiency of more than 50% is possible and required for good 20 kW systems (larger systems should have a slightly higher total efficiency).

The design of a ground station is challenging: It must have a good efficiency at low speeds and high torque, but also at high speed and low torque. To achieve this with a single electrical machine without a gearbox is difficult. A possible solution might be to add a two-speed gearbox.

For the control of airborne wind energy systems during normal operation nonlinear, model predictive control is not required, even though it might be of advantage for automated launch and landing, which was not subject of this research. Parameter varying PID controllers combined with nonlinear inversion are sufficient to achieve a good control performance, even though optimal control might give an even higher level of robustness.

The challenge to adapt the controller parameters to changing wind conditions automatically was partially solved: A numerical solution for the optimal reel-in force as function of the wind speed was presented (Fig. 7.16). Furthermore, the reel-out speed and force controller works fine in a large range of wind speed. Automatic adaption to changes of the turbulence intensity needs further investigations.

8.2 Outlook

8.2.1 Simulations

Extending the current simulation framework with more, different components would be very useful: For example with a rigid wing, multi-line systems and with synchronous generator models. This would enable a direct comparison of different airborne wind energy concepts in the same simulation environment and the same environmental conditions. Furthermore a simplified, fast simulation model as proposed by (van der Vlugt et al. 2015) should be developed and validated against the detailed, dynamic model as presented in this thesis, mainly as basis for fast energy and cost optimizations. A first approach in this direction, investigating the scaling effects of airborne wind energy systems

will be published in Fechner and Schmehl (2016a). An simplified, non-linear model of a tether with tether-sag could improve the development of winch controllers.

8.2.2 Optimization

The flight path should be further optimized, using mathematical optimization algorithms as suggested in (Gros et al. 2013). It should be investigated, if reeling in at the side of the wind window is more efficient as suggested by (Zgraggen et al. 2014a). Implementing an automated optimization algorithm is important to be able to investigate the performance of more different system configurations in a reasonable amount of time.

8.2.3 Estimations

The suggested control system needs an estimate of the wind speed at the height of the kite. The currently used approach (measure the ground wind speed and apply a wind profile) could be improved in various ways, for example by using the tether force to estimate the apparent speed. Because the sensors for the kite position and the heading of the kite are not very accurate and reliable, the development of a kite state estimator, that combines the date of different sensors with a simple KPS model would be very useful. Some initial work in this field was already done by (Ranneberg 2013) and (Peschel 2013). Furthermore, estimating and predicting the wind speed and wind turbulence not only based on the sensors of the kite system, but also by using meteorological data could help to improve the accuracy predicted turbulence and thus the power output. Finally a prediction of the duration of low wind periods, but also of lightning would help to minimize the down time due to landing.

8.2.4 Testing

The kite model should be further validated in real-world tests, which should be executed with accurate 3D- wind field measurements in place. Furthermore, tests with improved wings should be executed. For a validation of the proposed winch controller a new winch control hard- and software should be implemented, that allows the implementation of a fast force control loop. Long term testing in changing wind conditions would also be useful to verify and improve the robustness of the control system.

8.2.5 Control

To improve the flight path controller, it would be useful to improve the 2D Simulink model such that it has the same impulse response as the dynamic 3D model. When an approximated, fast 2D model is in place, then different methods can be used to improve the two controllers, one for flying straight and one for turning. In particular for determining the end time of the best turn action a simple model predictive controller might be useful.

Another approach to improve the flight path controller would be to use iterative learning control: Not only the best time for ending the turn actions, but also the position of the attractor points and the correction factors for c_1 and c_2 of the turn rate law could be improved by a learning algorithm, depending on the wind speed, the depower settings and the elevation angle. This could replace manual parameter tuning and would make it easier to adapt the controller to different wing- and actuator dynamics.

To improve the winch controller a motor controller with Direct Torque Control (DTC) as characterized for example by (Zelechowski 2005) could be used. This might improve the speed of the force control loop significantly. The depower controller could be extended to full angle of attack control by adding a angle of attack sensor or estimator. This could improve the robustness and the power output. Furthermore, the influence of the control strategy on the lifetime and power consumption of the actuators should be investigated.

8.2.6 Automated launch and landing

For the commercialization of airborne wind energy systems automated launch and landing is crucial. The first company, that demonstrated automated launch landing for an airborne wind energy system was Makani power, acquired by Google in 2013. (Cherubini et al. 2015) write:

> Makani has developed and tested its 8m, 20kW demonstrator, called 'Wing 7' that showed the capability of fully automatic operations and power production. ... Makani is currently developing a 600 kW prototype, 'the M600'. The M600 AWT has eight turbines, each with five propeller blades, and has a wingspan of 28 m. The prototype is now undergoing testing.

At least three companies (TwingTec, Switzerland, e-Kite, The Netherlands and KiteMill, Norway) are currently (2016) trying to apply the concept of vertical takeoff and

landing to systems, that work in pumping mode of operation. TwingTec is using three tilt-rotors, while the other two companies are using four vertical rotors without tilt mechanism. While this can work well for smaller kite power systems, the additional mass might become too large for large scale systems, because they have a higher wing loading.

Another company, Skysails GmbH, Germany has an automated launch and landing system for kites, that pull ships, but to the best of the authors knowledge it was not yet combined with a kite power system for electricity generation. From the point of view of the author it would be difficult to adapt this launch system for onshore applications, because it needs quite high wind speeds at low altitudes (a short, hydraulic mast) for launching. At least two more companies have automated launch- and landing systems in development (Ampyx Power, The Netherlands and Enerkite, Germany) using different principles of operation. Ampyx power was investigating different concepts, for example a cart that accelerates their kite-plane to take-off speed (Bontekoe 2010), but it is not known, which concept is their current favourite. Enerkite is implementing rotational launch and landing.

The team of Prof. Moritz Diehl is investigating rotational launch and landing since 2010 (Zanon et al. 2013), and Van et al. (2016) published a simulation study on autonomous take-off and landing of a tethered rigid aircraft using an on-board propeller. On the American Control Conference (ACC) 2016 it was explained, that while launching worked well in an experimental setup, automatic landing was not yet achieved.

The methodology, presented in this thesis (physical model, based on a particle system combined with a flight path planner that uses attractor points and turn actions) could well be applied not only to the normal operation of airborne wind energy systems, but also be used for research on automated launch and landing. This would close the last, missing gap on the road to the successful commercialisation.

APPENDIX A

Implementation of the FPC in Python

Implementation of the ($\mathbf{p}_k^{SE}$, ψ, χ) flight path controller with NDI and turn actions as explained in Sec. 6.2.4 in Python.

```
# -*- coding: utf-8 -*-
"""
* This file is part of FreeKiteSim.
*
* FreeKiteSim -- A kite-power system power simulation software.
* Copyright (C) 2013 by Uwe Fechner, Delft University
* of Technology, The Netherlands. All rights reserved.
*
* FreeKiteSim is free software; you can redistribute it and/or
* modify it under the terms of the GNU Lesser General Public
* License as published by the Free Software Foundation; either
* version 3 of the License, or (at your option) any later version.
*
* FreeKiteSim is distributed in the hope that it will be useful,
* but WITHOUT ANY WARRANTY; without even the implied warranty of
* MERCHANTABILITY or FITNESS FOR A PARTICULAR PURPOSE. See the GNU
* Lesser General Public License for more details.
*
* You should have received a copy of the GNU Lesser General Public
* License along with FreeKiteSim; if not, write to the Free Software
* Foundation, Inc., 51 Franklin Street, Fifth Floor, Boston, MA 02110-1301 USA
"""
import numpy as np
import scipy
from math import sin, cos, atan2, radians, degrees, pi

PERIOD_TIME = 1/50.0

TAU = 0.95 # Factor, that determines the time constant of D part of the turn rate controller

# Settings of the flight path controller
FPC_P    = 20.0 # P gain of the PID controller
FPC_I    =  1.2 # I gain of the PID controller
FPC_D    = 10.0 # D gain of the PID controller
FPC_GAIN = 0.016 * 1.6 # additional factor for P, I and D

C1 = 0.262    # identified steering sensitivity for the hydra kite
C2 = 6.27     # identified gravity sensitivity for the hydra kite
K_C1  =  0.6  # correction factor for C1, used by the NDI block  (0.8 < K_C1 < 1.2)
K_C2  =  0.4  # correction factor for C2, used by the NDI block (-1.5 < K_C2 > 1.5)
```

```
def saturation(value, min_, max_):
    """ Calculate a saturated value, that stays within the given limits. """
    result = value
    if result > max_:
        result = max_
    if result < min_:
        result = min_
    return result

def wrapToPi(value):
    """ Return a value in the range of +- pi. """
    if value < -pi:
        result = value + 2 * pi
    elif value > pi:
        result = value - 2 * pi
    else:
        result = value
    return result

def mergeAngles(alpha, beta, factor_beta):
    """ Calculate the weighted average of two angles. The weight of beta,
    factor_beta must be between 0 and 1. """
    x1 = sin(alpha)
    y1 = cos(alpha)
    x2 = sin(beta)
    y2 = cos(beta)
    x = x1 * (1.0 - factor_beta) + x2 * factor_beta
    y = y1 * (1.0 - factor_beta) + y2 * factor_beta
    return atan2(x, y)

class Integrator(object):
    """ Discrete integrator with external reset. """
    def __init__(self, I=1.0, x_0=0.0, period_time=PERIOD_TIME):
        """
        Constructor. Parameters:
        I:   integration constant
        x_0: initial ouput
        period time: period time of the discrete control system in seconds
        """
        self._output = x_0
        self._last_output = x_0
        self._I = I
        self.period_time = period_time

    def reset(self, x_0):
        """ Initialize the integrator with the value x_0. """
        self._output = x_0
        self._last_output = x_0

    def calcOutput(self, input_):
        """ Calculate the output of the integrator depending on the input_. This method
        can be called multiple times per time step. """
        self._output = self._last_output + input_ * self._I * self.period_time
        return self._output

    def getOutput(self):
        """ Return the current integrator output. """
        return self._output

    def getLastOutput(self):
        """ Return the integrator output at the end of the last timestep. """
        return self._last_output

    def onTimer(self):
        """ Update the integrator state. Must be called once per PERIOD_TIME. """
        self._last_output = self._output
```

This class implements the block diagrams Fig. 6.7, Fig. 6.8 and Fig. 6.10. Stateless Simulink blocks are represented as functions, statefull blocks as classes.

```
class FlightPathController(object):
    """
    FlightPathController as specified in chapter six.

    Main inputs are calls to the methods:
    - onNewControlCommand()
    - onNewSystemState()

    Main output is the set value of the steering u_s, returned by the method:
    calcSteering() This method needs the current time step as parameter.

    Once per time step the method onTimer() must be called.
    """
    def __init__(self):
        self.count = 0                # cycle number
        self.attractor = np.zeros(2) # attractor coordinates, azimuth and elevation in radian
        self.psi_dot_set = None       # desired turn rate in rad per second or None
        self.psi_dot_set_final = None # the same, but without D part
        self.phi = 0.0                # the azimuth angle of the kite position in radian
        self.beta = 0.0               # the elevation angle of the kite position in radian
        self.psi = 0.0                # heading of the kite in radian
        self.chi = 0.0                # course in radian
        self.chi_factor = 0.0         # 0.0 use psi only; 1.0 use chi only
        self.omega = 0.0              # angular velocity of the kite in degrees/s
        self.est_psi_dot = 0.0        # estimated turn rate
        self.chi_set = 0.0            # desired flight direction (bearing)
        self.u_d0 = 0.24              # minimal value of the depower setting for the fully powered kite
        self.u_d_max = 0.422          # maximal value of the depower setting for the fully depowered kite
        self.u_d_prime = 0.2          # normalized depower settings
        self.u_s_max = 0.99           # maximal value of the steering settings
        self.psi_dot_max = 3.0        # maximal value of the turn rate in radians per second
        self.K_d_s = 1.5              # influece of the depower settings on the steering sensitivity
        self.u_d = self.u_d0          # actual depower setting (0..1)
        self.c1 = C1 * K_C1           # identified value for hydra kite from paper [rad/m]
        self.v_a = 0.0                # apparent wind speed at the kite
        self.v_a_min = 8.0            # minimal apparent wind speed for full NDI
        self.ndi_gain = 1.0           # quotient of the output and the input of the NDI block
        self.int = Integrator()       # integrator for the I part of the pid controller
        self.int2 = Integrator()      # integrator for the D part of the pid controller
        self.P = FPC_P                # P gain of the PID controller
        self.I = FPC_I                # I gain of the PID controller
        self.D = FPC_D                # D gain of the PID controller
        self.gain = FPC_GAIN          # additional factor for P, I and D
        self.K_u = 5.0                # anti-windup gain for limited steering signal
        self.K_psi = 10.0             # anti-windup gain for limited turn rate
        self.err = 0.0                # error (input of the PID controller)
        self.res = np.zeros(2)        # residual of the solver
        self.u_s = 0.0                # steering output of the FPC, caculated by solve()
        self.k_psi_in = 0.0           # last value of the input of the K_psi block of the feedback loop
        self.k_u_in = 0.0             # last value of the input of the K_u block of the feedback loop
        self.reset_int1 = False       # flag to reset the integrator when the turn action becomes active
        self.radius = None            # set value of the radius of the last turn action
        self._N = 15                  # constant N of the filter of the D part
        self._i = 0                   # number of calls of solve
```

```
    def onNewControlCommand(self, attractor=None, psi_dot_set=None, radius=None):
        """
        Input:
        Either the attractor point (numpy array of azimuth and elevation in radian),
        or psi_dot, the set value for the turn rate in degrees per second.
        """
        if radius is not None:
            psi_dot_set = degrees(self.omega / radius) # desired turn rate during the turns
        self.radius = radius
        if psi_dot_set is None and self.psi_dot_set is not None:
            # reset integrator
            self.reset_int1 = True
        if attractor is not None:
            self.attractor[:] = attractor
        if psi_dot_set is not None:
            self.psi_dot_set_final = radians(psi_dot_set)
            self.psi_dot_set = self.psi_dot_set_final * 2.0
        else:
            self.psi_dot_set = None

    def onNewEstSysState(self, phi, beta, psi, chi, omega, v_a, u_d=None, u_d_prime=None, \
                               period_time=PERIOD_TIME):
        """
        Parameters:
        phi:  the azimuth angle of the kite position in radian
        beta: the elevation angle of the kite position in radian
        psi:  heading of the kite in radian
        """
        self.phi, self.chi = phi, chi
        self.omega = omega
        self.beta = beta
        if self._i > 0:
            delta = psi - self.psi
            if delta < -pi:
                delta += 2 * pi
            if delta > pi:
                delta -= 2 * pi
            self.est_psi_dot = (delta) / period_time
        self.psi = psi
        # Eq. 6.4: calculate the normalized depower setting
        if u_d_prime is None:
            self.u_d_prime = (u_d - self.u_d0) / (self.u_d_max - self.u_d0)
        else:
            self.u_d_prime = u_d_prime
        self.u_d = u_d
        self.v_a = v_a

    def _navigate(self, limit=50.0):
        """
        Calculate the desired flight direction chi_set using great circle navigation.
        Limit delta_beta to the value of the parameter limit (in degrees).
        """
        # navigate only if steering towards the attractor point is active
        if self.psi_dot_set is not None:
            return
        phi_set = self.attractor[0]
        beta_set = self.attractor[1]
        r_limit = radians(limit)
        if beta_set - self.beta > r_limit:
            beta_set = self.beta + r_limit
        if beta_set - self.beta < -r_limit:
            beta_set = self.beta - r_limit
        y = sin(phi_set - self.phi) * cos(beta_set)
        x = cos(self.beta) * sin(beta_set) - sin(self.beta) * cos(beta_set) * cos(phi_set - self.phi)
        self.chi_set = atan2(-y, x)
```

Implementation of the nonlinear, dynamic inversion (NDI) block according to Eqs. (6.12 and 6.13).

```
    def _linearize(self, psi_dot):
        """
        psi_dot: desired turn rate in radians per second
        fix_va: keep v_a fixed for the second term of the turn rate low; was useful in some
        simulink tests.
        """
        # calculate v_a_hat
        if self.v_a >= self.v_a_min:
            v_a_hat = self.v_a
        else:
            v_a_hat = self.v_a_min
        # calculate the steering from the desired turn rate
        u_s = (1.0 + self.K_d_s * self.u_d_prime) / (self.c1 * v_a_hat) \
              * (psi_dot - C2 * K_C2 / v_a_hat * sin(self.psi) * cos(self.beta))
        if abs(psi_dot) < 1e-6:
            psi_dot = 1e-6
        self.ndi_gain = saturation(u_s / psi_dot, -20.0, 20.0)
        if abs(self.ndi_gain) < 1e-6:
            self.ndi_gain = 1e-6
        return u_s

    def _calcSat1In_Sat1Out_SatIn_Sat2Out(self, x):
        """
        see Fig. 6.6
        x: vector of k_u_in, k_psi_in and int2_in
        """
        k_u_in   = x[0]
        k_psi_in = x[1]

        # calculate I part
        int_in = self.I * self.err + self.K_u * k_u_in + self.K_psi * k_psi_in
        int_out = self.int.calcOutput(int_in)

        # calculate D part
        int2_in = self._N * (self.err * self.D - self.int2.getLastOutput()) \
                          / (1.0 + self._N * self.int2.period_time)
        self.int2.calcOutput(int2_in)

        # calculate P, I, D output
        sat1_in = (self.P * self.err + int_out + int2_in) * self.gain

        # calcuate saturated set value of the turn rate psi_dot
        sat1_out = saturation(sat1_in, -self.psi_dot_max, self.psi_dot_max)
        # nonlinar inversion
        sat2_in = self._linearize(sat1_out)
        # calculate the saturated set value of the steering
        sat2_out = saturation(sat2_in, -self.u_s_max, self.u_s_max)
        return sat1_in, sat1_out, sat2_in, sat2_out, int_in

    def _calcResidual(self, x):
        """
        see Fig. 6.6
        x: vector of k_u_in, k_psi_in and int2_in
        """
        sat1_in, sat1_out, sat2_in, sat2_out, int_in = self._calcSat1In_Sat1Out_SatIn_Sat2Out(x)
        k_u_in = (sat2_out - sat2_in) / self.ndi_gain
        k_psi_in = sat1_out - sat1_in
        self.res[0] = k_u_in - x[0]
        self.res[1] = k_psi_in - x[1]
        return self.res
```

Implementation of the block diagram Fig. 6.7 and Eqs. (6.16 and 6.17).

```
    def calcSteering(self, parking, period_time):
        """
        Calculate the steering output u_s and the turn rate error err.
        If the parameter parking is True, only the heading is controlled, not the course.
        """
        self.int.period_time, self.int2.period_time = period_time, period_time
        self._navigate()
        # control the heading of the kite
        chi_factor = 0.0
        if self.omega > 0.8:
            chi_factor = (self.omega - 0.8) / 1.2
        if chi_factor > 0.85:
            chi_factor = 0.85
        self.chi_factor = chi_factor
        if not parking:
            control_var = mergeAngles(self.psi, self.chi, chi_factor)
        else:
            self.chi_factor = 0.0
            control_var = self.psi
        self.err = wrapToPi(self.chi_set - control_var)
        if self._i == 0 or self.reset_int1:
            self.int.reset(0.0)
            self.reset_int1 = False
        x = scipy.optimize.broyden1(self._calcResidual, [self.k_u_in, self.k_psi_in], f_tol=1e-14)
        sat1_in, sat1_out, sat2_in, sat2_out, int_in = self._calcSat1In_Sat1Out_SatIn_Sat2Out(x)
        self.k_u_in = (sat2_out - sat2_in) / self.ndi_gain
        self.k_psi_in = sat1_out - sat1_in
        if self.psi_dot_set is not None:
            if self.radius is not None:
                self.psi_dot_set_final = self.omega / self.radius # desired turn rate during the turns
            self.psi_dot_set = self.psi_dot_set * TAU + self.psi_dot_set_final * (1 - TAU)

            self.u_s = saturation(self._linearize(self.psi_dot_set), -1.0, 1.0)
        else:
            self.u_s = sat2_out

        self._i += 1
        return self.u_s

    def getErr(self):
        """ Return the heading/ course error of the controller. """
        return self.err

    def onTimer(self):
        """
        This method updates the integrators.
        Must be called once every PERIOD_TIME after calling calcSteering.
        """
        self.int.onTimer()
        self.int2.onTimer()
```

APPENDIX B

Results from a flight test on a 400 m to 700 m tether

The following tether length and power profiles were recorded during a flight test on 2012-06-23 at the Maasvlakte 2, The Netherlands, using a kite with a projected area of 10.18 m^2 attached to the 20 kW kite power demonstrator of Delft University of Technology and operating automated pumping cycles.

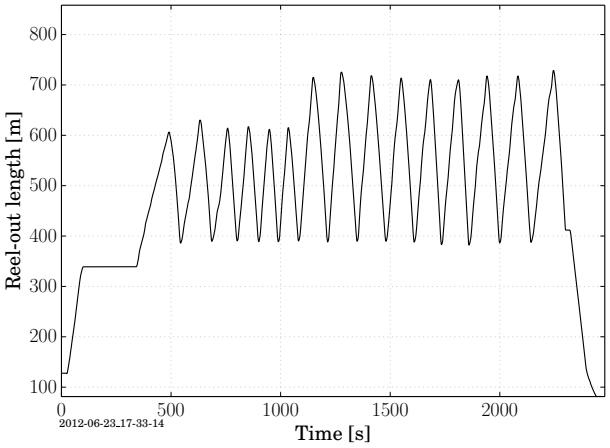

Figure B.1: *Reel-out length of the tether during a flight test on 2012-06-23 at the Maasvlakte 2, The Netherlands. The last nine cycles were using the full tether length. The very last cycle was omitted in the statistics, because it was ended prematurely.*

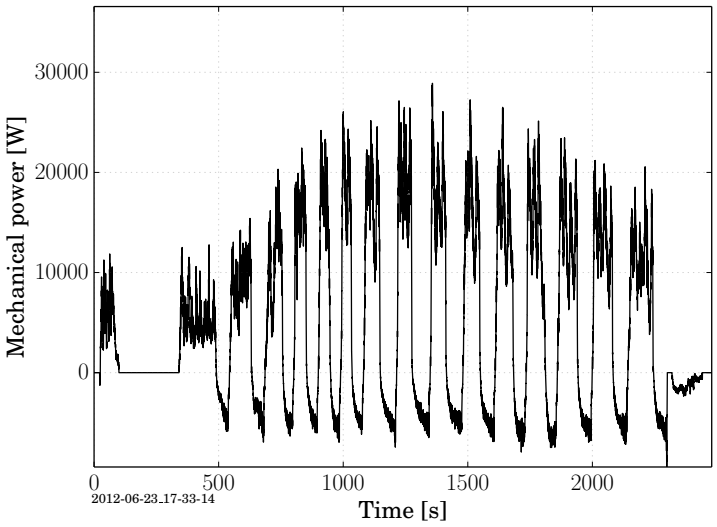

Figure B.2: *Measured mechanical power during a flight test on 2012-06-23 at Maasvlakte 2, The Netherlands. For the last nine cycles the system was operated at a tether length of about 400 m to 700 m. A comparison with the simulation results can be found in Sec. 7.4.7.*

Table B.1: *Average mechanical power, peak power, crest factor*[1] *of the reel-out power, duty cycle, pumping efficiency and cycle efficiency of eight power cycles, using 700 m tether length. The cycle efficiency is the product of the pumping efficiency and the duty cycle.*

Cycle	Start time [s]	$P_{\mathrm{m,av}}$ [W]	P_{max} [W]	$CF_{\mathrm{P,ro}}$	D [%]	η_{p}	η_{cyc}
1	1082	5968	25176	1.63	50.6	76.2	38.6
2	1215	6118	27149	1.60	47.3	76.3	36.0
3	1349	6114	28901	1.79	49.6	76.2	37.8
4	1481	6123	27248	1.84	54.1	76.2	41.2
5	1610	6336	26500	1.90	59.6	76.3	45.5
6	1734	6436	25132	1.87	62.0	77.0	47.8
7	1859	5879	23461	1.80	58.9	76.6	45.2
8	2000	5676	21190	1.68	58.8	76.4	44.9

[1] Quotient of the maximum and the average value of a physical quantity.

APPENDIX C

Summary of the Developed Methodology

The methodology for the design of kite-power control system as developed in this thesis can be summarized as follows:

1. Implement a simplified 2D kite model as explained in Sec. 6.2.1.
2. Implement a simplified winch system model as explained in Sec. 6.3.1.
3. Estimate the parameters c_1 and c_2 of the turn rate law, either by using measurement data with manual flight control as explained in Sec. 4.3.3 or based on the wing properties and on literature research.
4. Implement a flight path planner as explained in Chap. 5.3.
5. Develop a flight path controller, using the turn rate law as explained in Sec. 6.2.4.
6. Estimate or measure the winch parameters like max. speed, max. acceleration, inertia and efficiency.
7. Develop a winch controller, using the simplified winch model as explained in Sec. 6.3.2.
8. Determine the wind properties of the desired location using measurements and/or literature research as explained in Sec. 5.2.3.
9. Implement a dynamic system model as explained in Chap. 4.
10. Verify the developed control system against the dynamic system model in all relevant wind conditions. Optimize the controller parameters for maximal power output while not violating the constraints (like power and force) as explained in Chap. 7.
11. Validate the control system against the implemented system.

References

ABB. (2011). *Technical guide No. 1; Direct torque control - the world's most advanced AC drive technology*. Retrieved from www.abb.com/drives

Ahlgrim, Jim (Ed.). (2015). *IEA Wind 2014 Annual Report*. ISBN: 978-0-9905075-1-2.

Ahmed, M. S. (2014). *Optimisation de Contrôle Commande des Systèmes de Génération d'Électricité à Cycle de Relaxation* (PhD Thesis, Université de Grenoble). Retrieved from https://tel.archives-ouvertes.fr/tel-01071779

Ahmed, M., Hably, A. & Bacha, S. (2011). Power Maximization of a Closed-orbit Kite Generator System. In *50th ieee conference on decision and control and european control conference (ieee cdc-ecc 2011)* (p. 6). Orlando, FL, USA: IEEE.

Anderson et al., C. (2013). Assimulo, a simulation package for solving ordinary differential equations. Lund, Sweden: Lund University. Retrieved from http://www.jmodelica.org/assimulo

Archer, C. L. (2005). Evaluation of global wind power. *Journal of Geophysical Research*, *110*(D12), 1–20. doi:10.1029/2004JD005462

Archer, C. L., Delle Monache, L. & Rife, D. L. (2014, April). Airborne wind energy: Optimal locations and variability. *Renewable Energy*, *64*, 180–186. doi:10.1016/j.renene.2013.10.044

Argatov, I. & Silvennoinen, R. (2010a). Energy conversion efficiency of the pumping kite wind generator. *Renewable Energy*, *35*(5), 1052–1060. doi:10.1016/j.renene.2009.09.006

Argatov, I. & Silvennoinen, R. (2010b). Structural optimization of the pumping kite wind generator. *Structural Multidiscplinary Optimization*, *40*, 585–595. doi:10.1007/s00158-009-0391-3

Baayen, J. & Ockels, W. (2012). Tracking control with adaption of kites. *IET Control Theory and Applications*, *6*(2), 182. doi:10.1049/iet-cta.2011.0037

Becker, P. (2014). Our Sustainability Challenges. In *Sustainability Science* (Chap. Chapter 3, pp. 29–56). Amsterdam, Oxford, Waltham: Elsevier. doi:10.1016/B978-0-444-62709-4.00003-8

Bontekoe, E. (2010). *How to Launch and Retrieve a Tethered Aircraft, MSc Thesis* (MSc Thesis, Delft University of Technology).

Bosch, A., Schmehl, R., Tiso, P. & Rixen, D. (2014). Dynamic nonlinear aeroelastic model of a kite for power generation. *AIAA Journal of Guidance, Control and Dynamics*, *37*(5), 1426–1436. . doi:10.2514/1.G000545

Bosman, R., Reid, V., Vlasblom, M. & Smeets, P. (2013). Airborne wind energy tethers with high-modulus polyethylene fibers. In U. Ahrens, M. Diehl & R. Schmehl (Eds.), *Airborne Wind Energy* (Chap. 33, pp. 563–585). Berlin, Heidelberg: Springer. doi:10.1007/978-3-642-39965-7_33

Bottasso, C., Pizzinelli, P., Riboldi, C. & Tasca, L. (2014). LiDAR-enabled model predictive control of wind turbines with real-time capabilities. *Renewable Energy*, *71*, 442–452. doi:10.1016/j.renene.2014.05.041

Burton, T., Jenkins, N., Sharpe, D. & Bossanyi, E. (2001). *Wind Energy Handbook*. Chichester: John Wiley & Sons, Ltd. doi:10.1002/0470846062

Canale, M., Fagiano, L. & Milanese, M. (2010, March). High Altitude Wind Energy Generation Using Controlled Power Kites. *IEEE Transactions on Control Systems Technology*, *18*(2), 279–293. doi:10.1109/TCST.2009.2017933

Canale, M., Fagiano, L. & Milanese, M. (2009, March). KiteGen: A revolution in wind energy generation. *Energy*, *34*(3), 355–361. doi:10.1016/j.energy.2008.10.003

Cherubini, A., Papini, A., Vertechy, R. & Fontana, M. (2015). Airborne Wind Energy Systems: A review of the technologies. *Renewable and Sustainable Energy Reviews*, *51*, 1461–1476. doi:10.1016/j.rser.2015.07.053

Cochran, J., Mai, T. & Bazilian, M. (2014, January). Meta-analysis of high penetration renewable energy scenarios. *Renewable and Sustainable Energy Reviews*, *29*, 246–253. doi:10.1016/j.rser.2013.08.089

Coleman, J., Ahmad, H., Pican, E. & Toal, D. (2013). Non-Reversing Generators in a Novel Design for Pumping Mode Airborne Wind Energy Farm. In U. Ahrens, M. Diehl & R. Schmehl (Eds.), *Airborne Wind Energy* (Chap. 34, pp. 587–597). Berlin Heidelberg: Springer. doi:10.1007/978-3-642-39965-7_34

Costello, S. (2015). *Real-Time Optimization via Directional Modifier Adaptation, with Application to Kite Control* (PhD thesis, EPFL).

Diehl, M. (2013). Airborne Wind Energy: Basic Concepts and Physical Foundations. In U. Ahrens, M. Diehl & R. Schmehl (Eds.), *Airborne wind energy* (Chap. 1, pp. 3–22). Green Energy and Technology. Springer Heidelberg New York Dordrecht London. doi:10.1007/978-3-642-39965-7_1

Diehl, M. (2001). *Real-Time Optimization for Large-Scale Nonlinear Processes* (PhD thesis, Ruprecht-Karls-Universität Heidelberg).

Dréko, J. (2006). Sustainable development. [Online; accessed 27-October-2014]. Retrieved from http://en.wikipedia.org/wiki/File:Sustainable_development.svg

Eberhardt, B., Etzmuß, O. & Hauth, M. (2000). Implicit-Explicit Schemes for Fast Animation with Particle Systems. In N. Magnenat-Thalmann, D. Thalmann & B. Arnaldi (Eds.), *Computer animation and simulation 2000* (pp. 137–151). Eurographics. Vienna: Springer. doi:10.1007/978-3-7091-6344-3_11

EcoDriveCN. (2016). *Technical Specifications of V6-H series closed loop vector control and torque control frequency inverter*. EcoDriveCN drives. Retrieved 11th August 2016, from www.EcoDriveCN.com

Erhard, M., Horn, G. & Diehl, M. (2015). A quaternion-based model for optimal control of the SkySails airborne wind energy system. *Zeitschrift für Angewandte Mathematik und Mechanik*, (August), 1–18. arXiv: 1508.05494

Erhard, M. & Strauch, H. (2012). Control of Towing Kites for Seagoing Vessels. *submitted to IEEE Control Systems Magazine*, 1–12. arXiv: 1202.3641v3

Erhard, M. & Strauch, H. (2013). Theory and Experimental Validation of a Simple Comprehensible Model of Tethered Kite Dynamics Used for Controller Design. In U. Ahrens, M. Diehl & R. Schmehl (Eds.), *Airborne Wind Energy* (Chap. 8, pp. 141–165). Berlin Heidelberg: Springer. doi:10.1007/978-3-642-39965-7_8

Fagiano, L., Zgraggen, A. U., Morari, M. & Khammash, M. (2014). Automatic Crosswind Flight of Tethered Wings for Airborne Wind Energy: Modeling, Control Design and Experimental Results. *IEEE Transactions on Control Systems Technology*, *22*(4), 1433–1447. doi:10.1109/TCST.2013.2279592. arXiv: 1301.1064v2

Fagiano, L. (2009). *Control of Tethered Airfoils for High Altitude Wind Energy Generation: Advanced control methods as key technologies for a breakthrough in renewable energy generation* (PhD Thesis, POLITECNICO DI TORINO).

Fagiano, L. & Milanese, M. (2012). Airborne Wind Energy : an overview. Montréal, Canada: IEEE Control Systems Society.

Fagiano, L., Milanese, M. & Piga, D. (2010, March). High-Altitude Wind Power Generation. *IEEE Transactions on Energy Conversion*, *25*(1), 168–180. doi:10.1109/TEC.2009.2032582

Fagiano, L., Milanese, M. & Piga, D. (2012). Optimization of airborne wind energy generators. *International Journal of Robust and Nonlinear Control*, *22*, 2055–2083. doi:10.1002/rnc.1808

Furey, A. (2011). *Evolutionary Robotics in High Altitude Wind Energy Applications* (PhD, University of Sussex).

Gohl, F. & Luchsinger, R. H. (2013). Simulation Based Wing Design for Kite Power. In U. Ahrens, M. Diehl & R. Schmehl (Eds.), *Airborne Wind Energy* (Chap. 18, pp. 325–338). Berlin Heidelberg: Springer. doi:10.1007/978-3-642-39965-7_18

Goudarzi, M., Stonis, M. & Behrens, B.-a. (2014). Development of Lightweight Designs for the Production of Wind Turbine Towers. In M. F. Zaeh (Ed.), *Enabling Manufacturing Competitiveness and Economic Sustainability* (pp. 443–448). Cham: Springer International Publishing. doi:10.1007/978-3-319-02054-9

Gros, S., Zanon, M. & Diehl, M. (2013). A Relaxation Strategy for the Optimization of Airborne Wind Energy Systems. (pp. 1011–1016). Zürich, Switzerland: European Control Conference (ECC).

Hairer, E. & Wanner, G. (1996). *Solving Ordinary Differential Equations II, Stiff and Differential-Algebraic Problems* (2nd ed.). Berlin Heidelberg: Springer. doi:10.1007/978-3-642-05221-7

Harvest Ltd. (2016). *FVS Variable Frequency Drive*. Harvest Electric Technologies Co., Ltd. Retrieved 11th August 2016, from www.mediumvoltagedrive.com/2-frequency-converter-5.html

Heide, D., Bremen, L. von, Greiner, M., Hoffmann, C., Speckmann, M. & Bofinger, S. (2010, November). Seasonal optimal mix of wind and solar power in a future, highly renewable Europe. *Renewable Energy*, *35*(11), 2483–2489. doi:10.1016/j.renene.2010.03.012

Horn, G. & Diehl, M. (2013). Numerical Trajectory Optimization for AirborneWind Energy Systems Described by High Fidelity Aircraft Models. In U. Ahrens, R. Schmehl & M. Diehl (Eds.), *Airborne Wind Energy* (Chap. 11, pp. 205–218). Heidelberg, New York, Dordrecht, London: Springer. doi:10.1007/978-3-642-39965-7

Huscher, J. & Smith, D. (2013). *The unpaid health bill*. Health and Environment Alliance (HEAL). Brussels, Belgium.

International Energy Agency. (2012). *World Energy Outlook 2012, Executive Summary*. Paris, France.

Jehle, C. & Schmehl, R. (2014). Tracking Control on the Unit Sphere Applied to Traction Kites for Power Generation. *AIAA Journal Guidance, Control and Dynamics*, *37*(4), 1211–1222. doi:10.2514/1.62380

Katebi, R., Samson, J. & Vermillion, C. (2013). A Critical Assessment of Airborne Wind Energy Systems. *2nd IET Renewable Power Generation Conference (RPG 2013)*, 1–4. doi:10.1049/cp.2013.1852

KNMI, The Royal Netherlands Meteorological Institute. (2011). Cesar Tower Meteorological Profiles (Wind Data from Cabauw, TheNetherlands), validated. Retrieved from www.cesar-database.nl

Kost, C., Mayer, J., Thomsen, J. & Hartmann, N. (2013). *Levelized cost of electricity renewable energy technologies*. Fraunhofer Institute for Solar Energy Systems ISE. Freiburg, Germany.

Kroshko, D. (nodate). OpenOpt: free scientific-engineering software for mathematical modeling and optimization. Retrieved 8th July 2013, from http://www.openopt.org/

Loyd, M. (1980, May). Crosswind kite power (for large-scale wind power production). *Journal of Energy*, *4*(3), 106–111. doi:10.2514/3.48021

Lu, Y., Peng, Z., Miller, A. A., Zhao, T. & Johnson, C. W. (2015). How reliable is satellite navigation for aviation? Checking availability properties with probabilistic verification. *Reliability Engineering and System Safety*, *144*, 95–116. doi:10.1016/j.ress.2015.07.020

Mann, J. (1994, April). The spatial structure of neutral atmospheric surface-layer turbulence. *Journal of Fluid Mechanics*, *273*, 141. doi:10.1017/S0022112094001886

Mann, J. (1998, October). Wind field simulation. *Probabilistic Engineering Mechanics*, *13*(4), 269–282. doi:10.1016/S0266-8920(97)00036-2

Mathiesen, B. V., Lund, H. & Karlsson, K. (2011, February). 100% Renewable energy systems, climate mitigation and economic growth. *Applied Energy*, *88*(2), 488–501. doi:10.1016/j.apenergy.2010.03.001

Novara, C., Fagiano, L. & Milanese, M. (2011). Direct Data-Driven Inverse Control of a Power Kite for High Altitude Wind Energy Conversion. In *IEEE International Conference on Control Applications (CCA)*. Denver, CO, USA.

NREL, National Renewable Energy Laboratory. (2014). Life Cycle Assesment (LCA) Harmonization. Retrieved 31st October 2014, from http://en.openei.org/apps/LCA/

Obert, E. (2009). *Aerodynamic design of transport aircraft*. IOS Press. doi:10.3233/978-1-58603-970-7-i

Ockels, W. J. (2001). Laddermill, a novel concept to exploit the energy in the airspace. *Aircraft Design*, *4*(2-3), 81–97. doi:10.1016/s1369-8869(01)00002-7

Olivier, J. G., Janssens-Maenhout, G., Muntean, M. & Peters, J. A. (2013). *Trends in global CO2 emissions 2013 Report*. The Hague, The Netherlands: PBL Netherlands Environmental Assessment Agency, Institute for Environment and Sustainability (IES) of the European Commission's Joint Research Centre (JRC).

Peschel, J. (2013). *A cost effective kite state estimator for reliable control of kites* (MSc Thesis, Technische Universität Berlin).

Pineda, I., Azau, S., Moccia, J. & Wilkes, J. (2014). *Wind in Power: 2013 European Statistics*. THE EUROPEAN WIND ENERGY ASSOCIATION (EWEA).

Ranneberg, M. (2013). Sensor Setups for State and Wind Estimation for Airborne Wind Energy Converters. *arXiv*, 1–17. arXiv: 1309.1029v2

Ruiterkamp, R. & Sieberling, S. (2013). Description and Preliminary Test Results of a Six Degrees of Freedom Rigid Wing Pumping System. In U. Ahrens, M. Diehl & R. Schmehl (Eds.), *Airborne Wind Energy* (Chap. 27, pp. 443–458). Springer Heidelberg New York Dordrecht London. doi:10.1007/978-3-642-39965-7

Salvatore, J. (2013). *World Energy Perspective*. London: World Energy Council.

Schmehl, R., Noom, M. & Vlugt, R. v. d. (2013). Traction Power Generation with Tethered Wings. In *Airborne Wind Energy* (Chap. 2, pp. 23–45). Springer Berlin Heidelberg. doi:10.1007/978-3-642-39965-7_2

Schreuder, E. N. J. (2013a). *Development of an Adaptive Winch Controller for Kite-Power Generation*. Delft University of Technology.

Schreuder, E. N. J. (2013b). *Improving winch control performance in Kite Power Systems using gain scheduling and a compliant element* (MSc Thesis, Delft University of Technology).

Spera, D. A. (2008, October). *Models of Lift and Drag Coefficients of Stalled and Unstalled Airfoils in Wind Turbines and Wind Tunnels* (Technical Report No. NASA/CR–2008-215434).

Stull, R. B. (2000). *Meteorology for Scientists and Engineers* (2nd ed.). Thomson Learning.

Tamura, J. (2012). Calculation Method of Losses and Efficiency of Wind Generators. In S. Muyeen (Ed.), *Wind Energy Conversion Systems: Technology and Trends*

(Chap. Chapter 2, pp. 25–51). Green Energy and Technology. Springer London. doi:10.1007/978-1-4471-2201-2

Thorpe, D. (2011). *Modelling and Control of Tethered Kite Systems for Wind Energy Extraction* (Doctoral dissertation, RMIT University).

UNWCED, United Nations World Commission on Environment and Development. (1987). *Our Common Future (Brundtland Report)*. Oxford University Press. Oxford.

Vlugt, R. van der, Schmehl, R. & Noom, M. (2015). Quasi-Steady Model of a Pumping Kite Power System. *submitted to Renewable Energy*.

Van, E. N., Fagiano, L. & Schnez, S. (2016, July). On the autonomous take-off and landing of tethered wings for airborne wind energy. In *2016 american control conference (acc)* (pp. 4077–4082). doi:10.1109/ACC.2016.7525562

Veness, C. (1999). Calculate distance, bearing and more between Latitude/Longitude points. Retrieved 3rd December 2015, from http://www.movable-type.co.uk/scripts/latlong.html

Viré, A. (2012). How to float a wind turbine. *Reviews in Environmental Science and Bio/Technology*, *11*(3), 223–226. doi:10.1007/s11157-012-9292-9

Viré, A., Xiang, J., Milthaler, F., Farrell, P. E., Piggott, M. D., Latham, J.-P., … Pain, C. C. (2012). Modelling of fluid-solid interactions using an adaptive mesh fluid model coupled with a combined finite-discrete element model. *Ocean Dynamics*, *62*(10-12), 1487–1501. doi:10.1007/s10236-012-0575-z

Visioli, A. (2006). *Practical PID Control*. Springer London. doi:10.1007/1-84628-586-0

Vlugt, R. v. d., Peschel, J. & Schmehl, R. (2013a). Design and Experimental Characterization of a Pumping Kite Power System. In U. Ahrens, M. Diehl & R. Schmehl (Eds.), *Airborne Wind Energy* (Chap. 23, pp. 1–24). Green Energy and Technology. Springer Heidelberg New York Dordrecht London. doi:10.1007/978-3-642-39965-7

Vlugt, R. v. d., Schmehl, R. & Noom, M. (2013b). Quasi-Steady Kite Power System Model. *Renewable Energy*, 1–9.

Wildi, T. (2002). *Electrical Machines, Drives, and Power Systems* (5th ed.). Prentice Hall.

Williams, P., Lansdorp, B. & Ockels, W. J. (2007, August). Modeling and Control of a Kite on a Variable Length Flexible Inelastic Tether. In *Proceedings of the AIAA*

Modeling and Simulation Technologies Conference and Exhibit. Hilton Head, SC, USA. doi:10.2514/6.2007-6705

Wood, T. A., Hesse, H., Zgraggen, A. U. & Smith, R. S. (2015). Model-Based Identification and Control of the Velocity Vector Orientation for Autonomous Kites. In *2015 american control conference* (pp. 2377–2382). Chicago, IL, USA. doi:10.1109/ACC.2015.7171088

Yang, A. & Cui, Y. (2012). *Global Coal Risk Assessment: Data Analysis and Market Research*, World Resources Institute.

Zanon, M. & Diehl, M. (2013). A Relaxation Strategy for the Optimization of Airborne Wind Energy Systems. (pp. 1011–1016). Zürich, Switzerland: European Control Conference (ECC).

Zanon, M., Gros, S. & Diehl, M. (2013, July). Rotational Start-up of Tethered Airplanes Based on Nonlinear MPC and MHE. In *European Control Conference (ECC), 2013* (pp. 1023–1028).

Zelechowski, M. (2005). *Space Vector Modulated - Direct Torque Controlled (DTC-SVM) Inverter-Fed Induction Motor Drive* (PhD Thesis, Warsaw University of Technology). Retrieved from http://www.isep.pw.edu.pl/icg/pdf/phd/marcin%5C_zelechowski.pdf

Zgraggen, A. U., Fagiano, L. & Morari, M. (2015). Real-time Optimization and Adaptation of the Crosswind Flight of Tethered Wings for Airborne Wind Energy. *IEEE Transactions on Control Systems Technology*, *23*(2), 434–448. doi:10.1109/TCST.2014.2332537

Zgraggen, A. U., Fagiano, L. & Morari, M. (2014a). Automatic Retraction and Full Cycle Operation for a Class of Airborne Wind Energy Generators. *Preprints of the 19th World Congress of the International Federation of Automatic Control*, 5826–5831. doi:10.3182/20140824-6-ZA-1003.00624. arXiv: 1409.6151

Zgraggen, A. U., Fagiano, L. & Morari, M. (2014b). On Modeling and Control of the Retraction Phase for Airborne Wind Energy Systems. In *2014 IEEE 53rd Annual Conference on Decision and Control (CDC)* (pp. 5686–5691). Los Angeles, California, USA. doi:10.1109/CDC.2014.7040279

Zgraggen, A. U. (2014). *Automatic Power Cycles for Airborne Wind Energy Generators* (Dr. sc. ETH Zurich). doi:10.3929/ethz-a-010350742

Publications

Fechner, U. et al. (2014). Free KiteSim. Retrieved 10th February 2014, from https://bitbucket.org/ufechner/freekitesim

Fechner, U. et al. (2013). Kite Power System Optimizer. Retrieved 5th November 2014, from https://bitbucket.org/ufechner/awe_book

Fechner, U. & Schmehl, R. (2012a). Design of a Distributed Kite Power Control System. In *Proceedings of the IEEE Multi-Conference on Systems and Control* (pp. 800–805). IEEE. doi:10.1109/CCA.2012.6402695

Fechner, U. & Schmehl, R. (2016a). Downscaling of Airborne Wind Energy Systems. *Journal of Physics*, *753*, 102002. doi:10.1088/1742-6596/753/10/102002

Fechner, U. & Schmehl, R. (2014). Feed-Forward Control of Kite Power Systems. *Journal of Physics*, *524*(1), 12081. doi:10.1088/1742-6596/524/1/012081

Fechner, U. & Schmehl, R. (2016b, July). Flight Path Control of Kite Power Systems in a Turbulent Wind Environment. In *American Control Conference (ACC)* (pp. 4083–4088). Boston, MA, USA: IEEE. doi:10.1109/ACC.2016.7525563

Fechner, U. & Schmehl, R. (2016c). Flight Path Planning in a Turbulent Wind Environment. In *Airborne Wind Energy – Advances in Technology Development and Research* (Chap. 15, in press). Springer Berlin Heidelberg.

Fechner, U. & Schmehl, R. (2012b). High level control and optimization of kite power systems. In *Proceedings of 8th PhD Seminar on Wind Energy in Europe* (pp. 2–6). Zurich, Switzerland.

Fechner, U. & Schmehl, R. (2013). Model-Based Efficiency Analysis of Wind Power Conversion by a Pumping Kite Power System. In U. Ahrens, M. Diehl & R. Schmehl (Eds.), *Airborne Wind Energy* (Chap. 14, pp. 245–266). Berlin Heidelberg: Springer. doi:10.1007/978-3-642-39965-7_14

Fechner, U., Vlugt, R. V. D., Schreuder, E. & Schmehl, R. (2015). Dynamic Model of a Pumping Kite Power System. *Renewable Energy*, *83*, 705–716. doi:10.1016/j.renene.2015.04.028

Curriculum Vitae

Uwe Fechner was born 1960 in Berlin Spandau. He attended the Ernst-Barlach-Gymnasium (secondary school) in Kiel, Germany from 1970 until 1978, where he obtained his university-entrance diploma. He studied two years computer science at Kiel University and then went to Liverpool, England to do a voluntary social service at a home for mentally handicapped children. After working at Coventry Cathedral for 6 months he returned to Germany and attended a vocational academy for "chemical-technical assistants" in Neumünster. He finished this academy in July 1985.

From 1985 until 1998 he was working first two years at Kiel University, then for one year in an electronic laboratory, later founding and running a computer shop, a computer school and was working as independent software consultant. For one year he was working in the office of the "Refugee council of Schleswig-Holstein".

Later he was working as software and hardware developer for several companies in Kiel from January 1999 to March 2008. For five years he was developing security related control software for medical devices at Pegasus GmbH, Kiel. At the same time he was doing distant learning at FernUniversität Hagen and obtained his BSc in Information- and Communication Engineering in 2006.

From April 2008 to June 2010 he was working as project engineer at the University of Applied Science, Kiel in the field of power electronics (development of an highly

efficient power converter for electric vehicles). He obtained his MSc in electrical engineering (with Distinction) from FernUniversität Hagen in June 2010. Since July 2010 he is working as kite control researcher at Delft University of Technology, first at the Institute for Applied Sustainable Science, Engineering and Technology (ASSET) and since January 2013 at the faculty of aerospace engineering in the section wind energy.

In 2015 he was working first, as scientific advisor for the "Steinbeiss Institute for Technology Transfer and Integrated Systems", Karlsruhe, Germany, then for "enevate B.V.", The Hague, Netherlands and furthermore for Delft University of Technology before he started his own business, "aenarete – Wind Drones" in The Hague.